University of Milano-Bicocca

Department of Physics G. Occhialini
PhD program in Physics and Astronomy – XXXVII cycle

Non-perturbative QCD at all temperatures: Equation of State and Renormalization

Matteo Bresciani
Registration number 805396

Ph.D. Thesis

Tutor: Prof. **Leonardo Giusti**
Supervisor: Dr. **Michele Pepe**
Supervisor: Prof. **Mattia Dalla Brida**

Academic year 2023/2024

Contents

Introduction

Understanding the origins of the Universe is one of the open questions that has always fascinated physicists the most. Recently, significant technological and scientific advances have given Cosmology a remarkable boost. Notably, the establishment of Gravitational Waves (GWs) astronomy, combined with more traditional observational techniques, has unlocked new ways to explore and characterize the Universe from its primordial stages. In the future, several new space-based antennas (LISA [5], DECIGO [85]) designed to detect primordial GWs are expected to become operational. Simultaneously, the continuous improvement of collider experiments and the perspective of new accelerators like the ILC [9] will enable increasingly accurate investigations of Dark Matter. This progress will allow for a precise and quantitative study of cosmological phenomena that in the past could not be scrutinized due to technological limitations and/or the lack of experimental evidence.

This scenario enhances the interplay between Cosmology and High Energy Physics, as many features of the Early Universe are determined by the thermodynamic properties of the Standard Model (SM), one for all its Equation of State (EoS). For instance, it is believed that the EoS played a crucial role in shaping the spectrum of primordial GWs [136], as well as in influencing the abundance of Dark Matter candidates, such as Weakly Interacting Massive Particles [135] and/or axions [20, 68]. This calls for a continuous improvement of the accuracy and reliability of SM theoretical predictions, also to keep pace with the advances in the field of Cosmology.

In particular, this is true for the thermodynamic properties of Quantum Chromodynamics (QCD) and specifically for its EoS. On the theoretical side, the EoS has been computed from first principles on the lattice up to 2 GeV for $N_f = 2+1$ quark flavours [21, 13, 15], and up to 1 GeV for $N_f = 2+1+1$ flavours [20]. Related to this, the EoS of QCD is crucial for the interpretation of the data of relativistic heavy-ion collision experiments (e.g., ALICE [2], RHIC [71]), where the hot phase of QCD – the Quark-Gluon Plasma – is probed at temperatures on the order of a few hundred MeV.

For cosmological purposes, the EoS is relevant at all temperatures up to the electroweak scale of approximately 100 GeV. Currently, the only results for the EoS above ~ 1 GeV are obtained through a perturbative expansion within the thermal effective field theory of QCD [7, 82]. However, this expansion is known to converge poorly across the entire temperature range in question. This limitation represents a significant source of uncertainty in the SM EoS, propagating to cosmological models and weakening their

predictive capabilities.

The purpose of this thesis is to make a concrete step forward in the exploration from first principles of strong thermodynamics at very high temperatures, using lattice QCD. The main original contribution is the non-perturbative determination of the EoS for $N_f = 3$ massless fermions in the previously unexplored temperature range of 3–160 GeV, with an accuracy in the continuum limit of around 1% or better. This result is achieved through a completely new strategy that makes the very high temperature regime accessible to non-perturbative lattice studies. Furthermore, this approach is fully general and can be readily applied to QCD with five (massive) flavours.

The second main original contribution of this thesis addresses the technical aspect of non-perturbative renormalization of (composite) fields in the lattice theory. Several renormalization schemes have been proposed in the literature for this purpose [108, 110]. The key novelty of our approach is the use of finite temperature QCD – the same framework used for computing the EoS – to carry out the renormalization program. This framework has proven effective for the non-perturbative renormalization of the Energy Momentum tensor of the pure SU(3) Yang Mills theory [61]. More recently, we employed it for the first time in $N_f = 3$ lattice QCD for the non-perturbative renormalization of the flavour-singlet local vector current [22]. We are currently working on the non-perturbative renormalization of the QCD Energy-Momentum tensor [42] on the lattice. After discussing the renormalization strategy, we will present some preliminary non-perturbative results for the related renormalization constants.

List of publications

- **Bresciani, Dalla Brida, Giusti, Pepe.** *The QCD Equation of State with $N_f = 3$ flavours up to very high temperatures.* In preparation.
- **Giusti, Bresciani, Dalla Brida, Harris, Laudicina, Pepe, Rescigno.** *Non-perturbative thermal QCD at very high temperatures.* In: *42nd International Conference on High Energy Physics*, 2024. e-Print: https://arxiv.org/abs/2410.12626.
- **Bresciani, Dalla Brida, Giusti, Pepe.** *Progresses on high-temperature QCD: Equation of State and energy-momentum tensor.* PoS LATTICE2023 (2024), 192. e-Print: https://arxiv.org/abs/2312.11009, DOI: https://doi.org/10.22323/1.453.0192.
- **Bresciani, Dalla Brida, Giusti, Pepe, Rapuano.** *Thermal QCD for non-perturbative renormalization of composite operators.* PoS LATTICE2022 (2023), 364. e-Print: https://arxiv.org/abs/2211.13641, DOI: https://doi.org/10.22323/1.430.0364.
- **Bresciani, Dalla Brida, Giusti, Pepe, Rapuano.** *Non-perturbative renormalization of the flavour singlet local vector current with O(a)-improved Wilson fermions.* PoS LATTICE2021 (2022), 421. DOI: https://doi.org/10.22323/1.396.0421.
- **Bresciani, Dalla Brida, Giusti, Pepe, Rapuano.** *Non-perturbative renormalization of the QCD flavour-singlet local vector current.* Phys. Lett. B 835 (2022), 137579. e-Print: https://arxiv.org/abs/2203.14754, DOI: https://doi.org/10.1016/j.physletb.2022.137579.

Chapter 1

Quantum Chromodynamics

Quantum Chromodynamics (QCD) is the sector of the Standard Model which describes the strong interactions among quarks and gluons. It is a quantum field theory based on the gauge invariance with respect to the Lie group SU(3), called *colour* group. The gluons are represented as bosonic fields belonging to the algebra of SU(3), while the matter content of the theory is given by the quarks, fermionic fields with a triplet structure in colour space. QCD has $N_f = 6$ *flavours* of quarks.

In this Chapter we review the formulation of QCD in $\mathbb{R}^4$ spacetime with Euclidean metric. Given the gauge group and the field content, the first step to define QCD is to write the classical action of the theory. This is done by combining the fields and their derivatives to form all the possible terms that are Lorentz scalar, gauge invariant and have mass dimension ≤ 4. Following these principles, in Section 1.1 we will first derive the action of the pure gauge theory, called SU(3) Yang-Mills (YM) theory. We then write the QCD action in Section 1.2 by further considering the quark fields. In the limit of zero quark masses the classical action of QCD enjoys a large symmetry group, called chiral symmetry, discussed in Section 1.3. Given the classical action, two steps are required for the proper formulation of the theory at the quantum level: the definition of the path integral and the renormalization procedure (Sections 1.4 and 1.5). In Section 1.6 we will discuss the role of chiral symmetry in the quantized theory, and the related properties of QCD. Some of these properties have been explicitly checked in lattice QCD: throughout the Chapter we will reference some relevant results obtained from this framework.

1.1 SU(3) Yang-Mills action

The gauge field $A_\mu(x)$ is a bosonic field in the algebra of the colour group SU(3),

$$A_\mu(x) = A^a_\mu(x) T^a \,, \tag{1.1}$$

where T^a are the generators of the group defined in Appendix A. A gauge transformation on the field A_μ acts as follows,

$$\begin{aligned} A'_\mu(x) &= i\Omega(x)D_\mu(x)\Omega^\dagger(x) \\ &= \Omega(x)A_\mu(x)\Omega^\dagger(x) + i\Omega(x)\partial_\mu\Omega^\dagger(x)\,, \end{aligned} \tag{1.2}$$

where $\Omega \in \mathrm{SU}(3)$ is an element of the group and we defined the *covariant derivative*

$$D_\mu(x) = \partial_\mu - iA_\mu(x)\,. \tag{1.3}$$

It is convenient to introduce the *field strength tensor* $F_{\mu\nu}$, defined through the commutator of covariant derivatives,

$$\begin{aligned} F_{\mu\nu}(x) &= i[D_\mu(x), D_\nu(x)] \\ &= \partial_\mu A_\nu(x) - \partial_\nu A_\mu(x) - i\left[A_\mu(x), A_\nu(x)\right]\,, \end{aligned} \tag{1.4}$$

which transforms in the adjoint representation of the gauge group,

$$F'_{\mu\nu}(x) = \Omega(x)F_{\mu\nu}(x)\Omega^\dagger(x)\,. \tag{1.5}$$

Given these fields, there are only two terms that satisfy the properties of Lorentz and gauge invariance, and have mass dimension $d \leq 4$. The SU(3) Yang-Mills (YM) action reads [1]

$$S^G_\theta[A] = \int d^4x \left[\frac{1}{2g_0^2}\mathrm{tr}\left\{F_{\mu\nu}(x)F_{\mu\nu}(x)\right\} - i\theta q(x)\right]\,, \tag{1.6}$$

where $q(x)$ is called *topological charge density*,

$$q(x) \equiv \frac{1}{32\pi^2}\varepsilon_{\mu\nu\rho\sigma}\mathrm{tr}\left\{F_{\mu\nu}(x)F_{\rho\sigma}(x)\right\}\,, \tag{1.7}$$

and $\mathrm{tr}\{\cdot\}$ denotes the trace over colour. Notice that the structure of the YM action is completely dictated by symmetries. In particular gauge invariance dictates how gluons should interact among themselves, and forbids a mass term $\mathrm{tr}\{A_\mu A_\mu\}$ for the gauge field. The term containing the topological charge density, also called *θ-term*, was introduced by Polyakov [129] and violates parity as well as CP. However, strong CP breaking has not been observed yet in Nature. For instance, the neutron electric dipole moment is a physical quantity sensible to CP breaking in the strong sector, and experimental measurements [1, 70] give the strict upper bound $|\theta| \lesssim 10^{-10}$. Given this constraint on the parameter θ, we assume $\theta = 0$ and throughout all this thesis the continuum YM action will be

$$S^G[A] = \frac{1}{2g_0^2}\int d^4x\,\mathrm{tr}\left\{F_{\mu\nu}(x)F_{\mu\nu}(x)\right\}\,. \tag{1.8}$$

The only arbitrary parameter is the coupling constant g_0, which is dimensionless. The absence of dimensionful parameters makes the YM action invariant under a change of energy scale: this is a symmetry of the classical action known as *scale invariance*.

[1] Unless otherwise stated, we use the convention that repeated indices are summed.

1.2 QCD action

The matter content of QCD is given by the quark fields $\psi(x)$, $\overline{\psi}(x)$, with fermionic statistics. From the point of view of the Lorentz group, a quark is a spin-1/2 Dirac spinor. In colour space, quarks are triplets transforming as follows under the gauge group:

$$\psi'(x) = \Omega(x)\psi(x)\,, \quad \overline{\psi}'(x) = \overline{\psi}(x)\Omega^\dagger(x)\,, \quad \Omega \in \mathrm{SU}(3)\,. \tag{1.9}$$

Finally, we consider N_f flavours of quarks, the physical case being $N_f = 6$. Therefore a quark has N_f components in flavour space, 4 components in spinor space and $N_c = 3$ components in colour space. Using these fields we can write two new terms with mass dimension $d = 4$ satisfying the properties of Lorentz invariance and gauge invariance, which define the fermionic part of the QCD action:

$$S^F[A, \overline{\psi}, \psi] = \int d^4x\, \overline{\psi}(x) \left(\not{D} + M_0\right) \psi(x)\,. \tag{1.10}$$

Here $\not{D} = \gamma_\mu D_\mu$ and γ_μ are the Dirac matrices in spinor space defined in Appendix A. Gauge invariance dictates how quarks and gluons interact. This interaction is governed by the same coupling g_0 of the gluon-gluon interaction. We denote by M_0 the $N_f \times N_f$ real-valued matrix containing the bare masses of the quark flavours, which are free dimensionful parameters of the theory. In QCD it is possible to define the quark fields so that the matrix M_0 is diagonal. Finally, the complete QCD action is the YM one in equation (1.8) plus the fermionic part:

$$S[A, \overline{\psi}, \psi] = S^G[A] + S^F[A, \overline{\psi}, \psi]\,. \tag{1.11}$$

Again, gauge invariance dictates how quarks and gluons interact. In the special case of massless quarks, $M_0 = 0$, the only free parameter is the dimensionless coupling constant g_0 as in the pure gauge theory. In this limit scale invariance holds for the QCD action too.

1.3 Chiral symmetry

The representations of the Euclidean Lorentz group SO(4) are reducible to the direct sum of two fundamental representations of SU(2) [153], called *Weyl spinors*, classified by half integers, with an extra $\mathbb{Z}_2$ label called *chirality*. A Dirac spinor can be written as $(1/2, 0) \oplus (0, 1/2)$: the two Weyl spinors have spin 1/2 and opposite chirality. The chiral projectors $P_{R,L}$ allow to extract the two chiral components, conventionally labeled with *right* and *left*, from a Dirac spinor,

$$\psi_{R,L} = P_{R,L}\psi\,, \quad \overline{\psi}_{R,L} = \overline{\psi}P_{L,R}\,, \tag{1.12}$$

where

$$P_{R,L} = \frac{1}{2}(1 \pm \gamma_5)\,, \quad P_{R,L}^2 = 1\,, \quad P_{R,L}P_{L,R} = 0\,, \tag{1.13}$$

and γ_5 is introduced in Appendix A. In terms of chiral-projected fields the fermionic action (1.10) becomes

$$S^F = \int d^4x \Big\{ \overline{\psi}_R(x) \not{D} \psi_R(x) + \overline{\psi}_L(x) \not{D} \psi_L(x) + \overline{\psi}_R(x) M_0 \psi_L(x) + \overline{\psi}_L(x) M_0 \psi_R(x) \Big\} . \tag{1.14}$$

In the massless case $M_0 = 0$ the action S^F is invariant under global unitary rotations in flavour space of left and right components separately. This symmetry is called *chiral symmetry*,

$$\mathrm{U}(N_f)_R \times \mathrm{U}(N_f)_L \sim \mathrm{U}(1)_R \times \mathrm{U}(1)_L \times \mathrm{SU}(N_f)_R \times \mathrm{SU}(N_f)_L \,, \tag{1.15}$$

whose action on the fields is

$$\psi'_{R,L} = V_{R,L}\, \psi_{R,L} \,, \quad \overline{\psi}'_{R,L} = \overline{\psi}_{R,L}\, V^\dagger_{R,L} \tag{1.16}$$

where the matrices $V_{R,L}$ are elements of $\mathrm{U}(N_f)_{R,L}$. We also note that if a few flavors only were massless we could write a smaller chiral symmetry group among them. Combining left and right transformations, the chiral rotation on a Dirac spinor is

$$\psi' = (V_R P_R + V_L P_L)\, \psi \,, \quad \overline{\psi}' = \overline{\psi}(P_L V_R^\dagger + P_R V_L^\dagger) \,. \tag{1.17}$$

We now discuss separately the various components of the chiral symmetry group.

1.3.1 Flavour singlet

We first focus on the Abelian part $\mathrm{U}(1)_R \times \mathrm{U}(1)_L$: in this case the matrices of the chiral rotations are just complex phases,

$$V_{R,L} = e^{i\varepsilon^0_{R,L}} \,. \tag{1.18}$$

Using eq. (1.17) at the infinitesimal level, the Dirac spinor transforms as

$$\begin{aligned} \psi' &= \left[(1 + i\varepsilon^0_R) P_R + (1 + i\varepsilon^0_L) P_L \right] \psi \\ &= \left(1 + i\varepsilon^0_V + i\varepsilon^0_A \gamma_5 \right) \psi \,, \end{aligned} \tag{1.19}$$

where in the second line we defined the coefficients

$$\varepsilon^0_V = \frac{\varepsilon^0_R + \varepsilon^0_L}{2}, \quad \varepsilon^0_A = \frac{\varepsilon^0_R - \varepsilon^0_L}{2} \tag{1.20}$$

for the flavour-singlet *vector* and *axial* transformations. Therefore, the generators of the Abelian part of chiral symmetry can be rearranged to generate the $\mathrm{U}(1)_V \times \mathrm{U}(1)_A$ symmetry acting on Dirac spinors. The singlet vector rotation is

$$\psi' = e^{i\varepsilon^0_V} \psi \,, \quad \overline{\psi}' = \overline{\psi}\, e^{-i\varepsilon^0_V} \tag{1.21}$$

while the singlet axial is

$$\psi' = e^{i\varepsilon^0_A \gamma_5} \psi \,, \quad \overline{\psi}' = \overline{\psi}\, e^{i\varepsilon^0_A \gamma_5} \,. \tag{1.22}$$

1.3.2 Flavour non-singlet

Concerning the non-Abelian part $\mathrm{SU}(N_f)_L \times \mathrm{SU}(N_f)_R$ of the chiral symmetry, the matrices of the chiral rotation are

$$V_{R,L} = e^{i\varepsilon^a_{R,L} T^a}\,, \quad T^a \in \mathrm{su}(N_f)\,. \tag{1.23}$$

An infinitesimal transformation on a Dirac spinor leads to

$$\begin{aligned} \psi' &= [(1 + i\varepsilon^a_R T^a)P_R + (1 + i\varepsilon^a_L T^a)P_L]\,\psi \\ &= (1 + i\varepsilon^a_V T^a_V + i\varepsilon^a_A T^a_A)\,\psi\,, \end{aligned} \tag{1.24}$$

where in the second line we defined the coefficients

$$\varepsilon^a_V = \frac{\varepsilon^a_R + \varepsilon^a_L}{2}, \quad \varepsilon^a_A = \frac{\varepsilon^a_R - \varepsilon^a_L}{2} \tag{1.25}$$

and the vector and axial generators

$$T^a_V = T^a, \quad T^a_A = \gamma_5 T^a \tag{1.26}$$

with $a = 1, ..., {N_f}^2 - 1$. The commutation relations of these generators are

$$[T^a_V, T^b_V] = f^{abc} T^c_V\,, \quad [T^a_A, T^b_A] = f^{abc} T^c_V\,, \quad [T^a_A, T^b_V] = f^{abc} T^c_A\,. \tag{1.27}$$

The vector generators T^a_V satisfy the correct commutation rules for building up a Lie algebra. The related group is the flavour non-singlet vector group $\mathrm{SU}(N_f)_V$, whose action on a Dirac spinor is

$$\psi' = e^{i\varepsilon^a_V T^a}\psi\,, \quad \overline{\psi}' = \overline{\psi}\, e^{-i\varepsilon^a_V T^a}\,. \tag{1.28}$$

Instead, the $N_f^2 - 1$ non-singlet axial generators are not closed under the commutation relation. Therefore they cannot be arranged in a Lie algebra and they do not generate a Lie group. Under a non-singlet axial transformation the Dirac spinor changes as

$$\psi' = e^{i\varepsilon^0_A \gamma_5 T^a}\psi\,, \quad \overline{\psi}' = \overline{\psi}\, e^{i\varepsilon^a_A \gamma_5 T^a}\,. \tag{1.29}$$

1.4 Quantization

Given the classical action we now proceed to quantize the theory. At this point a disclaimer is in order. In what follows we will work with the formal continuum notation of QCD. However, the rigorous way to define QCD requires the theory to be discretized on a lattice. We dedicate Chapter 3 to the lattice formulation of QCD, which is a foundation of the original work presented in this thesis. Following the path integral formalism we introduce the (Euclidean) *partition function* of QCD,

$$\mathcal{Z} = \int DAD\overline{\psi}D\psi\, e^{-S[A,\overline{\psi},\psi]}\,, \tag{1.30}$$

where the integral is over all the field configurations, weighted by a Boltzmann-like factor, and S is the QCD action. In order to properly reproduce the Fermi-Dirac statistics, quark fields are (anti-commuting) Grassman variables (see for instance [115] for a textbook treatment). Primary quantities in a Euclidean quantum field theory are correlation functions of products of local composite operators $\mathcal{O}_i(x) = \mathcal{O}_i[A(x), \overline{\psi}(x), \psi(x)]$,

$$\langle \mathcal{O}_1(x_1) \cdots \mathcal{O}_n(x_n) \rangle = \frac{1}{\mathcal{Z}} \int DAD\overline{\psi}D\psi \, \mathcal{O}_1(x_1) \cdots \mathcal{O}_n(x_n) e^{-S[A,\overline{\psi},\psi]} \,, \tag{1.31}$$

that we can interpret in a statistical way as expectation values with respect to the path integral distribution. It can be shown [153] that, in the limit of Euclidean time going to infinity, these quantities are in one-to-one correspondence with vacuum expectation values of time-ordered products of field operators,

$$\langle \text{vac} | \mathcal{T}\{\hat{\mathcal{O}}_1(x_1) \cdots \hat{\mathcal{O}}_n(x_n)\} | \text{vac} \rangle \,, \tag{1.32}$$

which are the objects of interest in the canonical formalism of quantization.

The definitions (1.30) and (1.31) are completely formal expressions as they stand, and some work is needed to make them meaningful. Computations in the bare path integral in general give rise to divergent results. The procedure one follows to handle these infinities is called *regularization*, and actually it can be thought as part of the definition of the path integral. As anticipated, we are mainly interested in the lattice regularization of QCD, which amounts to the discretization of the theory on a hypercubic 4-dimensional lattice with lattice spacing a. This is the only known regularization that allows to rigorously define and compute non-perturbatively correlation functions in QCD, without any further assumption on the strong dynamics (see Chapter 3).

Quantities computed in regularized QCD are finite functions of the regulator and of the bare parameters of the theory, i.e. the bare coupling and quark masses. Now, the regulator must be removed but we cannot do it in the naive way, at fixed bare parameters, because this would give rise to physically meaningless divergencies. Consequently, the bare parameters (which have no physical meaning) must acquire a specific dependence on the regulator. This last step of the quantization of the theory is called *renormalization*, and it is the procedure of removing the regulator while changing the bare parameters so that the theory is matched to physics. This is achieved by imposing a set of *renormalization conditions*, one for each bare parameter of the theory. In the limit of vanishing quark masses, the renormalization condition is of the form

$$\mathcal{M}(g_0, a) = \mathcal{M}_{\text{phys}} \,, \tag{1.33}$$

where $\mathcal{M}$ is a physical observable with the dimension of a mass. On the left it is computed in the (lattice) regularized theory, while on the right its value in the physical world appears. This equation defines implicitly the dependence of the bare coupling on the regulator, $g_0 \to g_0(a)$. Further renormalization conditions must be imposed in a similar way in presence of bare quark masses. The set of imposed renormalization conditions define a *renormalization scheme*. We refer to Chapter 3 for the details on how the described renormalization procedure is carried out non-perturbatively in lattice QCD.

An important consequence of the renormalization condition eq. (1.33) is that the dimensionful quantity $\mathcal{M}_{\rm phys}$ is introduced as part of the definition of the quantum field theory. Therefore both in the pure SU(3) gauge theory and in (massless) QCD the scale invariance is explicitly broken by the quantization procedure, even though their classical actions are scale invariant. This goes under the name of *scale anomaly*. Any dimensionful quantity, that was not constrained by the renormalization scheme, is a prediction of the renormalized theory and is proportional to the proper power of the scale $\mathcal{M}_{\rm phys}$. For instance, hadron masses can be written as

$$M_{\rm had} = c_{\rm had} \cdot \mathcal{M}_{\rm phys}\,, \tag{1.34}$$

where $c_{\rm had}$ is a non-perturbative, dimensionless geometric coefficient to be computed in the renormalized theory.

1.5 Renormalization group

The renormalization procedure described above is enough to properly define and compute all the physical observables of the theory. In a quantum field theory it is also possible to introduce renormalized quantities which depend on a *renormalization energy scale* μ as part of their definition. For example we can introduce the renormalized parameters of the theory,

$$g_R^2 = Z_g(g_0, a\mu) g_0^2\,, \quad M_R = Z_M(g_0, a\mu) M_0\,, \tag{1.35}$$

where Z_g and Z_M are dimensionless renormalization factors which depend on the renormalization scale and scheme, on the regulator (the lattice, in this case) and on the bare coupling. In the definitions above a mass-independent renormalization scheme has been chosen [152], so that the renormalization factors do not depend on the quark masses.

More generally, the renormalized counterpart of a bare composite field $\mathcal{O}$ is

$$\mathcal{O}_R = \sum_\alpha Z_\alpha \mathcal{O}_\alpha\,, \quad \alpha : [\mathcal{O}_\alpha] \leq [\mathcal{O}]\,, \tag{1.36}$$

the sum over α running on all the operators with the same symmetries of $\mathcal{O}$ and with lower or equal mass dimension. Let's consider a set of fields whose renormalization pattern is simply $\mathcal{O}_{i,R} = Z_i \mathcal{O}_i$. When we insert these fields in a connected correlation function, the latter is renormalized as

$$\Gamma_R(p, g_R, M_R, \mu) = Z_\Gamma(g_0, a\mu)\, \Gamma_0(p, g_0, aM_0)\,, \tag{1.37}$$

where $Z_\Gamma = \prod_i Z_i$ collects the renormalization factors of the inserted local fields, and p denotes the set of 4-momenta flowing in the connected correlation function. The scale dependence of Γ_R is prescribed by the Callan-Symanzik equation, or *Renormalization Group Equation* [54, 145, 27, 148]. This is a non-perturbative result following from equation (1.37) by exploiting the μ-independence of the bare correlation function, $d\Gamma_0/d\mu = 0$:

$$\left\{ \mu \frac{\partial}{\partial \mu} + \beta(g_R) \frac{\partial}{\partial g_R} + \gamma_M(g_R) M_R \frac{\partial}{\partial M_R} - \gamma_\Gamma(g_R) \right\} \Gamma_R = 0\,, \tag{1.38}$$

where the functions

$$\beta(g_R) = \mu\frac{\partial}{\partial\mu}g_R\,, \quad \gamma_M(g_R) = \mu\frac{\partial}{\partial\mu}\ln Z_M\,, \quad \gamma_\Gamma(g_R) = \mu\frac{\partial}{\partial\mu}\ln Z_\Gamma \tag{1.39}$$

are differential equations encoding the running of renormalized parameters and renormalization constants with the scale μ. The function γ_M is called *mass anomalous dimension*, while γ_Γ is the anomalous dimension of the renormalized correlation function, coming from the multiplicative renormalization constant. Note that the β, γ_M and γ_Γ functions must be independent from the regularization, since they appear in a differential equation (1.38) for a renormalized correlation function. Moreover, being dimensionless they do not explicitly depend on the renormalization scale.

1.5.1 The Λ-parameter

From the definition of $\beta(g_R)$ in eq. (1.39) a special solution of the Callan-Symanzik equation emerges. If we separate the variables μ and g_R and integrate between $g_1 = g_R(\mu_1)$ and $g_2 = g_R(\mu_2)$ the following relation is found:

$$\mu_1 \exp\left\{-\int_{\overline{g}}^{g_1}\frac{dx}{\beta(x)}\right\} = \mu_2 \exp\left\{-\int_{\overline{g}}^{g_2}\frac{dx}{\beta(x)}\right\} \tag{1.40}$$

where for convenience we introduced a third value of the renormalized coupling $\overline{g}$. This equality tells us that the quantity appearing both sides is constant as the renormalization scale changes. In order to write it better we would like to send $\overline{g} \to 0$. The perturbative result for the β-function is usually written as

$$\beta(g) = -g^3\sum_{k=0}^{\infty} b_k g^{2k} \tag{1.41}$$

where the coefficients b_k depend on the renormalization scheme but for the first two, which are universal. For generic values of N_c and N_f we have

$$b_0 = \frac{1}{(4\pi)^2}\left(\frac{11}{3}N_c - \frac{2}{3}N_f\right)\,, \quad b_1 = \frac{1}{(4\pi)^4}\left[\frac{34}{3}N_c^2 - \left(\frac{13}{3}N_c - \frac{1}{N_c}\right)N_f\right]\,. \tag{1.42}$$

The perturbative result shows that $\beta(g) \to 0$ as $g \to 0$. Before setting $\overline{g} = 0$ in equation (1.40) we can subtract both sides the divergent part of $1/\beta(x)$. The scale invariant quantity finally reads

$$\begin{aligned}\Lambda/\mu \equiv &[b_0 g_R^2(\mu)]^{-b_1/(2b_0^2)} e^{-1/(2b_0 g_R^2(\mu))} \\ &\times \exp\left\{-\int_0^{g_R(\mu)} dx\left[\frac{1}{\beta(x)} + \frac{1}{b_0 x^3} - \frac{b_1}{b_0^2 x}\right]\right\}.\end{aligned} \tag{1.43}$$

This quantity is called Λ-*parameter* of the theory. The Λ-parameter is a completely non-perturbative result that solves the Callan-Symanzik equation in the $M_R = 0$ case

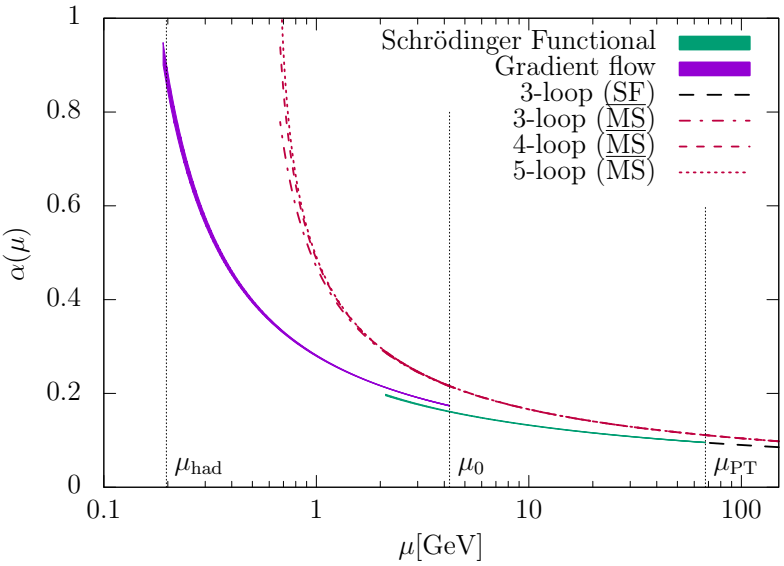

Figure 1.1: Running of the $N_f = 3$ QCD coupling $\alpha = g_R^2/(4\pi)$ renormalized in the Schrodinger functional and Gradient flow schemes, in comparison with perturbation theory [25].

and in absence of anomalous dimensions. Such quantities are also known as RGI, renormalization group invariants. Even though it is a renormalization scheme dependent object, it can be shown that the scheme dependence is exactly computable with a 1-loop calculation [154]. The Λ-parameter is a constant mass scale arising directly from the renormalization group of the QFT, even if the classical theory has no mass scales. This fact goes under the name of *dimensional transmutation*, as equation (1.43) trades the running of a dimensionless coupling g_R with the dimensionful scale Λ.

The Λ-parameter can be computed non-perturbatively in lattice QCD, as well as the β-function of a renormalized coupling and so the running of the coupling itself. This in turn allows to define in a fully non-perturbative way the renormalization constant Z_g in equation (1.35). The determination of the running coupling from the lattice has been achieved by employing renormalized couplings defined in finite volume schemes, such as the Schrodinger functional coupling [108] or the Gradient flow coupling [110]. The non-perturbative running of these couplings has been determined using the step scaling procedure proposed in [103]. Recent results in $N_f = 3$ QCD (three massless flavours) can be found in [45, 44, 28, 25], and have been obtained using the couplings mentioned above, whose running with the scale is represented in Figure 1.1. The quoted result for the Λ-parameter is

$$\Lambda^{(3)}_{\overline{\text{MS}}} = 341(12)\ \text{MeV}\,, \tag{1.44}$$

where the conversion to the perturbatively defined $\overline{\text{MS}}$ scheme is done after the fully non-perturbative computation.

1.5.2 Asymptotic freedom

As we can see from Figure 1.1, when the energy scale increases the strong coupling of QCD becomes smaller and smaller. This behaviour is known as *asymptotic freedom* [69], and can be predicted analytically by solving the running of the renormalized coupling in the small coupling regime. Using the perturbative result for the β-function (1.39), at leading order one finds

$$g_R^2(\mu_2) = \frac{g_R^2(\mu_1)}{1 + 2b_0 g_R^2(\mu_1) \ln(\mu_2/\mu_1)} \,. \tag{1.45}$$

The 1-loop (universal) coefficient b_0 of the β-function controls the behaviour of the coupling as we change the scale. If $b_0 > 0$, that is if

$$N_f < \frac{11}{2} N_c \,, \tag{1.46}$$

then the coupling decreases as the energy scale increases ($\mu_2 \gg \mu_1$). The physical case ($N_c = 3, N_f = 6$) is included in this scenario. Therefore the perturbative regime of QCD is the one at high energy. Note that the pure gauge theory ($N_f = 0$) is asymptotic-free for any number of colours $N_c > 0$.

1.5.3 RGI quark mass

If massive quarks are considered then the RGI quark mass arises as a special solution of the Callan-Symanzik equation (1.38), in a similar way as the Λ-parameter was derived:

$$\begin{aligned} M_{\mathrm{RGI}} \equiv & M_R(\mu) \left[2b_0 g_R^2(\mu)\right]^{-d_0/(2b_0)} \\ & \times \exp\left\{ - \int_0^{g_R(\mu)} dx \left[\frac{\gamma_M(x)}{\beta(x)} - \frac{d_0}{b_0 x} \right] \right\} , \end{aligned} \tag{1.47}$$

where the perturbative expansion of γ_M is

$$\gamma_M(g) = -g^2 \sum_{k=0}^{\infty} d_k g^{2k} \,, \quad d_0 = \frac{1}{(4\pi)^2} \frac{3(N_c^2 - 1)}{N_c} \,. \tag{1.48}$$

At variance of the Λ-parameter, M_{RGI} is a universal (i.e. scheme-independent) quantity. The RGI quark mass and the related running of the renormalized quark mass $M_R(\mu)$ can be determined non-perturbatively from the lattice [28, 128] adopting step scaling techniques in analogy to the determination of the running coupling and the Λ-parameter. This in turn allows to define in a non-perturbative way the mass renormalization constant Z_M of equation (1.35).

1.6 Chiral symmetry in QCD

We showed in Section 1.3 that the massless classical action of QCD is invariant under chiral symmetry, which is related to the freedom of redefining left-handed and right-handed components of quarks up to $\mathrm{U}(N_f)$ rotations in flavour space. At the quantum level a large part of this symmetry is broken. To start with, the $\mathrm{U}(1)_A$ subgroup is broken by the *chiral anomaly*, due to the non-invariance of the path integral measure under this symmetry. Massless QCD breaks chiral symmetry with the mechanism of *spontaneous symmetry breaking* (SSB), triggered by the fact that the quantum vacuum of the theory is not invariant under this symmetry. The broken generators are the non-singlet axial ones, and the $N_f^2 - 1$ associated Goldstone bosons are the *pions*. QCD at physical point have massive quarks, and this explicitly breaks chiral symmetry. The vector flavour subgroup $\mathrm{SU}(N_f)_V$ of chiral symmetry survives to non-zero quark masses if all the flavours have the same mass. The special case $N_f = 2$ is called *isospin symmetry*, and in Nature it is preserved at the percent level.

In the following Subsections we will focus in more details on the consequences of chiral symmetry in QCD and its breaking pattern, together with some remarkable non-perturbative numerical results which validate the theory.

1.6.1 Chiral Ward Identities

The consequences of chiral symmetry in QCD can be understood using the related Ward Identities (WI). Given a transformation of the fields whose infinitesimal form is

$$\psi' = \psi + \delta\psi\,, \quad \overline{\psi}' = \overline{\psi} + \delta\overline{\psi}\,, \quad A'_\mu = A_\mu + \delta A_\mu\,, \tag{1.49}$$

the WI is obtained by a change of variable in the path integral for the expectation value $\langle \mathcal{O} \rangle$ of a given interpolating field $\mathcal{O}$,

$$\pm\langle \mathcal{O}\,\mathrm{Tr}\,\delta J\rangle - \langle \mathcal{O}\delta S\rangle + \langle \delta\mathcal{O}\rangle = 0\,. \tag{1.50}$$

In this equation δS and $\delta\mathcal{O}$ are the variations of the action and of the interpolating field $\mathcal{O}$ under the infinitesimal transformation, and $J = 1 + \delta J$ its near-identity Jacobian. The trace $\mathrm{Tr}\,\{\cdot\}$ includes the sum over spacetime. The signs $\pm$ are respectively for transformations acting on bosonic or fermionic fields. Transformations for which the path integral measure is not invariant ($\delta J \neq 0$) are called *anomalous*.

A particular case is when the transformation is a continuous global symmetry of the classical action: the related Ward Identity can be found by first localizing the transformation. However, being a combination of the equations of motion, a Ward Identity is a non-perturbative result of QCD holding independently from the actual realization of the symmetry, although the breaking (either explicit or spontaneous) of the latter may change some terms appearing in the Ward Identity itself.

In the following we will derive the Ward Identities related to the non-anomalous ($\delta J = 0$) part of chiral symmetry in the formal continuum theory. Strictly speaking we should first regularize the theory, then derive the Ward Identities in the bare regularized

theory and finally replace the bare operators and parameters with their renormalized counterparts. However, it is possible to regularize QCD and then renormalize it so that the form of the (bare) chiral Ward Identities is respected. Provided that, we are authorized to formally derive them in the bare continuum theory. This is actually true for all the generators of chiral symmetry but for the singlet axial group, $\mathrm{U}(1)_A$. This is the only anomalous subgroup of chiral symmetry, because the integration measure of the *regularized* theory is not invariant. A naive treatment in the bare continuum theory would just overlook this.

Singlet vector Ward Identities

We consider a transformation of the quark fields under the $\mathrm{U}(1)_V$ subgroup of chiral symmetry, equation (1.21). The infinitesimal form reads

$$\psi' = (1 + i\varepsilon_V^0)\psi\,, \quad \overline{\psi}' = \overline{\psi}(1 - i\varepsilon_V^0)\,. \tag{1.51}$$

We localize the transformation $\varepsilon_V^0 \to \varepsilon_V^0(x)$ such that it vanishes for large distances (or, in case of compact support, on the boundary of the support). The variation of the action is

$$\delta S = -i \int d^4z\, \varepsilon_V^0(z) \partial_\mu^z V_\mu(z)\,, \tag{1.52}$$

where we defined the *flavour-singlet vector current* $V_\mu \equiv \overline{\psi}\gamma_\mu\psi$. Given the local operator $\mathcal{O}$, we obtain the Ward Identity

$$-i \int d^4z\, \varepsilon_V^0(z) \big\langle \partial_\mu^z V_\mu(z)\mathcal{O}(y)\big\rangle = \Big\langle \delta_{\varepsilon_V^0(y)}\mathcal{O}(y)\Big\rangle\,, \tag{1.53}$$

where on the right the variation of the local operator appears. We can choose the support of the local variation to be a single point by setting $\varepsilon_V^0(z) = \varepsilon_V^0\delta(z-x)$ and, at physical distance, we get

$$\partial_\mu^x \langle V_\mu(x)\mathcal{O}(y)\rangle = 0\,, \quad y \neq x\,. \tag{1.54}$$

This is sort of generalization of the Noether's current conservation. If we integrate both sides in $d^3\boldsymbol{x} = dx_1dx_2dx_3$ we get

$$\partial_{x_0}\big\langle \overline{V}(x_0)\mathcal{O}(y)\big\rangle = 0\,, \quad y_0 \neq x_0\,, \quad \overline{V}(x_0) \equiv \int d^3\boldsymbol{x}\, V_0(x_0,\boldsymbol{x}) \tag{1.55}$$

which states the conservation of the charge $\overline{V}$, known as *baryon number*. Since the $\mathrm{U}(1)_V$ subgroup of chiral symmetry is respected in QCD regardless the value of M_0, the baryon number is conserved for any value of the quark masses.

Non-singlet vector Ward Identities

We move now to the $\mathrm{SU}(N_f)_V$ subgroup of chiral symmetry, also called *generalized isospin*. The infinitesimal transformation of the fields reads

$$\psi' = (1 + i\varepsilon_V^a T^a)\psi\,, \quad \overline{\psi}' = \overline{\psi}(1 - i\varepsilon_V^a T^a)\,. \tag{1.56}$$

Working as we did for the singlet case we can similarly derive the integrated Ward Identity

$$-i\int d^4z\,\varepsilon_V^a(z)\Big\{\big\langle\partial_\mu^z V_\mu^a(z)\mathcal{O}(y)\big\rangle-\big\langle\overline{\psi}(z)[M_0,T^a]\psi(z)\mathcal{O}(y)\big\rangle\Big\}=\Big\langle\delta_{\varepsilon_V^a(y)}\mathcal{O}(y)\Big\rangle \quad (1.57)$$

where the (non-singlet) *vector current* $V_\mu^a \equiv \overline{\psi}\gamma_\mu T^a\psi$ was introduced. By choosing $\varepsilon_V^a(x)=\varepsilon_V^a\delta(z-x)$, at physical distance we get

$$\partial_\mu^x\big\langle V_\mu^a(x)\mathcal{O}(y)\big\rangle=\big\langle\overline{\psi}(x)[M_0,T^a]\psi(x)\mathcal{O}(y)\big\rangle\,,\quad y\neq x\,. \quad (1.58)$$

The commutator $[M_0,T^a]$ arises from the flavour structure of this transformation. In order to have a conserved current (and charge) for the isospin symmetry the commutator has to vanish, meaning that the N_f flavours must be degenerate (but not necessarily massless). In case a few flavours only are degenerate, then the isospin symmetry holds only among them. The breaking of isospin can thus be related to the difference of masses of the flavours. For these reasons V_μ^a is sometimes referred to as the *partially conserved vector current* (PCVC).

Non-singlet axial Ward Identities

The infinitesimal transformation under the axial generators are

$$\psi'=(1+i\varepsilon_A^a\gamma_5T^a)\psi\,,\quad \overline{\psi}'=\overline{\psi}(1+i\varepsilon_A^a\gamma_5T^a)\,. \quad (1.59)$$

Using the same machinery as before one can find the integrated Ward Identity

$$-i\int d^4z\,\varepsilon_A^a(z)\Big[\big\langle\partial_\mu^z A_\mu^a(z)\mathcal{O}(y)\big\rangle-\big\langle\overline{\psi}(z)\gamma_5\{M_0,T^a\}\psi(z)\mathcal{O}(y)\big\rangle\Big]=\Big\langle\delta_{\varepsilon_A^a(y)}\mathcal{O}(y)\Big\rangle\,. \quad (1.60)$$

Here we defined the (non-singlet) *axial current* $A_\mu^a\equiv\overline{\psi}\gamma_\mu\gamma_5T^a\psi$. We choose $\varepsilon_A^a(x)=\varepsilon_A^a\delta(z-x)$ and we get

$$\partial_\mu^x\big\langle A_\mu^a(x)\mathcal{O}(y)\big\rangle=\big\langle\overline{\psi}(x)\gamma_5\{M_0,T^a\}\psi(x)\mathcal{O}(y)\big\rangle\,,\quad y\neq x\,. \quad (1.61)$$

At variance of the vector case, the presence of one extra γ_5 leads to the anticommutator of the mass matrix M_0 with the generator T^a. This means that a conserved axial current is possible only if $M_0=0$. The axial current is also called *partially conserved axial current* (PCAC). A special case is when the N_f flavours have the same (bare) mass, $M_0=m_0\mathbb{1}_{N_f}$. In this case the PCAC relation becomes

$$\partial_\mu^x\big\langle A_\mu^a(x)\mathcal{O}(y)\big\rangle=2m_0\langle P^a(x)\mathcal{O}(y)\rangle\,,\quad y\neq x \quad (1.62)$$

where we defined the *pseudoscalar density* $P^a\equiv\overline{\psi}\gamma_5T^a\psi$.

Renormalization of currents and densities

The chiral Ward Identities allow to fix the renormalization of some of the currents and densities we have already introduced in a non-perturbative way. Let us start from the non-singlet vector current (isospin current). Recalling (1.36), its renormalization pattern is simply [2]

$$V^a_{\mu,R} = Z_V^{\rm ns} V^a_\mu \tag{1.63}$$

as there is no other operator with mass dimension $d \leq 3$ and same properties that could mix under renormalization. We consider the WI in equation (1.57) with $M_0 = 0$ (that is, we choose a mass-independent renormalization scheme). We choose the operator to be the vector current itself, $\mathcal{O} = V^b_\nu$. It is easy to show that $\delta_{\varepsilon^a_V(y)} V^b_\nu(y) = \varepsilon^a_V(y) f^{abc} V^c_\nu(y)$. If we finally choose $\varepsilon^a_V(z) = \varepsilon^a_V \delta(z-x)$ we get

$$\partial^x_\mu \Big\langle V^a_\mu(x) V^b_\nu(y) \mathcal{O}(z) \Big\rangle = i\delta(y-x) f^{abc} \langle V^c_\nu(y)\mathcal{O}(z)\rangle \,, \quad z \neq x, y \tag{1.64}$$

where we added the extra operator $\mathcal{O}$ to prevent correlation functions from vanishing. If we now replace all the fields with their renormalized counterparts we get

$$\partial^x_\mu \Big\langle V^a_{\mu,R}(x) V^b_{\nu,R}(y) \mathcal{O}_R(z) \Big\rangle = Z_V^{\rm ns} i\delta(y-x) f^{abc} \big\langle V^c_{\nu,R}(y)\mathcal{O}_R(z)\big\rangle \,, \quad z \neq x, y \tag{1.65}$$

and since the WI should hold for the renormalized quantities, we have to set $Z_V^{\rm ns} = 1$ which means that V^a_μ does not renormalize. The non-singlet axial current renormalizes multiplicatively too,

$$A^a_{\mu,R} = Z_A A^a_\mu \,. \tag{1.66}$$

Starting from the WI (1.60) with $M_0 = 0$, and choosing $\mathcal{O} = A^a_\nu$ one can proceed as we did for the vector current, and the result is that the axial current does not renormalize too: $Z_A = 1$. The non-singlet pseudoscalar density renormalizes multiplicatively,

$$P^a_R = Z_P P^a \,. \tag{1.67}$$

We use the PCAC relation (1.62) with $\mathcal{O} = P^b$. The renormalized counterpart is

$$\partial^x_\mu \Big\langle A^a_{\mu,R}(x) P^b_R(y) \Big\rangle = 2m_R \, Z_M^{-1} Z_P^{-1} \Big\langle P^a_R(x) P^b_R(y) \Big\rangle \,, \quad y \neq x \tag{1.68}$$

where we already set the axial current renormalization to unity. This relation tells us that

$$Z_M Z_P = 1 \quad \Rightarrow \quad Z_P = \frac{1}{Z_M} \tag{1.69}$$

to preserve the WI for renormalized fields. We may also define the *(non-singlet) scalar density* $S^a \equiv \overline{\psi} T^a \psi$, which belongs to the same chiral multiplet of P^a (that is, they

[2] For later purposes in this thesis, we reserve the symbol Z_V to the renormalization constant of the flavour-singlet vector current.

can be rotated one into the other by a chiral transformation) [3]. Therefore they must renormalize in the same way: $Z_S = Z_P$.

The *flavour-singlet scalar density* $S^0 \equiv \overline{\psi}\psi$ requires some care. Being a mass-dimension 3 scalar object, under renormalization it mixes with an infinite set of eventually divergent terms like $M_0\mu^2_{\rm cutoff}$, M_0^3, $M_0^4/\mu_{\rm cutoff}$ ... such that the total mass dimension is 3. Here, $\mu_{\rm cutoff}$ is the cutoff scale provided by the regulator, for instance $1/a$ on the lattice. Using the WIs we can still fix the overall renormalization factor Z_S^0, thanks to the fact that at zero quark masses all these extra additive terms do not appear. In eq. (1.60) we choose $\mathcal{O} = P^b$, whose variation under the axial generators is

$$\delta_{\varepsilon^a_A(y)} P^b(y) = i\varepsilon^a_A(y) \left(\frac{\delta^{ab}}{N_f} S^0 + d^{abc} S^c \right) . \tag{1.70}$$

We then select $\varepsilon^a_A(y) = \varepsilon^a_A \delta(y-x)$ and the PCAC Ward Identity with degenerate masses becomes

$$\partial^x_\mu \Big\langle A^a_\mu(x) P^b(y) \Big\rangle = 2m_0 \Big\langle P^a(x) P^b(y) \Big\rangle - \frac{\delta^{ab}}{N_f} \delta(y-x) \big\langle S^0(y) \big\rangle \, . \tag{1.71}$$

We already set $\langle S^c \rangle = 0$ coming from (1.70), because isospin symmetry is respected. If we consider the chiral limit ($m_0 = 0$) and we replace fields with renormalized ones we get $Z_S^0 = Z_P$. In conclusion, the flavour-singlet vector current renormalizes as

$$V_{\mu,R} = Z_V V_\mu \, . \tag{1.72}$$

Using equation (1.53) we see that also this current (and thus the baryon number) does not renormalize: $Z_V = 1$.

1.6.2 Spontaneous symmetry breaking of axial generators

As we anticipated, the $N_f^2 - 1$ non-singlet axial generators of the chiral symmetry group are spontaneously broken in massless QCD. The order parameter for this symmetry is the vacuum expectation value of the singlet scalar density $\big\langle S^0 \big\rangle$, known as *chiral condensate*. The density S^0 is not invariant under the non-singlet axial transformation (1.59). The massless action of QCD is invariant, therefore a non-zero value of the chiral condensate signals the breaking of this symmetry by the vacuum of the theory. In presence of a spontaneously broken symmetry the Goldstone's theorem [67] states the existence of one massless boson for each broken generator. These particles have the same quantum numbers of the broken charges. In the case of QCD the Ward Identity (1.71) at zero quark mass,

$$\partial^x_\mu \Big\langle A^a_\mu(x) P^b(y) \Big\rangle = -\frac{\delta^{ab}}{N_f} \delta(y-x) \big\langle S^0(y) \big\rangle \, , \tag{1.73}$$

reveals that in presence of SSB of chiral symmetry the axial current is not conserved. The associated broken charge is

$$\overline{A}^a_0(x_0) \equiv \int d^3\boldsymbol{x} \, A^a_0(x_0, \boldsymbol{x}) = \int d^3\boldsymbol{x} \, (\overline{\psi}\gamma_0\gamma_5 T^a \psi)(x_0, \boldsymbol{x}) \, , \tag{1.74}$$

[3] Being an ultraviolet property of the theory, the renormalization is not affected by the (spontaneous) breaking of chiral symmetry, which is a vacuum (infrared) effect.

meaning that the pions (the Goldstone bosons) are pseudoscalar mesons. Quark masses break explicitly chiral symmetry. The Goldstone mechanism does not apply in physical QCD, and the pions are massive particles. It is however interesting from the theoretical point of view to verify non-perturbatively if massless QCD exhibits the expected spontaneous breaking of chiral symmetry. Provided that, it can be shown that the pion mass squared is proportional to the (renormalized) quark mass, so that when the chiral limit is taken the pions become Golstone bosons. In the following we will review some non-perturbative results about these two topics.

Non-perturbative tests of chiral SSB

The SSB of chiral symmetry in the massless theory was proven from first principles in lattice QCD with $N_f = 2$ Wilson fermions [57, 49]. As we will discuss in Section 3.2, the Wilson discretization of the fermionic action explicitly breaks chiral symmetry. As a consequence the chiral condensate has power divergences that must be subtracted also in the chiral limit. Alternatively the *Banks-Casher relation* [12] can be used,

$$\lim_{\lambda\to 0}\lim_{m_R\to 0}\lim_{V\to\infty}\rho(\lambda,m)=\frac{\Sigma}{\pi}\,, \tag{1.75}$$

which links the zero mass and infinite volume limit of the chiral condensate

$$\Sigma=-\lim_{m_R\to 0}\lim_{V\to\infty}\frac{\langle S^0\rangle}{N_f} \tag{1.76}$$

to the value at the origin ($\lambda \to 0$) of the average spectral density $\rho(\lambda, m)$ of the Dirac operator in the zero mass and infinite volume limit. The spectral density ρ renormalizes multiplicatively, and it is not affected by power divergences. Through the Banks-Casher relation (1.75) it is possible to properly define and compute efficiently from the lattice the chiral condensate. This strategy was proven to work in [57], where the chiral condensate at fixed lattice spacing was computed in QCD with $N_f = 2$ flavours of Wilson fermions, at some values of the quark mass (see Figure 1.2a). The non-zero value in the chiral limit extrapolation is the non-perturbative signal of the SSB of chiral symmetry.

Pion mass and GMOR relation

In the presence of quark masses, the relevant Ward Identity for understanding the breaking of the axial generators is again the PCAC equation (1.71) with non-zero (renormalized) quark mass (we assume degenerate flavours). Starting from this equation it is possible to derive the *Gell Mann-Oakes-Renner* (GMOR) *relation* [55]:

$$\lim_{m_R\to 0}\frac{(M_\pi^m)^2(F_\pi^m)^2}{2m_R}=-\left.\frac{\langle S^0\rangle}{N_f}\right|_{m_R=0} \tag{1.77}$$

where M_π^m is the pion mass and F_π^m is the pion decay constant defined through

$$\langle 0|\overline{A}_0^a(x_0)|\pi^b\rangle = i\delta^{ab}M_\pi^m e^{-M_\pi x_0}F_\pi^m\,, \tag{1.78}$$

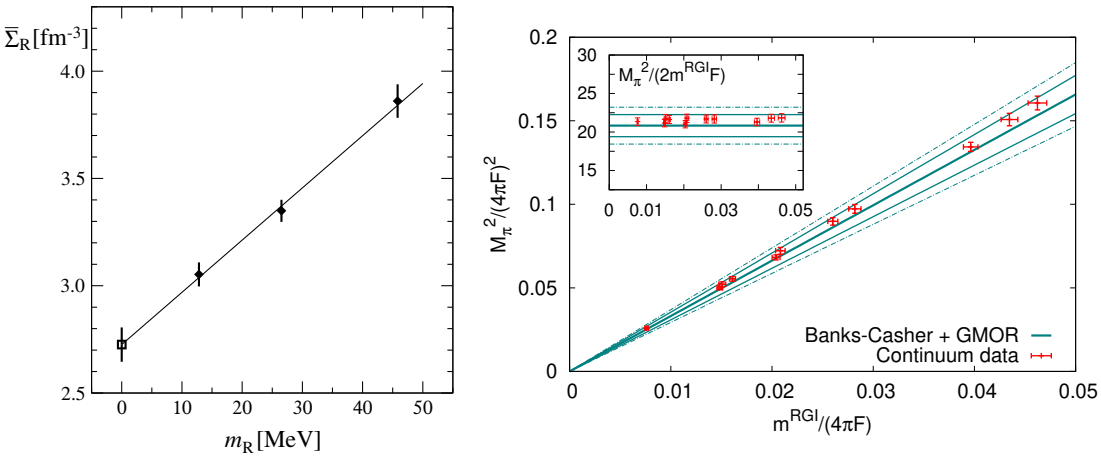

(a) (b)

Figure 1.2: Left: Zero quark mass extrapolation of the chiral condensate of QCD at fixed lattice spacing with $N_f = 2$ Wilson fermions. Plot from [57]. Right: Pion mass as a function of the RGI quark mass in $N_f = 2$ QCD. The central line is the GMOR prediction computed by taking the direct measure of the condensate with the Banks-Casher relation. Plot from [49].

both at non-zero quark masses. For small quark masses this relation can be reshaped in

$$(M_\pi^m)^2 = -2\frac{\langle S^0 \rangle}{N_f (F_\pi)^2} m_R + \mathrm{O}(m_R^2)\,, \tag{1.79}$$

where the coefficient of m_R is evaluated at zero quark mass. At leading order the pion mass is related to the square root of the quark mass times a coefficient containing the chiral condensate. As we take the chiral limit, the mass of the $N_f^2 - 1$ pions vanishes and we recover the Goldstone bosons.

A numerical test for this scaling was carried out in $N_f = 2$ QCD [49]. They computed for decreasing quark mass the pion mass M_π^m, the matrix element F_π^m and the chiral condensate (using the Banks-Casher relation) in the zero quark mass limit. Then they compared the behavior of M_π as a function of the quark mass with the prediction from equation (1.79), finding perfect agreement (see Figure 1.2b). From equation (1.34) we expect that, in general, hadron masses can be written as

$$M_{\mathrm{had}} \sim f(m_R/\mathcal{M}_{\mathrm{phys}})\mathcal{M}_{\mathrm{phys}}\,, \tag{1.80}$$

where f is a mild function of the quark mass. Pions are peculiar particles because they are pseudo-Goldstone bosons. The GMOR relation (1.79) allows to specify the dependence of the pion mass on the renormalized quark mass,

$$M_\pi \sim \sqrt{\mathcal{M}_{\mathrm{phys}}\, m_R}\,, \tag{1.81}$$

which in turn predicts that these particles are lighter with respect to other mesons in the QCD spectrum. This is actually observed in Nature, and can be interpreted as the signal of the missed SSB of chiral symmetry due to non-zero quark masses.

1.7 Topology of QCD

The topological charge density $q(x)$ we introduced in eq. (1.7) plays an important role in characterizing the vacuum structure of QCD and pure YM theory. In the presence of periodic boundary conditions for the fields the spacetime integral of $q(x)$, called *topological charge*, is an integer number:

$$Q = \int d^4x\, q(x)\,, \quad Q \in \mathbb{Z}\,. \tag{1.82}$$

It can be shown that, at the classical level, the field space of a non-Abelian gauge theory is factorized in *topological sectors*: gauge fields belonging to a sector have the same topological charge Q. Solutions of the classical field equations with non-zero topology are called *instantons* and constitute local minima of the action [16]. Moving to the quantum theory, QCD has many local minima classified by their topological charge. Therefore the partition function can be written as a sum of partition functions at fixed topological charge:

$$\mathcal{Z}_Q = \int DAD\overline{\psi}D\psi\, \delta_Q e^{-S[A,\overline{\psi},\psi]}\,. \tag{1.83}$$

Sometimes it is convenient to leave the θ-term in the path integral as a source. Being Q integer, the partition function can be written as

$$\mathcal{Z}(\theta) = \sum_{Q\in\mathbb{Z}} e^{-i\theta Q}\mathcal{Z}_Q\,. \tag{1.84}$$

This equation shows that the partition function is periodic in θ with period 2π. Under a parity transformation the topological charge flips sign, therefore the partition function is an even function of θ:

$$\mathcal{Z}(\theta) = \mathcal{Z}(-\theta). \tag{1.85}$$

The cumulants of the topological charge distribution can be generated by taking derivatives with respect to θ: assuming the theory is in a finite volume V,

$$c_n = -\frac{1}{V}\left(\frac{\partial}{\partial\theta}\right)^{2n} \ln\mathcal{Z}(\theta)\bigg|_{\theta=0}\,. \tag{1.86}$$

Property (1.85) implies that odd derivatives are all zero. In particular the expectation value of the topological charge, related to the first derivative, vanishes:

$$\langle Q\rangle = \frac{1}{\mathcal{Z}}\int DAD\overline{\psi}D\psi\,\left(\int d^4x\, q(x)\right) e^{-S[A,\overline{\psi},\psi]} = 0\,. \tag{1.87}$$

The $n = 1$ cumulant is the *topological susceptibility* and carries information on the fluctuations of the topological charge:

$$\chi_t \equiv c_1 = \frac{1}{V}\langle Q^2 \rangle = \int d^4x \, \langle q(x)q(0) \rangle \tag{1.88}$$

where in the second step we used translational invariance to set one of the densities in $x = 0$. These cumulants are primary quantities for the study of the properties of the distribution of the topological charge. In the infinite volume limit this distribution is a Gaussian with width controlled by the topological susceptibility. The leading non-Gaussianity correction is suppressed with the volume and it is related to the ratio c_2/χ_t, which was studied non-perturbatively in the pure gauge theory in [63].

Chapter 2

QCD thermodynamics

In this Chapter we drift towards the main topic of this thesis, that is QCD at non-zero temperature. There is a vivid interest in the physics community in studying the properties of QCD at high temperature, as it is relevant in understanding a broad spectrum of phenomena from high-energy particle physics to the cosmological evolution of the Universe. We are mainly interested in the equilibrium thermodynamics of a system of interacting quarks and gluons at zero chemical potential, whose properties are summarized by the QCD *Equation of State* (EoS). This is a characterizing property of QCD given by the temperature dependence of (for instance) the pressure, the entropy density and the energy density of QCD matter. In the first part of the Chapter we will review the setup of QCD at non-zero temperature in the path integral formalism. Then we will describe the main features of the high temperature phase of QCD and some related numerical results from the literature. The second part of the Chapter is dedicated to the thermal effective field theory (thEFT) of QCD, which is based on the factorization of the degrees of freedom of QCD at the three energy scales $\sim \pi T$, $\sim gT$, $\sim g^2 T/\pi$ where g is the QCD coupling. This effective theory can be employed to study phenomena at low three-momentum (i.e. long distances) compared to the temperature. The thEFT is the standard framework where perturbative computations in QCD at high temperature are carried out [141, 35, 83, 150, 8, 161, 82]. We dedicate the last Section to the perturbative determination of the QCD EoS: we will review and summarize the final expressions. This is the state of the art of the knowledge of the EoS of QCD at temperatures higher than ~ 1 GeV.

2.1 Finite temperature

At the quantum mechanical level, a thermal system of interacting quarks and gluons at zero quark chemical potential is described by the partition function ($k_B = 1$ in our units)

$$\mathcal{Z}(T, \mu_f) = \mathrm{Tr}\left\{ e^{-\widehat{H}/T} \right\} , \tag{2.1}$$

where $\widehat{H}$ is the Hamiltonian operator and T is the temperature of the thermal system. The trace is taken over all the states in the Hilbert space on which to the Hamiltonian $\widehat{H}$ acts. The partition function (2.1) admits a representation in terms of a path integral over the quark and gluon fields in Euclidean space. The expression is formally equivalent to the one we have already introduced in eq. (1.30), but now the QCD action (1.11) is replaced by

$$S[A,\overline{\psi},\psi] = \int_0^{1/T} dx_0 \int_V d^3\boldsymbol{x} \left[\frac{1}{2g_0^2}\mathrm{tr}\left\{F_{\mu\nu}(x)F_{\mu\nu}(x)\right\} + \overline{\psi}(x)\left(\not{D} + M_0\right)\psi(x)\right], \quad (2.2)$$

where the integral over the Euclidean time is restricted to $1/T$, and the fields satisfy (anti)periodic boundary conditions in the temporal direction:

$$\begin{aligned} A_\mu(x_0 + 1/T, \boldsymbol{x}) &= A_\mu(x_0, \boldsymbol{x})\,, \\ \psi(x_0 + 1/T, \boldsymbol{x}) &= -\psi(x_0, \boldsymbol{x})\,, \\ \overline{\psi}(x_0 + 1/T, \boldsymbol{x}) &= -\overline{\psi}(x_0, \boldsymbol{x})\,. \end{aligned} \quad (2.3)$$

If the theory is set up in a finite three-dimensional box of volume $V = L_1L_2L_3$, then gauge and quark fields satisfy periodic boundary conditions in the three spatial directions.

We may understand the physical meaning of the compact temporal direction as follows. Let's rewrite the partition function (2.1) using a complete set of states in the Hilbert space,

$$\mathcal{Z}(T) = \sum_n \langle n|e^{-\widehat{H}/T}|n\rangle = \sum_n \langle n|n\rangle\, e^{-E_n/T}\,, \quad (2.4)$$

where $\widehat{H}|n\rangle = E_n|n\rangle$. In the zero temperature limit, $1/T \to \infty$, only the vacuum of the theory contributes to the partition function. When the temperature is finite all the states in the sum (2.4) contribute, each weighted with the proper Boltzmann factor $\sim e^{-E_n/T}$. Given the partition function, we can now introduce the thermodynamic functions. In the formulas below we assume that the thermodynamic limit $V \to \infty$ is understood. The *free-energy density* is related to the logarithm of the partition function,

$$f(T) = -\frac{T}{V}\ln\mathcal{Z}(T)\,, \quad (2.5)$$

where we make explicit the temperature dependence only, but in principle the free-energy inherits from $\mathcal{Z}$ the dependence on all the parameters of the theory. Up to a sign, the free-energy density gives the *pressure*:

$$p = -f\,. \quad (2.6)$$

The derivative with respect to the temperature of $\ln\mathcal{Z}$ is the *energy density*,

$$e(T) = \frac{T^2}{V}\frac{\partial}{\partial T}\ln\mathcal{Z}(T)\,. \quad (2.7)$$

Another quantity that will be relevant in the following is the *entropy density*,

$$s(T) = -\frac{\partial}{\partial T}f(T)\,. \quad (2.8)$$

Entropy density, energy density and pressure satisfy the following relation,

$$Ts = e + p\,, \tag{2.9}$$

and their temperature dependence gives the Equation of State.

2.2 Thermodynamics from a moving frame

We can take advantage of the invariance of QCD under the Euclidean Lorentz group SO(4) to generalize the partition function defined in eq. (2.1) to a thermal system in a moving reference frame (see [91], paragraph 2),

$$\mathcal{Z}(L_0, \boldsymbol{\xi}) = \mathrm{Tr}\left\{ e^{-L_0(\widehat{H} - i\boldsymbol{\xi}\cdot\widehat{\boldsymbol{P}})} \right\}\,, \tag{2.10}$$

where L_0, $\widehat{H}$ and $\widehat{\boldsymbol{P}}$ are respectively the size of the compact direction of the system, the Hamiltonian operator and the total momentum operator. The vector $\boldsymbol{\xi} = (\xi_1, \xi_2, \xi_3)$ represents the Euclidean boost of the system. The free-energy density in presence of a non-zero shift can be defined as usual,

$$f(L_0, \boldsymbol{\xi}) = -\frac{1}{L_0 V} \ln \mathcal{Z}(L_0, \boldsymbol{\xi})\,, \tag{2.11}$$

where we explicitly indicate only the dependence on the temporal extension L_0 and on the shift $\boldsymbol{\xi}$. The partition function eq. (2.10) is equivalent to an Euclidean path integral with fields satisfying shifted boundary conditions in the temporal direction [60],

$$\begin{aligned} A_\mu(x_0 + L_0, \boldsymbol{x}) &= A_\mu(x_0, \boldsymbol{x} - L_0\boldsymbol{\xi})\,, \\ \psi(x_0 + L_0, \boldsymbol{x}) &= -\psi(x_0, \boldsymbol{x} - L_0\boldsymbol{\xi})\,, \\ \overline{\psi}(x_0 + L_0, \boldsymbol{x}) &= -\overline{\psi}(x_0, \boldsymbol{x} - L_0\boldsymbol{\xi})\,, \end{aligned} \tag{2.12}$$

while in a finite three-dimensional volume V the fields satisfy periodic boundary conditions in the spatial directions.

In the thermodynamic limit the following identity between free-energy densities holds as a consequence of the Lorentz invariance of the theory [59]:

$$f(L_0, \boldsymbol{\xi}) = f(L_0/\gamma, \mathbf{0})\,, \quad \gamma = 1/\sqrt{1 + \boldsymbol{\xi}^2}\,. \tag{2.13}$$

This means that the thermodynamics in the $\boldsymbol{\xi} \neq \mathbf{0}$ frame, at temperature $1/L_0$, is directly related to the thermodynamics in the $\boldsymbol{\xi} = \mathbf{0}$ frame with a lower temperature T,

$$T = \frac{\gamma}{L_0}\,, \quad \gamma = \frac{1}{\sqrt{1 + \boldsymbol{\xi}^2}}\,, \tag{2.14}$$

or equivalently a compact direction longer by a factor $\sqrt{1 + \boldsymbol{\xi}^2}$. If we consider instead the theory in finite spatial volume, it can be shown (see [59], and Appendix D.4) that the identity (2.13) holds up to corrections exponentially suppressed as $\sim e^{-M_{\mathrm{gap}} L_i}$ in the $M_{\mathrm{gap}} L_i \to \infty$ limit, where $M_{\mathrm{gap}} \propto T$ is the mass of the lightest screening state of the theory and L_i, $i = 1, 2, 3$ is each of the spatial sizes.

2.2.1 Ward Identities in a moving frame

Equation (2.13) generates interesting Ward Identities involving 1-point functions of the total momentum and/or total energy operators, which would be trivial in presence of standard (anti)periodic boundary conditions in the compact direction. In the following we will discuss a few examples which are relevant for the original work of this thesis. For further details and the proofs of the formulas we refer to Appendix D.

By differentiating once with respect to the shift ξ_k both sides of equation (2.13) we can relate the entropy in the rest frame to the shift-derivative of the free-energy in the moving frame,

$$Ts = \frac{1+\boldsymbol{\xi}^2}{\xi_k}\frac{\partial}{\partial \xi_k} f(L_0, \boldsymbol{\xi})\,, \quad T = \frac{1}{L_0\sqrt{1+\boldsymbol{\xi}^2}}\,, \tag{2.15}$$

where we stress that the temperature T is the one in the frame at rest with the thermal system. Using the quantum mechanical representation of the Euclidean thermal partition function, eq. (2.10), and the mapping $\widehat{P}_k \to -iT_{0k}$ between the momentum operator and the Energy-Momentum tensor $T_{\mu\nu}$ (defined in Appendix B), it is immediate to show that

$$\langle T_{0k}\rangle_{\boldsymbol{\xi}} = -\frac{\partial}{\partial \xi_k} f(L_0, \boldsymbol{\xi})\,, \tag{2.16}$$

where the expectation value on the left is taken in the shifted frame. Combining this result with equation (2.15) we get

$$Ts = -\frac{1+\boldsymbol{\xi}^2}{\xi_k}\langle T_{0k}\rangle_{\boldsymbol{\xi}}\,, \tag{2.17}$$

which in principle provides a practical way to compute the entropy density from numerical simulations, by measuring the relevant one-point function of the Energy-Momentum tensor in a shifted setup. Another interesting Ward Identity is obtained from (2.13) if we differentiate both sides with respect to L_0. Assuming a non-zero shift in the component ξ_k only we get

$$\langle T_{0k}\rangle_{\boldsymbol{\xi}} = \xi_k \left(\langle T_{00}\rangle_{\boldsymbol{\xi}} - \langle T_{jj}\rangle_{\boldsymbol{\xi}}\right)\,, \quad j \neq k\,, \xi_j = 0\,. \tag{2.18}$$

This Ward Identity will be relevant in the discussion of the non-perturbative renormalization of the lattice QCD Energy-Momentum tensor, see Chapter 5.

2.3 Thermal phases of QCD

Here we review some established non-perturbative results about the high-temperature regime of QCD. For the clarity of the presentation we discuss the pure SU(3) gauge theory first, and then we consider dynamical quarks.

2.3.1 SU(3) Yang-Mills theory

The action of the pure gauge theory is invariant under the global symmetry $\mathbb{Z}_3$, which is the centre of the SU(3) group [130, 146]. Centre transformations are defined as

$$\Omega(x_0 + 1/T, \boldsymbol{x}) = z\,\Omega(x_0, \boldsymbol{x})\,, \quad z = e^{2\pi i l/3} \in \mathbb{Z}_3 \quad (l = 0, 1, 2)\,, \tag{2.19}$$

where Ω is an element of SU(3). It is immediate to check that the centre-transformed field $A'_\mu(x)$, see equation (1.2), satisfies the same boundary conditions of the original field $A_\mu(x)$, eq. (2.3). In the quantum theory this symmetry can be exactly realized or spontaneously broken. This is associated to two phases for the pure gauge theory, connected by a first order transition [159] as the temperature increases. The low temperature phase is called *confined* phase, with glueballs as degrees of freedom. The *deconfined* high temperature phase is characterized by gluons as main degrees of freedom. The common choice of the order parameter for this transition is the expectation value of the *Polyakov loop*,

$$L(\boldsymbol{x}) \equiv \frac{1}{N_c}\mathrm{tr}\left\{\mathcal{T}e^{-i\int_0^{1/T} dx_0 A_0(x_0,\boldsymbol{x})}\right\}\,, \tag{2.20}$$

that is, the trace of the time-ordered exponential of the line integral of A_0 along a path wrapped around the compact direction. Under a $\mathbb{Z}_3$ transformation it becomes

$$L'(\boldsymbol{x}) = \frac{1}{N_c}\mathrm{tr}\left\{\Omega(1/T, \boldsymbol{x})\left(\mathcal{T}e^{-i\int_0^{1/T} dx_0 A_0(x_0,\boldsymbol{x})}\right)\Omega^\dagger(0, \boldsymbol{x})\right\} = z\,L(\boldsymbol{x})\,, \tag{2.21}$$

which means, as expected, that the Polyakov loop is not invariant under a centre transformation. Below the critical temperature $T_c \sim 300$ MeV the symmetry is respected, and the order parameter vanishes: $\langle L\rangle = 0$. Above T_c the symmetry is spontaneously broken as signaled by a $\langle L\rangle \neq 0$ value.

2.3.2 Full QCD

Dynamical fermions explicitly break the $\mathbb{Z}_3$ centre symmetry. The breaking is easily seen from the boundary conditions. When a centre transformation (2.19) is applied, the transformed fields satisfy the boundary conditions

$$\begin{aligned}\psi'(x_0 + 1/T, \boldsymbol{x}) &= \Omega(x_0 + 1/T, \boldsymbol{x})\psi(x_0 + 1/T, \boldsymbol{x}) \\ &= -z\,\Omega(x_0, \boldsymbol{x})\psi(x_0, \boldsymbol{x}) = -z\,\psi'(x_0, \boldsymbol{x})\,,\end{aligned} \tag{2.22}$$

with $z \in \mathbb{Z}_3$, while the original fields are antiperiodic in time. An analogous relation holds for the antiquark field $\overline{\psi}$. In QCD (at physical quark masses, see below) the phase transition is replaced by a smooth crossover from the hadronic phase to the deconfined phase, called *Quark-Gluon Plasma* (QGP).

It is interesting to study the critical behaviour of QCD in terms of the quark masses, as shown in the Columbia plot in Figure 2.1a recently reviewed in [40]. We consider the case of $N_f = 2 + 1$ QCD, with degenerate light quark masses. Let's start from the top-right corner of the plot, where quarks have very large masses. In this scenario

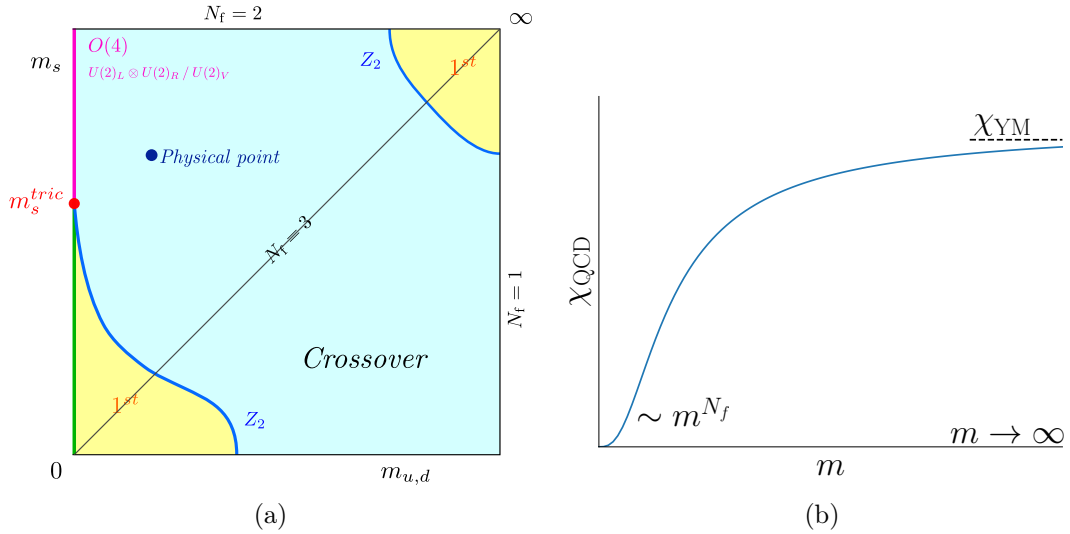

Figure 2.1: Left: Columbia plot showing the order and nature of the phase transition in QCD as functions of the light $m_{u,d}$ and strange m_s quark masses. Each point is a phase boundary with its own (pseudo-)critical temperature $T_c(m_{u,d}, m_s)$. Plot from [40]. Right: Qualitative dependence on the quark mass of the topological susceptibility in QCD at high temperature.

quarks are almost decoupled from the dynamics and effectively behave as static sources. Thus QCD "falls back" to the pure YM theory: the $\mathbb{Z}_3$ centre symmetry holds at low temperature and it is spontaneously broken at high temperature with a 1^{st} order phase transition. As we lower quark masses this phase transition becomes weaker and weaker till it vanishes along a critical line of 2^{nd} order transition. The light blue region of the plot is characterized by the absence of phase transition. The low and high temperature phases are smoothly connected by a crossover at some pseudo-critical temperature, which is a function of the quark masses. Notice that the physical point (blue point) lies in this regime. Near the chiral limit (bottom-left corner) the relevant symmetry is chiral symmetry, and the natural order parameter is the chiral condensate. At the chiral point ($m_{u,d} = m_s = 0$) the non-singlet axial generators of chiral symmetry are spontaneously broken at zero temperature (see Section 1.6). This symmetry is expected to be restored as the temperature increases through a 1^{st} order phase transition for $N_f \geq 3$ [127]. Some numerical explorations [14] show that the chiral condensate is actually suppressed as the temperature increases. Furthermore, the effective restoration of the non-singlet axial chiral symmetry at high temperature is signaled by the degeneracy of the vector and axial mesonic screening masses [46, 93] (left panel of Figure 2.2), as well as by the degeneracy of the positive and negative parity channels of the nucleon screening mass [64].

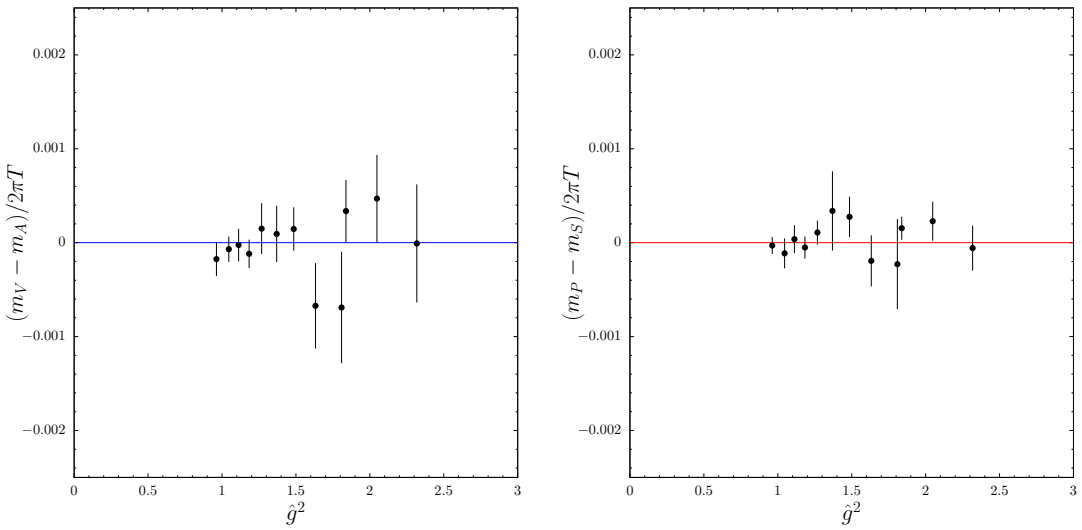

Figure 2.2: Plots from [93]. Left: degeneracy of vector-axial mesonic screening masses due to the effective restoration of the non-singlet axial chiral symmetry at high temperature. Right: Degeneracy of pseudoscalar-scalar mesonic screening masses due to the effective restoration of the $\mathrm{U}(1)_A$ symmetry at high temperature. These are continuum extrapolated results, generated with $N_f = 3$ $\mathrm{O}(a)$-improved Wilson fermions. $\hat{g}^2$ is the 2-loop $\overline{\mathrm{MS}}$ coupling. The temperature interval associated to the data is $1 - 160$ GeV.

2.4 Topology at high temperature

The topological susceptibility turns out to be suppressed as the temperature increases. The instanton gas model predicts

$$\chi_{\mathrm{YM}}(T) \sim T^{-7}\,, \quad T \to \infty \tag{2.23}$$

for the SU(3) pure gauge theory, while for QCD with N_f light flavours

$$\chi_{\mathrm{QCD}}(T) \sim m^{N_f}\, T^{-8}\,, \quad T \to \infty\,, \quad m \to 0\,. \tag{2.24}$$

The suppression of χ_{YM} with the temperature has been numerically observed for instance in [58]. There are also attempts with dynamical fermions to verify non-perturbatively the temperature dependence of the topological susceptibility of QCD, eq. (2.24) [20, 10]. One consequence of this temperature suppression is the effective restoration of the singlet axial subgroup $\mathrm{U}(1)_A$ of chiral symmetry, that is anomalously broken in QCD at zero temperature. At very high temperature this restoration shows off in the degeneracy of the mesonic screening masses in the pseudoscalar and scalar channels [93], see the right panel of Figure 2.2.

In parallel to the Columbia plot, Figure 2.1a, it is also interesting for the purposes of this thesis to understand the dependence of the topological susceptibility with the

quark mass, at given (high) temperature T. Moving from the bottom left corner to the top right corner of that plot the quark masses increase, fermions become more and more static and in the limit $m \to \infty$ they decouple. The theory approaches the pure gauge theory and thus in this limit $\chi_{\rm QCD}$ should plateau to $\chi_{\rm YM}$, which is expected to be higher since the suppression at small quark mass is lost and the topological susceptibility in pure gauge is less suppressed with the temperature than in QCD (compare equations (2.23) and (2.24)). Figure 2.1b shows qualitatively the described dependence of $\chi_{\rm QCD}$ on the quark mass. These observations will be relevant in Chapter 4, when we will discuss the strategy for the non-perturbative determination of the Equation of State of QCD at very high temperature.

2.5 Effective theory approach in thermal QCD

We discuss now a commonly used theoretical framework to study strong interactions at high temperature: the thermal effective theory of QCD (thEFT) [7]. At high temperatures it is possible to classify the degrees of freedom of QCD in *hard*, *soft* and *ultrasoft* modes, which contribute at the three energy scales $\pi T \gg gT \gg g^2 T/\pi$. Physics at long distances with respect to the compact direction can be described by an effective theory whose degrees of freedom are the soft and ultrasoft modes, while the hard modes contribute through the matching coefficients. This effective theory is called Electrostatic QCD. Following similar arguments, Electrostatic QCD can be further reduced to an effective theory for the ultrasoft modes only, called Magnetostatic QCD. Notice that the thEFT can be defined non-perturbatively (in the weak coupling sense) and is well suited, in principle, for numerical simulations [73, 125, 79, 116]. This said, the thEFT is the standard framework were perturbative calculations at high temperature are carried out.

2.5.1 Hard and soft modes

We start with the classification of the degrees of freedom of QCD in the $T \to \infty$ limit in the free theory case. The Fourier expansions for the quark and gluon fields are

$$A_\mu(x_0, \boldsymbol{x}) = T \sum_n \int \frac{d^3\boldsymbol{p}}{(2\pi)^3} e^{i(\omega_n x_0 + \boldsymbol{p}\cdot\boldsymbol{x})} \widetilde{A}_\mu(\omega_n, \boldsymbol{p}) \,, \quad \omega_n = 2n\pi T \,, \tag{2.25}$$

$$\psi(x_0, \boldsymbol{x}) = T \sum_n \int \frac{d^3\boldsymbol{p}}{(2\pi)^3} e^{i(\omega_n x_0 + \boldsymbol{p}\cdot\boldsymbol{x})} \widetilde{\psi}(\omega_n, \boldsymbol{p}) \,, \quad \omega_n = (2n+1)\pi T \,, \tag{2.26}$$

and the same for $\overline{\psi}$. The boundary conditions (2.3) replace the integrals in the compact direction with sums, and the Fourier modes ω_n with $n \in \mathbb{Z}$ are called *Matsubara frequencies*. We consider the free actions in Fourier space for gluons and fermions,

$$S^{G,\text{free}} = \frac{1}{2g_0^2} T \sum_n \int \frac{d^3\boldsymbol{p}}{(2\pi)^3} \widetilde{A}^{a,\dagger}_\mu(\omega_n, \boldsymbol{p}) \big[(2n\pi T)^2 + \boldsymbol{p}^2\big] \widetilde{A}^a_\mu(\omega_n, \boldsymbol{p}) \,, \tag{2.27}$$

$$S^{F,\text{free}} = T\sum_n \int \frac{d^3\boldsymbol{p}}{(2\pi)^3} \sum_{f=1}^{N_f} \widetilde{\bar{\psi}}_f(\omega_n,\boldsymbol{p})\big[i(2n+1)\pi T\gamma_0 + ip_k\gamma_k + m_{0,f}\big]\widetilde{\psi}_f(\omega_n,\boldsymbol{p})\,, \quad (2.28)$$

where the index f attached to the fermionic fields labels the N_f flavours. The inverse of the quantities in square brackets are the free gluon and quark propagators. We further assume that the three-momentum of the fields is small compared to the temperature, $|\boldsymbol{p}| \ll T$. This is true if we are interested in the physics at large spatial distances compared to size $1/T$ of the compact direction. We see that the fermionic modes are suppressed by a non-vanishing thermal mass $(2n+1)\pi T$, as well as the gluonic modes with $n \neq 0$ Matsubara frequencies. These are the *hard* modes, while the remaining $n = 0$ modes of the gluonic field are the *soft* modes. The latter fields are static, i.e. time-independent, and we denote them as follows:

$$A_\mu(x_0,\boldsymbol{x}) \to \bar{A}_\mu(\boldsymbol{x})\,. \quad (2.29)$$

As a consequence, the effective theory of soft modes is a three-dimensional theory, a fact that goes under the name of *dimensional reduction*. Gauge transformations are time-independent as well, and for the different fields read

$$\bar{A}_0'(\boldsymbol{x}) = \Omega(\boldsymbol{x})\bar{A}_0(\boldsymbol{x})\Omega^\dagger(\boldsymbol{x})\,, \quad (2.30)$$

$$\bar{A}_j'(\boldsymbol{x}) = \Omega(\boldsymbol{x})\bar{A}_j(\boldsymbol{x})\Omega^\dagger(\boldsymbol{x}) + i\Omega(\boldsymbol{x})\partial_j\Omega^\dagger(\boldsymbol{x})\,, \quad (2.31)$$

$$\bar{F}_{ij}'(\boldsymbol{x}) = \Omega(\boldsymbol{x})\bar{F}_{ij}(\boldsymbol{x})\Omega^\dagger(\boldsymbol{x})\,. \quad (2.32)$$

We now move to the full (interacting) theory and we assume that the classification of degrees of freedom remains valid also in this case. Given the field content of the effective theory, the related action includes all the terms which satisfy gauge invariance, Lorentz invariance and with mass dimension ≤ 4. Defining for convenience the differential operator $D_j\bar{A}_0 \equiv \partial_j\bar{A}_0 - i[\bar{A}_j,\bar{A}_0]$, we have

$$\begin{aligned} S_{\text{EQCD}} =& \frac{1}{g_E^2}\int d^3\boldsymbol{x}\Bigg[\frac{1}{2}\text{tr}\left\{\bar{F}_{ij}\bar{F}_{ij}\right\} + \text{tr}\left\{D_j\bar{A}_0 D_j\bar{A}_0\right\} \\ &+ m_E^2\text{tr}\left\{\bar{A}_0^2\right\} + \lambda^{(1)}\text{tr}\left\{\bar{A}_0^2\right\}^2 + \lambda^{(2)}\text{tr}\left\{\bar{A}_0^4\right\} + ...\Bigg]\,, \end{aligned} \quad (2.33)$$

the dots standing for terms with higher mass dimension and thus suppressed with the proper power of $1/T$. This theory is known as *Electrostatic QCD* (EQCD). Notice that, as a consequence of dimensional reduction, the component $\bar{A}_0$ is in the adjoint representation of the gauge group and therefore admits a mass term. The parameter m_E is the related mass and it is called *Debye mass*. The dimensionful coupling g_E^2, the mass m_E and the parameters $\lambda^{(1)}$ and $\lambda^{(2)}$ need to be matched to the full theory so to reproduce QCD, up to temperature-suppressed corrections due to the (infinitely many) higher dimensional operators that are missing in the effective action. In particular, at leading order in the effective theory $g_E^2 = g^2T$ where g is the coupling of QCD and the temperature comes from the integration over time of the time-independent effective action.

T	g/π	$(g/\pi)^2$
500 MeV	0.555	0.308
1 GeV	0.491	0.242
10 GeV	0.379	0.143
100 GeV	0.321	0.103
1 TeV	0.284	0.081
1 PeV	0.221	0.049

Table 2.1: Comparison of the values of the strong coupling at some temperatures. The coupling g is taken to be the $N_f = 3$ $\overline{\text{MS}}$ coupling at 5-loop [11] computed at the scale $\mu = 2\pi T$.

2.5.2 Soft and ultrasoft modes

The Debye mass $m_E \sim gT$ provides the "hard" energy scale of EQCD. Phenomena at energies much smaller than gT can be studied in an even simpler effective theory, obtained as a large-m_E expansion of EQCD. The *ultrasoft* degrees of freedom of this effective theory are the spatial components $\bar{A}_j(\boldsymbol{x})$ of the static gauge field, for which a mass term is forbidden by gauge invariance. The heavy $\bar{A}_0$ mode instead contributes through the matching coefficients. The action corresponding to this effective theory is

$$S_{\text{MQCD}} = \frac{1}{g_E^2} \int d^3\boldsymbol{x} \left[\frac{1}{2} \text{Tr} \left\{ \bar{F}_{ij} \bar{F}_{ij} \right\} + ... \right] , \tag{2.34}$$

where the dots stand for higher dimensional operators suppressed with the proper power of $1/m_E$. The effective theory described by the action (2.34) is called *Magnetostatic QCD* (MQCD). This is a confining theory and it is of non-perturbative nature. The only mass scale that appears is $g_E^2 = g^2 T$, meaning that, at the scales where this effective theory holds, every dimensionful quantity is proportional to an appropriate power of $g^2 T$ with a non-perturbative coefficient.

2.5.3 Scope of the effective theory

The thEFT approach relies on the assumption that, at high temperature, the degrees of freedom of QCD are factorized in hard, soft and ultrasoft modes. This is actually achieved if the three related energy scales, respectively $\sim \pi T$, $\sim gT$ and $\sim g^2 T/\pi$, satisfy the hierarchy

$$g^2 T/\pi \ll gT \ll \pi T \, . \tag{2.35}$$

Normalizing by πT we convert this relation to a hierarchy for the coupling constant:

$$\left(\frac{g}{\pi}\right)^2 \ll \frac{g}{\pi} \ll 1 \, . \tag{2.36}$$

The coupling is a logarithmically decreasing function of the temperature, so we may wonder at which temperature the relation (2.36) is actually respected. Table 2.1 shows

the values of the terms appearing in this relation, computed in perturbation theory, for temperatures from 500 MeV to 1 PeV. The picture that emerges is that, for temperatures $T \lesssim 100$ GeV, no clear separation of the three scales is present. At the electro-weak scale there might be some sign of hierarchy, with the soft and ultrasoft interaction strengths being respectively $\sim 1/3$ and $\sim 1/10$ with respect to the hard scale. Notice that for having the coupling g/π of the order of ~ 0.1 we should push the temperature to scales far above the ones considered.

2.5.4 The pressure of QCD in thermal effective theory

As a relevant example, we show how the pressure of QCD splits at the three scales of the effective theory [82]. We consider the pressure in the thermodynamic limit. From equation (2.6) it reads

$$p(T) = \lim_{V\to\infty} \frac{T}{V} \ln \left\{ \int DAD\overline{\psi}D\psi \, e^{-S[A,\overline{\psi},\psi]} \right\} \tag{2.37}$$

where S is the thermal QCD action (2.2). From now on we will assume the infinite volume limit and drop it from our equations. We also assume that $p(T)$ is defined so that $p(T=0) = 0$. We write the QCD pressure as

$$p(T) = p_E(T) + \frac{T}{V} \ln \left\{ \int D\bar{A}_k D\bar{A}_0 \, e^{-S_{\mathrm{EQCD}}} \right\} , \tag{2.38}$$

where p_E is the contribution of full QCD minus the pressure of EQCD, and it is a coefficient to be matched to the full theory. The EQCD pressure can be further factorized by extracting the contribution from MQCD,

$$\frac{T}{V} \ln \left\{ \int D\bar{A}_k D\bar{A}_0 \, e^{-S_{\mathrm{EQCD}}} \right\} = p_M(T) + \frac{T}{V} \ln \left\{ \int D\bar{A}_k \, e^{-S_{\mathrm{MQCD}}} \right\} , \tag{2.39}$$

where $p_M(T)$ is a matching coefficient between EQCD and MQCD and represents the difference of these two contributions to the pressure. We finally define the MQCD pressure

$$p_G(T) = \frac{T}{V} \ln \left\{ \int D\bar{A}_k \, e^{-S_{\mathrm{MQCD}}} \right\} , \tag{2.40}$$

which cannot be computed in perturbation theory, as we have already commented. Summing up all the terms we get

$$p(T) = p_E(T) + p_M(T) + p_G(T) , \tag{2.41}$$

which contribute respectively at the scales πT (hard), gT (soft) and g^2T/π (ultrasoft). This result is the starting point for the next Section, where it is used in the context of thermal perturbation theory for computing the perturbative Equation of State of the Quark-Gluon Plasma.

2.6 The EoS of QCD from thermal perturbation theory

In this Section we review the analytic results for the QCD pressure and entropy density in thermal perturbation theory [141, 35, 83, 150, 8, 161, 82]. This is, at present, the state of the art for the EoS of QCD for temperatures higher than ~ 1 GeV. The computation amounts to performing a weak coupling expansion in the thEFT, on top of the large temperature expansion. Therefore this computation will hold up to higher order corrections in both the expansions.

2.6.1 The Linde problem

Perturbation theory in the thEFT is intrinsically limited by the fact that, as discussed in Subsection 2.5.2, the ultrasoft modes of MQCD cannot be treated perturbatively. This is signaled by an infrared problem, called *Linde problem* [94], arising from the loops involving the ultrasoft modes (see also Appendix C.1). The weak coupling expansion of quantities in thEFT is thus possible only up to the perturbative order where the ultrasoft modes do not contribute. The maximum order depends on the mass dimension d of the observable: since the ultrasoft coupling g^2T has mass dimension 1, and it is the only mass scale of MQCD, ultrasoft modes will enter the perturbative expansion at order $\sim g^{2d}T^d$.

The observable of interest is the pressure at leading order of the thEFT. Actually the computation is performed on p/T, see eq. (2.37), which has mass dimension 3. Therefore we expect the perturbative expansion to break at order $\sim g^6T^3$.

2.6.2 Hard, soft, ultrasoft contributions

The pressure in the thEFT is decomposed in hard, soft and ultrasoft terms as in equation (2.41). Using dimensional arguments we can predict at which orders each of the scales will contribute [138].

- We start from the hard scale $\sim \pi T$. Parametrically, its contribution will be $p_E(T) \sim T \cdot (\pi T)^3$, and thus it will enter at all the usual even powers of g in the perturbative expansion.
- The soft scale $\sim gT$ contributes through $p_M(T) \sim T \cdot (gT)^3$, therefore it will enter the perturbative expansion from g^3 on including odd powers.
- The ultrasoft scale $\sim g^2T/\pi$ enters through $p_G(T) \sim T \cdot (g^2T/\pi)^3$, so it contributes starting from order $\sim g^6$ as anticipated. This contribution cannot be computed in perturbation theory.

It is also interesting to understand the impact on the pressure of higher order contributions from the large temperature expansion, coming from terms in the effective action suppressed with at least one power of $1/T$. Actually it turns out (see Appendix C.2) that the leading corrections from EQCD are of the order $\sim g^7T^4$, while the leading corrections from MQCD are of the order $\sim g^9T^4$. They are both beyond the perturbative order $\sim g^6$ on which we are interested, and thus can be neglected.

2.6.3 Pressure of QCD up to $g^6 \ln(g)$

We collect the results in thermal perturbation theory for the pressure of massless QCD with generic numbers of colours N_c and flavours N_f. The pressure has been fully computed up to order $\sim g^5$. The perturbative contribution from soft modes at order $\sim g^6$ is known, as well as the logarithmic divergence $\sim g^6 \ln(g)$ of the ultrasoft modes [82]. The missing terms at order $\sim g^6$ are the contribution of hard modes (see [117] for recent results), and the finite contribution of the ultrasoft degrees of freedom which is a non-perturbative coefficient. The expansion in powers of the strong coupling constant $\alpha_s = g^2/(4\pi)$ reads [82]

$$p(T) = \frac{8\pi^2}{45} T^4 \sum_{i=0}^{6} p_i(\mu) \left(\frac{\alpha_s(\mu)}{\pi} \right)^{i/2} , \tag{2.42}$$

and p is μ-independent up to higher orders. We list the perturbative coefficients:

$$p_0 = 1 + \frac{21}{32} N_f \tag{2.43}$$

$$p_1 = 0 \tag{2.44}$$

$$p_2 = -\frac{15}{4} \left(1 + \frac{5}{12} N_f \right) \tag{2.45}$$

$$p_3 = 30 \left(1 + \frac{1}{6} N_f \right)^{3/2} \tag{2.46}$$

$$\begin{aligned} p_4 = {} & 237.2 + 15.96 N_f - 0.4150 N_f^2 \\ & + \frac{135}{2} \left(1 + \frac{1}{6} N_f \right) \ln \left[\frac{\alpha_s}{\pi} \left(1 + \frac{1}{6} N_f \right) \right] \\ & - \frac{165}{8} \left(1 + \frac{5}{12} N_f \right) \left(1 - \frac{2}{33} N_f \right) \ln \frac{\mu}{2\pi T} \end{aligned} \tag{2.47}$$

$$\begin{aligned} p_5 = {} & \left(1 + \frac{1}{6} N_f \right)^{1/2} \Bigg[- 799.1 - 21.96 N_f - 1.926 N_f^2 \\ & + \frac{495}{2} \left(1 + \frac{1}{6} N_f \right) \left(1 - \frac{2}{33} N_f \right) \ln \frac{\mu}{2\pi T} \Bigg] \end{aligned} \tag{2.48}$$

$$\begin{aligned} p_6 = {} & \Bigg[- 659.2 - 65.89 N_f - 7.653 N_f^2 \\ & + \frac{1485}{2} \left(1 + \frac{1}{6} N_f \right) \left(1 - \frac{2}{33} N_f \right) \ln \frac{\mu}{2\pi T} \Bigg] \cdot \\ & \cdot \ln \left[\frac{\alpha_s}{\pi} \left(1 + \frac{1}{6} N_f \right) \right] - 475.6 \ln \frac{\alpha_s}{\pi} \\ & + q_a(N_f) \ln^2 \frac{\mu}{2\pi T} + q_b(N_f) \ln \frac{\mu}{2\pi T} + q_c(N_f) \, . \end{aligned} \tag{2.49}$$

The terms $q_a(N_f), q_b(N_f), q_c(N_f)$ are α_s-independent polynomials in N_f. Two of them, $q_a(N_f)$, $q_b(N_f)$,are fixed requiring to cancel the μ-dependence arising from the terms of orders $\alpha_s(\mu), \alpha_s^2(\mu)$:

$$q_a(N_f) = -\frac{1815}{16}\left(1+\frac{5}{12}N_f\right)\left(1-\frac{2}{33}N_f\right)^2 , \tag{2.50}$$

$$q_b(N_f) = 2932.9 + 42.83N_f - 16.48N_f^2 + 0.2767N_f^3 . \tag{2.51}$$

The third one, $q_c(N_f)$, represents the proper $\sim g^6$ contribution that cannot be computed in perturbation theory, and thus it is left as a free parameter.

2.6.4 Entropy of QCD up to $g^6\ln(g)$

Given the pressure, the other thermodynamic quantities can be computed in perturbation theory by applying standard thermodynamic relations. We are particularly interested in the entropy density, that is related to the pressure through a derivative in the temperature:

$$\begin{aligned} s(T) &= \frac{dp}{dT} = \frac{4p(T)}{T} + \frac{8\pi^2}{45}T^4\sum_{i=0}^{6}\frac{dp_i}{dT}\left(\frac{\alpha_s(\mu)}{\pi}\right)^{i/2} \\ &= \frac{8\pi^2}{45}T^3\sum_{i=0}^{6}\left(4p_i + T\frac{dp_i}{dT}\right)\left(\frac{\alpha_s(\mu)}{\pi}\right)^{i/2} . \end{aligned} \tag{2.52}$$

The nonzero derivatives of the pressure coefficients p_i are

$$T\frac{dp_4}{dT} = \frac{165}{8}\left(1+\frac{5}{12}N_f\right)\left(1-\frac{2}{33}N_f\right) , \tag{2.53}$$

$$T\frac{dp_5}{dT} = -\frac{495}{2}\left(1+\frac{1}{6}N_f\right)^{3/2}\left(1-\frac{2}{33}N_f\right) , \tag{2.54}$$

$$\begin{aligned} T\frac{dp_6}{dT} &= -\frac{1485}{2}\left(1+\frac{1}{6}N_f\right)\left(1-\frac{2}{33}N_f\right)\ln\left[\frac{\alpha_s}{\pi}\left(1+\frac{1}{6}N_f\right)\right] \\ &\quad -2\,q_a(N_f)\ln\frac{\mu}{2\pi T} - q_b(N_f) . \end{aligned} \tag{2.55}$$

Once pressure and entropy density are known, the energy density can be reconstructed for instance using the relation $Ts = e + p$.

In Figure 2.3 we see the perturbative result for the entropy density in the $N_c = 3$, $N_f = 3$ case, as a function of the renormalized coupling g^2. Different curves correspond to perturbation theory at increasing order up to $\sim g^6\ln g$. We set $q_c = 0$. The plot shows the poor convergence rate of this perturbative expansion. As the order increases an alternating sign behaviour emerges, which survives until the coupling drops to very small values (that is, very high temperature). This is true in particular between ~ 1 GeV, which is the highest temperature where the EoS of QCD has been determined from lattice QCD [21, 20, 13, 15], and the electro-weak scale ~ 100 GeV. The main purpose of this thesis is to compute non-perturbatively for the first time the EoS of $N_f = 3$ QCD in this relevant interval of temperatures.

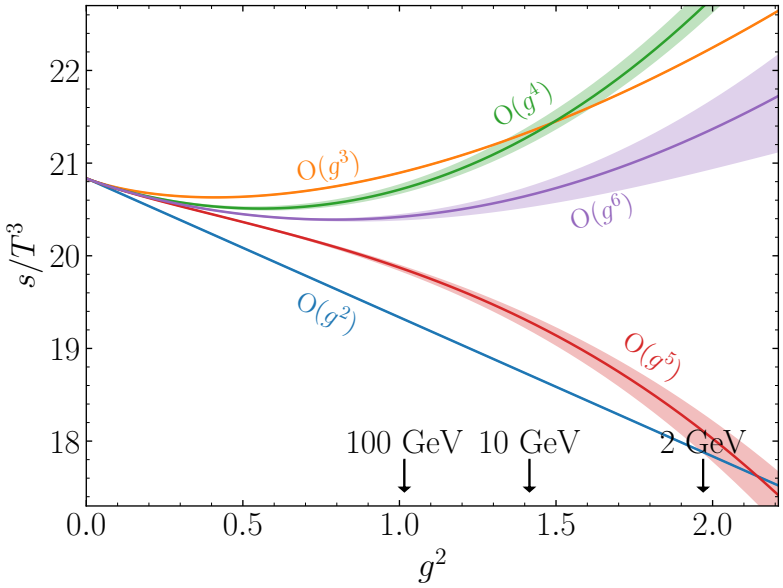

Figure 2.3: Perturbative result for the $N_f = 3$ entropy density in the thEFT, up to the different perturbative orders. The coupling g is the $\overline{\text{MS}}$ coupling at 5-loop [11]. We choose the value $\mu = 2\pi T$ for the renormalization scale, and the errorbands come from varying the scale between $1.5\pi T$ and $2.5\pi T$. A larger interval results in larger errorbands.

Chapter 3

QCD on the lattice

In this Chapter we describe the lattice definition of QCD in the path integral formalism. The lattice is introduced as the discretization of the 4-dimensional Euclidean spacetime $\mathbb{R}^4$ on a grid with lattice spacing a. The resulting (infinite) hypercubic lattice is the set of points

$$\left\{ x_\mu / a \in \mathbb{Z}\,, \quad \mu = 0, 1, 2, 3 \right\}. \tag{3.1}$$

We denote the lattice spacing with a, which is the distance between two neighboring sites of the lattice. We also consider the lattice theory in finite volume with sizes L_0, L_1, L_2, L_3. In Fourier space, the Brillouin zone associated to the spacetime lattice is defined with momenta satisfying $|p| \leq \pi/a$, and this provides naturally an ultraviolet regulator to the theory.

In the discretized theory the fields are defined on the sites of the lattice. Thus QCD on the lattice and in finite volume has a finite number of degrees of freedom, and the partition function eq. (1.30) can be rigorously defined as the integral over all the independent variables. QCD correlation functions are then defined as the continuum limit $a \to 0$ and the thermodynamic limit of their lattice counterparts, after the proper renormalization of the theory. In this sense the lattice regularization provides a theoretically sound way to investigate the properties of QCD from first principles. In this regularization, the Euclidean path integral can be computed using numerical simulations.

The Chapter is organized as follows. We first review the discretization of the QCD path integral on the lattice, following Wilson's prescription [155, 156]. Then we discuss the renormalization of the lattice theory and the continuum limit. In conclusion we overview the most common strategies for lattice QCD simulations, based on the Hybrid Monte Carlo algorithm.

3.1 Lattice gauge theory

We discretize the gauge action following Wilson's procedure [155]. On each site of the lattice the gauge degrees of freedom are chosen to be elements of the gauge group SU(3),

$$U_\mu(x) \in \mathrm{SU}(3)\,, \tag{3.2}$$

called *link variables*. The link gauge-transforms as

$$U'_\mu(x) = \Omega(x)\, U_\mu(x)\, \Omega^\dagger(x + a\hat{\mu})\,, \quad \Omega \in \mathrm{SU}(3)\,, \tag{3.3}$$

meaning that the trace of closed loops of links is a gauge invariant quantity. The smallest closed path on the lattice is a square of four links lying on one of the planes of the 4-dimensional space,

$$U_{\mu\nu}(x) \equiv U_\mu(x)\, U_\nu(x + a\hat{\mu})\, U^\dagger_\mu(x + a\hat{\nu})\, U^\dagger_\nu(x)\,, \tag{3.4}$$

and it is called *plaquette field*. The Wilson's lattice gauge action [155] is the sum over all the plaquettes on the lattice, in all the possible orientations [1]:

$$S^G = \frac{1}{g_0^2} \sum_x \sum_{\mu,\nu} \mathrm{Re\ tr}\left\{1 - U_{\mu\nu}(x)\right\}\,. \tag{3.5}$$

This is a proper discretization of the gauge action because in the classical $a \to 0$ limit it tends to the pure SU(3) Yang-Mills action. This can be seen by interpreting the link $U_\mu(x)$ as the lattice counterpart of the continuum parallel transporter

$$\mathcal{P} e^{-ia \int_0^1 dz A_\mu(x + za\hat{\mu})} \in \mathrm{SU}(3)\,, \tag{3.6}$$

defined on a straight line between the two points x, $x + a\hat{\mu}$. In this view, the link variable can be written as

$$U_\mu(x) = e^{-iaA_\mu(x + \frac{a}{2}\hat{\mu})} \tag{3.7}$$

where A_μ is now a lattice version of the field appearing in eq. (3.6). If we replace in the lattice gauge action (3.5) and we expand at order $\sim a^4$, we get the correct continuum Yang-Mills action up to higher orders in the lattice spacing. We can see in Figure 3.1 a representation of both the link field and the plaquette field on a hyperplane of the lattice.

The partition function for the discretized gauge theory is defined through the integral over all the link variables,

$$\mathcal{Z} = \int DU\, e^{-S^G[U]}\,, \quad DU = \prod_{x,\mu} dU_\mu(x)\,, \tag{3.8}$$

where $dU_\mu(x)$ denotes the Haar measure for the SU(3) group integration. This measure is invariant under left and right multiplication by elements of the group SU(3),

$$dU = d(VU) = d(UV)\,, \quad V \in \mathrm{SU}(3)\,, \tag{3.9}$$

and it satisfies the normalization condition

$$\int dU = 1\,. \tag{3.10}$$

[1] We consider the case without θ-term: $\theta = 0$.

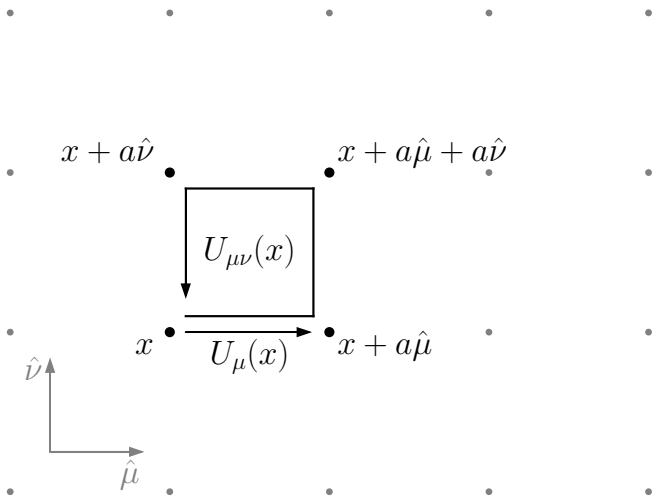

Figure 3.1: The lattice plane $\hat{\mu}$-$\hat{\nu}$, the elementary link variable $U_\mu(x)$, the closed path of the plaquette $U_{\mu\nu}(x)$.

Property (3.9) implies that the link integration measure is gauge invariant,

$$dU_\mu(x) = d\left(\Omega(x)\, U_\mu(x)\, \Omega^\dagger(x + a\hat{\mu})\right) , \quad \Omega \in \mathrm{SU}(3) , \tag{3.11}$$

a fact that, together with the gauge invariance of the action S^G, guarantees the partition function (3.8) to be gauge invariant. The integration measure on the lattice is finite and gauge invariant thanks to the fact that the gauge variables are chosen in the compact group SU(3). The convention adopted for perturbative computations in QCD is to define the path integral over the fields $A_\mu(x)$ belonging to the algebra of the gauge group. In this case a gauge-fixing procedure [50] is required for the proper definition of the integration measure of the path integral.

3.2 Fermions on the lattice

Fermionic fields take values on the sites of the lattice. The lattice counterpart of the Dirac action eq. (1.10) has the form

$$S^F = a^4 \sum_x \overline{\psi}(x)\, [D(x) + M_0]\, \psi(x) , \tag{3.12}$$

where the operator D is a lattice realization of the continuum Dirac operator, see below. The partition function of lattice QCD thus reads

$$\mathcal{Z} = \int DU\, D\overline{\psi} D\psi\, e^{-(S^G[U] + S^F[U,\overline{\psi},\psi])} , \tag{3.13}$$

where the integration measure for the Grassman-valued fermions is

$$D\overline{\psi} = \prod_{x,f,\alpha,a} d\overline{\psi}^a_{f,\alpha}(x)\,, \quad D\psi = \prod_{x,f,\alpha,a} d\psi^a_{f,\alpha}(x)\,, \tag{3.14}$$

the indices f, α, a labeling flavour, spin and colour components, respectively.

The choice of the lattice operator D is a delicate point because of the *Nielsen-Ninomiya no-go theorem* [120, 122, 121, 51]. Calling $\tilde{D}(p)$ the Fourier transform (see Appendix E) of the lattice Dirac operator, the theorem states that the following properties cannot be satisfied simultaneously:

1. $\tilde{D}(p)$ is a smooth function of p with period $2\pi/a$,
2. $\tilde{D}(p) \sim i\gamma_\mu p_\mu + \mathrm{O}(ap^2)$ as $p_\mu \to 0$,
3. $\tilde{D}(p)$ is invertible in the Brillouin zone $\forall p \neq (0,0,0,0)$,
4. $\{\tilde{D}, \gamma_5\} = 0$.

Property 1 is necessary for the Dirac operator to be local in position space [2]. Property 2 guarantees that the proper continuum Dirac operator is recovered when the lattice regularization is removed. Property 3 implies that the propagator (that is, the inverse of the Dirac operator) has one pole only, and thus it is associated to one fermion only. Finally, if the Dirac operator satisfies property 4 then it preserves chiral symmetry.

The no-go theorem forces us to give up at least one of these properties. Our choice is to follow Wilson's prescription for the Dirac operator [155], which does not respect property 4. It is instructive to introduce the Wilson-Dirac operator in two steps: we consider first the naive discretization of the Dirac operator and discuss how the Nielsen-Ninomiya theorem applies to it, and then we move to the Wilson's discretization.

3.2.1 Naive lattice Dirac operator

As an example we consider the naive discretization of the Dirac operator,

$$D_{\mathrm{naive}} = \frac{1}{2}\gamma_\mu(\nabla^*_\mu + \nabla_\mu)\,, \tag{3.15}$$

where the discrete forward and backward covariant derivatives are given in Appendix A.3. In Fourier space, the naive fermionic action in the non-interacting limit reads

$$S^{F,\mathrm{free}}_{\mathrm{naive}} = \int_{-\pi/a}^{\pi/a} \frac{d^4p}{(2\pi)^4}\, \widetilde{\overline{\psi}}(p) \left[i\gamma_\mu \frac{1}{a}\sin(ap_\mu) \right] \widetilde{\psi}(p)\,. \tag{3.16}$$

The inverse of the quantity in square brackets gives the free quark propagator, whose poles are associated to the fermionic particles described by this theory. The naive free

[2] In general, a local lattice Dirac operator involves only next-neighbour interactions, or interactions over a distance of a few lattice points, of the fermionic fields. However a more general notion of locality can be defined [78].

propagator has poles where $\sin(ap_\mu) = 0$, that is at each of the $2^4 = 16$ corners of the Brillouin zone. This results in 16 species of fermions which remain also when the regulator is removed. This effect is known as *fermion doubling problem*: the naive Dirac operator does not respect property 3 of the no-go theorem.

3.2.2 Wilson-Dirac operator

Wilson's prescription for the Dirac operator [155] adds to the naive discretization a Laplacian multiplied by one power of the lattice spacing,

$$D_{\mathrm{w}} = \frac{1}{2}\left[\gamma_\mu(\nabla^*_\mu + \nabla_\mu) - a\nabla^*_\mu\nabla_\mu\right] , \tag{3.17}$$

and the related Wilson fermionic action reads

$$S^F = a^4 \sum_x \overline{\psi}(x) \left\{ \frac{1}{2}\left[\gamma_\mu(\nabla^*_\mu + \nabla_\mu) - a\nabla^*_\mu\nabla_\mu\right] + M_0 \right\} \psi(x) . \tag{3.18}$$

As for the naive action, we consider the Wilson fermionic action in the non-interacting limit in Fourier space:

$$S^{F,\mathrm{free}} = \int_{-\pi/a}^{\pi/a} \frac{d^4p}{(2\pi)^4} \widetilde{\overline{\psi}}(p) \left[i\gamma_\mu \frac{1}{a}\sin(ap_\mu) + \frac{2}{a}\sum_\mu \sin^2\left(\frac{ap_\mu}{2}\right) \right] \widetilde{\psi}(p) . \tag{3.19}$$

Again, the quantity in square brackets is the inverse of the free quark propagator. The Wilson term modifies the naive propagator so that at fixed lattice spacing all the poles disappear but the $p = (0,0,0,0)$ one. In a different perspective, the Wilson term gives a mass of the order $\sim 1/a$ to the 15 spurious species of the naive Dirac operator, so that in the continuum limit they decouple from the theory. The price to pay is that the Wilson term explicitly breaks chiral symmetry, i.e. property 4. The absence of chiral symmetry at non-zero lattice spacing is source of some extra work in the renormalization of the theory, as we will discuss later. Chiral symmetry however is restored when the continuum limit of the renormalized lattice theory is taken.

In conclusion we comment that there exist other discretizations of the Dirac operator that, in addition to properties 1–3, respect also a lattice version of property 4, called Ginsparg-Wilson relation [56, 98, 118, 119]. However these discretizations are typically much more expensive to simulate compared to Wilson fermions.

3.3 Renormalization and continuum limit

The renormalization of lattice QCD needs to be carried out in a fully non-perturbative way. The renormalization of the bare parameters requires to impose some conditions on physical observables computed on the lattice, so that the bare parameters become regulator-dependent. This prescribes how they should change while the continuum limit $a \to 0$ is taken.

We begin with the renormalization of the bare coupling g_0. The conceptual procedure is described in Section 1.4, and in particular the renormalization condition is given in eq. (1.33). Since quantities measured on the lattice are naturally expressed in units of the lattice spacing a, in practice the renormalization of the coupling is carried out by determining the value of a in physical units as a function of g_0,

$$a(g_0) = \frac{a\mathcal{M}(g_0, a)}{\mathcal{M}_{\text{phys}}}\,, \tag{3.20}$$

where the dimensionless numerator is the output of the lattice calculation and $\mathcal{M}_{\text{phys}}$ is the physical quantity that defines the renormalization condition. Once the function (3.20) is known other dimensionless quantities can be expressed in physical units. For this reason the described procedure is also called *scale setting* [144]. This renormalization scheme is known as *hadronic scheme* since the involved physical quantities are usually hadronic masses or decay constants. The resulting function $a(g_0)$ can be inverted so to obtain the dependence of the bare coupling on the lattice spacing, $g_0(a\mathcal{M}_{\text{phys}})$. Given this dependence, renormalization group considerations impose that, at leading order, the coupling decreases logarithmically as the scale $\sim 1/a$ is pushed to the ultraviolet,

$$g_0^2(a) = -\frac{1}{2b_0 \ln(a\mathcal{M}_{\text{phys}})}\,, \quad \lim_{a\to 0} g_0(a) = 0\,, \tag{3.21}$$

where b_0 is the universal leading order coefficient of the β-function, see eq. (1.41). In the continuum limit the β-function of the coupling vanishes too, which means that the point $g_0 = 0$ is a fixed point of the renormalization group flow.

Quark masses are renormalized, at fixed g_0, by imposing further renormalization conditions. A popular choice is to match lattice-computed ratios of hadronic masses to their physical value,

$$\left.\frac{M_i}{M_j}\right|_{g_0,\, am_1,\, ...,\, am_{N_f}} = \left.\frac{M_i}{M_j}\right|_{\text{phys}} \tag{3.22}$$

where i, j are different hadrons. N_f such conditions are needed to tune all the bare masses. Note that mass ratios are pure numbers, so they do not introduce extra energy scales in the renormalized theory and are directly accessible to lattice calculations. Usually the hadron masses ratios appearing in eq. (3.22) are conveniently chosen so that each ratio is possibly more sensible to one of the quark masses to be renormalized, and weakly dependent on all the others.

In practice, equations (3.20) and (3.22) are solved numerically for several values of the bare coupling and quark masses. In this way several lattices can be renormalized so that they represent the same physics but with finer resolutions (that is, decreasing lattice spacing): this is the definition of a *line of constant physics*. Physical quantities in QCD are then defined as the continuum limit $a \to 0$ of their discretizations measured on lattices with bare parameters tuned along a line of constant physics. The continuum limit is obtained by extrapolation at decreasing lattice spacing.

3.4 Scale-dependent renormalization

We now focus on renormalized quantities which depend on a renormalization scale. The lattice discretization allows us to define these quantities non-perturbatively, and to determine from first principles their running by solving the Renormalization Group Equation (1.38). An example is the computation from the lattice of the running coupling, as anticipated in Subsection 1.5.1. In such a computation arises the technical difficulty of accommodating on the same lattice the hadronic scale ~ 200 MeV used for the renormalization of the lattice, and the energy scale where the running coupling needs to be evaluated, that can be of the order of tens of GeV. This goes under the name of *window problem*. In the following we will comment more on this aspect, given its general relevance in designing lattice QCD simulations. Then we will discuss how the use of finite volume renormalization schemes and the step scaling procedure [103] offer an elegant solution to overcome this problem.

3.4.1 Window problem

Predictions from the lattice are obtained via continuum extrapolations. As a general statement we can say that cutoff effects are small if the ultraviolet scale $\sim 1/a$ is much higher than the typical energy scale of the observables under investigation. A constraint comes from the bottom too, because lattice simulations are performed in a finite volume. Being L the size of the lattice, the infrared energy scale $1/L$ should be much smaller than the energy scale of the observables, otherwise finite volume effects may not be negligible. Let us consider two energy scales, $\mu_1 \ll \mu_2$, to be accommodated on the same lattice. Then, the following hierarchy should be respected:

$$1/L \ll \mu_1 \ll \mu_2 \ll 1/a\,. \tag{3.23}$$

We see that, given a lattice spacing a fine enough for the second inequality to be respected, the number of lattice sites L/a should be large enough so that the first inequality is respected too. In other words, when we try to accommodate on the same lattice observable at very different energy scales, the lattice should be at the same time very fine and very large. In a typical lattice simulation the number of points in each direction is $L/a \sim \mathrm{O}(100)$, and thus the energy window that can be accommodated on a lattice with controlled systematic effects and reasonable computational effort is fairly narrow. The window problem occurs for instance when computing on the lattice the running of scale-dependent renormalized quantities, where the renormalization scale μ needs to be pushed to very high energies [103] compared, for instance, to the hadronic scale used for the scale setting. Another relevant case is the study of QCD thermodynamics at temperatures $T \gg 100$ MeV [46] using lattice QCD. In this context $\mu \sim T$ is the high temperature of the thermal system.

A solution to overcome the window problem is to split the energy window in many smaller intervals that can fit into separate lattice computations [41]. On each individual lattice the window condition is easily respected because there are no largely separated scales to accommodate, and the hadronic renormalization enters at low energy only. The

concrete realization of this strategy is the step scaling procedure applied to a finite volume renormalization scheme, as discussed in the following.

3.4.2 Step scaling for the running coupling

We consider a renormalized dimensionless observable $\Theta(L/\Lambda)$ defined in a finite box of volume L^4, such that L and the Λ-parameter are the only relevant scales as the notation suggests [3]. We introduce the finite volume renormalized coupling

$$\overline{g}^2_{\rm FV}(\mu) \equiv \frac{\Theta(L/\Lambda) - \Theta^{(0)}}{\Theta^{(1)}}\,, \quad \mu = 1/L\,, \tag{3.24}$$

where the coefficients $\Theta^{(0)}$, $\Theta^{(1)}$ are respectively the tree-level and 1-loop coefficients in the perturbative expansion of the observable. Notice that the definition (3.24) is a convenient choice such that $\overline{g}^2_{\rm FV} \to g_0^2$ in the $g_0 \to 0$ limit, but the renormalized coupling remains fully non-perturbative. The renormalization scale μ is set to coincide with the inverse of the size of the box. This means that the running of the coupling with μ is defined through a finite volume effect. As it is common practice, we choose a mass-independent renormalization scheme. We introduce the step scaling function [103]

$$\sigma(\overline{g}^2_{\rm FV}(\mu), s) = \overline{g}^2_{\rm FV}(\mu/s)\,, \quad \mu = 1/L\,, \quad s > 1\,, \tag{3.25}$$

as the function that evolves the renormalized coupling from the scale μ to the scale μ/s. The non-perturbative determination of the step scaling function proceeds as follows. One first renormalizes the theory by imposing that the finite volume coupling assumes a prescribed value,

$$\overline{g}^2_{\rm FV}(g_0^2, a/L) = \tilde{g}^2\,. \tag{3.26}$$

Then, the corresponding value of the step scaling function is the coupling itself computed on lattices at the bare couplings fixed by (3.26), but with lattice size sL/a. The full procedure is repeated for many conveniently chosen values of $\tilde{g}^2$. The advantage of this approach is that only the scales $1/L$, $1/(sL)$ matter, and the scale ratio $s \sim {\rm O}(1)$ is chosen so that both scales can be simulated with cutoff effects under control. With mild assumptions, the knowledge of the step scaling function is equivalent to knowing the β-function of the renormalized coupling. The running of the renormalized coupling can be derived by recursively step scaling from some low-energy scale $1/L_{\rm max}$ up to the high-energy scale $1/L_{\rm min}$, where $L_{\rm min} = L_{\rm max}/s^n \ll L_{\rm max}$ and n is the number of steps in the recursion. The low scale $1/L_{\rm max}$ can be converted to physical units using an hadronic renormalization scheme as explained in Section 3.3. On the other end, if the scale $1/L_{\rm min}$ is high enough, the non-perturbative running can be connected to perturbation theory so to extend it for arbitrary high energies.

The first numerical computation of the running coupling in the SU(3) YM theory was performed in [104] using a renormalized coupling in the Schrodinger functional scheme [108]. The complete running, including the matching to perturbation theory and the

[3] Any other scale on which Θ may depend is assumed to be a uniquely specified function of L.

determination of the Λ-parameter (using eq. (1.43)) was computed for the first time in [29]. The first computation of the running coupling with dynamical quarks was done in [6]. We refer to [25] for a recent determination, see also Figure 1.1 and the related Λ-parameter in eq. (1.44).

3.5 Finite renormalization

Apart from the obvious SO(4) symmetry in Euclidean spacetime, the lattice regularization may break also some internal symmetries of the theory. The related Ward Identities are violated on the lattice and they need to be properly renormalized to restore the correct continuum limit. In the following we will first discuss the case of the singlet vector subgroup $\mathrm{U}(1)_V$ of chiral symmetry. This symmetry is respected on the lattice, and thus the related WI for the conservation of the baryon number holds at non-zero lattice spacing too. Then we will discuss the renormalization pattern for the PCAC WI, which is broken by Wilson fermions.

3.5.1 Flavour-singlet vector current with Wilson fermions

The (massive) Wilson action is invariant under a singlet vector rotation of the fields, eq. (1.51). We thus expect that the singlet vector current is conserved also on the lattice. Indeed the lattice counterpart of the WI (1.54) is

$$\left\langle \partial^*_\mu V^c_\mu(x)\mathcal{O}(y)\right\rangle = 0\,, \quad x \neq y\,, \tag{3.27}$$

where ∂^*_μ is the lattice backward derivative, and we defined the conserved lattice flavour-singlet vector current

$$V^c_\mu(x) = \frac{1}{2}\Big[\overline{\psi}(x+a\hat{\mu})U^\dagger_\mu(x)(\gamma_\mu+1)\psi(x) + \overline{\psi}(x)U_\mu(x)(\gamma_\mu-1)\psi(x+a\hat{\mu})\Big]\,. \tag{3.28}$$

These expressions can be obtained as in the formal continuum theory (see equation (1.54)), by applying equation (1.50) to the lattice path integral. In this example the regularized theory produces a WI which is formally identical to the one derived in the continuum. By following the very same arguments of Subsection 1.6.1, one can show that the vector current (3.28) coincides with its renormalized version: $Z_V = 1$. The definition (3.28) is also called *point-split* lattice vector current. One may wonder what happens if on the lattice we use a continuum-like definition of vector current, usually called *local* vector current:

$$V^l_\mu(x) = \overline{\psi}(x)\gamma_\mu\psi(x)\,. \tag{3.29}$$

The discrepancy can be quantified by taking the difference of the two,

$$V^c_\mu(x) - V^l_\mu(x) = aX_\mu(x)\,, \tag{3.30}$$

where

$$X_\mu = \frac{1}{2}\left[\overline{\psi}(x)(\gamma_\mu-1)\nabla_\mu\psi(x) + \overline{\psi}(x)\overleftarrow{\nabla}_\mu(\gamma_\mu+1)\psi(x)\right] \tag{3.31}$$

is a dimension-4 operator [151] and the lattice derivative $\overleftrightarrow{\nabla}_\mu$ is defined in (A.12). The naive conclusion from eq. (3.30) would be that the two currents differ by lattice artifacts, and thus in the continuum limit they will be the same. This argument however does not take into account the renormalization of the operator X^a_μ, which according to eq. (1.36) may mix with operators of lower or equal dimension. For symmetry and dimensional reasons X_μ can mix with the vector current only. Specifically we have

$$X_{\mu,R} = Z_X \left[X_\mu + \frac{c(g_0)}{a} V^l_\mu \right] . \tag{3.32}$$

The overall renormalization constant Z_X is at most logarithmically divergent as $\sim \ln a$. In a mass-independent renormalization scheme the coefficient $c(g_0)$ is mass-independent as the notation suggests. Moreover, in [149] it was shown that this coefficient can't depend on a renormalization scale. The effect of the operator $X_{\mu,R}$ can be recast in a redefinition of the local vector current, by replacing in eq. (3.30):

$$V^c_\mu = V^l_\mu (1 - c(g_0)) + a \frac{X_{\mu,R}}{Z_X} \equiv Z^l_V(g_0) V^l_\mu + \mathrm{O}(a) . \tag{3.33}$$

The last term is a "true" lattice artifact because the renormalized operator $X_{\mu,R}$ gives a finite contribution when inserted in a on-shell correlation function, and Z_X diverges at most logarithmically with the lattice spacing. As a consequence, the local discretization of the vector current has a finite renormalization $Z^l_V(g_0) = 1 + c(g_0)$ which tends to unity as $g_0 \to 0$.

In presence of mass-degenerate flavours the non-singlet vector current is conserved on the lattice too, and all these arguments apply also in that case. In particular we can introduce a point-split or local version on the lattice, and the latter needs to be renormalized with a finite renormalization constant.

We remark that finite renormalization factors like Z_V must be taken into account even if in the continuum they go to unity. The reason is that when the fields in a correlation function are all renormalized, its lattice artifacts are integer powers of the lattice spacing possibly corrected by $\sim \ln a$, terms which we collectively denote as $\mathrm{O}(a)$, see equation (3.33). The presence of unrenormalized fields instead generates $\sim 1/\ln(a)$ effects that would make the convergence to the continuum much slower.

3.5.2 PCAC with Wilson fermions

The fermionic Wilson action breaks chiral symmetry. The lattice analog of the PCAC WI (1.62) with degenerate quark masses reads

$$\left\langle \partial^*_\mu A^a_\mu(x) \mathcal{O}(y) \right\rangle = 2 m_0 \langle P^a(x) \mathcal{O}(y) \rangle + a \langle X^a(x) \mathcal{O}(y) \rangle , \quad x \neq y , \tag{3.34}$$

where the lattice point-split axial current is

$$A^a_\mu(x) = \frac{1}{2} \Big[\overline{\psi}(x) U_\mu(x) \gamma_\mu \gamma_5 T^a \psi(x + a\hat{\mu}) + \overline{\psi}(x + a\hat{\mu}) U^\dagger_\mu(x) \gamma_\mu \gamma_5 T^a \psi(x) \Big] \tag{3.35}$$

and X^a is a dimension-5 operator. We are in the same circumstance of the WI (3.27), when the local discretization of the vector current is employed. However, differently from that case, the present operator X^a cannot be recast in the four-divergence of a local field, and thus a lattice conserved axial current cannot be defined. As we discussed before, the effect of the renormalization of the operator X^a can be taken into account by renormalizing the fields and parameters appearing in eq. (3.34), up to discretization effects. Specifically we can write

$$\left\langle \partial^*_\mu A^a_{\mu,R}(x)\mathcal{O}(y)\right\rangle = 2m_R\langle P^a_R(x)\mathcal{O}(y)\rangle + \mathrm{O}(a)\,, \quad x\neq y\,. \tag{3.36}$$

In this equation, the axial current renormalizes multiplicatively, $A^a_{\mu,R} = Z_A A^a_\mu$, where $Z_A(g_0)$ is a finite renormalization constant which goes to 1 in the continuum limit. The quark mass renormalizes additively and multiplicatively,

$$m_R = Z_m\, m_q\,, \quad m_q = m_0 - m_{\rm cr}\,, \tag{3.37}$$

where m_q is called the subtracted quark mass and $m_{\rm cr}(g_0)$ is the critical mass, while the renormalization factor $Z_m(g_0, a\mu)$ depends on a renormalization scale. The lattice pseudoscalar current renormalizes multiplicatively too, $P^a_R = Z_P P^a$. Since the left-hand side of equation (3.36) is finite, the right-hand side must be finite and this implies that the product $Z_m Z_P$ is a finite number which goes to 1 in the continuum limit. Notice that in a mass-independent renormalization scheme, the dependence on the bare parameters of the renormalization constants above is only with respect to the bare coupling g_0, and not the quark masses.

It is convenient to introduce a definition of mass which renormalizes only multiplicatively, using the PCAC relation:

$$m_{\rm PCAC} \equiv \frac{\left\langle \partial^*_\mu A^a_\mu(x)\mathcal{O}(y)\right\rangle}{\langle P^a(x)\mathcal{O}(y)\rangle}\,, \quad m_R = Z_A Z_P^{-1} m_{\rm PCAC}\,. \tag{3.38}$$

According to eq. (3.36), the choice of the operator $\mathcal{O}$ will affect the definition of the PCAC mass only by $\mathrm{O}(a)$ lattice artifacts which vanish in the continuum limit. The bare quark mass in practical lattice simulations may be tuned so that the renormalized PCAC mass have some prescribed value. In particular, equation (3.38) can be employed to compute the critical mass $m_{\rm cr}$, by looking at the value of the bare mass such that $m_{\rm PCAC} = 0$ [37, 88].

On the lattice one can also introduce the local version of the axial current, defined as the continuum one:

$$A^{l,a}_\mu(x) \equiv \overline{\psi}(x)\gamma_\mu\gamma_5 T^a\psi(x)\,. \tag{3.39}$$

After proper renormalization, lattice correlation functions containing the local or conserved axial current will converge to the same continuum limit but with different $\mathrm{O}(a)$ effects. Notice that the renormalization constant Z^l_A of the local discretization, eq. (3.39), is different from the one of the point-split definition (3.35): $Z^l_A \neq Z_A$.

In conclusion we mention that the finite renormalization constants can be determined by imposing the validity of the Ward Identities at finite lattice spacing (up to cutoff

effects), see for instance [19, 111, 112, 106, 77]. This in turn provides a practical way to compute them non-perturbatively in lattice QCD. As part of the original contribution of this thesis, in Chapter 5 we will see this renormalization program at work for the non-perturbative renormalization of the flavour-singlet local vector current and for the Energy-Momentum tensor of QCD. The Ward Identities for the latter are generated by the invariance of the continuum theory under SO(4) spacetime transformations.

3.6 Improvement

In the previous Subsection we saw that the breaking of chiral symmetry by Wilson fermions is source in general of $\mathrm{O}(a)$ lattice artifacts which may give large contributions to continuum limit extrapolations. The Symanzik continuum effective theory [147] is a powerful tool which allows us to systematically improve the lattice theory in order to reduce the lattice artifacts. In some sense, it can be viewed as an extension of the renormalization of composite operators to include irrelevant operators, in order to parameterize and subtract the leading discretization effects [143]. In the following, we will review the Symanzik effective field theory and the procedure to $\mathrm{O}(a)$-improve lattice QCD with Wilson fermions, so that the leading discretization effects of lattice observables are of order $\sim a^2$.

3.6.1 Symanzik effective theory

Near the continuum limit lattice QCD may be regarded as a high energy theory defined at the cutoff scale $\sim 1/a$, whose low energy behaviour can be described in terms of a local effective theory in the continuum:

$$S_{\text{lat}} \to S_{\text{eff}} = \int d^4x \left[\mathcal{L}_0(x) + a\mathcal{L}_1(x) + a^2\mathcal{L}_2(x) + ... \right] . \tag{3.40}$$

In this expression, $\mathcal{L}_0$ is the continuum QCD Lagrangian while $\mathcal{L}_k$, $k \geq 1$, are local fields with the symmetries of the lattice QCD action (which, in this context, is regarded as the *full theory*) and mass dimension $4 + k$.

We focus on the $\mathcal{L}_1$ term. In general, all the continuum gauge- and Lorentz-invariant local fields with mass dimension 5 that respect the other symmetries of the Wilson action are allowed. Notably, these terms can break chiral symmetry. We list here the operators that contribute to the effective term $\mathcal{L}_1$ [96] :

$$\begin{aligned}
\mathcal{L}_{1,1} &= \overline{\psi} i\sigma_{\mu\nu} F_{\mu\nu} \psi \,, \\
\mathcal{L}_{1,2} &= \overline{\psi} D_\mu D_\mu \psi \,, \\
\mathcal{L}_{1,3} &= m_0 \,\mathrm{tr}\left\{ F_{\mu\nu} F_{\mu\nu} \right\} \,, \\
\mathcal{L}_{1,4} &= m_0 \,\overline{\psi} \gamma_\mu D_\mu \psi \,, \\
\mathcal{L}_{1,5} &= m_0^2 \,\overline{\psi} \psi \,,
\end{aligned} \tag{3.41}$$

where D_μ is the (continuum) covariant derivative and integration by parts has been used to reduce the number of terms. The matrix $\sigma_{\mu\nu}$ is a combination of γ matrices,

defined in Appendix A. We assume for simplicity mass-degenerate flavours, with bare mass m_0. These are operators in the continuum theory, but the coefficients of the linear combination that defines $\mathcal{L}_1$ depend on the lattice details. The lattice local fields inserted in correlation functions have an effective representation too:

$$\mathcal{O}_{\rm lat} \to \mathcal{O}_{\rm eff} = \mathcal{O}_0 + a\mathcal{O}_1 + a^2\mathcal{O}_2 + ... \tag{3.42}$$

As for the action, the field $\mathcal{O}_0$ is the continuum counterpart of $\mathcal{O}_{\rm lat}$ while $\mathcal{O}_k$, $k \geq 1$, are continuum higher dimensional fields with the appropriate symmetries. We are now interested in the representation of the lattice correlation function $\langle O_{\rm lat}\rangle_{\rm lat}$ in the effective theory. We will assume the correlation function to be properly renormalized and on-shell, i.e. all the inserted fields are at a physical non-vanishing distance. Using equations (3.40) and (3.42) at first order in the effective theory we get

$$\langle \mathcal{O}_{\rm lat}\rangle_{\rm lat} = \langle \mathcal{O}_0\rangle - a\left(\langle \mathcal{O}_0 S_1\rangle_c - \langle \mathcal{O}_1\rangle\right) + \mathrm{O}(a^2)\,, \tag{3.43}$$

where we defined $S_k = \int d^4x \mathcal{L}_k(x)$. We denote with $\langle\cdot\rangle_{\rm lat}$ correlation functions in the lattice theory, while $\langle\cdot\rangle$ stands for the continuum theory. The Symanzik effective theory thus allows us to point out the sources of discretization effects in quantities computed from the lattice.

3.6.2 O(a)-improvement of the Wilson action

The lattice theory is defined up to terms which vanish in the continuum limit. Leveraging on this arbitrariness we can add to the lattice action and fields some irrelevant counterterms which mimic the terms appearing in the Symanzik effective theory, and tune their coefficients so to cancel the corresponding effective contributions.

The O(a)-improvement of the Wilson theory thus requires to add to the lattice action a discretized version of the operators listed in (3.41). Since we are considering correlation functions with fields at physical distance, it is possible to use the equations of motion for the fields and reduce the operator basis to 3 independent fields. We choose to keep $\mathcal{L}_{1,1}$, $\mathcal{L}_{1,3}$ and $\mathcal{L}_{1,5}$, and the counterterms to the action are

$$\delta S = a^5 \sum_x \left[c_1\widehat{\mathcal{L}}_{1,1} + c_3\widehat{\mathcal{L}}_{1,3} + c_5\widehat{\mathcal{L}}_{1,5}\right]\,, \tag{3.44}$$

where the hat means that the fields are on the lattice. This choice of operator basis is convenient because we can discretize $\widehat{\mathcal{L}}_{1,3}$ and $\widehat{\mathcal{L}}_{1,5}$ so that they have the same structure of the pure gauge action and of the mass term in the original lattice action. Their presence can thus be absorbed in a redefinition of the coupling and quark mass:

$$g_0^2 \to g_0^2(1 + b_g a m_q)\,, \quad a m_q \to a m_q(1 + b_m a m_q)\,. \tag{3.45}$$

The coefficients b_g, b_m are g_0-dependent improvement coefficients. They should be tuned so to cancel O(am_q) effects from on-shell quantities in presence of non-zero quark masses.

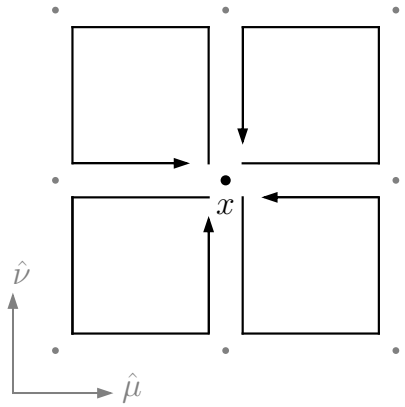

Figure 3.2: Clover plaquette loops associated to $Q_{\mu\nu}(x)$.

The only operator left in our discussion is $\widehat{\mathcal{L}}_{1,1}$. The O($a$)-improved Wilson action for lattice QCD thus reads

$$S = S^G + S^F + a^5 \sum_x \frac{1}{4} c_{\rm sw}(g_0^2) \overline{\psi}(x) \sigma_{\mu\nu} \widehat{F}_{\mu\nu}(x) \psi(x) \,, \tag{3.46}$$

with $\widehat{F}_{\mu\nu}$ being the clover discretization of the field-strength tensor:

$$\widehat{F}_{\mu\nu}(x) = \frac{i}{8a^2} \Big[Q_{\mu\nu}(x) - Q_{\nu\mu}(x) \Big] \,. \tag{3.47}$$

The sum of plaquettes represented by $Q_{\mu\nu}(x)$ is shown in Figure 3.2. The improvement term is known as Sheikholeslami-Wohlert term [140]. The coefficient $c_{\rm sw}$ is a function of the bare coupling and can be tuned appropriately so to cancel O(a) effects from the theory. For lattice QCD with Wilson plaquette action and Wilson fermions, this coefficient is known in perturbation theory up to 2-loop [157, 124], and it was determined non-perturbatively for the $N_f = 3$ case in [160]:

$$c_{\rm sw}(g_0) = \frac{1 - 0.194785\, g_0^2 - 0.110781\, g_0^4 - 0.0230239\, g_0^6 + 0.137401\, g_0^8}{1 - 0.460685\, g_0^2} \,. \tag{3.48}$$

This non-perturbative result was carried out by imposing the validity of the O(a)-improved lattice PCAC relation up to corrections of order $\sim a^2$ [107, 81, 105].

3.6.3 O(a)-improvement of local fields

The O(a)-improvement of the action is enough to make spectral quantities [4] approach the continuum limit with $\sim a^2$ discretization errors. However if one is interested in matrix elements of some given fields, then the latter must be improved too. Again, the improvement is done by adding irrelevant counterterms to the local fields so that the corresponding O(a) terms in the Symanzik effective theory are removed. In the following we consider the examples of the local vector current and of the axial current, in Wilson lattice QCD with mass-degenerate quarks.

Improvement of the vector current

The improvement of the flavour-singlet vector current involves operators with mass dimension 4 and same properties of the vector current [17, 18]:

$$\partial_\nu(\overline{\psi}\sigma_{\mu\nu}\psi)\,, \quad m_0 V_\mu^{c,l}\,. \tag{3.49}$$

The second term is proportional to the vector current itself, and it is responsible for a shift in the renormalization constant by O(am) effects. The O(a)-improved and renormalized vector currents thus read

$$\begin{aligned}(V_{I,R})^c_\mu &= (1+b_V^c am_q)\Big[V_\mu^c + a\,c_V^c\,\partial_\nu(\overline{\psi}\sigma_{\mu\nu}\psi)\Big]\,,\\ (V_{I,R})^l_\mu &= Z_V(1+b_V^l am_q)\,\Big[V_\mu^l + a\,c_V^l\,\partial_\nu(\overline{\psi}\sigma_{\mu\nu}\psi)\Big]\,,\end{aligned} \tag{3.50}$$

where now the derivatives and the improving field are discretized on the lattice. The improvement coefficients $b_V^{c,l}(g_0)$, $c_V^{c,l}(g_0)$ depend on the bare coupling and can be tuned so to remove O(a) lattice artifacts in on-shell correlation functions where the currents are inserted.

Improvement of the axial current

We consider now the improvement of the axial current, which involves the operators

$$\partial_\mu P^a\,, \quad m_0 A_\mu^a\,, \tag{3.51}$$

where $P^a = \overline{\psi}\gamma_5 T^a\psi$ is the pseudoscalar density. Similarly as for the vector current we write the improved and renormalized axial current as

$$(A_{I,R})^a_\mu = Z_A(1+b_A am_q)\Big[A_\mu^a + a\,c_A\,\partial_\mu P^a\Big]\,, \tag{3.52}$$

where the derivative and the pseudoscalar density on the right are meant on the lattice. The improvement coefficients $b_A(g_0)$, $c_A(g_0)$ of the axial current and can be tuned so to remove O(a) lattice artifacts in on-shell correlation functions where this current is inserted. As a relevant example, the O(a)-improved axial current allows to define an O(a)-improved version of the PCAC mass eq. (3.38) [105].

[4] We call spectral quantities all those observables that do not depend on the details of any operator, such as particle masses or cumulants of the partition function.

3.7 Numerical simulations of lattice QCD

Lattice regularized gauge theories have a finite (although very large) number of degrees of freedom and thus are well suited for numerical simulations on HPC machines. Numerical evaluations of the path integral are made possible by the parallelism between the Euclidean theory and statistical systems. Indeed the path integral may be regarded as a statistical partition function with field configurations sampled according to the Boltzmann-like distribution $\sim e^{-S}$. The problem of numerical evaluation of the path integral is thus equivalent to the problem of sampling field configurations according to a prescribed probability distribution.

The fields involved in a lattice QCD simulations are the link field $U_\mu(x)$ and the quark fields $\overline{\psi}(x)$, $\psi(x)$. Fermionic fields are collections of Grassman (anti-commuting) variables, whose direct sampling in a ordinary lattice QCD simulation is prohibitively expensive from the computational viewpoint. The first step is to perform analytically the functional integral over fermions, so that the resulting path integral is over the gauge field only [5]. For N_f flavours we have

$$\mathcal{Z} = \int DU D\overline{\psi} D\psi \, e^{-S^G[U] - S^F[U,\overline{\psi},\psi]} = \int DU \prod_{i=1}^{N_f} (\det D_i[U]) \; e^{-S^G[U]} \,, \tag{3.53}$$

where $D_i[U]$ is the massive Wilson-Dirac operator of the i-th flavour. The link field thus follows the normalized probability distribution

$$P[U] = \frac{1}{\mathcal{Z}} \prod_{i=1}^{N_f} (\det D_i[U]) \; e^{-S^G[U]} \,, \tag{3.54}$$

and a generic Euclidean correlator $\langle \mathcal{O} \rangle$ can be interpreted as the statistical expectation value of the field $\mathcal{O}$ with respect to the distribution $P[U]$, after the integration of the fermionic degrees of freedom:

$$\langle \mathcal{O} \rangle = \frac{1}{\mathcal{Z}} \int DU D\overline{\psi} D\psi \, \mathcal{O}[U,\overline{\psi},\psi] \, e^{-S^G[U] - S^F[U,\overline{\psi},\psi]} = \int DU \, P[U] \mathcal{O}[U] \,. \tag{3.55}$$

The probability distribution (3.54) is well defined as far as the product of determinants is real and positive. If the lattice Dirac operator is γ_5-hermitian (as it is for the Wilson-Dirac operator), then its determinant is real:

$$\det D = \det(\gamma_5 D^\dagger \gamma_5) = (\det D^\dagger) = (\det D)^* \,. \tag{3.56}$$

In this case the positiveness is obvious if an even number of degenerate flavours is considered. With an odd number of flavours positiveness is not automatically guaranteed. In particular, it is not in the case of a single flavour in the Wilson (improved) discretization.

The usual approach for sampling gauge configurations according to $P[U]$ is to employ Markov Chains, as discussed in the following Subsections. Assuming that we can

[5] The drawback of the analytic integration of fermions is that the theory looses manifest locality.

sample $P[U]$, the expectation value of a local field $\langle\mathcal{O}\rangle$ can be approximated through the statistical estimator

$$\overline{\mathcal{O}} = \frac{1}{N}\sum_{i=1}^{N}\mathcal{O}_i\,, \quad \mathcal{O}_i = \mathcal{O}[U_i]\,, \quad \langle\mathcal{O}\rangle \approx \overline{\mathcal{O}} + \mathrm{O}(1/\sqrt{N})\,, \tag{3.57}$$

where U_i are N configurations of the gauge field, and the scaling $\sim N^{-1/2}$ of the statistical error is guaranteed by the central limit theorem in the $N \to \infty$ limit.

3.7.1 Markov Chains

A Markov Chain (MC) is a stochastic process based on generating a sequence of configurations

$$U_0 \xrightarrow{T} U_1 \xrightarrow{T} \cdots U_n \xrightarrow{T} \cdots \tag{3.58}$$

according to the *transition probability* $T(U'|U)$ [53, 97]. The transition probability is defined on the space of all configurations, and it is the conditional probability of sampling the new configuration U', given the current configuration U. The transition probability thus depends on the configuration, but not on the index of the configuration along the chain, called *Markov time*. This property is referred to as *time-homogeneity*. Transition probabilities are non-negative for any choice U', U and satisfy the completeness condition

$$\sum_{U'} T(U'|U) = 1\,, \tag{3.59}$$

where the sum is over all the configuration space. If the transition probability satisfies

$$T(U'|U) > 0 \quad \forall\, U, U'\,, \tag{3.60}$$

then the MC is called *ergodic*. In view of sampling configurations according to a chosen distribution, ergodicity is a fundamental property for a MC. Calling $P_0[U]$ the initial probability distribution of the configurations, at Markov time $t = 0$, it can be shown that ergodicity is a sufficient condition such that the limit

$$\lim_{t\to\infty} P_t = \lim_{t\to\infty} T^t P_0 = P_{\mathrm{eq}} \tag{3.61}$$

exists, is unique and does not depend on the starting distribution.

We have to understand now how to define an ergodic MC so that the equilibrium distribution P_{eq} is the desired one. Given a target probability distribution $P[U]$, it is possible to show [134] that, if the MC is ergodic and satisfies the *detailed balance* condition,

$$T(U'|U)P[U] = T(U|U')P[U']\,, \tag{3.62}$$

then $P[U]$ is the (unique) fixed point for chain of probability distributions sampled by the MC:

$$\lim_{t\to\infty} P_t = P\,. \tag{3.63}$$

From this equation we see that the MC eventually samples the target distribution after a certain number of steps in Markov time. The initial phase where the MC looses memory of the original distribution and stabilizes to $P[U]$ is called *thermalization*.

A simple way to build a transition probability T that satisfies the detailed balance with respect to the probability distribution P is the Metropolis-Hastings algorithm [113, 76]. We split the transition probability in two steps,

$$T(U'|U) = P_{\text{acc}}(U'|U) P_{\text{prop}}(U'|U)\,, \tag{3.64}$$

where P_{acc} stands for the acceptance probability, and P_{prop} for proposal probability. At each update of the MC, a new configuration U' is proposed with probability P_{prop}, and accepted as new sample of the chain with probability P_{acc}. If rejected, the starting configuration U is kept as new element of the MC. A transition probability defined through the following acceptance probability satisfies the detailed balance with respect to the target distribution P,

$$P_{\text{acc}}(U'|U) = \min\left\{1, \frac{P_{\text{prop}}(U|U')P[U']}{P_{\text{prop}}(U'|U)P[U]}\right\} = \min\left\{1, \frac{P[U']}{P[U]}\right\}, \tag{3.65}$$

where second equality holds if the proposal probability is symmetric: $P_{\text{prop}}(U'|U) = P_{\text{prop}}(U|U')$. Notice in particular that only the relative target probability enters the definition of P_{acc}, and therefore the normalization of the target distribution is not required.

The last ingredient for the definition of the MC is the proposal distribution P_{prop} which is not constrained by the Metropolis-Hastings and is in principle independent from the target distribution. Usually the proposal probability is chosen in order to maximize the acceptance probability and thus the efficiency of the MC sampling in exploring the phase space of configurations.

3.7.2 Markov Chain sampling and autocorrelation

Configurations sampled with MCs are in general correlated, because the transition probability to a new configuration depends on the current configuration. Therefore the samples $\mathcal{O}_i$ are correlated along the Markov time, i.e. they exhibit *autocorrelation*. This propagates to the estimation of the uncertainty of $\overline{\mathcal{O}}$ of eq. (3.57), as discussed in the following. The (squared) statistical uncertainty of $\overline{\mathcal{O}}$ is given by [158, 97]

$$\sigma^2_{\overline{\mathcal{O}}} = \langle\!\langle \left(\overline{\mathcal{O}} - \langle\mathcal{O}\rangle\right)^2 \rangle\!\rangle = \frac{1}{N^2}\sum_{i,j} \langle\!\langle \mathcal{O}_i \mathcal{O}_j \rangle\!\rangle - \langle\mathcal{O}\rangle^2\,, \tag{3.66}$$

where $\langle\!\langle \cdot \rangle\!\rangle$ denotes the average over independent MCs, while the indices i, j are as usual for the Markov time on a given chain. With this notation it also holds that $\langle\!\langle \overline{\mathcal{O}} \rangle\!\rangle = \langle\mathcal{O}\rangle$. The samples $\mathcal{O}_i$, $\mathcal{O}_j$ are correlated along a chain, therefore $\langle\!\langle \mathcal{O}_i \mathcal{O}_j \rangle\!\rangle \neq \langle\!\langle \mathcal{O}_i \rangle\!\rangle \langle\!\langle \mathcal{O}_j \rangle\!\rangle$. After some manipulations, the squared statistical uncertainty of $\overline{\mathcal{O}}$ can be rewritten as

$$\sigma^2_{\overline{\mathcal{O}}} = \frac{\text{var}\,[\mathcal{O}]}{N} 2\,\tau^{\mathcal{O}}_{\text{int}}\,, \tag{3.67}$$

where we defined the variance of the operator $\mathcal{O}$ as

$$\mathrm{var}\left[\mathcal{O}\right] = \langle \mathcal{O}^2 \rangle - \langle \mathcal{O} \rangle^2 \tag{3.68}$$

while $\tau_{\mathrm{int}}^{\mathcal{O}}$ is the integrated autocorrelation time of the observable $\mathcal{O}$,

$$\tau_{\mathrm{int}}^{\mathcal{O}} = \frac{1}{2}\left[1 + 2\sum_{t=1}^{N-1}\frac{\Gamma_{\mathcal{O}}(t)}{\Gamma_{\mathcal{O}}(0)}\right], \tag{3.69}$$

and $\Gamma_{\mathcal{O}}$ is the autocorrelation function

$$\Gamma_{\mathcal{O}}(t) = \langle\langle \mathcal{O}_0 \mathcal{O}_t \rangle\rangle - \langle \mathcal{O} \rangle^2 . \tag{3.70}$$

If the MC is homogeneous in the Markov time, then the average $\langle\langle \cdot \rangle\rangle$ is invariant under translations along the MC and thus the autocorrelation function depends only on the distance t in Markov time, as suggested by the notation. Equation (3.67) tells us that the autocorrelation reduces the number of samples to the effective number $N/(2\tau_{\mathrm{int}}^{\mathcal{O}})$ of independent samples.

Many strategies are available for properly taking into account the autocorrelation along a Markov chain. The Γ-*method* [158] estimates the error on ensemble averages as in equation (3.67), by explicitly computing the integrated autocorrelation time. The computation of τ_{int} requires the knowledge of the autocorrelation function $\Gamma(t)$, estimated as

$$\overline{\Gamma}_{\mathcal{O}}(t) = \frac{1}{N-t}\sum_{i=1}^{N-t}\left(\mathcal{O}_{i+t} - \overline{\mathcal{O}}\right)\left(\mathcal{O}_i - \overline{\mathcal{O}}\right) . \tag{3.71}$$

It can be shown that this function is exponentially suppressed for $t \to \infty$, while its relative error increases exponentially at large Markov time. The Γ-method estimates the integrated autocorrelation time by cutting the integral of eq. (3.69) to some chosen Markov distance W [158],

$$\tau_{\mathrm{int}}^{\mathcal{O},W} = \frac{1}{2}\left[1 + 2\sum_{t=1}^{W}\frac{\overline{\Gamma}_{\mathcal{O}}(t)}{\overline{\Gamma}_{\mathcal{O}}(0)}\right], \tag{3.72}$$

and the error with respect to (3.69) is exponentially suppressed as $\sim W$.

Other popular strategies for taking into account autocorrelation are the so-called *binning* methods. The idea is to exploit the exponential suppression of the autocorrelation function in Markov time, by grouping samples in bins which are averaged separately. The autocorrelation of binned samples will be exponentially suppressed with the size of the bins. If the latter is large enough (a few $\tau_{\mathrm{int}}^{\mathcal{O}}$, say), then the statistical analysis on the bins can be carried out assuming they are independent samples.

3.7.3 Hybrid Monte Carlo

In the following we will describe the Hybrid Monte Carlo algorithm [48], which is a realization of Markov Chains for simulating lattice QCD. We will also introduce some

of the strategies which are commonly employed in its practical implementation, most of them dealing with the proper treatment of quarks on the lattice. We refer for instance to [97] for further details, and also to the documentation of `openQCD` [99], the package adopted for the numerical simulations in this thesis.

We are interested in sampling link fields for QCD following the distribution

$$P[U] = \frac{1}{\mathcal{Z}} e^{-S[U]}\,, \quad S[U] = S^G[U] - \sum_{i=1}^{N_f} \mathrm{Tr}\left\{\ln D_i[U]\right\}\,, \tag{3.73}$$

where the quark determinants have been included in the action $S[U]$ which therefore may be a non-local function of the link field.

Following the Metropolis-Hastings prescription discussed of Subsection 3.7.1, each new configuration in the MC is first generated with a proposal distribution P_{prop}, and then accepted with probability P_{acc}. On one hand, the acceptance probability is uniquely specified by the target distribution (3.73). Notice in particular that the (unknown) normalization $1/\mathcal{Z}$ of the latter is not required for the evaluation of P_{acc}.

On the other hand, in the HMC the new configuration is generated from the old one through the fictitious time evolution of an auxiliary Hamiltonian system, using classical Hamilton's equations. This procedure is called *molecular dynamics*. The molecular dynamics requires to extend the link variables of the gauge field to a 5-dimensional space,

$$U_\mu(x) \to U_\mu(x,\tau)\,, \tag{3.74}$$

where the τ-direction is the (fictitious) time for the Hamiltonian evolution. We then introduce the auxiliary $\mathfrak{su}(3)$-valued momenta $\pi_\mu(x,\tau) = \pi^a_\mu(x,\tau)T^a$, conjugated to the link variables. The fictitious Hamiltonian of the system is thus

$$H[U,\pi] = \frac{1}{2}(\pi,\pi) + S[U]\,, \quad (\pi,\pi) \equiv \sum_x \pi^a_\mu(x,\tau)\pi^a_\mu(x,\tau)\,, \tag{3.75}$$

and the related partition function

$$\int D\pi DU\, e^{-H[\pi,U]} = \text{const.} \times \int DU\, e^{-S[U]} \tag{3.76}$$

coincides with the original one up to an irrelevant constant coming from the Gaussian integration over the momenta. In particular, the target probability distribution (3.73) generalizes to

$$P[\pi,U] = \frac{1}{\mathcal{Z}_\pi \mathcal{Z}} e^{-H[\pi,U]}\,. \tag{3.77}$$

The evolution of the fields along τ is governed by the Hamilton's equations

$$\begin{cases} \dfrac{d}{d\tau}\pi_\mu(x,\tau) = -F_\mu(x,\tau) \\ \dfrac{d}{d\tau}U_\mu(x,\tau) = \pi_\mu(x,\tau)U_\mu(x,\tau) \end{cases}, \quad F_\mu(x,\tau) = \left.\frac{\delta S[U]}{\delta U_\mu(x)}\right|_\tau \tag{3.78}$$

which are usually called molecular dynamics (MD) equations. The MD equations are deterministic, and their solution is uniquely determined by the initial configuration of the fields. Crucially, the Hamiltonian (3.75) is conserved along the MD trajectory. This means that

$$P_{\rm acc} = \min\left\{1,\, e^{-(H[U(\tau_{\rm max}),\pi(\tau_{\rm max})]-H[U(0),\pi(0)])}\right\} = 1\,, \tag{3.79}$$

and thus the proposed gauge configuration is always accepted. Therefore each HMC step works as follows:

1. The initial gauge field is $U_\mu(x,0) = U_\mu(x)$, $U_\mu(x)$ being the last link configuration, while the momenta are extracted according to a Gaussian distribution: $\pi(x,0) \sim e^{-\frac{1}{2}(\pi,\pi)}$. The Gaussian initialization of the momenta sets a random value of the kinetic energy of the Hamiltonian system, and thus randomly selects a hyper-surface at given energy in the (π, U) configuration space.

2. Fields are evolved according to the MD equations from time $\tau = 0$ to time $\tau = \tau_{\rm max}$. The MD evolution makes the system flow on the fixed-energy hyper-surface, changing globally the link configuration.

3. The field $U_\mu(x, \tau_{\rm max})$ at the end of the molecular dynamics is taken as new element of the chain. The auxiliary momentum field is always resampled at the beginning of a MD trajectory.

3.7.4 Discretized Hybrid Monte Carlo

In practical QCD simulations the MD equations are numerically integrated using finite-step techniques, in which the MD time τ is discretized in many steps of size $\delta\tau$. The infinitesimal form of the MD equations is

$$\begin{cases} \pi_\mu(x,\tau+\delta\tau) = \pi_\mu(x,\tau) - \delta\tau F_\mu(x,\tau) + \mathrm{O}((\delta\tau)^2) \\ U_\mu(x,\tau+\delta\tau) = \big[1 + \delta\tau\pi_\mu(x,\tau)\big] U_\mu(x,\tau) + \mathrm{O}((\delta\tau)^2) \end{cases} \tag{3.80}$$

and this suggests to define the infinitesimal time evolution operators

$$\begin{aligned} &\mathcal{I}_\pi(\delta\tau) : \pi,\, U \to \pi - \delta\tau F,\, U \\ &\mathcal{I}_U(\delta\tau) : \pi,\, U \to \pi,\, e^{\delta\tau\pi} U \end{aligned} \tag{3.81}$$

where the spacetime position x and the Lorentz index μ are understood. Combining powers of these elementary operators it is possible to define different discretized evolution operators,

$$\mathcal{I}(\tau, N) = \mathcal{F}(\mathcal{I}_\pi, \mathcal{I}_U, \tau, N)\,, \tag{3.82}$$

which evolve the initial fields configuration along the MD trajectory with total time τ in N elementary steps. For instance the *leapfrog integrator* is the operator

$$\mathcal{I}_{\rm LPFR}(\tau, N) = \left[\mathcal{I}_\pi\left(\frac{\delta\tau}{2}\right) \mathcal{I}_U(\delta\tau)\, \mathcal{I}_\pi\left(\frac{\delta\tau}{2}\right)\right]^N, \quad \delta\tau = \frac{\tau}{N}\,. \tag{3.83}$$

The leapfrog is a so-called symplectic integrator, meaning that it is exactly time-reversible and respects Liouville's theorem. However symplectic integrators do not conserve the Hamiltonian (3.75) by errors proportional to powers of the integration step $\delta\tau$, the power depending on the order of the integrator. The leapfrog is a 2^{nd} order integrator, and so the energy violation is of the order of $\sim (\delta\tau)^2$. Another popular scheme is the Omelyan 2^{nd} integrator [123], which is optimized so that the coefficient multiplying the $\sim (\delta\tau)^2$ violation is minimized. Finally, we mention the Omelyan 4^{th} order integrator, with energy violations proportional to $\sim (\delta\tau)^4$. We notice that the use of symplectic integrators is mandatory for the correctness of the HMC sampling [134].

In contrast with the theoretical formulation of the HMC of Subsection 3.7.3, the fact that now the Hamiltonian in not exactly conserved renders non-trivial the accept-reject step prescribed by the Metropolis-Hastings procedure. We may thus reformulate the HMC loop as follows:

1. The initial gauge field is $U_\mu(x,0) = U_\mu(x)$, $U_\mu(x)$ being the last link configuration, while the momenta are extracted according to a Gaussian distribution: $\pi(x,0) \sim e^{-\frac{1}{2}(\pi,\pi)}$.

2. Fields are evolved according to the discretized MD equations from time $\tau = 0$ to time $\tau = \tau_{\text{max}}$, using some finite-step symplectic technique. The MD evolution makes the system flow on the (almost) fixed-energy hyper-surface, changing globally the link configuration.

3. The accept-reject step is performed on the proposed configurations $U_\mu(x,\tau_{\text{max}})$, $\pi_\mu(x,\tau_{\text{max}})$, with acceptance probability

$$P_{\text{acc}} = \min\left\{1,\, e^{-(H[U(\tau_{\text{max}}),\pi(\tau_{\text{max}})]-H[U(0),\pi(0)])}\right\}, \tag{3.84}$$

   where we stress that now the variation of the Hamiltonian in general is non-zero. If rejected, the proposed configuration is discarded and the original link field $U_\mu(x,0)$ is taken as new element of the chain. The auxiliary momentum field is always resampled at the beginning of a MD trajectory.

Typically the HMC is efficient when the acceptance probability P_{acc} is high. This is achieved by reducing the energy loss ΔH along the molecular dynamics. The parameters which define the HMC (the total MD time τ_{max}, the integration step $\delta\tau$, the integration scheme) are in principle arbitrary and can be optimized to maximize the acceptance while keeping the computational effort under control.

3.7.5 Pseudo-fermions

Let us consider for now QCD with $N_f = 2$ (degenerate) flavours of fermions discretized with the Wilson prescription. The related probability distribution

$$P[U] = \frac{1}{\mathcal{Z}} |\det(D[U])|^2\, e^{-S^G[U]} \tag{3.85}$$

is real and positive, and requires to take into account the determinant of the Dirac operator. The Dirac operator is a square matrix with indices over spin, colour, flavour and lattice sites. The direct computation of its determinant is thus not practical. A solution to this problem is to take advantage of the properties of bosonic Gaussian integrals. By introducing the fictitious complex bosonic field ϕ, the contribution of the determinant can be included through an additional term in the action in the following way,

$$\begin{aligned} |\det(D[U])|^2 \propto \int D\phi\, e^{-S^{\rm pf}[U,\phi]}\,, \quad D\phi = \prod_{x,f,\alpha,a} d\phi^a_{f,\alpha}(x) d\phi^a_{f,\alpha}(x)^*\,, \\ S^{\rm pf}[U,\phi] = (D^{-1}[U]\phi, D^{-1}[U]\phi)\,, \end{aligned} \tag{3.86}$$

where $(\cdot,\cdot)$ is the scalar product for the field ϕ. This auxiliary field has the same indices of a quark field: for this reason it is called *pseudo-fermion*. At the beginning of the HMC, the pseudo-fermion field is sampled according to the probability distribution $\sim e^{-S^{\rm pf}}$. This is a Gaussian-like distribution and thus can be sampled with standard methods [97]. Then in the molecular dynamics the field ϕ stays unchanged, but $S^{\rm pf}$ contributes to the evolution of the momenta with the force term

$$F^{\rm pf}_\mu(x) = \frac{\delta S^{\rm pf}}{\delta U_\mu(x)}\,. \tag{3.87}$$

The evaluation of this force requires the solution of the Dirac equation, which is the most expensive part in terms of numerical effort in lattice QCD simulations.

3.7.6 Frequency splitting of the quark determinant

It is often useful to split the fermionic force in the molecular dynamics so to separate the contributions from different parts of the Dirac spectrum. This can be achieved with the Hasenbusch factorization [75, 74]

$$|\det(D)|^2 = \det(DD^\dagger + \mu^2) \times \det\left(\frac{DD^\dagger}{DD^\dagger + \mu^2}\right)\,, \tag{3.88}$$

and consequently the pseudo-fermion action becomes

$$S^{\rm pf}[U,\phi_1,\phi_2] = \left(\phi_1, (DD^\dagger + \mu^2)^{-1}\phi_1\right) + \left(\phi_2, \phi_2 + \mu^2 (DD^\dagger)^{-1}\phi_2\right) \tag{3.89}$$

where ϕ_1, ϕ_2 are two independent auxiliary pseudo-fermion fields. In this way the sea quarks contribute to the evolution with two forces F_1, F_2 so that F_1 mostly depends on the eigenvalues of the Dirac spectrum higher than the "mass" parameter μ^2, while F_2 on the lower eigenvalues. Notice that in the two contributions to the action (3.89), the inversion of the matrix $(DD^\dagger + \mu^2)$ in the first term is faster than the inversion of $(DD^\dagger)$ in the second, because μ^2 acts as an infrared regulator. The spitting (3.88) can be performed multiple times if needed, with more pseudo-fermions and more force terms.

The advantages of the splitting are twofold. On one side, two (or more) forces tend to fluctuate less along the molecular dynamics, than one force only [75, 74]. This allows

to have a coarser MD integration without affecting the acceptance rate too much. On the other side, with some tuning of μ^2 it is possible to make the most expensive force F_2 small compared to F_1. In combination with a multiple step integration this results in an important speed up of HMC simulations for QCD, see the next Subsection.

3.7.7 Hierarchical molecular dynamics

In lattice QCD simulations it often happens that the forces contributing to the molecular dynamics evolution have different magnitude. For instance, the force coming from sea quarks are usually smaller than the force F_0 from the gauge action. In addition, in the previous subsection we discussed that the Hasenbusch splitting allows to further separate the quark contribution in two (or more) terms possibly of different magnitudes. When a hierarchy in the magnitude and cost of forces emerges it may be convenient to have different MD step sizes, so that smaller forces are treated with coarser integrations [139]. For example, assume that the three forces discussed above are in the relative relation $F_2 \ll F_1 \lesssim F_0$, F_1, F_2 being respectively the high- and low-mode quark forces. We define the level-1 integrator

$$\mathcal{I}_1(\tau, N_1) = \mathcal{F}(\mathcal{I}_\pi^{F_2},\, \mathcal{I}_0,\, \tau,\, N) \tag{3.90}$$

which evolves the fields for the total MD time τ in N steps, with step size $\delta\tau = \tau/N$. Notice that only the force F_2 is considered for the evolution of momenta, while the kernel for the evolution of the gauge field is replaced by the level-0 integrator $\mathcal{I}_0$. The latter is defined as

$$\mathcal{I}_0(\delta\tau, N_0) = \mathcal{F}(\mathcal{I}_\pi^{F_0,F_1},\, \mathcal{I}_U,\, \delta\tau,\, N_0) \tag{3.91}$$

and evolves the fields for the total time $\delta\tau$ in N_0 steps, considering the forces F_0, F_1. In this way each time the force F_2 is integrated at level-1 with the step $\delta\tau$, the forces F_0, F_1 are integrated N_0 times at level-0 with the finer step $\delta\tau/N_0$. The hierarchy in computational time of the forces is the opposite to that in the magnitude, with the expensive low-mode quark force F_2 as smaller contribution to the evolution. After a proper tuning of the parameters, this two-level integration has very good chances to speed up the HMC algorithm, roughly by a factor N_0 compared to the plain single level integration.

3.7.8 Rational HMC

We come now to the strategy for simulating one single quark flavour. As we said, in general for (improved) Wilson fermions we cannot theoretically exclude that the quark determinant is negative for a given gauge configuration. However if the single flavour has a large mass (e.g. the strange or charm quark) then the subset of exceptional configurations where the determinant is negative is expected to have a very small measure, so that its contribution to the path integral can be assumed to be negligible [6]. In this circumstance

[6] More generally, this statement is true when the Dirac operator has a large gap in its spectrum. This may also be related to dynamical effects, such as when the theory is simulated at finite temperature.

we can replace the Wilson-Dirac operator D with the positive operator

$$|Q| = \sqrt{Q^2}\,, \quad Q = \gamma_5 D\,. \tag{3.92}$$

The operator $|Q|$ is well defined but not directly accessible and it can be computed only by approximation. If we call R some approximation for $1/\sqrt{Q^2}$, then we can write the determinant of $|Q|$ as

$$\det(|Q|) = \det(|Q|RR^{-1}) = \det(|Q|R)\det(R^{-1})\,. \tag{3.93}$$

The relevant part $\det(R^{-1})$ can be represented using pseudo-fermions,

$$\det(R^{-1}) \propto \int D\phi\, e^{-(\phi, R\phi)}\,. \tag{3.94}$$

The term $\det(|Q|R)$ is expected to be close to identity and weakly dependent on the gauge configuration, if the approximation R is good enough. It is usually estimated stochastically and included in the observables as a reweighting factor [100]. The operator R is in principle any good approximation to the function $1/\sqrt{x}$. We focus on the rational HMC (RHMC) [86], which employs the Zolotarev (n, n)-order rational approximation in the interval $[\varepsilon, 1]$,

$$\frac{1}{\sqrt{x}} \approx R_{n,\varepsilon}(x) = A\frac{(x+a_1)\cdots(x+a_{2n-1})}{(x+a_2)\cdots(x+a_{2n})}\,, \tag{3.95}$$

where $A, a_1, ..., a_{2n}$ are known and the error is guaranteed to be at most

$$\delta = \max_{x\in[\varepsilon,1]} \left|1 - \sqrt{x}R_{n,\varepsilon}(x)\right| \tag{3.96}$$

if the approximation is applied in the defining interval. In our case, calling $[r_a, r_b]$ an interval that includes all the eigenvalues of $|Q|$, we define

$$R \equiv r_b R_{n,\varepsilon}(r_b^{-2}Q^2)\,, \quad \varepsilon = (r_a/r_b)^2 \tag{3.97}$$

where the degree n of the Zolotarev polynomial (that is, the number of its poles) is a tunable parameter. Assuming r_a, r_b to be known, n should be set so that the error on the approximation drops below some chosen threshold. In practice, the spectral range $[r_a, r_b]$ of the operator Q can be measured in a dedicated set of simulations, for instance using a power method algorithm. The poles of the rational approximation can be ordered according to the magnitude of the related forces. This naturally leads to a frequency splitting where the different subsets of poles give rise to different force contributions.

Chapter 4

Equation of State of QCD at high temperature

This Chapter is devoted to the numerical computation of the QCD Equation of State (EoS) at zero chemical potential and for temperatures between 3 GeV and 160 GeV. This is the main original contribution of this thesis. To set the stage we first review the state of the art in the computation of the QCD EoS, both in terms of results and methodology. After a summary of the the main novelties of our approach, we show the details of the numerical computation.

4.1 State of the art

The standard technique adopted in literature for the computation of the EoS in lattice QCD is called *integral method*. The primary quantity that is determined from the lattice is the trace anomaly $\mathcal{I}$ of the Energy-Momentum tensor,

$$\mathcal{I} = e - 3p = -\frac{T}{V}\frac{d\ln\mathcal{Z}}{d\ln a}\,, \tag{4.1}$$

where T is the temperature, V the spatial volume, $\mathcal{Z}$ the QCD partition function and a the lattice spacing. The ultraviolet power divergence of this quantity is usually removed by subtracting the trace anomaly itself computed at the low reference temperature $T_{\rm ref}$:

$$\Delta\mathcal{I}(T) = \mathcal{I}(T) - \mathcal{I}(T_{\rm ref})\,. \tag{4.2}$$

The trace anomaly $\mathcal{I}$ is computed at many temperatures on the lattice, and then the pressure is obtained from the integral

$$\frac{p(T)}{T^4} - \frac{p(T_{\rm ref})}{T_{\rm ref}^4} = \int_{T_{\rm ref}}^{T} dT'\,\frac{\Delta\mathcal{I}(T')}{(T')^5}\,. \tag{4.3}$$

Finally, the entropy and energy densities can be computed through standard thermodynamic relations. The reference pressure $p(T_{\rm ref})$ may be set to zero or approximated

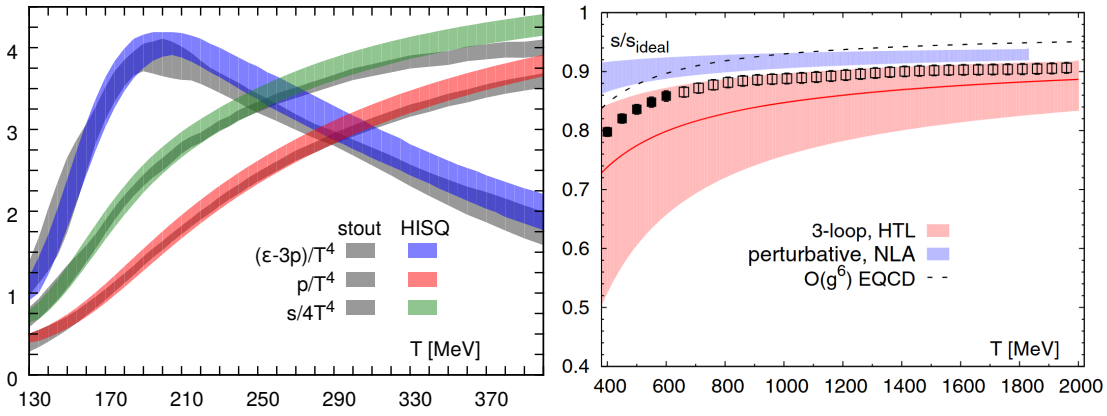

(a) (b)

Figure 4.1: Left: comparison of the $N_f = 2+1$ QCD EoS between two computations with different discretizations of staggered fermions [21, 13]. Plot from [13]. Right: entropy density of $N_f = 2+1$ QCD computed in [15] with staggered quarks. Filled markers are continuum extrapolated results, empty markers are continuum estimated results. The comparison with 3-loop HTL and weak coupling expansion in the thermal effective theory is shown. The bands correspond to a variation of the renormalization scale $\mu = 2\pi T$ by the factors 1/2 and 2.

using a low energy model such as the hadron resonance gas [84]. Using this strategy, the QCD EoS has been determined for temperatures up to $\sim$ 500 MeV [13, 21] with $N_f = 2+1$ flavours of staggered quarks in two different discretizations. The comparison of the results is shown in Figure 4.1a. More recently, calculations up to 2 GeV were presented for $N_f = 2+1$ staggered quarks [15]. The resulting entropy density is shown in Figure 4.1b, compared to the Hard Thermal Loop (HLT) prediction [72] and the weak coupling expansion in the thermal effective theory [89]. Finally, the EoS is known up to 1 GeV for $N_f = 2+1+1$ staggered quarks [20].

4.1.1 Perturbative computation

For temperatures above $\sim$ 1-2 GeV, the EoS in QCD is currently known only from a perturbative expansion in the strong coupling g within the framework of thermal effective theory of QCD [89, 82], as discussed in Chapter 2. There is however evidence from lattice QCD that the perturbative expansion struggles to reproduce the properties of QCD matter up to temperatures of the order of the electro-weak scale [62, 46, 64]. Figure 4.2 shows the entropy of the pure gauge theory computed in Ref. [62], in the temperature interval from the critical point T_c up to $\sim 230T_c$. The perturbative result is also shown for increasing loop orders: it is clear that, by its own, perturbation theory cannot describe in a satisfactory way the non-perturbative results even at the highest temperatures. The perturbative expansion at order $\sim g^6$ has an unknown coefficient, q_c, coming from the non-perturbative ultrasoft dynamics. In Figure 4.2 the light blue curve

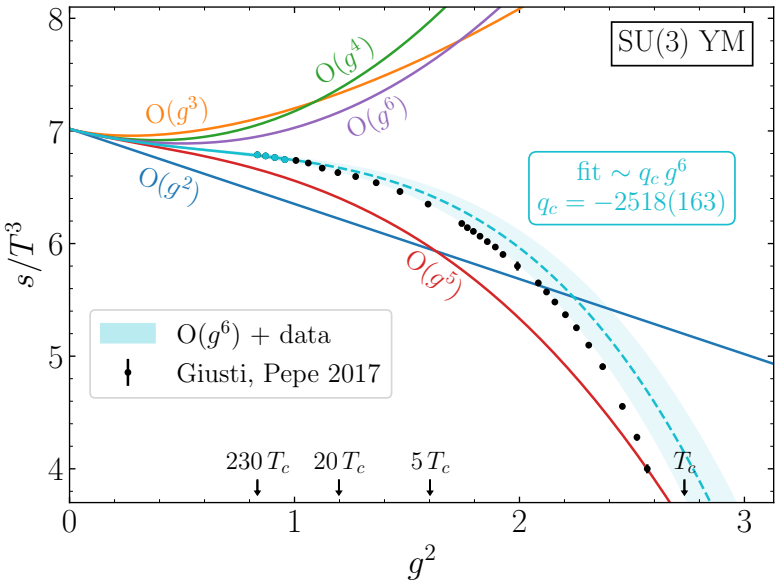

Figure 4.2: Entropy density in the pure SU(3) Yang-Mills theory, compared to perturbation theory. Data from [62]. The coupling g is the 5-loop $\overline{\text{MS}}$ coupling.

represents the perturbative series where q_c has been fitted using the points at highest temperatures (highlighted in blue in the plot), where the effective theory is expected to work better. Only after this constrain has been imposed there is some agreement between the perturbative expansion and lattice data, apparently also at lower temperatures. However, the fitted $\sim g^6$ term contributes by $\sim 50\%$ of the total of the interaction at the highest temperature considered. Similar conclusions have been drawn in QCD in Refs. [46] and [65], where the mesonic and baryonic screening masses were computed non-perturbatively in the temperature interval 1 GeV – 160 GeV.

4.2 Strategy

In this Section we describe our strategy for the determination of the entropy density of QCD at very high temperatures. Our method relies on two key novelties with respect to standard procedures. First, we use shifted boundary conditions to directly access the entropy density of QCD [59, 42] without the need of the zero-temperature subtraction. Second, we abandon the hadronic scheme and instead we determine the lines of constant physics by imposing that a renormalized coupling, defined non-perturbatively, assumes a prescribed value [46]. This allows us to overcome the window problem that could arise when accommodating both the high temperature and the hadronic scale on the same lattice.

4.2.1 Entropy density in the continuum

We start from continuum chiral QCD in infinite spatial volume, at finite temperature and in a moving reference frame. We recall from Section 2.2 that the latter is realized by imposing shifted boundary conditions for the fields along the compact direction, of size L_0 :

$$\begin{aligned} A_\mu(x_0 + L_0, \boldsymbol{x}) &= A_\mu(x_0, \boldsymbol{x} - L_0\boldsymbol{\xi})\,, \\ \psi(x_0 + L_0, \boldsymbol{x}) &= -\psi(x_0, \boldsymbol{x} - L_0\boldsymbol{\xi})\,, \\ \overline{\psi}(x_0 + L_0, \boldsymbol{x}) &= -\overline{\psi}(x_0, \boldsymbol{x} - L_0\boldsymbol{\xi})\,, \end{aligned} \tag{4.4}$$

where $\boldsymbol{\xi} = (\xi_1, \xi_2, \xi_3)$ is the shift vector. The entropy density of QCD can be written as

$$\frac{s}{T^3} = \frac{1 + \boldsymbol{\xi}^2}{\xi_k} \frac{1}{T^4} \frac{\partial}{\partial \xi_k} f(L_0, \boldsymbol{\xi})\,, \quad T = \frac{1}{L_0\sqrt{1 + \boldsymbol{\xi}^2}}\,, \tag{4.5}$$

where T is the temperature of the thermal system at rest, and f is the free-energy density. We explicitly indicate only the dependence on L_0 and $\boldsymbol{\xi}$, even though the free-energy depends also on all the other parameters of the theory. The power divergence resulting from the mixing of the free energy with the identity is removed by the derivative in the shift, so that the entropy in eq. (4.5) is well defined when the parameters of the theory are renormalized.

With the numerical computation in mind, it is convenient to rewrite the free-energy density as follows:

$$\begin{aligned} f(L_0, \boldsymbol{\xi}) &= f(L_0, \boldsymbol{\xi})|_{m_0 \to \infty} + \Big[f(L_0, \boldsymbol{\xi}) - f(L_0, \boldsymbol{\xi})|_{m_0 \to \infty} \Big] \\ &= f_\infty(L_0, \boldsymbol{\xi}) - \int_0^\infty dm_0 \, \frac{\partial}{\partial m_0} f(L_0, \boldsymbol{\xi})\,. \end{aligned} \tag{4.6}$$

In the first line we added and subtracted the free-energy f_∞ of QCD at infinite bare quark mass. In the second line we replaced the last term with the integral in the bare quark mass of the derivative with respect to m_0 of $f(L_0, \boldsymbol{\xi})$. The derivative gives the expectation value of the scalar density operator (referred to as chiral condensate in the following),

$$\langle \overline{\psi}\psi \rangle_{\boldsymbol{\xi}} = \frac{\partial}{\partial m_0} f(L_0, \boldsymbol{\xi})\,, \tag{4.7}$$

and this leads to

$$\frac{\partial}{\partial \xi_k} f(L_0, \boldsymbol{\xi}) = \frac{\partial}{\partial \xi_k} f_\infty(L_0, \boldsymbol{\xi}) - \int_0^\infty dm_0 \, \frac{\partial}{\partial \xi_k} \langle \overline{\psi}\psi \rangle_{\boldsymbol{\xi}, m_0}\,. \tag{4.8}$$

We now focus on the the $m_0 \to \infty$ contribution. In this limit, the free-energy of QCD is equivalent to the free-energy density of the $N_f = 0$ theory, i.e. the pure Yang-Mills theory at the same bare parameters. Following [61, 62] we can assume that, within the interval of temperatures relevant for our study, the shift-derivative of the free-energy in

pure gauge is a smooth function of the bare coupling. We take the derivative with respect to the bare coupling,

$$\frac{d}{dg_0^2}\left(\frac{\partial}{\partial\xi_k}f_\infty(L_0,\boldsymbol{\xi})\right) = -\frac{1}{g_0^2}\frac{\partial}{\partial\xi_k}\big\langle S^G\big\rangle_{\boldsymbol{\xi}}^{\rm YM}\,, \tag{4.9}$$

where on the right appears the expectation value of the gauge action S^G, computed in the pure gauge theory with shifted boundary conditions. We obtain the desired quantity by adding to the free case $f^{G(0)}$ the integral in the bare coupling of eq. (4.9) from $g_0^2 = 0$ up to the desired value of g_0^2, in formulas

$$\frac{\partial}{\partial\xi_k}f_\infty(L_0,\boldsymbol{\xi}) = \frac{\partial}{\partial\xi_k}f^{G(0)}(L_0,\boldsymbol{\xi}) - \int_0^{g_0^2} du\,\frac{1}{u}\frac{\partial}{\partial\xi_k}\big\langle S^G\big\rangle_{\boldsymbol{\xi},u}^{\rm YM}\,. \tag{4.10}$$

We finally write the entropy of QCD as

$$\frac{s}{T^3} = \frac{s_\infty}{T^3} + \frac{\chi}{T^3}\,, \tag{4.11}$$

where

$$s_\infty = s^{G(0)} - \frac{1+\boldsymbol{\xi}^2}{\xi_k}\frac{1}{T}\int_0^{g_0^2} du\,\frac{1}{u}\frac{\partial}{\partial\xi_k}\big\langle S^G\big\rangle_{\boldsymbol{\xi},u}^{\rm YM} \tag{4.12}$$

is computed in the pure Yang-Mills theory but at the bare parameters of QCD, and

$$\chi = -\frac{1+\boldsymbol{\xi}^2}{\xi_k}\frac{1}{T}\int_0^{\infty} dm_0\,\frac{\partial}{\partial\xi_k}\big\langle\overline{\psi}\psi\big\rangle_{\boldsymbol{\xi},m_0} \tag{4.13}$$

is computed in QCD.

4.2.2 Entropy density on the lattice

On the lattice shifted boundary conditions for the gauge field are enforced on the link variables,

$$U_\mu(x_0+L_0,\boldsymbol{x}) = U_\mu(x_0,\boldsymbol{x}-L_0\boldsymbol{\xi})\,, \tag{4.14}$$

while equation (4.4) sets the boundary conditions for the discretized quark fields. The lattice theory is formulated in the finite volume $V = L_1L_2L_3$, and periodic boundary conditions are imposed on the fields in the spatial directions:

$$\begin{aligned} U_\mu(x_0,x_k+L_k) &= U_\mu(x_0,x_k)\,,\\ \psi(x_0,x_k+L_k) &= \psi(x_0,x_k)\,,\\ \overline{\psi}(x_0,x_k+L_k) &= \overline{\psi}(x_0,x_k)\,, \end{aligned} \tag{4.15}$$

with $k = 1,2,3$. We now reconsider on the lattice the formulas we derived in the continuum. We use the same symbols for continuum and lattice quantities, since any ambiguity is resolved by the context. The entropy density is given by

$$\frac{s}{T^3} = \frac{1+\boldsymbol{\xi}^2}{\xi_k}\frac{1}{T^4}\frac{\Delta}{\Delta\xi_k}f(L_0,\boldsymbol{\xi})\,, \tag{4.16}$$

where

$$\frac{\Delta}{\Delta\xi_k} f(L_0, \boldsymbol{\xi}) = \frac{L_0}{4a} \left[f\left(L_0, \boldsymbol{\xi} + \frac{2a}{L_0}\hat{k}\right) - f\left(L_0, \boldsymbol{\xi} - \frac{2a}{L_0}\hat{k}\right)\right] \tag{4.17}$$

is the 2-point discrete symmetric derivative of the free-energy with respect to the k-th component of the shift [1]. The lattice version of equation (4.11) is formally the same,

$$\frac{s}{T^3} = \frac{s_\infty}{T^3} + \frac{\chi}{T^3}\,, \tag{4.18}$$

with s_∞ given by

$$s_\infty = s^{G(0)} + g_0^2\, s^{G(1)} - \int_0^{g_0^2} du \left(\frac{1+\boldsymbol{\xi}^2}{\xi_k} \frac{1}{uT} \frac{\Delta}{\Delta\xi_k} \langle S^G \rangle^{\rm YM}_{\boldsymbol{\xi},u} + s^{G(1)} \right) \tag{4.19}$$

where for later convenience we subtracted the entropy density at 1-loop order, and

$$\chi = -\frac{1+\boldsymbol{\xi}^2}{\xi_k} \frac{1}{T} \int_0^\infty dm_0\, \frac{\Delta}{\Delta\xi_k} \langle \overline{\psi}\psi \rangle_{\boldsymbol{\xi},m_0}\,. \tag{4.20}$$

The discrete shift-derivatives of the gauge action and of the chiral condensate are defined analogously to eq. (4.17). In order to take the continuum limit, the quantities (4.19) and (4.20) must be summed at the same values of g_0^2 and L_0/a defined by a line of constant physics in QCD.

4.2.3 Renormalization and lines of constant physics

We determine the lines of constant physics by fixing, at finite lattice spacing, the value of a renormalized coupling defined non-perturbatively. We choose the Schrödinger functional (SF) coupling $\overline{g}^2_{\rm SF}(\mu)$, whose non-perturbative running with the renormalization scale μ is known precisely in the continuum [25, 28]. The renormalization condition reads

$$\overline{g}^2_{\rm SF}(g_0^2, a\mu) = \overline{g}^2_{\rm SF}(\mu)\,, \quad a\mu \ll 1\,, \quad \mu \sim T\,, \tag{4.21}$$

where g_0 is the bare coupling and the renormalization scale μ is identified with the temperature T. This condition fixes the dependence of the bare coupling constant g_0^2 on the lattice spacing, for values of a at which the scale μ and therefore the temperature can be easily accommodated. As a consequence, each temperature can be simulated at several lattice resolutions and the continuum limit can be performed with confidence at moderate computational effort. The chosen values of the temperature and the corresponding values of the renormalized SF coupling are reported in Table 4.1. We refer to Appendix B of Ref. [46] for all the technical details.

4.3 Lattice parameters

We discretize QCD with the Wilson plaquette gauge action and $N_f = 3$ flavours of massless O(a)-improved Wilson fermions. This is the same setup employed in Refs. [25, 28]

[1] We use the two-point discrete derivative due to constraints related to the simulation software.

T	$\bar{g}^2_{\rm SF}(\mu = T\sqrt{2})$	T (GeV)
T_0	1.01636	164.6(5.6)
T_1	1.11000	82.3(2.8)
T_2	1.18446	51.4(1.7)
T_3	1.26569	32.8(1.0)
T_4	1.3627	20.63(63)
T_5	1.4808	12.77(37)
T_6	1.6173	8.03(22)
T_7	1.7943	4.91(13)
T_8	2.0120	3.040(78)

Table 4.1: Values of the Schrödinger functional coupling in $N_f = 3$ QCD with Wilson action used to renormalize the bare parameters at the physical temperatures considered in this work, reported in the last column.

for the non-perturbative determination of the running coupling, that we use to define the lines of constant physics. In our study we consider the 9 temperatures of Table 4.1. Being suppressed as $\sim (m/T)^2$, the effect of the light quark masses is completely negligible at these temperatures. At each temperature the line of constant physics is defined at the resolutions $L_0/a = 4, 6, 8, 10$ following the renormalization procedure outlined above. Given the lines of constant physics, the critical mass $m_{\rm cr}$ is determined by requiring that the PCAC mass, computed in a SF setup, vanishes [37, 46]. The values of inverse bare coupling $\beta = 6/g_0^2$, the critical hopping parameter $\kappa_{\rm cr} = 1/(2am_{\rm cr} + 8)$ and the improvement coefficient $c_{\rm sw}$ at given temperature and given L_0/a are reported in Table F.3. The sizes of the lattice in the spatial directions are fixed to $L/a = L_1/a = L_2/a = L_3/a = 144$. The aspect ratio TL of our lattices thus ranges between 10 and 25. The choice of the shift $\boldsymbol{\xi}$ is in principle arbitrary within the range

$$-\frac{L_k}{2L_0} \leq \xi_k \leq \frac{L_k}{2L_0}\,, \quad k = 1, 2, 3 \tag{4.22}$$

due to periodic boundary conditions in spatial directions. Following [43, 22, 46] we set $\boldsymbol{\xi} = (1, 0, 0)$, which turns out to make discretization effects milder. We compute the shift-derivatives with the 2-point symmetric discretization at the values

$$\boldsymbol{\xi}_\pm = (1 \pm 2a/L_0, 0, 0)\,, \quad \boldsymbol{z}_\pm = (L_0 \pm 2a, 0, 0)\,, \tag{4.23}$$

where for convenience we introduced the vector $\boldsymbol{z} = L_0\boldsymbol{\xi}$ which gives the displacement in space due to the shift. With these choices, $\Delta\xi_1 = 4a/L_0$.

4.4 Pure Yang-Mills contribution

In this Section we discuss the computation of the contribution s_∞ defined in eq. (4.19). Using the shift vectors of eq. (4.23), the explicit expression for the discrete derivative

appearing in (4.19) is

$$\frac{\Delta}{\Delta\xi_1}\langle S^G\rangle^{\rm YM}_{\boldsymbol{\xi}} = \frac{L_0}{4a}\left(\langle S^G\rangle^{\rm YM}_{\boldsymbol{\xi}_+} - \langle S^G\rangle^{\rm YM}_{\boldsymbol{\xi}_-}\right) . \tag{4.24}$$

At fixed lattice spacing we estimate the integral in the bare coupling using numerical quadratures. This requires the determination from the lattice of the derivative in equation (4.24) at the values of the bare coupling uniquely prescribed by the chosen quadrature recipe, in the interval $[0, g_0^2]$. Notice that the two expectation values come from independent numerical simulations at the two shifts. We opt for splitting the integration in many terms evaluated with different quadratures, as described in the following.

4.4.1 Integral in the bare coupling

At given L_0/a, we first compute the integral appearing in eq. (4.19) for the value of g_0^2 associated to the temperature T_1. We split the integration in intervals as follows:

$$\int_0^{g_0^2|_{T_1}} du\,(\cdots) = \int_0^{6/15} du\,(\cdots) + \int_{6/15}^{6/9} du\,(\cdots) + \int_{6/9}^{g_0^2|_{T_1}} du\,(\cdots)\,, \tag{4.25}$$

where $g_0^2|_{T_i}$ is the value of the bare coupling at temperature T_i given the lattice resolution L_0/a, and the dots stand for the integrand function. In the first interval $g_0^2 \in [0,\, 6/15]$ the integral is computed with a 2-point trapezoidal rule (3-point Simpson rule for $L_0/a = 4$). The interval $g_0^2 \in [6/15,\, 6/9]$ is covered with a 3-point Gauss quadrature. The third interval, $g_0^2 \in [6/9,\, g_0^2|_{T_1}]$, is computed with another 3-point Gauss quadrature. For the resolutions $L_0/a = 4, 6$ there is also another quadrature in the interval $g_0^2 \in [6/9,\, g_0^2|_{T_0}]$, computed with a 3-point Gauss quadrature for $L_0/a = 4$ and with the midpoint rule for $L_0/a = 6$. At the lower temperatures T_i, $i > 1$, the value of the integral is obtained by adding to the T_{i-1} result the integral in the interval $g_0^2 \in [g_0^2|_{T_{i-1}},\, g_0^2|_{T_i}]$,

$$\int_0^{g_0^2|_{T_i}} du\,(\cdots) = \int_0^{g_0^2|_{T_{i-1}}} du\,(\cdots) + \int_{g_0^2|_{T_{i-1}}}^{g_0^2|_{T_i}} du\,(\cdots)\,, \tag{4.26}$$

where the second integral is estimated with a 3-point Gauss quadrature for $i = 2, 3, 4, 5, 6$, and a 5-point Gauss quadrature for $i = 7, 8$. The entire recursion is summarized in Table 4.2.

4.4.2 Results

The pure gauge ensembles for the computation of s_∞ have been generated in Monte Carlo simulations where the basic sweep is a combination of heatbath and over-relaxation [3] updates of the link variables, using the Cabibbo–Marinari scheme [26, 39, 38]. The values of bare couplings simulated and the number of measurements of the pure gauge action are reported in Table F.4. Figure 4.3 shows a representative case for the integrand function in g_0^2. The vertical lines are the upper bounds to the integrals at different temperatures,

interval			quadrature	
0	$\le g_0^2 \le$	6/15	3 (Simpson)	$L_0/a = 4$
			2 (trapezoid)	$L_0/a = 6, 8, 10$
6/15	$\le g_0^2 \le$	6/9	3 (Gauss)	
6/9	$\le g_0^2 \le$	$g_0^2\|_{T_0}$	3 (Gauss)	$L_0/a = 4$
			1 (midpoint)	$L_0/a = 6$
6/9	$\le g_0^2 \le$	$g_0^2\|_{T_1}$	3 (Gauss)	
$g_0^2\|_{T_{i-1}}$	$\le g_0^2 \le$	$g_0^2\|_{T_i}$	3 (Gauss)	$1 < i < 7$
			5 (Gauss)	$i = 7, 8$

Table 4.2: Sequence of quadratures for the computation of the integral in g_0^2 appearing in eq. (4.19).

interval			value
0	$\le g_0^2 \le$	6/15	0.007(18)
6/15	$\le g_0^2 \le$	6/9	−0.020(17)
6/9	$\le g_0^2 \le$	$g_0^2\|_{T_1}$	−0.0315(16)
$g_0^2\|_{T_1}$	$\le g_0^2 \le$	$g_0^2\|_{T_2}$	−0.0340(10)
$g_0^2\|_{T_2}$	$\le g_0^2 \le$	$g_0^2\|_{T_3}$	−0.0486(12)

interval			value
$g_0^2\|_{T_3}$	$\le g_0^2 \le$	$g_0^2\|_{T_4}$	−0.0766(17)
$g_0^2\|_{T_4}$	$\le g_0^2 \le$	$g_0^2\|_{T_5}$	−0.1255(21)
$g_0^2\|_{T_5}$	$\le g_0^2 \le$	$g_0^2\|_{T_6}$	−0.2075(20)
$g_0^2\|_{T_6}$	$\le g_0^2 \le$	$g_0^2\|_{T_7}$	−0.4232(27)
$g_0^2\|_{T_7}$	$\le g_0^2 \le$	$g_0^2\|_{T_8}$	−1.066(11)

Table 4.3: Contributions to the integral in g_0^2 shown in Figure 4.3, computed from 6×144^3 lattices. Each line corresponds to one quadrature, see Table 4.2.

see equations (4.25) and (4.26). For the data in Figure 4.3 we report in Table 4.3 the various contributions from the quadratures. Notice in particular that the integral in the interval $g_0^2 \in [0, 6/15]$ is well compatible with zero, meaning that we can safely connect to the 1-loop perturbative result. At each temperature, the accuracy on s_∞ is $\sim 0.5\%$ for $L_0/a = 4, 6$, $\sim 1\%$ for $L_0/a = 8$ and $\sim 1.5\%$ for $L_0/a = 10$. The final results for s_∞ at fixed lattice spacing are reported in Table 4.7.

4.5 Quark contribution

In this Section we describe the computation of the integral in the bare mass which defines the contribution χ, eq. (4.20), to the QCD entropy density. We first note that, with Wilson fermions, the expression (4.20) for χ is formally the same with the bare quark mass replaced by the bare subtracted quark mass $m_q = m_0 - m_{\rm cr}(L_0/a, g_0^2)$:

$$\chi = -\frac{1+\boldsymbol{\xi}^2}{\xi_k}\frac{1}{T}\int_0^\infty dm_q\, \frac{\Delta}{\Delta\xi_k}\langle\overline{\psi}\psi\rangle_{\boldsymbol{\xi},m_q}\,. \tag{4.27}$$

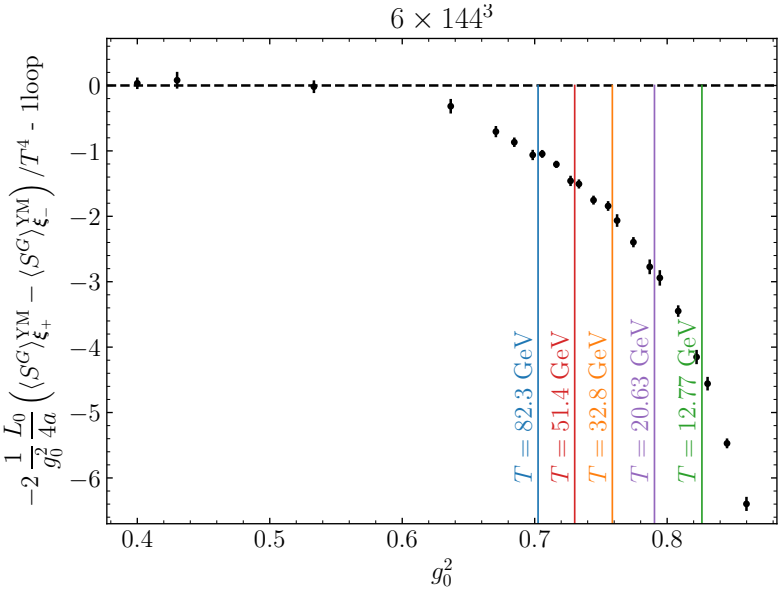

Figure 4.3: Plot of the integrand function of the g_0^2 integral, computed on 6×144^3 lattices. The vertical lines denote the integration bounds for obtaining the integral at the indicated temperature.

The integrand function is the shift-derivative of the chiral condensate. With the notation introduced in Subsection 4.3, we explicitly write it as

$$\frac{\Delta}{\Delta\xi_1}\langle\overline{\psi}\psi\rangle_{\boldsymbol{\xi}} = \frac{L_0}{4a}\left(\langle\overline{\psi}\psi\rangle_{\boldsymbol{\xi}_+} - \langle\overline{\psi}\psi\rangle_{\boldsymbol{\xi}_-}\right) . \tag{4.28}$$

At given L_0/a and g_0^2 we estimate the integral in the bare quark mass with an optimized combination of Gauss quadratures. At each value of bare mass prescribed by the quadrature recipe, we perform two simulations of QCD with $N_f = 3$ degenerate massive flavours at the two shifts for the computation of the discrete derivative, see eq. (4.28). In the following we give more details on the integration procedure.

4.5.1 Integral in the bare mass

After the change of variable $\widetilde{m}_q = m_q/T$, we split the integral χ in three parts:

$$\begin{aligned}\chi &= -2\left(\int_0^{\widetilde{m}_1} d\widetilde{m}_q + \int_{\widetilde{m}_1}^{\widetilde{m}_2} d\widetilde{m}_q + \int_{\widetilde{m}_2}^{\infty} d\widetilde{m}_q\right)\frac{\Delta}{\Delta\xi_k}\langle\overline{\psi}\psi\rangle_{\boldsymbol{\xi},\widetilde{m}_q} \\ &\equiv \chi_{\rm peak} + \chi_{\rm tail} + \chi_{\rm res} .\end{aligned} \tag{4.29}$$

In $\chi_{\rm res}$ we further change variable to the hopping parameter $\kappa = 1/(2am_0 + 8)$, so that the integration interval becomes compact. The conversion with $\widetilde{m}_q$ is

$$\kappa = \frac{1}{2(aT\widetilde{m}_q + am_{\rm cr} + 4)} , \quad \widetilde{m}_q = \frac{1}{aT}\left(\frac{1}{2\kappa} - 4 - am_{\rm cr}\right) \tag{4.30}$$

$\widetilde{m}_q$		value	L_0/a
$\widetilde{m}_1$		5.0	$4, 6, 8, 10$
$\widetilde{m}_2$	$\Big\{$	35.0	4
		20.0	$6, 8, 10$

(a)

integral	interval	points
χ_{peak}	$\widetilde{m}_q \in [0, \widetilde{m}_1]$	10 (Gauss)
χ_{tail}	$\widetilde{m}_q \in [\widetilde{m}_1, \widetilde{m}_2]$	7 (Gauss)
χ_{res}	$\kappa \in [0, \kappa_2]$	3 (Gauss)

(b)

Table 4.4: Left: choice of the masses $\widetilde{m}_1$, $\widetilde{m}_2$ used to split the integral in the mass. Right: quadratures used for integrating the three contributions to χ.

and leads to

$$\chi_{\text{res}} = -\frac{2}{aT}\int_0^{\kappa_2} \frac{d\kappa}{2\kappa^2}\frac{\Delta}{\Delta\xi_k}\langle\overline{\psi}\psi\rangle_{\boldsymbol{\xi},\kappa}\,, \quad \kappa_2 = \kappa(\widetilde{m}_2)\,. \tag{4.31}$$

Notice that the values of κ in the conversion (4.30) depend on L_0/a and g_0 through the critical mass.

The choice of the masses $\widetilde{m}_1$, $\widetilde{m}_2$ is arbitrary in principle. Using perturbation theory as a guideline, we fixed $\widetilde{m}_1$, $\widetilde{m}_2$ so that the integral χ_{peak} gives the bulk of the result, χ_{tail} contributes by $\sim 20\%$ and the last χ_{res} is a subdominant term which estimates the asymptotic behaviour of the integral for very large values of the mass. The chosen values are reported in Table 4.4a. See also Appendix F.2 for further details on the exploratory perturbative study. Table 4.4b summarizes the definition of the three contributions to χ, together with the chosen number of points for the Gauss quadratures. χ_{peak} is the main contribution and we integrate it with a $n = 10$ Gauss quadrature. We use 10 more points for the computation of the rest of the integral, divided in a $n = 7$ quadrature for χ_{tail} and a $n = 3$ quadrature for χ_{res}, the last performed with the hopping parameter as integration variable. We can finally list the steps for the numerical computation of χ.

- At given L_0/a and g_0^2, determine the 20 points for the Gauss quadrature using Tables 4.4.
- At the values of bare mass corresponding to the Gauss points, compute the chiral condensate $\langle\overline{\psi}\psi\rangle$ in two lattice QCD simulations at the two shifts for the discrete derivative (4.28).
- Estimate the three contributions χ_{peak}, χ_{tail}, χ_{res} using the quadrature formula

$$\chi_{a,b} = -2\,\frac{L_0}{4a}\sum_{i=1}^{n}\omega_i^{(a,b,n)}\left(\langle\overline{\psi}\psi\rangle_{\boldsymbol{\xi}_+} - \langle\overline{\psi}\psi\rangle_{\boldsymbol{\xi}_-}\right)\Big|_i\,, \tag{4.32}$$

  where $\chi_{a,b}$ is the integral with support in $[a, b]$, and the index i runs over the different Gauss points. The coefficients $\omega_i^{(a,b,n)}$ are uniquely fixed by the quadrature recipe and depend on the integration interval and on the degree of the quadrature, see Appendix F.1 for the notation.

At given L_0/a and g_0^2, the computation of χ requires in total 20×2 simulations. Taking advantage of the peculiarities of the quantity of interest, we managed to highly optimize

the numerical approach so that the computation was feasible with moderate computational effort. We summarize these aspects in the following. Further details can be found in the related Appendices.

4.5.2 Simulating at large mass

The simulations for the computation of χ have bare quark masses with values ranging from $m_q = 0$ to infinity. Notice that, as a consequence of the Gauss quadrature, simulations at the exact chiral point are not required. The heavier the quarks, the less they contribute to the dynamics: in particular, their forces in the molecular dynamics become weaker and thus can be treated with coarser integrators. Furthermore, the gap in the spectrum of Dirac operator increases with the quark mass, and this makes the Dirac operator well conditioned. These observations suggest that a proper tuning of the simulation parameters as the quark mass increases may really speed up the computation of the integral χ. The detailed description of the tuning procedure and of the final choices for the algorithms can be found in Appendix F.6. As a result, simulations with hopping parameter $\kappa \lesssim 0.10$ turned out to be up to 10 times cheaper than the ones near the chiral limit.

In our simulations we employed a version of the package `openQCD-1.6` [99] modified for including shifted boundary conditions. Further details on the computational setup and on the generation of our ensembles can be found in Appendix F.5.

4.5.3 Variance reduction of the chiral condensate

The chiral condensate is the primary observable for the computation of the integral χ. On a given gauge configuration, we estimate stochastically the trace of the quark propagator using U(1) random sources, see Appendix F.7. Calling $\mathcal{O}$ the stochastic estimator, its variance is given by the sum of the variances coming from the Markov Chain of gauge configurations and from the random sources,

$$\text{var}\left[\mathcal{O}\right] = \text{var}\left[\mathcal{O}\right]_U + \frac{1}{N_s}\text{var}\left[\mathcal{O}\right]_\eta \,, \tag{4.33}$$

where the latter is suppressed with the number of sources sampled at fixed gauge configuration. The hopping expansion of the two contributions reveals that they scale differently at small κ,

$$\text{var}\left[\mathcal{O}\right]_U \sim \kappa^6 \,, \quad \text{var}\left[\mathcal{O}\right]_\eta \sim \kappa^4 \,, \quad \kappa \to 0 \,. \tag{4.34}$$

This would eventually make the contribution from the variance due to the random sources dominant in simulations at large bare quark mass. The naive, and computationally expensive, solution would be to increase the number of sampled sources with $\propto \kappa^{-2}$ as the hopping parameter decreases. Following Ref. [66] we introduced an improved estimator $\widetilde{\mathcal{O}}$ for the chiral condensate, built by subtracting the quark propagator by its leading order in the hopping parameter expansion. Clearly, the central value of the estimator is not affected by the subtraction, i.e. $\langle\widetilde{\mathcal{O}}\rangle = \langle\mathcal{O}\rangle$, while the total variance $\text{var}[\widetilde{\mathcal{O}}]$ of the improved operator scales as $\sim \kappa^6$. As a result, at the smallest values of κ the variance

temp	χ_{peak}/T^3	χ_{tail}/T^3	χ_{res}/T^3	χ/T^3	σ_χ/χ
T_1	12.826(19)	2.852(21)	0.031(22)	15.71(4)	0.23%
T_3	12.944(23)	2.672(24)	0.08(3)	15.70(5)	0.29%
T_5	13.192(20)	2.420(21)	0.104(29)	15.72(4)	0.26%
T_7	13.648(27)	2.27(4)	0.27(3)	16.18(5)	0.34%

Table 4.5: Selection of results of the three contributions to the bare mass integral, on a lattice 6×144^3.

on the improved chiral condensate is more than one order of magnitude smaller than the unimproved counterpart. The details of the subtraction and the numerical tests can be found in Appendix F.8.

4.5.4 Optimization of the statistics

The error squared of the estimated integral χ, from equation (4.32), is the sum in quadrature of the errors on the chiral condensates, weighted by the square of the Gauss weights. The latter are maximum in the middle of the integration interval and decrease symmetrically towards the boundaries. This means that the Gauss points contribute differently to the error of χ, with the central points contributing the most. This suggests that the statistics of the points can be tuned so to minimize the computational cost at fixed target accuracy for χ. In this optimization we also considered that points at high mass are cheaper to simulate and that the variance of $\langle\overline{\psi}\psi\rangle$ decreases for increasing mass. This led to the optimized number of measurements of the chiral condensate reported in Table F.8. The tuning was performed for a target relative error on χ of $\sim 0.5\%$ for $L_0/a = 4, 6, 8$, and $\sim 1\%$ for $L_0/a = 10$. Appendix F.9 contains the detailed description of the minimization problem, and some numerical checks on the effectiveness of this optimization.

4.5.5 Results

In this Subsection we show some representative results of the computation of the integral in the bare mass χ at fixed bare parameters. Figure 4.4 shows the shape of the integrand function from lattices of size 6×144^3, at the temperatures T_1, T_3, T_5, T_7. For better readability the plot shows points up to $\widetilde{m}_q \approx 15$. The points are interpolated with a spline, and the errors are smaller than the markers. Each point in the plot is a combination of data coming from simulations of QCD at two shifts in order to compute the discrete derivative of the chiral condensate. The contributions χ_{peak}, χ_{tail}, χ_{res} related to the data shown in Figure 4.4 are reported in Table 4.5. As commented, the dominant contribution comes from the peak of the integrand function, followed by the tail contribution and finally the residual, which is of the order of a ~ 1.5 sigma of the full result. The statistics for this computation was tuned according to Table F.8. The precision of these data is a few permille, even better than the target accuracy of 0.5%.

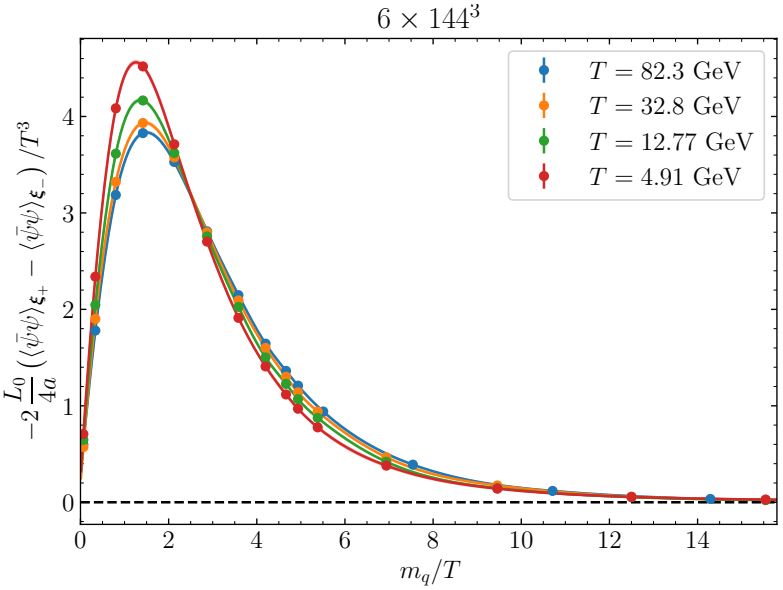

Figure 4.4: Plot of the integrand function of the mass integral at 6×144^3 and shown temperatures.

4.5.6 Accuracy of Gauss quadratures

The Gauss quadrature of order n integrates exactly polynomials up to order $2n - 1$. When used to estimate the integral of a generic function, a systematic effect may be introduced because of the underlying polynomial interpolation of the function itself. In order to estimate this systematics, at some selected bare parameters we improved the computation of the integral χ using the Kronrod extension of the Gauss quadrature, which allows us to increase the accuracy by adding points to the Gauss quadrature. This check is reported in Appendix F.4, and we find perfect agreement.

4.6 Perturbative results

We discuss the perturbative computation of the entropy density at 1-loop on the lattice. We will use these results for the 1-loop improvement of the non-perturbative data. We consider lattice perturbation theory with N_f flavours of mass-degenerate O(a)-improved Wilson fermions. Notations and conventions are reported in Appendix E. We write the 1-loop expansion of the entropy density in bare lattice perturbation theory as follows,

$$s = s^{(0)} + g_0^2\, s^{(1)}\,, \quad s^{(i)} = s^{G(i)} + s^{F(i)}\,, \quad i = 0, 1\,, \tag{4.35}$$

where both the tree-level and 1-loop orders are separated in two contributions labelled as gluonic and fermionic. In the presence of shifted boundary conditions each term of this expansion can be computed from the discrete derivative with respect to the shift of

the corresponding term in the perturbative expansion of the free-energy density. For the latter we write the 1-loop expansion in lattice perturbation theory as [42]

$$f(L_0, \boldsymbol{\xi}) = f^{(0)} + g_0^2 f^{(1)}\,, \tag{4.36}$$

where the non-interacting case is

$$f^{(0)} = (N_c^2 - 1) f^{G(0)} + N_c N_f f^{F(0)} \tag{4.37}$$

while at 1-loop we have

$$\begin{aligned} f^{(1)} = (N_c^2 - 1)\Bigg\{ & N_c f^{G(1,N_c)} + \frac{1}{N_c} f^{G(1,\frac{1}{N_c})} + N_f \Bigg[f^{F(1,N_f)} + \mathcal{F}^{F1} + \mathcal{F}^{F2} \\ & + \frac{\partial f^{F(0)}}{\partial a m_0} \left({am_{\rm cr}}^{(1,N_c)} + \delta {am_{\rm cr}}^{(1,N_c,0)} + N_f \delta {am_{\rm cr}}^{(1,N_c,1)} \right) \Bigg] \Bigg\}\,. \end{aligned} \tag{4.38}$$

The terms $\mathcal{F}^{F1}$ and $\mathcal{F}^{F2}$ represent the contributions from the improvement in the Wilson action. We explicitly added the 1-loop corrections due to the critical mass $am_{\rm cr}$, and the counterterms $\delta {am_{\rm cr}}^{(1,N_c,0)}$, $\delta {am_{\rm cr}}^{(1,N_c,1)}$ are the corresponding lattice artifacts. The expansion of the critical mass at 1-loop in lattice perturbation theory can be found in Appendix (E.2). The coefficients of the free-energy density up to 1-loop, appearing in equations (4.37)-(4.38), are collected in Appendix E.3.

Given the perturbative result for the free-energy, the entropy density is computed as

$$\frac{s^{(0)}}{T^3} = \frac{1+\boldsymbol{\xi}^2}{\xi_k} \frac{1}{T^4} \frac{\Delta f^{(0)}}{\Delta \xi_k}\,, \quad \frac{s^{(1)}}{T^3} = \frac{1+\boldsymbol{\xi}^2}{\xi_k} \frac{1}{T^4} \frac{\Delta f^{(1)}}{\Delta \xi_k}\,. \tag{4.39}$$

More explicitly, the gauge and fermionic components at tree-level are

$$\frac{s^{G(0)}}{T^3} = ({N_c}^2 - 1) \frac{1+\boldsymbol{\xi}^2}{\xi_k} \frac{1}{T^4} \frac{\Delta}{\Delta \xi_k} f^{G(0)}\,, \tag{4.40}$$

$$\frac{s^{F(0)}}{T^3} = N_c N_f \frac{1+\boldsymbol{\xi}^2}{\xi_k} \frac{1}{T^4} \frac{\Delta}{\Delta \xi_k} f^{F(0)}\,, \tag{4.41}$$

while at 1-loop

$$\frac{s^{G(1)}}{T^3} = ({N_c}^2 - 1) \frac{1+\boldsymbol{\xi}^2}{\xi_k} \frac{1}{T^4} \frac{\Delta}{\Delta \xi_k} \left(N_c f^{G(1,N_c)} + \frac{1}{N_c} f^{G(1,\frac{1}{N_c})} \right)\,, \tag{4.42}$$

$$\begin{aligned} \frac{s^{F(1)}}{T^3} = & ({N_c}^2 - 1) N_f \frac{1+\boldsymbol{\xi}^2}{\xi_k} \frac{1}{T^4} \frac{\Delta}{\Delta \xi_k} \Bigg[f^{F(1,N_f)} + \mathcal{F}^{F1} + \mathcal{F}^{F2} \\ & + \frac{\partial f^{F(0)}}{\partial a m_0} \left({am_{\rm cr}}^{(1,N_c)} + \delta {am_{\rm cr}}^{(1,N_c,0)} + N_f \delta {am_{\rm cr}}^{(1,N_c,1)} \right) \Bigg]\,. \end{aligned} \tag{4.43}$$

L_0/a	$s^{G(0)}/T^3$	$s^{F(0)}/T^3$	$s^{G(1)}/T^3$	$s^{F(1)}/T^3$
4	8.362055	24.759901	−1.0064	−3.1652
6	7.483779	16.646853	−0.7572	−1.5690
8	7.259770	14.812035	−0.7055	−1.0643
10	7.167555	14.304311	−0.6879	−0.9279

Table 4.6: Entropy density for $N_c = 3$, $N_f = 3$ at 1-loop in lattice perturbation theory, in the thermodynamic limit and at given values of L_0/a.

4.6.1 Numerical computation

We computed numerically the values of the 1-loop coefficients of the entropy density in lattice perturbation theory, at fixed L/a and in the infinite volume limit. The lattice parameters have been tuned as described in Subsection 4.3. We considered lattices with temporal sizes $L_0/a = 4, 6, 8, 10$, while the spatial size, common to the three spatial directions, ranged between $L/a = 48$ and $L/a = 288$. We adopted several strategies to safely extrapolate to the infinite volume limit. Here we summarize the main results, see Appendix E.4 for a detailed discussion.

The tree-level gluonic entropy $s^{G(0)}$ can be expressed analytically to the infinite volume limit. The computation is still numerical but no extrapolation is needed for it. The integrals for the tree-level fermionic entropy $s^{F(0)}$ and the mass counterterm entering at 1-loop involve the tree-level quark propagator only, and show exponentially suppressed finite volume effects. We therefore took their values on the largest lattice as an estimate of the infinite volume limit. The coefficients $s^{G(1)}$, $s^{F(1)}$ contain integrals with more than one loop momentum. We computed them numerically in coordinate space [102] using a Fast Fourier Transform algorithm for the gluonic and fermionic propagators. At the larger volumes we used quadruple precision to keep the numerical accuracy under control. The 1-loop coefficients of the entropy density approach the infinite volume limit as slowly as $\sim a/L$, and this would require to compute them at very large spatial volumes for a safe extrapolation to the thermodynamic limit. However, we managed to improve the convergence rate by explicitly subtracting the slowest varying finite volume effects. The residual effects are of the order of $\sim (a/L)^3$ and they are sufficiently small that we can quote the values at the largest volume $L/a = 288$ as an estimate for the thermodynamic limit. The results for the entropy density up to 1-loop in the thermodynamic limit and at fixed L_0/a are reported in Table 4.6.

4.7 Entropy of QCD

In this Section we combine the contributions s_∞ and χ to determine the entropy density of QCD, and extrapolate to the continuum limit the 1-loop improved data. The uncertainty of the continuum results is mostly of statistical nature and any source of systematic effects gives a subdominant contribution, as we comment in the following.

4.7.1 Finite volume effects

The entropy density is the derivative with respect to the shift of the free-energy density of QCD. Following Ref. [59], in Appendix D.4 we show that the free-energy density has exponentially suppressed finite size effects with $M_{\rm gap}L$, $M_{\rm gap}$ being the lightest mass in the screening spectrum of the theory. According to the effective theory of thermal QCD, see Section 2.5, this mass is proportional to the temperature. Therefore finite volume effects for the entropy are expected to be exponentially suppressed with exponent $\propto TL$, where $10 \lesssim TL \lesssim 25$ in our simulations. We explicitly checked that finite volume effects are negligible with respect to our statistical accuracy, by comparing results for the entropy from simulations with spatial sizes $L/a = 144$ and $L/a = 288$ at the temperatures T_1 and T_8 (see Table 4.1) and at some selected bare parameters. The quantitative description of this test is reported in Appendix F.12.

4.7.2 Restricting to zero topology

At high temperatures we expect the topological charge distribution to be strongly peaked in the trivial topological sector, where the topological charge $Q = 0$. In the instanton gas model, the topological susceptibility scales as $\sim T^{-8}m^3$ for thermal QCD with three light quarks and as $\sim T^{-7}$ for the pure SU(3) Yang-Mills theory. At the temperatures 3 GeV $\lesssim T \lesssim$ 160 GeV considered in this study, the $Q = 0$ sector of the QCD phase space gives by far the dominant contribution to the path integral, so that for all practical purposes we can restrict our study to the trivial topology sector. The systematics introduced by neglecting the non-zero topology phase space is much below the statistical accuracy of our numerical results.

This said, at the largest values of g_0^2 and resolutions $L_0/a = 4, 6$ we observed some topological activity in our pure gauge ensembles. In QCD simulations, $Q \neq 0$ sectors were sampled only at temperature T_8 and at the largest values of bare quark masses, where the topological susceptibility is less suppressed. By comparing results for the gauge action and chiral condensate projected at given topological sectors, we explicitly checked that topological fluctuations give a negligible effect within our statistical accuracy. This result is in agreement with other studies in the literature [15]. However we decided to enlarge the errors of $\left\langle S^G \right\rangle$ to a conservative 1-2% for data at $L_0/a = 4, 6$ and $g_0^2 \gtrsim 0.9$ in order to safely take into account any systematic effect due to topology. Further details and the numerical checks can be found in Appendix F.11.

4.7.3 Continuum limit

The results for the entropy density s/T^3 at finite lattice spacing of Table 4.7 need to be extrapolated to the continuum limit at fixed temperature. Our lattice action is non-perturbatively O(a)-improved, and since the entropy density is a spectral quantity we expect its cutoff effects to start at the order $\sim a^2$. We performed the 1-loop improvement

T	L_0/a	$\beta = 6/g_0^2$	s_∞/T^3	χ/T^3	s/T^3
T_0	4	8.7325	7.7511(77)	22.7717(77)	30.523(11)
	6	8.9950	7.070(25)	15.811(52)	22.881(58)
T_1	4	8.3033	7.6890(77)	22.6784(91)	30.367(12)
	6	8.5403	7.017(25)	15.709(36)	22.726(44)
	8	8.7325	6.806(29)	14.320(80)	21.126(85)
	10	8.8727	6.851(86)	13.92(15)	20.77(17)
T_2	4	7.9794	7.6279(77)	22.588(10)	30.216(13)
	6	8.2170	6.967(25)	15.801(39)	22.768(46)
	8	8.4044	6.754(29)	14.356(71)	21.111(77)
	10	8.5534	6.803(86)	13.85(16)	20.65(18)
T_3	4	7.6713	7.5523(77)	22.523(12)	30.076(14)
	6	7.9091	6.901(25)	15.696(45)	22.597(52)
	8	8.0929	6.686(29)	14.244(78)	20.930(83)
	10	8.2485	6.741(86)	13.80(16)	20.54(18)
T_4	4	7.3534	7.4479(77)	22.465(11)	29.913(13)
	6	7.5909	6.806(25)	15.711(41)	22.517(48)
	8	7.7723	6.585(29)	14.349(80)	20.934(85)
	10	7.9322	6.642(86)	14.13(17)	20.77(19)
T_5	4	7.0250	7.2931(77)	22.387(12)	29.680(14)
	6	7.2618	6.659(25)	15.716(41)	22.375(48)
	8	7.4424	6.433(29)	14.547(89)	20.980(94)
	10	7.6042	6.502(87)	13.89(19)	20.40(21)
T_6	4	6.7079	7.0626(77)	22.385(13)	29.447(15)
	6	6.9433	6.429(25)	15.865(48)	22.294(54)
	8	7.1254	6.192(29)	14.535(71)	20.726(77)
	10	7.2855	6.268(87)	14.35(19)	20.62(21)
T_7	4	6.3719	6.6319(77)	22.512(18)	29.144(20)
	6	6.6050	5.979(25)	16.184(54)	22.164(60)
	8	6.7915	5.725(30)	14.98(12)	20.70(12)
	10	6.9453	5.778(87)	14.72(16)	20.49(18)
T_8	6	6.2735	4.885(27)	17.034(68)	21.919(74)
	8	6.4680	4.637(31)	16.02(13)	20.65(13)
	10	6.6096	4.571(88)	15.51(19)	20.09(21)

Table 4.7: Results for the contributions s_∞ and χ to the entropy, and the total value s, at fixed lattice spacing.

of the bare data at given L_0/a and g_0^2 as follows,

$$s(L_0/a, g_0^2) \to s(L_0/a, g_0^2) \cdot \frac{s^{(0)} + g_0^2\, s^{(1)}}{s^{(0)}(a/L_0) + g_0^2\, s^{(1)}(a/L_0)}\,, \tag{4.44}$$

where at the denominator appears the 1-loop result on the lattice for the entropy density discussed in Section 4.6, see in particular Table 4.6, while at the numerator there is the entropy density at 1-loop in continuum perturbation theory [82]. We report here the two coefficients for reference:

$$s^{(0)}/T^3 = \frac{32\pi^2}{45} + \frac{7\pi^2}{15} N_f\,, \quad s^{(1)}/T^3 = -\frac{2}{3} - \frac{5}{18} N_f\,. \tag{4.45}$$

The 1-loop improvement subtracts cutoff effects up to order $\sim g^2$ at all orders in the lattice spacing. This means that the leading discretization effects are expected to be $\sim a^2 g^3$. The 1-loop improved data are represented in the top panel of Figure 4.5. In this plot points at different temperatures are shifted downward for better readability.

We extrapolated the results to the continuum limit using a global fit that parametrizes the temperature dependence of the discretization effects in terms of polynomials of a renormalized coupling. The natural choice in our setup is the non-perturbative Schrödinger functional coupling used to define the lines of constant physics. The general functional form we used for the extrapolations is

$$f(g, a/L_0) = p(g) + \left(\frac{a}{L_0}\right)^2 \left(p_{23}\, g^3 + p_{24}\, g^4\right) + \left(\frac{a}{L_0}\right)^3 \left(p_{33}\, g^3 + p_{34}\, g^4\right)\,, \tag{4.46}$$

where $p(g)$ is non-zero only at the values $g_i = \overline{g}_{\rm SF}(\sqrt{2}T_i)$ of the coupling listed in Table 4.1. These values represent the continuum limits at the temperatures $T_0, T_1, ..., T_8$, and for convenience we define them as $p_i \equiv p(g_i)$, $i = 0, ..., 8$. The coefficients p_{ij} instead parametrize the cutoff effects across all the temperatures.

We explored a variety of parameter combinations to assess the discretization effects and ensure that systematic uncertainties were well-controlled. At first sight, the data can be fitted with pure $(a/L_0)^2$ corrections, i.e. $p_{33} = p_{34} = 0$, with a good fit quality. However these fits are primarily influenced by the $L_0/a = 4$ data, which are significantly more accurate than data from finer lattices. This results in very small errors for the continuum limits p_i of the entropy (of the order of $\lesssim 0.1\%$). The high accuracy of the coarsest data arises from their intrinsically smaller variance compared to finer lattices, and the necessity of generating sufficiently long Monte Carlo histories for a sensible estimation of the errors.

To avoid being overly constrained by the coarsest lattice data, we considered fits in which the uncertainty for the $L_0/a = 4$ points was increased to the one of the $L_0/a = 6$ points. We utilized these modified fits as a consistency check for other extrapolations and to gain a better understanding of the cutoff effects. Inflating the error of the coarsest points increases the uncertainty of the fit parameters. For the simple $\sim (a/L_0)^2$ fits, a ~ 1 sigma effect can also be observed in the central values. To stabilize these fits, we

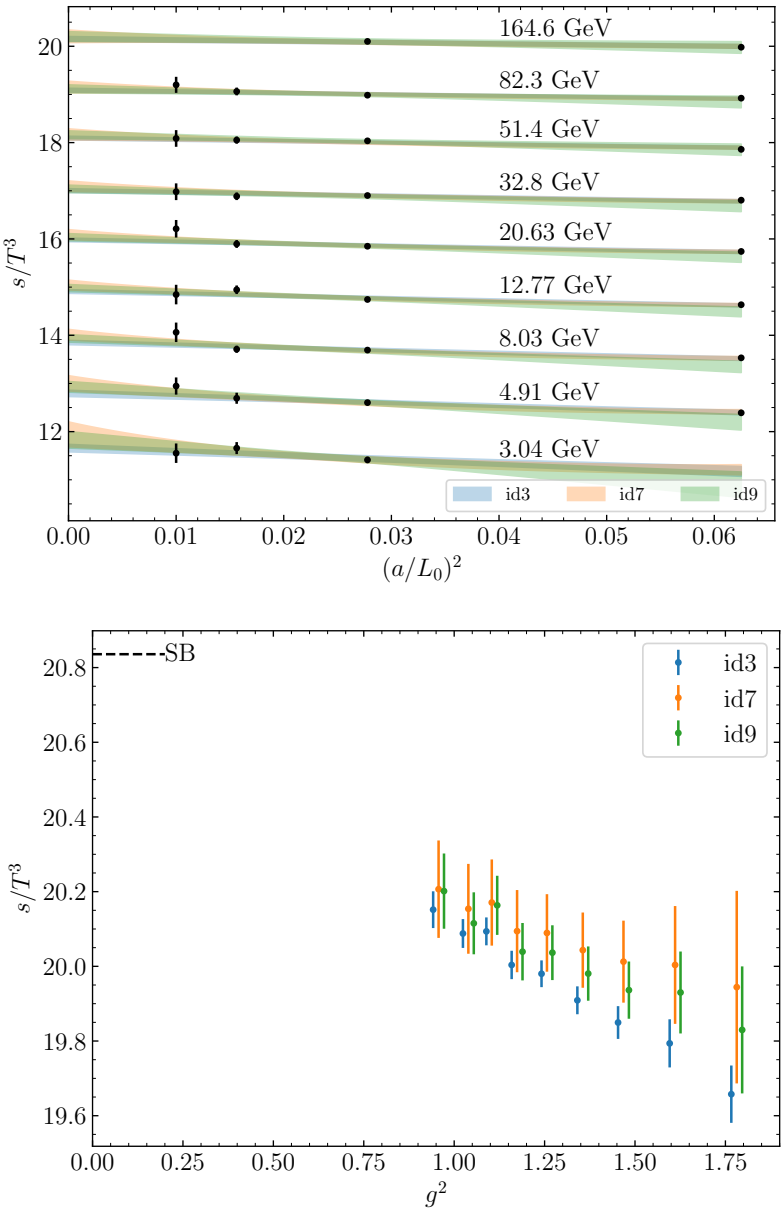

Figure 4.5: Top: plot of the 1-loop improved entropy density at fixed lattice spacing a/L_0 and for all the temperatures T_n, $n = 0, ..., 8$. The points at temperature T_n have been shifted downward by n for better readability. The three fits of Table 4.8 are shown as the shadowed bands. The fit id9 is performed with $L_0/a = 6, 8, 10$ data, but has been extended up to $(1/4)^2$. Bottom: Comparison of the entropy in the continuum limit extrapolated according to the three fits id3, id7 and id9. The entropy is plotted as a function of the $\overline{\text{MS}}$ coupling at 5-loop [11] computed at the renormalization scale $\mu = 2\pi T$. The points have been spaced horizontally by 0.015 for better readability.

T (GeV)		id3 4I	id7 4I	id9 (best fit) N4
164.6(5.6)	p_0	20.152(49)	20.21(13)	20.20(10)
82.3(2.8)	p_1	20.088(39)	20.15(12)	20.115(83)
51.4(1.7)	p_2	20.094(37)	20.17(12)	20.163(79)
32.8(1.0)	p_3	20.004(38)	20.09(11)	20.039(77)
20.63(63)	p_4	19.980(36)	20.09(10)	20.037(73)
12.77(37)	p_5	19.909(37)	20.04(10)	19.981(73)
8.03(22)	p_6	19.850(44)	20.01(11)	19.936(77)
4.91(13)	p_7	19.794(64)	20.00(16)	19.93(11)
3.040(78)	p_8	19.658(77)	19.94(26)	19.83(17)
	p_{23}	-1.7(40)	6(47)	1(14)
	p_{24}	-0.7(33)	-13(37)	-4(11)
	p_{33}		-29(155)	
	p_{34}		42(123)	
	χ^2/d.o.f	0.636	0.568	0.643

Table 4.8: Parameters of the selected representative fits shown in Figure 4.5. The parameters p_1–p_8 are the continuum limit extrapolations of the entropy for the temperatures T_0–T_8, at the temperatures reported in the first column. The coefficients $p_{23}, ..., p_{34}$ parametrize the cutoff effects of the continuum limit extrapolation. The label 4I indicates the dataset where the errors of $L_0/a = 4$ data have been enlarged to the ones of $L_0/a = 6$ data. The label N4 is for the dataset without $L_0/a = 4$ points.

added $\sim (a/L_0)^3$ corrections represented by the coefficients p_{33} and/or p_{34}. These fits are basically unaffected by the error inflation.

Given that fits including $L_0/a = 4$ points require $(a/L_0)^3$ terms for stability, we also attempted to extrapolate to the continuum using data with resolutions $L_0/a = 6, 8, 10$ and only quadratic terms in the fit function. These fits proved to be stable under variations of the powers of g, and those including both g^3 and g^4 were more conservative in the determination of the fit parameters.

A complete list of all combinations of fits considered can be found in Appendix F.10 From this investigation, we selected three fits as the most representative. The corresponding coefficients are reported in Table 4.8. The fits are labeled as id3, id7, and id9, and are classified based on the dataset used for the extrapolation. The dataset 4I includes all the data, with the uncertainty for the $L_0/a = 4$ data enlarged as discussed above. The N4 dataset excludes the $L_0/a = 4$ points. The quality of all fits is good, as indicated by the χ^2/dof values in the last row of the Table.

The three selected fits are displayed in the top panel of Figure 4.5. The comparison of the continuum extrapolated entropy density in these three cases can be seen in the bottom panel of the same Figure. The fits id3 and id7 represent the most aggressive and conservative ways, respectively, to incorporate all the available data. Notably, they

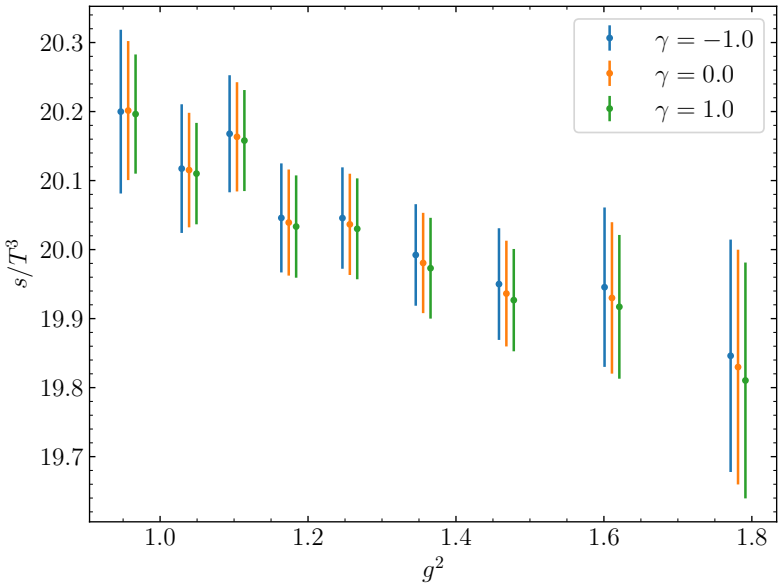

Figure 4.6: Stability of the best fit id9 under logarithmic corrections $\sim [\alpha(\pi/a)]^\gamma$ to the leading cutoff effects $\sim a^2$, for the three values of γ given in the legend.

exhibit a systematic ~ 1 sigma tension in their central values. Conversely, fit id9 does not include the (error-inflated) $L_0/a = 4$ points, rendering it insensitive to any systematics arising from these coarse data. The central values of its parameters interpolate between those of the id3 and id7 fits, with uncertainties sufficiently conservative to be compatible with both. The extrapolation at T_0 in fit id9 is particularly influenced by the other temperatures because one point only is considered. However, p_0 is perfectly compatible with the analogous parameter from fit id7, and this makes us confident in the statistical significance of this extrapolation.

Therefore we have selected id9 as the best fit. The related parameters p_0–p_8 listed in Table 4.8 provide the entropy density s/T^3 of QCD in the continuum limit at temperatures T_0–T_8. The values at temperatures T_0 through T_7 have an accuracy of approximately 0.4%, while the entropy at the lowest temperature T_8 shows a precision of around 0.8%. The covariance matrix of these fit parameters is reported in Table F.12.

In conclusion, we explicitly checked that no logarithmic corrections to the leading cutoff effects [80] can be seen within our statistical accuracy. To this aim, we modified the fit function for id9 to include an effective description of the logarithmic corrections by means of powers of the coupling evaluated at the cutoff scale π/a,

$$f(g, a/L_0) = p(g) + [\alpha(\pi/a)]^\gamma \left(\frac{a}{L_0}\right)^2 \left(p_{23}\, g^3 + p_{24}\, g^4\right) , \tag{4.47}$$

where $\alpha = g^2/(4\pi)$. The extrapolations turned out to be very stable under the variation of the (effective) anomalous dimension γ in the interval $[-1, 1]$. Figure 4.6 shows the comparison among the continuum extrapolations with $\gamma = -1, 0, 1$.

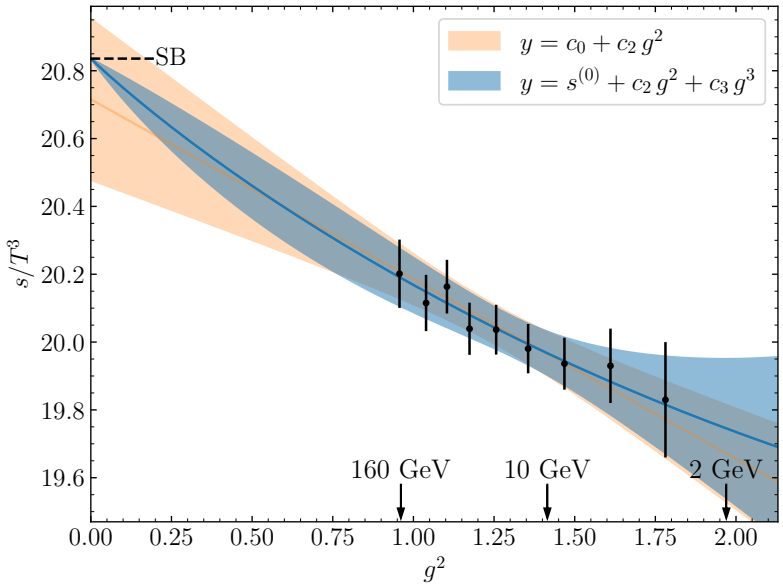

Figure 4.7: Continuum extrapolated entropy density as a function of the 5-loop $\overline{\text{MS}}$ coupling g^2. The bands are two different fit forms, the blue one being our final interpolation.

4.7.4 Parameterization of the entropy density

The last column of Table 4.8 contains our best estimation of the QCD entropy density in the continuum limit, at the different values of the temperature. These data are shown in Figure 4.7 as function of the 5-loop $\overline{\text{MS}}$ coupling g, evaluated at the scale $\mu = 2\pi T$. Notice that for our purposes this is only a convenient way to parametrize the temperature dependence the non-perturbative data, which makes comparison with perturbation theory easier. We chose to parametrize the continuum extrapolated results with a polynomial in the coupling g. The simplest choice is a straight line in the coupling squared, $s/T^3 = c_0 + c_2\, g^2$, where both the intercept and the slope are free parameters. We obtain the coefficients $c_0 = 20.72(24)$, $c_2 = -0.53(18)$, with $\chi^2/\text{d.o.f.} = 0.7$. Notably, the intercept is perfectly compatible with the Stefan-Boltzmann value $s^{(0)} = 20.836$. The parameter c_2 is not compatible with the 1-loop value, but this is somehow expected because it effectively includes the contributions from all the higher orders. This fit is shown in Figure 4.7 as the orange shadowed band. We have selected as final parameterization of the entropy density in the interval of temperatures covered by our data the following polynomial,

$$\begin{aligned} s/T^3 &= s^{(0)} + c_2\, g^2 + c_3\, g^3\,, \\ c_2 &= -0.95(47)\,, \quad c_3 = 0.28(40)\,, \end{aligned} \tag{4.48}$$

where the intercept is fixed to the Stefan-Boltzmann value while c_2, c_3 come from the fit ($\chi^2/\text{d.o.f.} = 0.7$). The covariance of the two coefficients is $c_{23} = -0.1873$. Notice that the slope c_2 is also compatible with the perturbative result $s^{(1)} = -1.5$, even though with a large error. This fit is shown in Figure 4.7 as the blue shadowed band.

4.8 Discussion of the results

We have tried to fit the numerical data using as a guideline the perturbative result for the entropy density from the thermal effective theory, equation (2.52). The slope quoted in eq. (4.48) is compatible with the 1-loop result. We fixed it to $s^{(1)}$ and fitted the data with two higher order terms, $c_3\, g^3$ and $c_4\, g^4$. Proceeding in this way, we progressively increased the order of the fit polynomial leaving the two highest order coefficients as free parameters, to be determined from the fit. All the lowest coefficients were set to the perturbative result. If the quality of the fit was good, and if the fit parameters were compatible with perturbation theory, we fixed them to the perturbative result and moved to the next order.

It turned out that the fit parameters are compatible within ~ 1 sigma with the perturbative coefficients. After constraining all the known perturbative expansion, we could finally fit from our data the unknown coefficient q_c encoding the non-perturbative contribution from the ultrasoft modes at $\mathrm{O}(g^6)$. We obtained the value $q_c = -2033(191)$, with a good fit quality ($\chi^2/\mathrm{d.o.f.} = 0.9$). This result is however expected to include contributions from higher orders in the coupling. We investigated the stability by fitting the data including a $\sim g^7$ correction. The fit ($\chi^2/\mathrm{d.o.f.} = 0.7$) returns $q_c = -4722(1864)$ and $c_7 = 0.25(17)$, so both with a $\sim 50\%$ uncertainty. The two fits deviate from each other at low temperatures, but in the interval of our numerical data and up to the Stefan-Boltzmann limit they appear to be in good agreement, see the top panel of Figure 4.8.

The fit with q_c as the only free parameter is also shown in the bottom panel of Figure 4.8, where it is extended to lower temperatures to compare with other lattice determinations of the entropy density from the literature [21, 13, 15]. Perturbation theory by its own is of little help in describing the temperature dependence of the entropy density, in particular in the temperature interval 3 GeV–160 GeV considered in this study. Conversely, the perturbative expansion constrained with our numerical data apparently reproduces the lattice results down to ~ 500 MeV. Notice however that at the highest temperature $T \simeq 160$ GeV the contribution to the interaction from the fitted g^6 term is still $\sim 30\%$ of the total.

As a check of consistency, we fitted our data together with the weighted average of the lattice results at $T = 400$ MeV using all the known perturbative expansion supplemented by the q_c term at g^6, and the higher order correction $c_7\, g^7$. This fit is the purple shadowed band in the bottom panel of Figure 4.8. The resulting coefficients are $q_c = -2606(583)$, $c_7 = 0.05(4)$ and $\chi^2/\mathrm{d.o.f.} = 0.82$. The additional point at low temperature forces the coefficient c_7 to vanish, while q_c remains compatible with the previous estimate within errors.

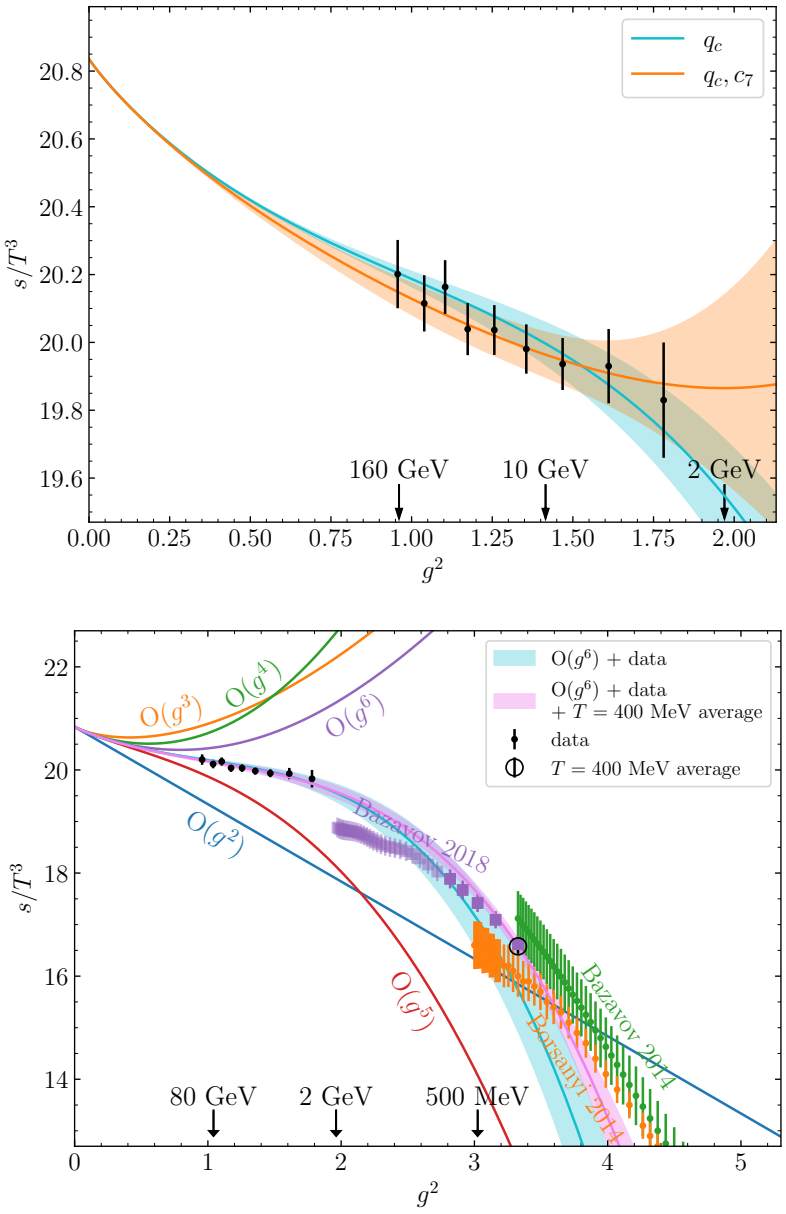

Figure 4.8: Top: entropy density in the continuum versus g^2. The light blue fit includes all the known perturbative orders, with q_c as free parameter at order $\sim g^6$. The same for the orange fit, with the additional free parameter p_7 at order $\sim g^7$. Bottom: comparison of our numerical data (black points) with the unconstrained perturbation theory and lattice results at lower temperatures from Refs. [21, 13, 15]. The light blue shadowed band represents the perturbative expansion with q_c fitted from our data. The purple shadowed band is the fit of the perturbative expansion with q_c and a $\sim g^7$ term. We included in this fit the weighted average of the points at $T = 400$ MeV.

Chapter 5

Thermal QCD and non-perturbative renormalization

The definition of QCD on the lattice requires the determination of renormalization constants of (composite) fields, such that their renormalized correlation functions approach the correct limit when extrapolated to the continuum. The renormalization of a bare operator depends on the ultraviolet properties of the operator itself, and it is not sensible to the infrared details of the theory (on the lattice, up to discretization effects). This allows us to define non-perturbative renormalization schemes in convenient lattice setups, possibly with reduced systematic effects and easy to simulate. A popular choice that is employed to this purpose is, for instance, the Schrödinger functional scheme [96, 108, 105].

In this thesis we explore the use of QCD at finite temperature with shifted and twisted (for quarks only) boundary conditions as a non-perturbative renormalization scheme for some lattice composite operators. This setup is a generalization of the one described in Section 2.2 to include an imaginary chemical potential. This renormalization scheme proved to be successful for the non-perturbative renormalization of the Energy-Momentum tensor in pure gauge theory [61]. We have applied this new strategy for the first time in full QCD for the non-perturbative renormalization of the flavour-singlet local vector current [22], as described in Section 5.2. The ultimate goal is to use thermal QCD with shifted and twisted boundary conditions for the non-perturbative renormalization of the EMT in lattice QCD, where the features of this framework can be exploited at their full potential [42]. In Section 5.3 we discuss the renormalization strategy for the EMT and show some preliminary non-perturbative results for the renormalization constants [23].

5.1 Shifted and twisted boundary conditions

In this Section we generalize the discussion of Section 2.2 to take into account an imaginary chemical potential. The partition function of thermal QCD in a moving frame and

with an imaginary chemical potential $\mu_{\mathcal{I}}$ reads [42]

$$\mathcal{Z}(L_0, \boldsymbol{\xi}, \mu_{\mathcal{I}}) = \mathrm{Tr}\left\{ e^{-L_0(\widehat{H} - i\boldsymbol{\xi}\cdot\widehat{\boldsymbol{P}} - i\mu_{\mathcal{I}}\widehat{N})} \right\} , \tag{5.1}$$

where L_0 is the size of the compact direction, $\boldsymbol{\xi} = (\xi_1, \xi_2, \xi_3)$ is the Euclidean boost and the operators $\widehat{H}$, $\widehat{\boldsymbol{P}}$ and $\widehat{N}$ are respectively the Hamiltonian of the system, the total momentum operator and the quark number operator. The trace is over the states of the Hilbert space. The partition function (5.1) is equivalent to a Euclidean path integral where fields satisfy shifted boundary conditions in the compact direction, supplemented by twisted boundary conditions for fermionic fields,

$$\begin{aligned} A_\mu(x_0 + L_0, \boldsymbol{x}) &= A_\mu(x_0, \boldsymbol{x} - L_0\boldsymbol{\xi}) , \\ \psi(x_0 + L_0, \boldsymbol{x}) &= -e^{i\theta_0}\psi(x_0, \boldsymbol{x} - L_0\boldsymbol{\xi}) , \\ \overline{\psi}(x_0 + L_0, \boldsymbol{x}) &= -e^{-i\theta_0}\overline{\psi}(x_0, \boldsymbol{x} - L_0\boldsymbol{\xi}) , \end{aligned} \tag{5.2}$$

where we defined the twist phase $\theta_0 = -L_0\mu_{\mathcal{I}}$. The results of Section 2.2 generalize straightforwardly in presence of a non-zero imaginary chemical potential. We define the free-energy density as

$$f(L_0, \boldsymbol{\xi}, \theta_0) = -\frac{1}{L_0 V} \ln \mathcal{Z}(L_0, \boldsymbol{\xi}, \theta_0) \tag{5.3}$$

where we explicitly indicate the dependence on L_0, $\boldsymbol{\xi}$ and θ_0. The free-energy density is even and periodic in θ_0, with period $2\pi/3$ [133], because of the interplay of the twist phase with the centre $\mathbb{Z}_3$ of the gauge group SU(3). The SO(4) invariance of the free-energy in the thermodynamic limit now reads

$$f(L_0, \boldsymbol{\xi}, \theta_0) = f(L_0/\gamma, \mathbf{0}, \theta_0) , \quad \gamma = 1/\sqrt{1 + \boldsymbol{\xi}^2} , \tag{5.4}$$

where the parameter θ_0 does not change because the conserved quark number is a Lorentz invariant quantity. The shift lowers the temperature from $1/L_0$ to $T = \gamma/L_0$ in the rest frame. The same holds for the chemical potential, which is $\gamma\mu_{\mathcal{I}}$ in the rest frame. We can now reformulate some of the Ward Identities we already derived in Section 2.2. The one-point function of the time-space component of the EMT is formally the same but for the θ_0-dependence,

$$\langle T_{0k} \rangle_{\boldsymbol{\xi}, \theta_0} = -\frac{\partial}{\partial \xi_k} f(L_0, \boldsymbol{\xi}, \theta_0) , \tag{5.5}$$

while the expression for the entropy in eq. (2.17) generalizes to

$$Ts = -\frac{1 + \boldsymbol{\xi}^2}{\xi_k} \langle T_{0k} \rangle_{\boldsymbol{\xi}, \theta_0} - i\mu_{\mathcal{I}} \langle V_0 \rangle_{\boldsymbol{\xi}, \theta_0} , \tag{5.6}$$

where $V_\mu = \overline{\psi}\gamma_\mu\psi$ is the flavour-singlet vector current. The θ_0-dependence of the free-energy is related to the expectation value of the temporal component of the vector current,

$$\langle V_0 \rangle_{\boldsymbol{\xi}, \theta_0} = -iL_0 \frac{\partial}{\partial \theta_0} f(L_0, \boldsymbol{\xi}, \theta_0) , \tag{5.7}$$

which is an odd function of θ_0. Combining equations (5.5) and (5.7) it can be shown that

$$\langle T_{0k}\rangle_{\boldsymbol{\xi},\theta_0^A} - \langle T_{0k}\rangle_{\boldsymbol{\xi},\theta_0^B} = \frac{i}{L_0}\int_{\theta_0^A}^{\theta_0^B} d\theta_0\, \frac{\partial}{\partial\xi_k}\langle V_0\rangle_{\boldsymbol{\xi},\theta_0}\,, \tag{5.8}$$

which gives the dependence of the one-point function $\langle T_{0k}\rangle_{\boldsymbol{\xi},\theta}$ on the parameter θ_0. Finally, the Ward Identity (2.18) becomes

$$\langle T_{0k}\rangle_{\boldsymbol{\xi},\theta_0} = \xi_k\left(\langle T_{00}\rangle_{\boldsymbol{\xi},\theta_0} - \langle T_{jj}\rangle_{\boldsymbol{\xi},\theta_0}\right)\,, \quad j\neq k\,, \xi_j = 0\,. \tag{5.9}$$

These Ward Identities will be crucial in the discussion of the non-perturbative renormalization of the Energy-Momentum tensor in lattice QCD.

5.2 Renormalization of the QCD flavour-singlet local vector current

We first applied thermal QCD with shifted and twisted boundary conditions to the non-perturbative determination of the renormalization constant for the lattice flavour-singlet local vector current, as described in the following.

5.2.1 Vector current in the continuum

In continuum QCD, the flavour-singlet vector current

$$V_\mu(x) = \overline{\psi}(x)\gamma_\mu\psi(x) \tag{5.10}$$

is the conserved current associated to the invariance of the theory under the $\mathrm{U}(1)_V$ subgroup of chiral symmetry. The bare flavour-singlet vector current coincides with its renormalized version as discussed in Section 1.6. If we consider QCD at finite temperature with shifted and twisted boundary conditions (5.2), this property becomes manifest through equation (5.7). Indeed the free-energy is a spectral quantity with an additive power-divergent term: its derivative in the twist parameter θ_0 is thus finite and renormalized once the bare parameters of the theory have been renormalized.

5.2.2 Vector current on the lattice

We consider for definiteness lattice QCD with $N_f = 3$ flavours of $\mathrm{O}(a)$-improved Wilson fermions, and Wilson plaquette action. The $\mathrm{U}(1)_V$ symmetry is respected by the lattice regularization, therefore at non-zero lattice spacing there exists a definition of the vector current that is conserved and coincides with its renormalized version (see also Section 3.5):

$$V_\mu^c(x) = \frac{1}{2}\left[\bar{\psi}(x+a\hat{\mu})U_\mu^\dagger(x)\,(\gamma_\mu+1)\,\psi(x) + \bar{\psi}(x)U_\mu(x)\,(\gamma_\mu-1)\,\psi(x+a\hat{\mu})\right]\,. \tag{5.11}$$

However, other discretizations of this current can also be considered like, for instance, the local vector current,

$$V_\mu^l(x) = \overline{\psi}(x)\gamma_\mu\psi(x)\,, \tag{5.12}$$

which closely resembles on the lattice the corresponding continuum expression. The use of the local vector current requires the computation of its finite renormalization constant $Z_V(g_0^2)$. On the other hand, the local vector current has the numerically appealing feature of involving only fields at a single lattice point. This often implies smaller statistical fluctuations of correlators where the vector current is inserted, and smaller lattice artifacts.

On the lattice, shifted and twisted boundary conditions for the fermionic fields have the analogous expression of the continuum case, eq. (5.2), while the conditions for the link field are obtained by replacing A_μ with U_μ, see also eq. (4.14). In the three spatial directions, each of size L, all the fields satisfy standard periodic boundary conditions. At finite temperature and in presence of twisted boundary conditions for the fermions, the one-point functions $\langle V_0^c \rangle_{\boldsymbol{\xi},\theta_0}$, $\langle V_0^l \rangle_{\boldsymbol{\xi},\theta_0}$ of the conserved and local currents do not vanish. Moreover they coincide with the one-point functions of the $\mathrm{O}(a)$-improved vector currents [17],

$$\hat{V}_\mu^{c,l}(x) = V_\mu^{c,l}(x) - \frac{a}{4}\, c_V^{c,l}\, (\partial_\nu + \partial_\nu^*) \left(\overline{\psi}(x)\, [\gamma_\mu, \gamma_\nu]\, \psi(x)\right) , \tag{5.13}$$

because the expectation value of the $\mathrm{O}(a)$ terms vanish due to translational invariance. These observations suggest to define the renormalization constant as

$$Z_V(g_0^2) = \lim_{a/L_0 \to 0} Z(g_0^2, a/L_0)\,, \quad Z(g_0^2, a/L_0) = \left. \frac{\langle V_0^c \rangle_{\boldsymbol{\xi},\theta_0}}{\langle V_0^l \rangle_{\boldsymbol{\xi},\theta_0}} \right|_{g_0^2, L_0/a} , \tag{5.14}$$

where the expectation values are in the thermodynamic limit. Notice that thanks to the spectral gap due to the finite temperature we can impose the renormalization condition at zero subtracted quark mass. In this definition the limit is taken at fixed bare coupling g_0^2, that is at fixed lattice spacing. Since in the continuum the vector current does not need any renormalization, the ratio of one-point functions depends on the twist phase θ_0 and on the shift $\boldsymbol{\xi}$ only by means of lattice artifacts which vanish when the $a/L_0 \to 0$ limit is taken. The residual $\mathrm{O}(a^2)$ discretization effects are part of the definition of the renormalization constant. They will be removed when taking the continuum limit of correlation functions with the renormalized flavour-singlet local vector current inserted.

5.2.3 Perturbative computation

As a first exploration of the strategy, we computed the renormalization constant Z_V in lattice perturbation theory at 1-loop. This computation is also instrumental for the 1-loop improvement of the lattice data. At fixed lattice spacing we expand Z_V as follows,

$$Z_V(g_0^2, a/L_0) = Z_V^{(0)}(a/L_0) \left[1 + \frac{N_c^2 - 1}{N_c}\, Z_V^{(1)}(a/L_0)\, g_0^2\right] + \mathrm{O}(g_0^4)\,, \tag{5.15}$$

where the tree-level $Z_V^{(0)}$ and 1-loop $Z_V^{(1)}$ coefficients, extrapolated to the infinite spatial volume limit, can be found in Appendix G.1. The tree-level value $Z_V^{(0)}(a/L_0)$ is

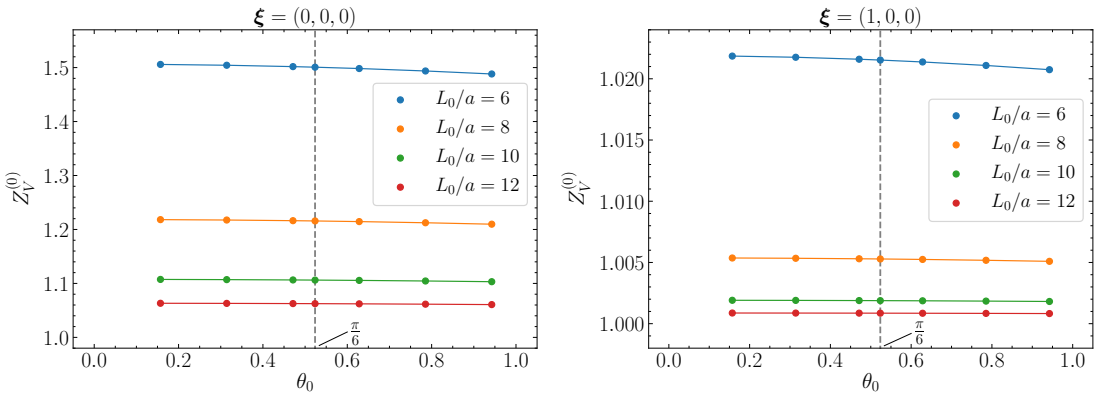

Figure 5.1: The lattice artifacts of the renormalization constant of the flavour-singlet local vector current at tree-level in perturbation theory as a function of θ_0. Values for various sizes L_0/a of the lattice in the temporal direction are shown: the left panel refers to the case of periodic boundary conditions (no shift) and the right one to shifted boundary conditions with shift $\boldsymbol{\xi} = (1,0,0)$.

shown in Figure 5.1 as a function of θ_0, for several values of a/L_0 and for the two shifts $\boldsymbol{\xi} = (0,0,0)$ (left panel) and $\boldsymbol{\xi} = (1,0,0)$ (right panel). When a/L_0 becomes smaller and smaller, $Z_V^{(0)}(a/L_0)$ approaches the asymptotic value of 1 quadratically in a/L_0. Discretization effects turn out to be more than one order of magnitude smaller for the shift $\boldsymbol{\xi} = (1,0,0)$ with respect to the case of standard periodic boundary conditions, a fact which is confirmed also at the next order in the perturbative expansion. For this reason we have chosen the shift $\boldsymbol{\xi} = (1,0,0)$ for carrying out the non-perturbative calculation. A similar reduction of lattice artifacts for $\boldsymbol{\xi} = (1,0,0)$ was observed in the computation of the entropy density in the SU(3) Yang-Mills theory [61, 62] and of the QCD mesonic screening masses [46]. The plots also show that the dependence of discretization effects on θ_0 is very mild. The free-energy density is even in θ_0, therefore the interval of non-trivial values is half of the period: $\theta_0 \in [0, \pi/3]$. For the non-perturbative computation we have chosen the value $\theta_0 = \pi/6$, in the middle of this interval.

5.2.4 Non-perturbative computation

For our choice $\boldsymbol{\xi} = (1,0,0)$ of the shift, in the continuum the expectation value of the vector current in the moving frame is related to the one in the rest frame by the SO(4) transformation

$$\begin{cases} \langle V_0 \rangle_{\boldsymbol{\xi},\theta_0} = \gamma \left(\langle V_0 \rangle_{\mathbf{0},\theta_0} - \langle V_1 \rangle_{\mathbf{0},\theta_0} \right) \\ \langle V_1 \rangle_{\boldsymbol{\xi},\theta_0} = \gamma \left(\langle V_1 \rangle_{\mathbf{0},\theta_0} + \langle V_0 \rangle_{\mathbf{0},\theta_0} \right) \end{cases} , \tag{5.16}$$

where the expectation value $\langle \cdot \rangle_{\mathbf{0},\theta_0}$ is computed in the rest frame. This suggests to combine the components $\mu = 0, 1$ of the vector currents on the lattice to effectively increase the statistics. Furthermore, by exploiting the perturbative result we can improve

$\beta = 6/g_0^2$	$L_0/a = 4$	$L_0/a = 6$	$L_0/a = 8$	$L_0/a = 10$
5.3000	0.8082(20)	0.761(7)	0.762(5)	0.761(7)
5.6500	0.8389(22)	0.787(6)	0.792(6)	0.784(7)
6.0433	0.8826(21)	0.820(5)	0.820(5)	0.803(7)
6.6096	0.9126(18)	0.842(5)	0.841(6)	0.839(6)
7.6042	0.9459(22)	0.871(5)	0.869(6)	0.871(6)
8.8727	0.9774(17)	0.898(6)	0.884(5)	0.890(6)
11.500	1.0078(18)	0.934(4)	0.917(5)	0.923(6)

Table 5.1: Values of the ratio of one-point functions in eq. (5.17), obtained from Monte Carlo simulations at $\theta_0 = \pi/6$ and shift $\boldsymbol{\xi} = (1, 0, 0)$ on lattices with size $(L_0/a) \times 96^3$.

at 1-loop our definition of Z_V so to mitigate cutoff effects. We thus replace $Z_V(g_0^2, a/L_0)$ of equation (5.14) with the new definition

$$\begin{aligned} Z_V(g_0^2, a/L_0) = & \frac{\langle V_0^c \rangle_{\boldsymbol{\xi},\theta_0} + \langle V_1^c \rangle_{\boldsymbol{\xi},\theta_0}}{\langle V_0^l \rangle_{\boldsymbol{\xi},\theta_0} + \langle V_1^l \rangle_{\boldsymbol{\xi},\theta_0}} \\ & + 1 + c_1 g_0^2 - Z_V^{(0)}(a/L_0) \left[1 + \frac{8}{3} Z_V^{(1)}(a/L_0)\, g_0^2 \right] , \end{aligned} \tag{5.17}$$

where the 1-loop coefficient c_1 is [52, 142]

$$c_1 = \frac{1}{12\pi^2} \Big[-20.617798655(6) + 4.745564682(3)\ c_{\rm sw} + 0.543168028(5)\ c_{\rm sw}^2 \Big] , \tag{5.18}$$

and the improvement coefficient is $c_{\rm sw} = 1 + 0.26590(7) g_0^2$ [95]. We computed non-perturbatively the ratio of vector currents in equation (5.17) from lattice QCD simulations at the 7 values of the inverse bare coupling squared $\beta = 6/g_0^2$ given in Table 5.1. Details on the algorithm used can be found in Appendix G.3. For the determination of the critical hopping parameter we refer to Appendix B of Ref. [46]. For each value of β, we simulate the 4 lattice resolutions $L_0/a = 4, 6, 8, 10$ with a statistics of 100 measurements at $L_0/a = 4, 6$, 400 measurements at $L_0/a = 8$, and 1000 measurements for $L_0/a = 10$. The spatial sizes of the lattice are fixed to $L/a = 96$. Our observables exhibit autocorrelation times always less than 2 trajectories, and they are taken into account by a proper binning of the data. We explicitly checked finite volume effects by performing simulations at some selected bare parameters on lattices with spatial size 288^3, and as expected no effects were found within our statistical accuracy. Table 5.1 reports the raw results from lattice simulations of the ratio of vector currents in eq. (5.17).

The left plot in Figure 5.2 shows the 1-loop improved numerical results at all the considered values of β, as functions of $(a/L_0)^2$. In the $a/L_0 \to 0$ limit we can parametrize the lattice artifacts of Z_V as follows,

$$\begin{aligned} Z_V(g_0^2, a/L_0) = & Z_V(g_0^2) + C_1 \cdot (a/L_0)^2 \\ & + C_2 \cdot (a\Lambda_{\rm QCD}) \cdot (a/L_0) + C_3 \cdot (a\Lambda_{\rm QCD})^2 + \ \ldots , \end{aligned} \tag{5.19}$$

$\beta = 6/g_0^2$	$Z_V(g_0^2)$
5.3000	0.768(7)
5.6500	0.794(7)
6.0433	0.809(7)
6.6096	0.833(7)
7.6042	0.864(7)
8.8727	0.878(7)
11.500	0.918(6)

Table 5.2: Values of $Z_V(g_0^2)$ obtained by extrapolating to $a/L_0 \to 0$ the perturbatively improved definition in eq. (5.17) for the data in Table 5.1.

where we expect the leading power to be $\sim a^2$ because of O(a) improvement, and the dots stand for higher order terms in the lattice spacing. The term C_2 is present and separate from others because we are not taking a continuum limit. However, $a\Lambda_{\rm QCD}$ is a small factor at the values of β considered. The $(a\Lambda_{\rm QCD})^2$ term is part of the definition of Z_V, and vanishes quadratically in the lattice spacing when a renormalized correlator involving the flavour-singlet vector current is extrapolated to the continuum limit.

We performed two extrapolations to the $a/L_0 \to 0$ limit, considering first both the C_1, C_2 terms of equation (5.19), and then the C_1 term only. The extrapolated values are compatible, and this confirms that the residual linear dependence in a/L_0 in equation (5.19) is negligible for all the values of $\beta = 6/g_0^2$ we considered. To be conservative, we average the two extrapolations at each β, and we take the largest error as the final uncertainty. The errors we obtain are less than 1% and are fully dominated by statistics. The extrapolated numbers at fixed β are reported in Table 5.2, and plotted in the right panel of Figure 5.2 where they are compared to the perturbative prediction for the renormalization constant up to 2 loops [142]. The final result of this study is the polynomial interpolation

$$Z_V^{\rm fit}(g_0^2) = 1 - c_1\, g_0^2 - c_2\, g_0^4 + c_3\, g_0^6 \tag{5.20}$$

where we enforce the value of the coefficients c_1 and c_2 to be the 1-loop and 2-loop results [52, 142], while the coefficient of the additional g_0^6 term is fitted to describe the mild bending of the data at larger values of the bare coupling. As a result

$$\begin{aligned} c_1 &= -0.1294299254732376\,, \\ c_2 &= -0.04683170849543621\,, \\ c_3 &= -0.016(3)\,, \end{aligned} \tag{5.21}$$

with c_1 from eq. (5.18) by inserting $c_{\rm sw} = 1$, c_2 from [142], and c_3 from the fit (χ^2/d.o.f. = 0.31). The fit is shown as the red shadowed band in the right panel of Figure 5.2.

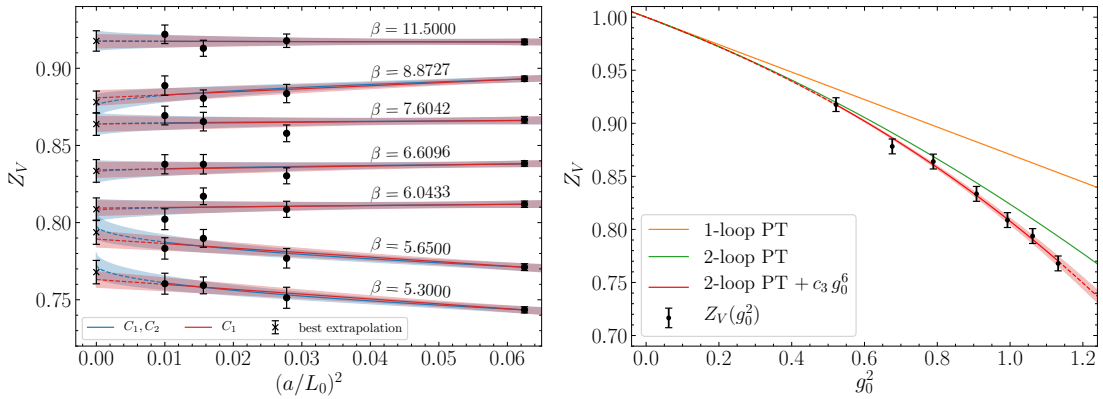

Figure 5.2: Left: Linear (blue) and quadratic (red) extrapolations to $a/L_0 \to 0$ of the perturbatively improved renormalization constant $Z_V(g_0^2)$ at the 7 values of the bare coupling considered in this study. The shaded bands correspond to one standard deviation confidence limit. Right: Comparison between the non-perturbative calculation of $Z_V(g_0^2)$ (black symbols), the 1-loop (orange line), and the 2-loop (green line) perturbative results. The red line is a fit of the numerical data where we enforce the 2-loop result and determine the coefficient of the g_0^6 term.

5.3 Renormalization of the Energy-Momentum tensor in lattice QCD

In the study of the QCD thermodynamics, a central role is played by the Energy-Momentum tensor (EMT) of QCD. Its correlation functions encode many physical properties of QCD at finite temperature, see Ref. [114] for a recent review. For instance, the one-point function in a shifted frame is related to the entropy density, see eq. (2.17). These quantities can be computed from first principles on the lattice once the discretized EMT has been properly renormalized. In the following we discuss a numerical strategy to determine the renormalization constants of the EMT non-perturbatively, based on considering QCD with shifted and twisted boundary conditions [61, 132]. As part of the original contribution of this thesis we will also show some preliminary numerical results, which bode well for the feasibility of the full computation.

5.3.1 The Energy-Momentum tensor in the continuum

We consider the symmetric and gauge-invariant definition of the QCD EMT $T_{\mu\nu}$ [92, 33], see also Appendix B for the notation. In the continuum the EMT splits into a singlet and a 9-dimensional representation of the SO(4) group. Under renormalization, the singlet component mixes with the identity operator, while there are no other fields of mass dimension ≤ 4 which may mix with the non-singlet representation. Moreover, the bare and renormalized non-singlet EMT components coincide because the latter is related to a conserved current associated to the invariance of the theory under the group of spacetime

translations. This property becomes manifest if we formulate QCD at finite temperature with shifted and twisted boundary conditions in the compact direction for the fields, see equation (5.2). The spacetime components of the EMT satisfy the identity [42]

$$\langle T_{0k} \rangle_{\boldsymbol{\xi},\theta_0} = -\frac{\partial f_{\boldsymbol{\xi},\theta_0}}{\partial \xi_k} \,, \tag{5.22}$$

where $f_{\boldsymbol{\xi},\theta_0}$ is a shorthand notation for the free-energy (5.3) where only the shift $\boldsymbol{\xi}$ and twist θ_0 dependence are explicit. The free-energy density is a spectral quantity with an additive power-divergent term. Its derivative with respect to the shift is thus finite, once the bare parameters of the theory have been renormalized. Therefore T_{0k} and all the other non-singlet components of the EMT are finite too. For later convenience we introduce the definition

$$\mathcal{V}_{0,k}^{AB} = -\frac{i}{L_0} \int_{\theta_0^A}^{\theta_0^B} d\theta_0 \, \frac{\partial}{\partial \xi_k} \langle V_0 \rangle_{\boldsymbol{\xi},\theta_0} \,, \tag{5.23}$$

where V_μ is the flavour-singlet vector current and L_0 is the size of the compact direction. In combination with eq. (5.8), this leads to

$$\mathcal{V}_{0,k}^{AB} = \langle T_{0k} \rangle_{\boldsymbol{\xi},\theta_0^B} - \langle T_{0k} \rangle_{\boldsymbol{\xi},\theta_0^A} \,, \tag{5.24}$$

a relation that turns out to be convenient to exploit on the lattice.

5.3.2 Renormalization of the Energy-Momentum tensor on the lattice

The lattice regularization breaks the SO(4) symmetry down to its discrete hypercubic subgroup SW_4. The non-singlet EMT components split into the sextet and triplet representations of this discrete group [33]. These two representations renormalize separately, and no other lattice field is involved in their renormalization. Since only discrete spacetime translations are allowed, the bare non-singlet EMT is not a conserved current. As a consequence, the fields in each representation require a finite renormalization whose Z-factors depend only on the bare coupling g_0^2. We focus on the non-perturbative definition of the sextet and triplet representations of the lattice EMT, which follow the renormalization pattern

$$T_{\mu\nu}^{R,\{i\}} = Z_G^{\{i\}} T_{\mu\nu}^{G,\{i\}} + Z_F^{\{i\}} T_{\mu\nu}^{F,\{i\}}, \quad i = 3, 6 \,, \tag{5.25}$$

where $T_{\mu\nu}^{G,\{i\}}$ and $T_{\mu\nu}^{F,\{i\}}$ are the dimension-4 gauge-invariant lattice operators in the i-dimensional representation of the hypercubic group [33, 42], see Appendix B. We will fix the renormalization constants by imposing that the lattice fields (5.25) satisfy a set of Ward Identities which are satisfied by the EMT in the continuum, up to cutoff effects (see also Section 3.5).

We consider on the lattice the shifted and twisted setup introduced in Sections 5.1 and 5.2. Using the definition (5.25) together with equation (5.22) at two values of the

twist phase, θ_0^A and θ_0^B, and exploiting equation (5.24), we can write our master formula for the computation of the renormalization constants of the sextet representation:

$$\begin{pmatrix} \langle T_{0k}^{G,\{6\}} \rangle_{\boldsymbol{\xi},\theta_0^A} & \langle T_{0k}^{F,\{6\}} \rangle_{\boldsymbol{\xi},\theta_0^A} \\ \\ \langle T_{0k}^{G,\{6\}} \rangle_{\boldsymbol{\xi},\theta_0^B} & \langle T_{0k}^{F,\{6\}} \rangle_{\boldsymbol{\xi},\theta_0^B} \end{pmatrix} \begin{pmatrix} Z_G^{\{6\}} \\ \\ Z_F^{\{6\}} \end{pmatrix} = \begin{pmatrix} -\dfrac{\Delta f_{\boldsymbol{\xi},\theta_0^A}}{\Delta \xi_k} \\ \\ -\dfrac{\Delta f_{\boldsymbol{\xi},\theta_0^A}}{\Delta \xi_k} + \mathcal{V}_{0,k}^{AB} \end{pmatrix} + \mathrm{O}(a^2) \,. \tag{5.26}$$

The partial derivative in the shift has been replaced by finite differences up to discretization effects and it is give in eq. (4.17). Then, the lattice counterpart of the Ward Identity (5.9)

$$\langle T_{0k}^{R,\{6\}} \rangle_{\boldsymbol{\xi},\theta_0} = \xi_k \langle T_{0j}^{R,\{3\}} \rangle_{\boldsymbol{\xi},\theta_0} \quad (j \neq k, \xi_j = 0) \tag{5.27}$$

gives access to the renormalization constants of the triplet representation. In full analogy to the case of Z_V, see equation (5.19), by dimensional arguments the leading lattice artifacts of the renormalization constants for $a \to 0$ are

$$Z\left(g_0^2, aT\right) = Z(g_0^2) + C_1 \cdot (aT)^2 + C_2 \cdot (a\Lambda_{\mathrm{QCD}})aT + C_3 \cdot (a\Lambda_{\mathrm{QCD}})^2 + \ \ldots \,. \tag{5.28}$$

In this equation, Z is a shorthand notation for any of the Z-factors in eq. (5.25), and $T = 1/(L_0\sqrt{1+\boldsymbol{\xi}^2})$ is the temperature of the thermal system. We include a $T \to 0$ limit at fixed g_0^2 in the definition of the renormalization constants, so that the leading discretization effects C_1, C_2 are suppressed. All the residual lattice artifacts will disappear when a renormalized correlator of the lattice EMT will be extrapolated to the continuum limit.

5.3.3 Renormalization strategy at work

In the following we give some details on the lattice determination of the quantities appearing in the master equation (5.26). Although the strategy is general, we choose the Wilson formulation of lattice QCD with $N_f = 3$ flavours of massless O(a)-improved Wilson fermions. The derivative in the shift of the free-energy density appearing in equation (5.26) can be computed, at fixed g_0^2 and L_0/a, following the procedure extensively discussed in Chapter 4 and in Appendix F in the context of the non-perturbative determination of the QCD entropy density at high temperature. The result we obtained is reported in Table 5.3, and has an accuracy of few permille. We thus focus on the lattice computation of the integral $\mathcal{V}_{0,k}^{AB}$ and of the bare matrix elements of the EMT. For this exploratory computation of the renormalization constants we generated ensembles on 6×96^3 lattices, at inverse bare coupling squared $\beta = 6/g_0^2 = 8.8727$ and shift $\boldsymbol{\xi} = (1,0,0)$. This setup is analogous to the one adopted for the computation of the QCD EoS, and we refer to Chapter 4 for any unexplained detail.

$\frac{1}{T^4}\frac{\Delta f_{\boldsymbol{\xi},\theta_0^A}}{\Delta\xi_1}$	$\mathcal{V}_{0,k}^{AB}/T^4$
-11.381(24)	2.9286(71)

Table 5.3: Numerical results for the shift-derivative of the free-energy density and the θ_0-integral defined in equation (5.29). The lattice parameters are given in Subsection 5.3.3.

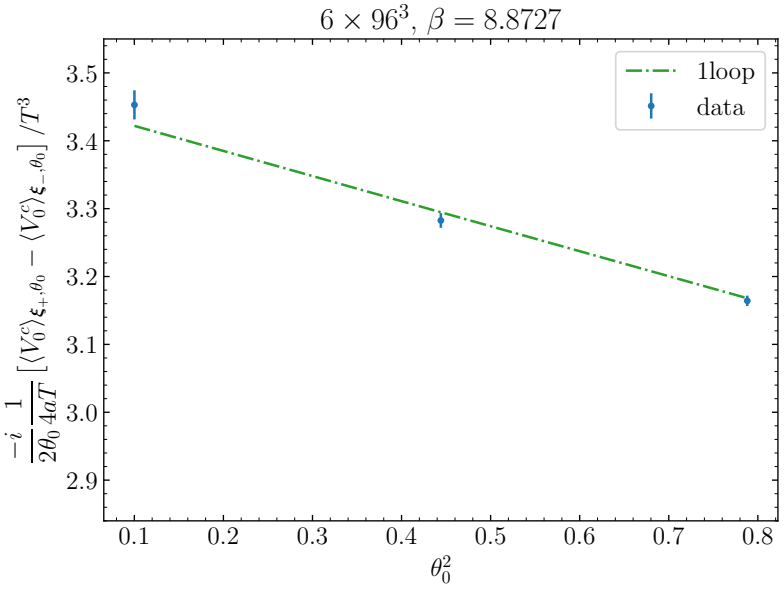

Figure 5.3: Integrand function of eq. (5.29) sampled at the values of the twist phase θ_0 prescribed by the Gauss quadrature. For comparison, the 1-loop result in lattice perturbation theory is shown.

5.3.4 Integral in the twist phase

On the lattice, the integral $\mathcal{V}_{0,1}^{AB}$ in equation (5.26) can be written as

$$\mathcal{V}_{0,1}^{AB} = -\frac{i}{L_0}\int_{\theta_0^A}^{\theta_0^B} d\theta_0 \, \frac{\Delta}{\Delta\xi_1}\langle V_0^R\rangle_{\boldsymbol{\xi},\theta_0} = -\frac{i}{L_0}\int_{(\theta_0^A)^2}^{(\theta_0^B)^2} d\theta_0^2 \, \frac{1}{2\theta_0}\frac{\Delta}{\Delta\xi_1}\langle V_0^R\rangle_{\boldsymbol{\xi},\theta_0} \,, \tag{5.29}$$

where the discrete derivative in the shift of the one-point function of the vector current reads

$$\frac{\Delta}{\Delta\xi_1}\langle V_0^R\rangle_{\boldsymbol{\xi},\theta_0} = \frac{L_0}{4a}\left(\langle V_0^R\rangle_{\boldsymbol{\xi}_+,\theta_0} - \langle V_0^R\rangle_{\boldsymbol{\xi}_-,\theta_0}\right) . \tag{5.30}$$

The derivatives are taken in direction $k = 1$ with a 2-point symmetric discretization, at the shifts $\boldsymbol{\xi}_\pm = (1 \pm 2a/L_0, 0, 0)$, see also Section 4.3. In place of V_0^R we may use the conserved current V_0^c, or the renormalized local current $Z_V V_0^l$. For this study, we choose the former. At fixed lattice spacing we estimate the integral with a 3-point Gauss quadrature, after performing a change of variable from θ_0 to θ_0^2. The change of variable is convenient because the integrand function is odd in θ_0, meaning that a polynomial representation of it, like the Gauss quadrature, would contain odd powers of θ_0 only. With the change to θ_0^2 we effectively halve the degree of the polynomial, so that with a 3-point quadrature we obtain the same accuracy that we would get with a 6-point quadrature of the original integral. The periodicity and symmetry properties of the free-energy in θ_0 suggest to choose the values $\theta_0^A = 0$ and $\theta_0^B = 3\pi/10$. These values cover the most of the allowed interval $[0, \pi/3]$ and thus maximize the signal on $\mathcal{V}_{0,1}^{AB}$. This results in better precision because the statistical error of $\langle V_0\rangle$ is mostly independent from θ_0. At given g_0 and L_0/a, the numerical estimation requires to simulate lattices at the 3 values of θ_0 prescribed by the Gauss quadrature and at the two shifts for the discrete derivative (6 independent simulations in total). Details on the algorithm employed for the simulations can be found in Appendix G.3. Figure 5.3 shows the numerically determined integrand function, compared with its 1-loop result at finite L_0/a. The resulting value of the integral is reported in Table 5.3, and its accuracy is of the order of a few permille.

5.3.5 1-point functions of the bare EMT

The 1-point functions of the bare EMT appearing in the matrix on the left-hand side of equation (5.26) are computed as they stand from numerical simulations. Table 5.4 shows some preliminary numerical results at the chosen bare parameters for this exploratory study. Data at $\theta_0 = 0$ come from ensembles with $L/a = 288$ while data at $\theta_0 = 3\pi/10$ from ensembles with $L/a = 96$. The 1-point functions are averaged over the volume, and the number of measurements is tuned so as to reach a comparable statistical precision in the two ensembles. The relative error on the $\langle T^F\rangle$ components is a few permille, while on the $\langle T^G\rangle$ components is about 1%. Finite volume effects are exponentially suppressed with the mass of the lightest screening state [59], which is proportional to the temperature. Considering the results of Appendix F.12, we expect that finite volume effects are negligible within the accuracy of this explorative study.

$\theta_0^A = 0$			$\theta_0^B = 3\pi/10$		
$\langle T_{01}^{F,\{6\}} \rangle / T^4$	-6.343(15)	0.24%	$\langle T_{01}^{F,\{6\}} \rangle / T^4$	-4.0535(88)	0.22%
$\langle T_{01}^{G,\{6\}} \rangle / T^4$	-2.822(22)	0.78%	$\langle T_{01}^{G,\{6\}} \rangle / T^4$	-2.677(34)	1.26%
$\langle T_{02}^{F,\{3\}} \rangle / T^4$	-6.846(12)	0.17%	$\langle T_{02}^{F,\{3\}} \rangle / T^4$	-4.375(16)	0.36%
$\langle T_{02}^{G,\{3\}} \rangle / T^4$	-3.130(44)	1.39%	$\langle T_{02}^{G,\{3\}} \rangle / T^4$	-2.862(54)	1.88%
$L/a = 288$, $n_{\mathrm{trj}} = 100$			$L/a = 96$, $n_{\mathrm{trj}} = 2000$		

Table 5.4: Preliminary results for the 1-point functions of the sextet and triplet bare EMT. The bare parameters are $L_0/a = 6$, $\beta = 8.8727$.

	Sextet ($i = 6$)	Triplet ($i = 3$)
$Z_G^{\{i\}}$	1.349(61)	1.37(10)
$Z_F^{\{i\}}$	1.194(29)	1.037(51)

Table 5.5: Preliminary results for the renormalization constants, computed at $\beta = 8.8727$.

5.3.6 Renormalization constants

Using in equation (5.26) the results described so far, we obtain a first estimation of the renormalization constants of the sextet components of the EMT. Then, equation (5.27) leads to the renormalization constants of the triplet components. The resulting preliminary values can be found in Table 5.5. The accuracy on the renormalization constants ranges between 2% and 7%, and the error is largely dominated by the one of the 1-point functions $\langle T^G \rangle$, see Figure 5.4. The reason can be traced back to the fact that the solution of the master equation (5.26) requires differences like $\langle T^G \rangle_{\boldsymbol{\xi},\theta_0^B} - \langle T^G \rangle_{\boldsymbol{\xi},\theta_0^A}$, see also Appendix G.2. These 1-point functions are weakly dependent on θ_0, therefore the signal mostly cancels while the errors, which are basically independent from the value of θ_0, sum in quadrature. This is expected because the twist phase is a sea quark effect for gluonic observables. Within this precision, the contributions to the variance coming from the integral in the mass and the integral in the twist phase are completely subdominant.

5.3.7 Outlook

We plan to extend the computation of the renormalization constants of the EMT for several values of bare coupling and L_0/a in order to perform the extrapolation in eq. (5.28) with confidence at each chosen value of g_0^2. This will allow us, in particular, to provide a functional dependence of the renormalization constants with respect to the bare coupling, as we did for Z_V in Section 5.2. To assess the feasibility of the calculation we have to take into account the scaling with L_0/a of the statistical error of the one-point functions of the vector current and of the tensor. However, these encouraging preliminary results suggest that a final accuracy of a few percent or better may be achievable. In conclusion,

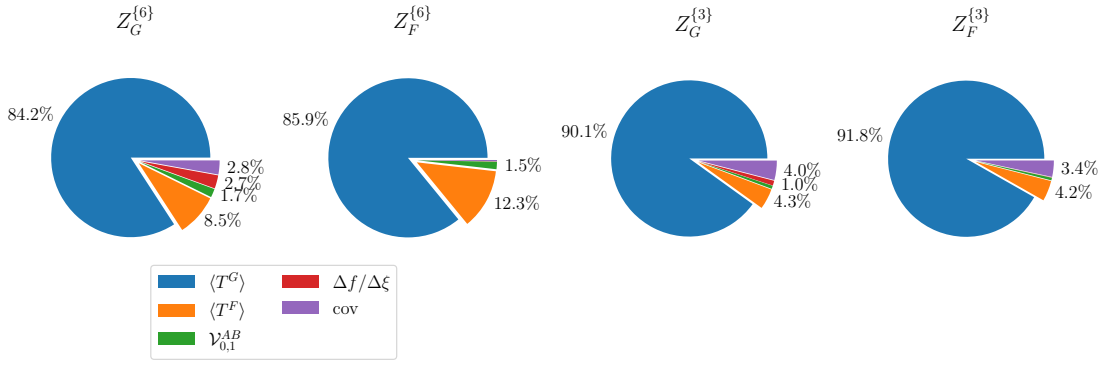

Figure 5.4: Breakdown of the contributions to the variance of the renormalization constants.

we notice that our program for the renormalization of the EMT of QCD is in large overlap with the determination of the QCD Equation of State. Actually the renormalized sextet component of the EMT is directly related to the entropy of QCD, see for instance equation (5.5) at zero imaginary chemical potential.

Conclusions

The thermodynamic properties of strongly interacting particles are of fundamental interest for describing many phenomena, from particle physics to cosmology. The Equation of State (EoS) of QCD is a key quantity with direct impact, for instance, in the analysis of data from heavy-ion collision experiments [2, 71], as well as in understanding the physics of the Early Universe. In the latter case, the EoS is needed up to temperatures of the order of the electro-weak scale. The advent of gravitational wave astronomy, along with advancements in precision Dark Matter searches at colliders, opened a new era for cosmology that demands increasingly accurate predictions from theoretical physics [136, 135]. This is especially true for the EoS of QCD, for which non-perturbative lattice calculations are available in the literature only up to temperatures of 1–2 GeV [21, 13, 15].

The main original result of this thesis is the first non-perturbative calculation on the lattice of the EoS at 9 temperature values covering the range from 3 GeV to 160 GeV. This result was obtained by employing a completely new strategy that allowed us to simulate QCD at very high temperatures. At every temperature, the entropy density has been computed at several lattice spacings to achieve solid continuum extrapolations, which have accuracies of the order of 1% or better. The computation has been carried out considering $N_f = 3$ massless flavours of O(a)-improved Wilson fermions, but our method is fully general and can be applied without further conceptual difficulties to QCD with five (massive) flavours.

The continuum results for the entropy exhibit a linear behaviour in the strong coupling constant squared, pointing straight to the Stefan-Boltzmann limit. Despite the very high temperature, this behaviour is not captured by perturbation theory [82] alone. This observation confirms a trend noted for the EoS of the pure SU(3) Yang-Mills theory [62], and more recently observed for the screening spectrum of thermal QCD [46, 64]. When the known perturbative series, supplemented by effective higher order interactions, is constrained with the numerical results, some agreement is observed also at lower temperatures down to $\sim$ 500 MeV, where results to compare with are available from the literature.

The second main contribution of this thesis is the exploration of the use of thermal QCD with shifted and twisted boundary conditions for the non-perturbative renormalization of composite operators. We discussed the renormalization of the flavour-singlet local vector current [22], which was the first application in lattice QCD of this renor-

malization framework. We also presented preliminary non-perturbative results for the renormalization constants of the lattice Energy-Momentum tensor. The renormalization constants of the non-singlet components have been determined for one value of the lattice spacing with a precision of a few percent at a moderate computational effort. Being a notoriously challenging renormalization problem, these results are very promising for a more extensive and precise determination.

Appendix A

Notation and conventions

A.1 SU(N_c) conventions

The special unitary group SU(N_c) is the Lie group of unitary $N_c \times N_c$ matrices with unit determinant. Its generators $T_a \in \mathfrak{su}(N_c)$, $a = 1, ..., N_c^2 - 1$ are hermitian traceless matrices chosen to satisfy the normalization condition

$$\mathrm{tr}\,\{T_a T_b\} = \frac{1}{2}\delta_{ab}\,. \tag{A.1}$$

Their commutation and anti-commutation relations read

$$[T_a, T_b] = i f_{abc} T_c\,, \quad \{T_a, T_b\} = \frac{1}{N_c}\mathbb{1}_{N_c}\delta_{ab} + d_{abc}T_c \tag{A.2}$$

where the structure constants f_{abc} are completely anti-symmetric, while d_{abc} is completely symmetric. In the physical case $N_c = 3$, that is the one in interest in this thesis, The generators can be represented as $T_a = \lambda_a/2$, $a = 1, ..., 8$ where the matrices λ_a are the 3×3 Gell-Mann matrices.

A.2 Dirac matrices

In 4-dimensional Euclidean space and in chiral representation, the Dirac matrices are given by

$$\gamma_0 = \begin{pmatrix} 0 & -\mathbb{1}_2 \\ -\mathbb{1}_2 & 0 \end{pmatrix}\,, \quad \gamma_k = \begin{pmatrix} 0 & -i\sigma_k \\ i\sigma_k & 0 \end{pmatrix}\,, \quad k = 1, 2, 3\,, \tag{A.3}$$

where σ_1, σ_2, σ_3 are the Pauli matrices. The γ-matrices are hermitian, $\gamma_\mu^\dagger = \gamma_\mu$, and satisfy the anti-commutation relation

$$\{\gamma_\mu, \gamma_\nu\} = 2\delta_{\mu\nu}\,\mathbb{1}_4\,. \tag{A.4}$$

We define the fifth matrix $\gamma_5 = \gamma_0\gamma_1\gamma_2\gamma_3$, with the properties

$$\gamma_5^\dagger = \gamma_5\,, \quad \gamma_5^2 = \mathbb{1}_4\,, \quad \{\gamma_\mu, \gamma_5\} = 0\,. \tag{A.5}$$

The trace of the product of an odd number of γ-matrices vanishes. Useful identities are

$$\mathrm{tr}\left\{\gamma_\mu\gamma_\nu\right\} = 4\delta_{\mu\nu}\,, \tag{A.6}$$

$$\mathrm{tr}\left\{\gamma_\mu\gamma_\nu\gamma_\rho\gamma_\sigma\right\} = 4\left(\delta_{\mu\nu}\delta_{\rho\sigma} - \delta_{\mu\rho}\delta_{\nu\sigma} + \delta_{\mu\sigma}\delta_{\nu\rho}\right)\,, \tag{A.7}$$

$$\begin{aligned}\mathrm{tr}\{\gamma_{\mu_1}\gamma_{\mu_2}\gamma_{\mu_3}\gamma_{\mu_4}\gamma_{\mu_5}\gamma_{\mu_6}\} &= \delta_{\mu_1\mu_2}\mathrm{tr}\left\{\gamma_{\mu_3}\gamma_{\mu_4}\gamma_{\mu_5}\gamma_{\mu_6}\right\} \\ &- \delta_{\mu_1\mu_3}\mathrm{tr}\left\{\gamma_{\mu_2}\gamma_{\mu_4}\gamma_{\mu_5}\gamma_{\mu_6}\right\} + \delta_{\mu_1\mu_4}\mathrm{tr}\left\{\gamma_{\mu_2}\gamma_{\mu_3}\gamma_{\mu_5}\gamma_{\mu_6}\right\} \\ &- \delta_{\mu_1\mu_5}\mathrm{tr}\left\{\gamma_{\mu_2}\gamma_{\mu_3}\gamma_{\mu_4}\gamma_{\mu_6}\right\} + \delta_{\mu_1\mu_6}\mathrm{tr}\left\{\gamma_{\mu_2}\gamma_{\mu_3}\gamma_{\mu_4}\gamma_{\mu_5}\right\}\,.\end{aligned} \tag{A.8}$$

We also introduce the hermitian matrices

$$\sigma_{\mu\nu} = \frac{i}{2}[\gamma_\mu, \gamma_\nu]\,. \tag{A.9}$$

A.3 Lattice derivatives

We collect here the definitions of lattice covariant derivatives.

$$a\nabla_\mu\psi(x) = U_\mu(x)\psi(x+a\hat{\mu}) - \psi(x) \tag{A.10}$$

$$a\nabla^*_\mu\psi(x) = \psi(x) - U^\dagger_\mu(x-a\hat{\mu})\psi(x-a\hat{\mu}) \tag{A.11}$$

$$a\overline{\psi}(x)\overleftarrow{\nabla}_\mu = \overline{\psi}(x+a\hat{\mu})U^\dagger_\mu(x) - \overline{\psi}(x) \tag{A.12}$$

$$a\overline{\psi}(x)\overleftarrow{\nabla}^*_\mu = \overline{\psi}(x) - \overline{\psi}(x-a\hat{\mu})U_\mu(x-a\hat{\mu}) \tag{A.13}$$

We also introduce the notation

$$\overleftrightarrow{\nabla}_\mu = \nabla_\mu - \overleftarrow{\nabla}_\mu \tag{A.14}$$

$$\overleftrightarrow{\nabla}^*_\mu = \nabla^*_\mu - \overleftarrow{\nabla}^*_\mu \tag{A.15}$$

Appendix B

The QCD Energy-Momentum tensor

In this Appendix we give the notation and conventions on the definition of the Energy-Momentum tensor (EMT) of QCD in use in this thesis, both in the continuum and on the lattice.

B.1 The Energy-Momentum tensor in the continuum

The EMT is the conserved current associated to the invariance of continuum QCD under the SO(4) group. We consider the symmetric and gauge invariant definition of the EMT of QCD [92, 33]. We may write it as the sum of the two components

$$T_{\mu\nu} = T^G_{\mu\nu} + T^F_{\mu\nu}\,, \tag{B.1}$$

where

$$T^G_{\mu\nu} = \frac{1}{g_0^2}\left\{F^a_{\mu\alpha}F^a_{\nu\alpha} - \frac{1}{4}\delta_{\mu\nu}F^a_{\alpha\beta}F^a_{\alpha\beta}\right\} \tag{B.2}$$

and

$$T^F_{\mu\nu} = \frac{1}{4}\left\{\overline{\psi}\gamma_\mu \overleftrightarrow{D}_\nu \psi + \overline{\psi}\gamma_\nu \overleftrightarrow{D}_\mu \psi\right\} - \frac{1}{4}\delta_{\mu\nu}\overline{\psi}\left\{\frac{1}{2}\gamma_\alpha \overleftrightarrow{D}_\alpha + M_0\right\}\psi\,. \tag{B.3}$$

The differential operator $\overleftrightarrow{D}_\mu$ is defined as

$$\overleftrightarrow{D}_\mu = D_\mu - \overleftarrow{D}_\mu\,, \quad \overleftarrow{D}_\mu = \overleftarrow{\partial}_\mu + iA_\mu\,, \tag{B.4}$$

and D_μ is the covariant derivative (1.3).

B.2 The Energy-Momentum tensor on the lattice

We consider the Wilson lattice regularization of QCD. We discretize the EMT by replacing the fields and the derivatives appearing in the continuum expressions with their

lattice counterparts. We use the same notation of the continuum, as any ambiguity will be resolved by the context. We define [33, 32, 31, 30]

$$T_{\mu\nu} = T^G_{\mu\nu} + T^F_{\mu\nu}\,, \tag{B.5}$$

where

$$T^G_{\mu\nu} = \frac{1}{g_0^2}\left\{F^a_{\mu\alpha}F^a_{\nu\alpha} - \frac{1}{4}\delta_{\mu\nu}F^a_{\alpha\beta}F^a_{\alpha\beta}\right\}\,, \tag{B.6}$$

with

$$F^a_{\mu\nu} = 2\,\mathrm{tr}\left\{\widehat{F}_{\mu\nu}T^a\right\}\,, \quad F_{\mu\nu} = F^a_{\mu\nu}T^a\,, \tag{B.7}$$

and with $\widehat{F}_{\mu\nu}$ being the clover discretization of the field strength tensor, see equation (3.47). The fermionic part reads

$$\begin{aligned} T^F_{\mu\nu} =& \frac{1}{8}\Big\{\overline{\psi}\gamma_\mu\big[\overleftrightarrow{\nabla}^*_\nu + \overleftrightarrow{\nabla}_\nu\big]\psi + \overline{\psi}\gamma_\nu\big[\overleftrightarrow{\nabla}^*_\mu + \overleftrightarrow{\nabla}_\mu\big]\psi\Big\} \\ &- \frac{1}{4}\delta_{\mu\nu}\overline{\psi}\Big\{\frac{1}{4}\gamma_\alpha\Big(\overleftrightarrow{\nabla}^*_\alpha + \overleftrightarrow{\nabla}_\alpha\Big) + M_0\Big\}\psi\,, \end{aligned}$$

where $\overleftrightarrow{\nabla}_\mu$ and $\overleftrightarrow{\nabla}^*_\mu$ are defined in equations (A.14) and (A.15).

B.2.1 Decomposition in the hypercubic group

The lattice regularization breaks the SO(4) symmetry of the continuum theory to its hypercubic subgroup SW_4. The lattice EMT splits in the singlet, triplet and sextet representations of this group. The sextet components are

$$T^{G,\{6\}}_{\mu\nu} = (1-\delta_{\mu\nu})\frac{1}{g_0^2}\left\{F^a_{\mu\alpha}F^a_{\nu\alpha}\right\}\,, \tag{B.8}$$

$$T^{F,\{6\}}_{\mu\nu} = (1-\delta_{\mu\nu})\frac{1}{8}\left\{\overline{\psi}\gamma_\mu\left[\overleftrightarrow{\nabla}^*_\nu + \overleftrightarrow{\nabla}_\nu\right]\psi + \overline{\psi}\gamma_\nu\left[\overleftrightarrow{\nabla}^*_\mu + \overleftrightarrow{\nabla}_\mu\right]\psi\right\}\,, \tag{B.9}$$

the triplet components are

$$T^{G,\{3\}}_{\mu\nu} = \frac{1}{g_0^2}\Big\{F^a_{\mu\alpha}F^a_{\mu\alpha} - F^a_{\nu\alpha}F^a_{\nu\alpha}\Big\}\,, \tag{B.10}$$

$$T^{F,\{3\}}_{\mu\nu} = \frac{1}{4}\Big\{\overline{\psi}\gamma_\mu\left[\overleftrightarrow{\nabla}^*_\mu + \overleftrightarrow{\nabla}_\mu\right]\psi - \overline{\psi}\gamma_\nu\left[\overleftrightarrow{\nabla}^*_\nu + \overleftrightarrow{\nabla}_\nu\right]\psi\Big\}\,, \tag{B.11}$$

and finally the singlet components read

$$T^{G,\{1\}}_{\mu\nu} = \delta_{\mu\nu}\frac{1}{4g_0^2}F^a_{\alpha\beta}F^a_{\alpha\beta}\,, \tag{B.12}$$

$$T^{F,\{1a\}}_{\mu\nu} = \delta_{\mu\nu}\frac{1}{16}\overline{\psi}\Big\{\gamma_\alpha\Big(\overleftrightarrow{\nabla}^*_\alpha + \overleftrightarrow{\nabla}_\alpha\Big)\Big\}\psi\,, \tag{B.13}$$

$$T^{F,\{1b\}}_{\mu\nu} = \delta_{\mu\nu}\overline{\psi}\psi\,. \tag{B.14}$$

Appendix C

Details on the thermal effective theory of QCD

C.1 The Linde problem

Perturbation theory at finite temperature suffers from a convergence problem that was pointed out by Linde [94]. Any quantity can be computed only up to to some perturbative order, since beyond that all the diagrams contribute at the same order and the expansion breaks down. The maximum order is in general quantity-dependent, and this problem holds no matter how weak the coupling g is.

To sketch the problem let's consider the perturbative computation of the free-energy density, equation (2.5). The contributing diagrams are all the possible vacuum bubbles. Following the argument by Linde [94] [1] we consider the diagram in figure C.1, with N vertices, $N+1$ loops and $2N$ gluon propagators. The associated integral has the form

$$\sim g^{2N} \prod_{i=1}^{N+1} \left(T \int \frac{d^3 \boldsymbol{p}_i}{(2\pi)^3} \right) \frac{1}{\boldsymbol{p}_1^2 + m^2} \prod_{i=2}^{N} \left(\frac{1}{\boldsymbol{p}_i^2 + m^2} \right)^2 \frac{1}{\boldsymbol{p}_{N+1}^2 + m^2} \,, \tag{C.1}$$

where we restricted to the zero Matsubara modes and we introduced a mass m as infrared regulator. The integral has a mass dimension equal to $3(N+1)-2-4(N-1)-2 = 3-N$, and once solved the mass m is the only quantity that can carry this dimensionality. Therefore the result will have the parametric form

$$\sim g^{2N} \frac{T^{N+1}}{\pi^{3N+3}} m^{3-N} = \frac{1}{\pi^{2N}} \left(\frac{g}{\pi} \right)^6 T^4 \left(\frac{g^2 T}{\pi m} \right)^{N-3} . \tag{C.2}$$

The obvious comment is that massless particles develop worse and worse IR divergences as the loop order increases. However we know that the thermal medium screens the particles and this translates in an effective IR regulator, which arises naturally in the context of thermal effective theory. The following scenarios may happen [90]:

[1] See also Philipsen's lectures [126].

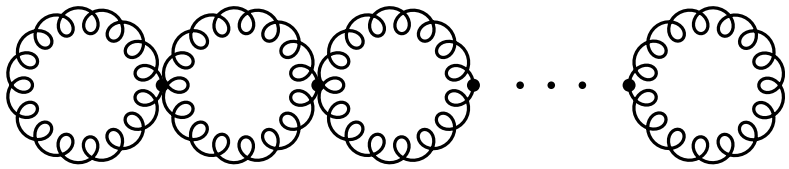

Figure C.1: Loop diagram contributing to the free-energy density of QCD at order g^{2N}, where N is the number of vertices.

- The loop lines contain heavy fields with thermal mass $m \sim \pi T$, like the fermions or the non-zero Matsubara frequencies of the gauge field. The weak coupling expansion makes sense provided $g^2 T \ll \pi^2 T$, that is $(g/\pi)^2 \ll 1$. In this case diagrams are always IR-safe and the contribution is computable in perturbation theory, giving rise to the usual expansion in even powers of the coupling.

- The loop lines contain the soft field $\bar{A}_0$, whose thermal mass is $m \sim m_E \sim gT$ (the Debye mass). The perturbative expansion is still computable as far as $g^2 T \ll \pi g T \to g/\pi \ll 1$, and odd powers of the coupling appear as a characterizing feature.

- The loop lines contain the ultrasoft chromo-magnetic field, whose energy scale is $\sim g^2 T/\pi$. In this case the contributions (C.2) are all of the same order $\sim g^6$, independently from the number of loops N. This generates an infinite tower of Feynman diagrams that in general cannot be resummed, breaking the perturbative approach.

The last scenario is known as *Linde problem* and signals that MQCD cannot be treated in perturbation theory. Therefore the weak coupling expansion of a QCD observable in thermal perturbation theory makes sense only up to the loop order where MQCD does not contribute. For the pressure, this happens at order $\sim g^6$.

C.2 Higher order contributions to the pressure in the effective theory

It is interesting to estimate the contributions to the pressure coming from higher order operators in the thermal effective theory. The hope is that their contribution is beyond the maximum perturbative order we are interested in, that is $\sim g^6$.

Following [82], we start from the higher order contributions to Electrostatic QCD. The next operators to be added are dimension 6 terms that have been classified in [34] and, parametrically speaking, they are the 4-dimensional operators we already considered with two extra powers of the covariant derivative D_k or of the field $\bar{A}_0$. The diagrams generated by these operators encode the interactions with the hard scales of the full theory that have been integrated out, and thus they should contain at least one extra

power of g^2 and they are suppressed with $(\pi T)^2$. Therefore these diagrams generate contributions to the pressure of the order

$$\sim T \cdot g^2 \frac{1}{(\pi T)^2} D_j D_k \mathcal{L}_{\rm EQCD} \sim g^7 T^4 \,, \tag{C.3}$$

where we used the fact that covariant derivatives have mass dimension 1 and the relevant mass scale is $m_E \sim gT$. The Electrostatic Lagrangian has mass dimension 3, so that $\mathcal{L}_{\rm EQCD} \sim (gT)^3$. As hoped, higher order operators in EQCD can be omitted as their contribution to the perturbative expansion starts at order $\sim g^7$.

We repeat the same analysis for Magnetostatic QCD. The next higher order operators which correct the MQCD action (2.34) are of mass dimension 6, and they encode the interaction of ultrasoft modes with the soft modes of EQCD that in this context is the "full" theory. Proceeding as before we can quote the contribution from the generated diagrams:

$$\sim T \cdot g_E^2 \frac{1}{(gT)^2} \frac{D_j D_k}{m_E} \mathcal{L}_{\rm MQCD} \sim g^9 T^4 \,. \tag{C.4}$$

At variance of eq. (C.3), here we have the coupling g_E^2 because now EQCD is the complete theory. For the same reason the cutoff scale is the soft scale $m_E \sim gT$, and the relevant dynamical mass scale is $\sim g^2 T$. The magnetostatic Lagrangian contributes as $\mathcal{L}_{\rm MQCD} \sim (g^2 T)^3$. One extra power of m_E appears at the denominator for dimensional reasons (the full contribution must be of mass dimension 4). The contribution of higher dimensional operators starts at order $\sim g^9$ in perturbation theory. Also in this case the conclusion is that we can neglect them if we restrict to order $\sim g^6$.

Appendix D

Thermodynamics and Lorentz invariance

In this Appendix we report some theoretical details on the framework of thermal field theory with shifted boundary conditions, whose main properties are discussed in Section 2.2. We refer to that Section for all the unexplained notations.

D.1 Shifted boundary conditions

In this Section we proof that the partition function eq. (2.10) for a thermal system on a moving frame is equivalent to an Euclidean path integral with fields satisfying shifted boundary conditions in the compact temporal direction [60] of size L_0. For simplicity consider a system with one scalar bosonic field ϕ. We write the propagation in time from an initial state $|\phi(0,\boldsymbol{x})\rangle$ to the final state $|\phi(L_0,\boldsymbol{x})\rangle$ as

$$\langle\phi(L_0,\boldsymbol{x})|e^{-L_0(\widehat{H}-i\boldsymbol{\xi}\cdot\widehat{\boldsymbol{P}})}|\phi(0,\boldsymbol{x})\rangle\,, \tag{D.1}$$

where $\widehat{H}$ is the Hamiltonian of the system and $\boldsymbol{\xi}$ is the Euclidean Lorentz boost. The total momentum operator $\widehat{\boldsymbol{P}}$ generates translations in space,

$$\begin{aligned}|\phi(0,\boldsymbol{x})\rangle = \widehat{\phi}(0,\boldsymbol{x})|0\rangle &= e^{-i\boldsymbol{x}\cdot\widehat{\boldsymbol{P}}}\widehat{\phi}(0,\boldsymbol{0})e^{i\boldsymbol{x}\cdot\widehat{\boldsymbol{P}}}|0\rangle \\ &= e^{-i\boldsymbol{x}\cdot\widehat{\boldsymbol{P}}}\widehat{\phi}(0,\boldsymbol{0})|0\rangle\,,\end{aligned} \tag{D.2}$$

where $|0\rangle$ is the thermal vacuum of the theory. Using this property in the equation above we get

$$\langle\phi(L_0,\boldsymbol{x})|e^{-L_0(\widehat{H}-i\boldsymbol{\xi}\cdot\widehat{\boldsymbol{P}})}|\phi(0,\boldsymbol{x})\rangle = \langle\phi(L_0,\boldsymbol{x})|e^{-L_0\widehat{H}}|\phi(0,\boldsymbol{x}-L_0\boldsymbol{\xi})\rangle\,. \tag{D.3}$$

The path integral is the trace over the Hilbert space, meaning that the final state must be identified with the initial one. This enforces the boundary condition

$$\phi(L_0,\boldsymbol{x}) = \phi(0,\boldsymbol{x}-L_0\boldsymbol{\xi}) \tag{D.4}$$

on the bosonic field ϕ. The proof is the same for fermionic fields, with an extra -1 entering when the trace over the Grassmann-valued fields is taken.

D.2 Generalized periodic boundary conditions

We now consider a thermal quantum field theory in a finite volume of sizes L_0, L_1, L_2, L_3. In general, we may formalize the boundary conditions on fields as follows [59]. In $\mathbb{R}^4$ we introduce the *primitive vectors* as a set of linearly independent vectors. We collect these vectors in a *primitive matrix* $V \in \mathrm{GL}(4,\mathbb{R})$, whose columns are the components of the primitive vectors in an orthonormal basis of $\mathbb{R}^4$. For example we may consider the following primitive matrices:

$$V_{\mathrm{pbc}} = \begin{pmatrix} L_0 & 0 & 0 & 0 \\ 0 & L_1 & 0 & 0 \\ 0 & 0 & L_2 & 0 \\ 0 & 0 & 0 & L_3 \end{pmatrix}, \quad V_{\mathrm{sbc}} = \begin{pmatrix} L_0 & 0 & 0 & 0 \\ \xi_1 L_0 & L_1 & 0 & 0 \\ \xi_2 L_0 & 0 & L_2 & 0 \\ \xi_3 L_0 & 0 & 0 & L_3 \end{pmatrix}. \tag{D.5}$$

The boundary conditions are imposed by identifying the fields at the positions x_μ and $x_\mu + V_{\mu\nu} m_\nu$, $m_\mu \in \mathbb{Z}$, up to a sign if the field is fermionic. Therefore V_{pbc} is associated to periodic boundary conditions, and V_{sbc} to shifted boundary conditions along time plus periodic in space. In this second case we also have the constraint on the shift

$$-\frac{L_k}{2L_0} < \xi_k \leq \frac{L_k}{2L_0} \tag{D.6}$$

due to the spatial periodicity. The finite volume theory is finally obtained by restricting the fields to a subset of $\mathbb{R}^4$ called *primitive cell*:

$$\mathcal{C} = \left\{ x \in \mathbb{R}^4 \,|\, x_\mu = V_{\mu\nu} t_\nu,\, 0 \leq t_\mu \leq 1 \right\}. \tag{D.7}$$

The partition function of the finite volume theory depends on the primitive matrix, in addition to all the parameters of the infinite volume theory. In a Lorentz invariant theory the (Euclidean) rotation

$$V \to RV\,, \quad R \in \mathrm{SO}(4) \tag{D.8}$$

leaves the theory unchanged. In addition, the finite volume partition function is invariant under a transformation of the primitive matrix under the discrete group $\mathrm{SL}(4,\mathbb{Z})$. This allows to replace the primitive vectors by linear combinations among themselves with integer coefficients.

Summarizing, the primitive matrices V, V' are associated to the same finite volume partition function (even though with different boundary conditions) if they can be related by a $\mathrm{SO}(4)$ and/or $\mathrm{SL}(4,\mathbb{Z})$ transformations:

$$V' = RVM\,, \quad R \in \mathrm{SO}(4)\,, \quad M \in \mathrm{SL}(4,\mathbb{Z})\,. \tag{D.9}$$

This establishes an equivalence relation $V' \sim V$ between the two primitive matrices.

D.3 Shift and Lorentz invariance

In this Section we use the formalism we introduced to proof the Lorentz invariance in the thermodynamic limit of the free-energy density, eq. (2.13), which we report here for convenience:

$$f(L_0, \boldsymbol{\xi}) = f(L_0/\gamma, \mathbf{0}) \,, \quad \gamma = 1/\sqrt{1+\boldsymbol{\xi}^2} \,. \tag{D.10}$$

We also refer to the original literature for further details [59]. We start from the finite volume theory and assume $\boldsymbol{\xi} = (\xi, 0, 0)$. The primitive matrix with shifted boundary conditions (see eq. (D.5)) becomes

$$V_{\rm sbc} = \begin{pmatrix} L_0 & 0 & 0 & 0 \\ \xi L_0 & L_1 & 0 & 0 \\ 0 & 0 & L_2 & 0 \\ 0 & 0 & 0 & L_3 \end{pmatrix} \tag{D.11}$$

and it is associated to the partition function

$$\mathcal{Z}(V_{\rm sbc}) = \mathrm{Tr}\left\{ e^{-L_0(\widehat{H} - i\xi \widehat{P}_1)} \right\} \tag{D.12}$$

where we write explicitly the dependence on the primitive matrix to stress that we are in finite volume. As first step we rotate to the rest frame by applying a Lorentz transformation to the primitive vectors:

$$RV_{\rm sbc} = \begin{pmatrix} L_0/\gamma & L_1\gamma\xi & 0 & 0 \\ 0 & L_1\gamma & 0 & 0 \\ 0 & 0 & L_2 & 0 \\ 0 & 0 & 0 & L_3 \end{pmatrix} \,, \quad R = \begin{pmatrix} \gamma & \gamma\xi & 0 & 0 \\ -\gamma\xi & \gamma & 0 & 0 \\ 0 & 0 & 1 & 0 \\ 0 & 0 & 0 & 1 \end{pmatrix} \,. \tag{D.13}$$

For better interpreting the rotated matrix, we further transform it under the $\mathrm{SL}(4,\mathbb{Z})$ group so to make it resemble the structure of the original matrix $V_{\rm sbc}$:

$$V_1 = M^{-1} R V_{\rm sbc} M = \begin{pmatrix} \gamma L_1 & 0 & 0 & 0 \\ -\xi\gamma L_1 & L_0/\gamma & 0 & 0 \\ 0 & 0 & L_2 & 0 \\ 0 & 0 & 0 & L_3 \end{pmatrix} \,, M = \begin{pmatrix} 0 & 1 & 0 & 0 \\ -1 & 0 & 0 & 0 \\ 0 & 0 & 1 & 0 \\ 0 & 0 & 0 & 1 \end{pmatrix} \,. \tag{D.14}$$

According to the equivalence (D.9), $V_{\rm sbc} \sim V_1$ and the finite volume partition functions are the same: $\mathcal{Z}(V_{\rm sbc}) = \mathcal{Z}(V_1)$. In parallel to equation (D.12), we may interpret $\mathcal{Z}(V_1)$ as the partition function of a thermal system with screening Hamiltonian $\tilde{H}$, whose eigenstates propagate along the direction given by the first column of the primitive matrix V_1,

$$\mathcal{Z}(V_1) = \mathrm{Tr}\left\{ e^{-\gamma L_1(\tilde{H} + i\xi\tilde{\omega})} \right\} \,, \tag{D.15}$$

where $\tilde{\omega}$ is the momentum operator generating the translations along the second primitive vector. The theory has shifted boundary conditions along the first column and periodic

boundary conditions in the sub-volume $L_0/\gamma \times L_2 \times L_3$. Note that the temperature is still the inverse of the "short" direction, $T = \gamma/L_0$, even though it is along the second primitive vector.

Assuming that the Hamiltonian $\tilde{H}$ has a translationally invariant vacuum and a mass gap, in the $L_1 \to \infty$ limit the partition function $\mathcal{Z}(V_1)$ will become insensitive to the phase $\xi\tilde{\omega}$. It can be shown that the effect of the phase is suppressed exponentially with the lightest mass in the spectrum of $\tilde{H}$, see also below. Therefore, in this limit the following identity among free-energies holds,

$$\lim_{L_1\to\infty} f(V_1) = \lim_{L_1\to\infty} f(V_{\text{diag}})\,, \tag{D.16}$$

where we introduced the diagonal primitive matrix

$$V_{\text{diag}} = \begin{pmatrix} L_1\gamma & 0 & 0 & 0 \\ 0 & L_0/\gamma & 0 & 0 \\ 0 & 0 & L_2 & 0 \\ 0 & 0 & 0 & L_3 \end{pmatrix}\,, \tag{D.17}$$

which is associated to periodic boundary conditions. The limits $L_2, L_3 \to \infty$ can be taken as well, and in conclusion the primitive matrices V_{sbc} and V_{diag} describe the same thermal system in the thermodynamic limit, but for the fact that the temperature changes from $1/L_0$ to $T = 1/(L_0\sqrt{1+\xi^2})$. The invariance of the infinite volume theory under 3d rotations allows to generalize the result to any vector $\boldsymbol{\xi}$. This completes the proof of equation (2.13).

D.4 Finite volume

We address here the finite volume corrections [59, 46] to the Lorentz invariance of the free-energy density, equation (2.13), in the first direction (so in the limit $L_1 \to \infty$) and assuming shift $\boldsymbol{\xi} = (\xi, 0, 0)$. Referring to the notation introduced in Subsection D.3, we focus on the free-energy $f(V_1)$ associated to the partition function (D.15),

$$\begin{aligned} f(V_1) &= -\frac{1}{L_0 V}\ln \mathcal{Z}(V_1) = -\frac{1}{L_0 V}\ln\left(\sum_n \langle n|e^{-\gamma L_1(\tilde{H}+i\xi\tilde{\omega})}|n\rangle\right) \\ &= -\frac{1}{L_0 V}\ln\left(\sum_n e^{-\gamma L_1(E_0+\Delta E_n+i\xi\omega_n)}\right)\,, \end{aligned} \tag{D.18}$$

where the states $|n\rangle$, $n \geq 0$ of the Hilbert space are simultaneously eigenstates of the screening Hamiltonian $\tilde{H}$ and of the momentum operator $\tilde{\omega}$. These states live in the sub-volume $L_0/\gamma \times L_2 \times L_3$ with primitive matrix

$$\overline{V}_1 = \begin{pmatrix} L_0/\gamma & 0 & 0 \\ 0 & L_2 & 0 \\ 0 & 0 & L_3 \end{pmatrix}\,, \tag{D.19}$$

which encodes periodic boundary conditions. We call ΔE_n the energy gap of the state n above the energy E_0 associated to the vacuum state $|0\rangle$ of the screening Hamiltonian, and ω_n the Matsubara frequencies of the momentum operator. Since in the $L_1 \to \infty$ limit only the vacuum contributes, the free-energy in that limit is given by E_0. We may separate the vacuum term,

$$f(V_1) = \frac{1}{L_0 V} \cdot L_1 \gamma E_0 + \mathcal{I}_1 \,, \tag{D.20}$$

where

$$\mathcal{I}_1 = -\frac{1}{L_0 V} \ln \left(1 + \sum_{n>0} e^{-\gamma L_1 (\Delta E_n + i\xi\omega_n)} \right) \tag{D.21}$$

is the finite volume correction to the free-energy. Thermal effective theory arguments (see Section 2.5) allow to say that, at asymptotically high temperatures T, the lightest exited states above the vacuum have a mass-gap $M_{\text{gap}} \propto T$. The heaviest scale in the effective approach is the fermionic one $\sim \pi T$. Therefore we expect the lightest eigenstates to be purely gluonic 1-particle states with mass equal to M_{gap} and energies $\ll \pi T$. These states give the leading contributions to the finite volume effects,

$$\mathcal{I}_1 \approx -\frac{1}{L_0 V} \sum_{\substack{1-\text{particle} \\ \text{states}}} e^{-\gamma L_1 (\Delta E + i\xi p_1)} + \cdots \,, \tag{D.22}$$

where we defined

$$\Delta E = \sqrt{M_{\text{gap}}^2 + \boldsymbol{p}^2} \,, \quad \boldsymbol{p} = \left(\gamma \frac{2\pi n_1}{L_0}, \frac{2\pi n_2}{L_2}, \frac{2\pi n_3}{L_3} \right) \,, \quad n_1, n_2, n_3 \in \mathbb{Z} \tag{D.23}$$

the energy of the states and the allowed momenta in the box with $\overline{V}_1$ as primitive matrix.

Equation (D.22) shows that finite volume effects on $f(V_1)$ decay exponentially as $M_{\text{gap}} L_1 \to \infty$:

$$f(V_1) - \lim_{L_1 \to \infty} f(V_1) = \mathcal{I}_1 + \cdots \sim e^{-M_{\text{gap}} L_1} \,. \tag{D.24}$$

Since $f(V_{\text{sbc}}) = f(V_1)$, the same holds for $f(V_{\text{sbc}})$. The result generalizes to arbitrary shift $\boldsymbol{\xi}$ and to the other limits $L_{2,3} \to \infty$.

D.5 Proofs of Ward Identities on a moving frame

In this Section we prove the relations reported in Subsection 2.2.1.

D.5.1 Proof of equation (2.15)

We differentiate once with respect to the shift ξ_k both sides of equation (2.13):

$$\frac{\partial}{\partial \xi_k} f(L_0, \boldsymbol{\xi}) = \frac{\partial}{\partial \xi_k} f(T, \boldsymbol{0}) \,, \quad T = \frac{1}{L_0 \sqrt{1 + \boldsymbol{\xi}^2}} \,. \tag{D.25}$$

On the right-hand side, we exchange the derivative in the shift with a derivative in the temperature,

$$\frac{\partial}{\partial \xi_k} f(T, \mathbf{0}) = \frac{\partial T}{\partial \xi_k} \frac{\partial}{\partial T} f(T, \mathbf{0}) = \frac{\xi_k}{1 + \boldsymbol{\xi}^2} \, Ts \,, \tag{D.26}$$

where we introduced the entropy density of the system through its thermodynamic definition (2.8). Therefore, the entropy in the not-shifted frame can be related to the derivative in the shift of the free-energy in the shifted frame,

$$Ts = \frac{1 + \boldsymbol{\xi}^2}{\xi_k} \frac{\partial}{\partial \xi_k} f(L_0, \boldsymbol{\xi}) \,, \quad T = \frac{1}{L_0 \sqrt{1 + \boldsymbol{\xi}^2}} \,, \tag{D.27}$$

where we stress that the temperature T is the one in the frame at rest with the thermal system. This completes the proof.

D.5.2 Proof of equation (2.18)

Another interesting Ward Identity is obtained from (2.13) We differentiate both sides of equation (2.13) with respect to L_0:

$$L_0 \frac{\partial}{\partial L_0} f(L_0, \boldsymbol{\xi}) = L_0 \frac{\partial}{\partial L_0} f(T, \mathbf{0}) \,, \quad T = \frac{1}{L_0 \sqrt{1 + \boldsymbol{\xi}^2}} \,. \tag{D.28}$$

From the left-hand side we obtain

$$L_0 \frac{\partial}{\partial L_0} f(L_0, \boldsymbol{\xi}) = -f(L_0, \boldsymbol{\xi}) - \langle T_{00} \rangle_{\boldsymbol{\xi}} - \sum_i \xi_i \langle T_{0i} \rangle_{\boldsymbol{\xi}} \,, \tag{D.29}$$

where the correspondence $\widehat{H} \to -T_{00}$ between the total energy operator and the Energy-Momentum tensor (defined in Appendix B) has been used. From the right-hand side we get

$$L_0 \frac{\partial}{\partial L_0} f(L_0/\gamma, \mathbf{0}) = \frac{\partial T}{\partial L_0} \frac{\partial}{\partial T} f(T, \mathbf{0}) = Ts \,, \tag{D.30}$$

with $T = L_0/\gamma$ temperature in the frame at rest with the thermal system. Using equation (2.17) we get a Ward Identity involving only quantities measured in the frame where the thermal system is moving:

$$f(L_0, \boldsymbol{\xi}) + \langle T_{00} \rangle_{\boldsymbol{\xi}} + \sum_i \xi_i \langle T_{0i} \rangle_{\boldsymbol{\xi}} = \frac{1 + \boldsymbol{\xi}^2}{\xi_k} \langle T_{0k} \rangle_{\boldsymbol{\xi}} \,. \tag{D.31}$$

We may assume that the shift is not zero in the component ξ_k only. Using the mapping $f(L_0, \boldsymbol{\xi}) \to -\langle T_{jj} \rangle_{\boldsymbol{\xi}}$, with $j \neq k$, we get the desired relation

$$\langle T_{0k} \rangle_{\boldsymbol{\xi}} = \xi_k \left(\langle T_{00} \rangle_{\boldsymbol{\xi}} - \langle T_{jj} \rangle_{\boldsymbol{\xi}} \right) \,, \quad j \neq k \,, \xi_j = 0 \,. \tag{D.32}$$

Appendix E

Entropy density in lattice perturbation theory

E.1 Notation

The notation follows Appendix E of Ref. [42], from which we retrieve the relevant results which are instrumental for our discussion. We consider lattice QCD with N_f flavours of mass-degenerate O(a)-improved Wilson fermions, on a lattice with compact size L_0 and spatial sizes L_1, L_2, L_3.

Bosonic fields

We introduce the Fourier transform of the field A_μ as

$$A_\mu(x) = \int_{p_{\boldsymbol{\xi}}} \widetilde{A}_\mu(p)\, e^{ip(x+\frac{a}{2}\hat{\mu})}\,, \tag{E.1}$$

where the notation $\int_{p_{\boldsymbol{\xi}}}$ stands for

$$\int_{p_{\boldsymbol{\xi}}} f(p) = \frac{1}{L_0 L_1 L_2 L_3} \sum_n f(p) \tag{E.2}$$

and, in presence of shifted and twisted boundary conditions, the momenta in the bosonic Brillouin zone are

$$p_0 = \frac{2\pi n_0}{L_0} - \sum_{k=1}^{3} p_k \xi_k\,, \quad p_k = \frac{2\pi n_k}{L_k} \tag{E.3}$$

where $n_\mu = 0, 1, ..., L_\mu/a - 1$. In the infinite spatial volume limit the integral (E.2) becomes

$$\int_{p_{\boldsymbol{\xi}}} f(p) \xrightarrow{L_i\to\infty} \frac{1}{L_0} \sum_{n_0} \int_{BZ} \frac{d^3\boldsymbol{p}}{(2\pi)^3}\, f(p)\,, \tag{E.4}$$

where BZ stands for the Brillouin zone. In momentum space the free gluonic propagator reads

$$D^{ab}_{\mu\nu}(p) = \frac{\delta_{ab}\delta_{\mu\nu}}{D_G(p)}\,, \quad D_G(p) = \sum_{\mu=0}^{3} \hat{p}^2_\mu\,, \quad \hat{p}_\mu = \frac{2}{a}\sin\Big(\frac{ap_\mu}{2}\Big)\,. \tag{E.5}$$

Fermionic fields

The Fourier transform for fermionic fields is

$$\psi(x) = \int_{p_{\boldsymbol{\xi},\theta}} \widetilde{\psi}(p)\, e^{ipx}\,, \quad \overline{\psi}(x) = \int_{p_{\boldsymbol{\xi},\theta}} \widetilde{\overline{\psi}}(p)\, e^{-ipx}\,, \tag{E.6}$$

where the integral $\int_{p_{\boldsymbol{\xi},\theta}}$ is defined as in eq. (E.2). In presence of shifted and twisted boundary conditions, the momenta in the fermionic Brillouin zone are

$$p_0 = \frac{2\pi n_0}{L_0} + \frac{\theta_0}{L_0} + \frac{\pi}{L_0} - \sum_{k=1}^{3} p_k\xi_k\,, \quad p_k = \frac{2\pi n_k}{L_k} + \frac{\theta_k}{L_k} \tag{E.7}$$

where $n_\mu = 0, 1, ..., L_\mu/a - 1$. The fermionic propagator is

$$S(p) = \frac{-i\gamma_\mu \overline{p}_\mu + m_0(p)}{D_F(p)}\,, \tag{E.8}$$

where

$$D_F(p) = \sum_{\mu=0}^{3} \overline{p}^2_\mu + m_0^2(p)\,, \quad m_0(p) = m_0 + \frac{a}{2}\sum_{\mu=0}^{3}\hat{p}^2_\mu\,, \quad \overline{p}_\mu = \frac{1}{a}\sin(ap_\mu)\,. \tag{E.9}$$

E.1.1 Some relevant integrals

We report a collection of integrals that appear in tree-level and 1-loop calculations in lattice perturbation theory. We define the notation $\mathrm{c}_\mu = \cos(ap_\mu)$.

$$B^{(0)} = \int_{p_{\boldsymbol{\xi}}} \frac{1}{D_G(p)} \tag{E.10}$$

$$B^{(3)}_\mu = \int_{p_{\boldsymbol{\xi}}} \frac{\mathrm{c}_\mu(p)}{D_G(p)} \tag{E.11}$$

$$F^{(4)}_{\mu\nu} = \int_{p_{\boldsymbol{\xi},\theta}} \frac{\bar{p}_\mu \mathrm{c}_\nu(p)}{D_F(p)} \tag{E.12}$$

$$F^{(5)}_{\mu} = \int_{p_{\boldsymbol{\xi},\theta}} \frac{m_0(p)\bar{p}_\mu}{D_F(p)} \tag{E.13}$$

$$F^{(6)}_{\mu\nu} = \int_{p_{\boldsymbol{\xi},\theta}} \frac{m_0(p)\bar{p}_\mu \mathrm{c}_\nu(p)}{D^2_F(p)} \tag{E.14}$$

$$F^{(7)}_{\mu} = \int_{p_{\boldsymbol{\xi},\theta}} \frac{m_0^2(p)\bar{p}_\mu}{D^2_F(p)} \tag{E.15}$$

$$F^{(8)} = \int_{p_{\boldsymbol{\xi},\theta}} \frac{m_0(p)}{D_F(p)} \tag{E.16}$$

L_0/a	$\delta am_{\rm cr}^{(0)} \times 10^3$	$\delta am_{\rm cr}^{(1,N_f,0)} \times 10^3$	$\delta am_{\rm cr}^{(1,N_f,1)} \times 10^3$
4	-1.5131	1.7730	0.9087
6	-0.6384	0.0380	0.0851
8	-0.3209	0.0026	0.0196
10	-0.1835	0.0008	0.0072
12	-0.1145	0.0009	0.0034
14	-0.0761	0.0008	0.0019
16	-0.0531	0.0007	0.0011

Table E.1: Cutoff effects to the 1-loop critical mass for the O(a)-improved theory ($c_{\rm sw} = 1$), obtained from Table 7.1 of Ref. [88].

E.2 Critical mass at 1-loop

We consider the critical mass $m_{\rm cr}$ computed requiring the PCAC mass to vanish in the Schrodinger functional setup [88, 124]. At 1-loop

$$am_{\rm cr} = am_{\rm cr}^{(0)} + \delta am_{\rm cr}^{(0)} + g_0^2 \left(am_{\rm cr}^{(1)} + \delta am_{\rm cr}^{(1,0)} + N_f \delta am_{\rm cr}^{(1,1)} \right) , \tag{E.17}$$

where $am_{\rm cr}^{(0)} = 0$ and we define

$$am_{\rm cr}^{(1)} = \frac{N_c^2 - 1}{N_c} \, am_{\rm cr}^{(1,N_c)} , \tag{E.18}$$

$$\delta am_{\rm cr}^{(1,0)} = \frac{N_c^2 - 1}{N_c} \, \delta am_{\rm cr}^{(1,N_c,0)} , \tag{E.19}$$

$$\delta am_{\rm cr}^{(1,1)} = \frac{N_c^2 - 1}{N_c} \, \delta am_{\rm cr}^{(1,N_c,1)} , \tag{E.20}$$

with [124]

$$\begin{aligned} am_{\rm cr}^{(1,N_c)} = & -0.16285705871085(1) + c_{\rm sw}\, 0.04348303388205(10) \\ & + c_{\rm sw}^2\, 0.01809576878142(1) . \end{aligned} \tag{E.21}$$

At this order, the improvement coefficient is $c_{\rm sw}$ is either 0 or 1 for the unimproved or improved theory. The quantities $\delta am_{\rm cr}^{(0)}$, $\delta am_{\rm cr}^{(1,N_c,0)}$, $\delta am_{\rm cr}^{(1,N_c,1)}$ are the cutoff effects in the determination of the critical mass in lattice perturbation theory, therefore they have a dependence on the lattice spacing. Their values for $c_{\rm sw} = 1$ are reported in Table E.1. In our perturbative calculations at 1-loop, the proper chiral limit is thus obtained by setting the bare quark mass to the tree-level value of E.17.

E.3 Free-energy at 1-loop

In this section we collect the computation of the free-energy density in lattice perturbation theory. Results are taken from Appendix F of Ref. [42]. At tree-level we have

$$f^{G(0)} = \int_{p_{\boldsymbol{\xi}}} \ln\Big[a^2\, D_G(p)\Big]\,, \quad f^{F(0)} = -2\int_{p_{\boldsymbol{\xi}}} \ln\Big[a^2 D_F(p)\Big]\,. \tag{E.22}$$

The 1-loop gluonic contributions are

$$f^{G(1,N_c)} = \Big\{(B^{(0)})^2 - \frac{1}{2}\sum_\sigma \Big[B^{(0)} - B^{(3)}_\sigma\Big]^2 + \frac{1}{2}a^2K_1 + \frac{1}{24}a^4K_2 - \frac{1}{2a^2}B^{(0)}\Big\}\,, \tag{E.23}$$

$$f^{G(1,\frac{1}{N_c})} = \frac{1}{2}\Big\{\sum_\sigma \Big[B^{(0)} - B^{(3)}_\sigma\Big]^2 + \frac{1}{8a^4}\Big\}\,, \tag{E.24}$$

where we defined the integrals

$$K_1 = \int_{p_{\boldsymbol{\xi}};q_{\boldsymbol{\xi}};k_{\boldsymbol{\xi}}} \frac{\bar\delta(p+q+k)}{D_G(p)D_G(q)D_G(k)} \sum_\mu \hat p_\mu^2\, \hat q_\mu^2\,, \tag{E.25}$$

$$K_2 = \int_{p_{\boldsymbol{\xi}};q_{\boldsymbol{\xi}};k_{\boldsymbol{\xi}}} \frac{\bar\delta(p+q+k)}{D_G(p)D_G(q)D_G(k)} \sum_\mu \hat p_\mu^2\, \hat q_\mu^2\, \hat k_\mu^2 \tag{E.26}$$

and the delta function is

$$\bar\delta(p) = (2\pi)^4\delta^{(4)}(p) = a^4\sum_x e^{ipx}\,. \tag{E.27}$$

The fermionic term at 1-loop is

$$f^{F(1,N_f)} = B^{(0)}\left[\frac{1}{a^2} - a\,(am_0+4)\,F^{(8)}\right] + \int_{q_{\boldsymbol{\xi}};p_{\boldsymbol{\xi},\theta};k_{\boldsymbol{\xi},\theta}} \frac{\bar\delta(p-q-k)}{D_G(q)D_F(p)D_F(k)}\times$$
$$\left[am_0(k)\sum_\sigma \bar r_\sigma \bar p_\sigma + am_0(p)\sum_\sigma \bar k_\sigma \bar r_\sigma - m_0(k)m_0(p)\sum_\sigma \mathrm{c}_\sigma(r) + \sum_\sigma \bar p_\sigma \bar k_\sigma\,(\mathrm{c}_\sigma(r)-3)\right]\,, \tag{E.28}$$

where $r = p + k$. The contributions at 1-loop $\mathcal{F}^{F1}$ and $\mathcal{F}^{F2}$ come from the improving term of the Wilson action are

$$\mathcal{F}^{F1} = -\frac{ac_{\rm sw}}{2}\int_{q_{\boldsymbol{\xi}};p_{\boldsymbol{\xi},\theta};k_{\boldsymbol{\xi},\theta}} \frac{\bar\delta(p-q-k)}{D_G(q)D_F(p)D_F(k)}\Bigg\{a\sum_{\sigma\rho}\Big[(\bar p_\rho + \bar k_\rho)\bar q_\sigma(\bar p_\sigma \bar k_\rho - \bar k_\sigma \bar p_\rho)\Big]$$
$$-\sum_\sigma\Big\{\bar q_\sigma\big[m_0(k)\bar p_\sigma - m_0(p)\bar k_\sigma\big]\sum_{\rho\neq\sigma}\big[\mathrm{c}_\rho(p) + \mathrm{c}_\rho(k)\big]\Big\}\Bigg\}\,, \tag{E.29}$$

$$\mathcal{F}^{F2} = \frac{a^2 c_{\rm sw}^2}{8} \int_{q_{\boldsymbol{\xi}};p_{\boldsymbol{\xi},\theta};k_{\boldsymbol{\xi},\theta}} \frac{\bar{\delta}(p-q-k)}{D_G(q)D_F(p)D_F(k)} \Bigg\{ m_0(p)m_0(k) \sum_\sigma \Big\{ \bar{q}_\sigma^2 \Big[3 + \sum_{\rho\neq\sigma} \mathrm{c}_\rho(q) \Big] \Big\}$$

$$+ 2 \sum_{\sigma\rho} \bar{k}_\sigma \bar{q}_\sigma \bar{p}_\rho \bar{q}_\rho \Big(2 - \mathrm{c}_\sigma(q) + \sum_{\lambda\neq\rho} \mathrm{c}_\lambda(q) \Big) - \sum_{\sigma\rho} \bar{k}_\sigma \bar{p}_\sigma \bar{q}_\rho^2 \Big(1 - 2\mathrm{c}_\sigma(q) + \sum_{\lambda\neq\rho} \mathrm{c}_\lambda(q) \Big) \Bigg\} . \quad \text{(E.30)}$$

In conclusion, the 1-loop mass counterterm enters through the derivative in the bare mass of the tree-level fermionic free-energy:

$$\frac{\partial f^{F(0)}}{\partial a m_0} = -4F^{(8)} . \quad \text{(E.31)}$$

E.4 Infinite volume limit

We discuss the infinite volume limit of the integrals that appear in the perturbative expansion of the free-energy (see Section E.3), which are relevant for our study. For the simplest integrals it is possible to express the infinite volume limit analytically. Instead, we compute the 1-loop integrals numerically in finite volume, and then we extrapolate to the thermodynamic limit. Taking advantage of the analytic results, we managed to subtract the leading finite volume effects and thus speed up the convergence to the infinite volume limit.

E.4.1 Analytic infinite volume of $B^{(0)}$

For this computation we assume for simplicity that the shift is in the first direction only: $\boldsymbol{\xi} = (\xi, 0, 0)$. To keep the notation lighter we will also assume that all dimensionful quantities are multiplied by the proper power of the lattice spacing a so to become dimensionless; for instance, $p_\mu \to a p_\mu$, $L_\mu \to L_\mu/a$. The momenta in the Brillouin zone are given by equation (E.3) and, in particular, p_0 mixes with p_1 only. It is convenient to define the not-shifted zero momentum

$$\tilde{p}_0 = \frac{2\pi n_0}{L_0} , \quad n_0 = 0, ..., L_0 - 1 , \quad \text{(E.32)}$$

and the inverse of the gluon propagator can be written as

$$D_G(p) = \sum_\mu \hat{p}_\mu^2 = 2 \sum_\mu (1 - \cos p_\mu) = 8 - 2 \left[\cos(\tilde{p}_0 - \xi p_1) + \sum_{i=1}^{3} \cos p_i \right] . \quad \text{(E.33)}$$

In the infinite volume limit $L_i \to \infty$ the integral $B^{(0)}$ becomes

$$B^{(0)} \xrightarrow{L_i\to\infty} B_\infty^{(0)} \equiv \frac{1}{L_0} \sum_{n_0} \int_{-\pi}^{\pi} \frac{d^3\boldsymbol{p}}{(2\pi)^3} \frac{1}{8 - 2\left[\cos(\tilde{p}_0 - \xi p_1) + \sum_i \cos p_i\right]} , \quad \text{(E.34)}$$

where we replaced the discrete sums over p_1, p_2, p_3 with (continuum) integrals over the Brillouin zone. Using the Schwinger representation

$$\frac{1}{A} = \int_0^{+\infty} d\alpha\, e^{-\alpha A} \tag{E.35}$$

our integral becomes

$$B_\infty^{(0)} = \frac{1}{L_0} \sum_{n_0} \int_{-\pi}^{\pi} \frac{d^3\boldsymbol{p}}{(2\pi)^3} \int_0^{+\infty} d\alpha\, e^{-8\alpha} e^{2\alpha\left[\cos(\tilde{p}_0 - \xi p_1) + \sum_i \cos p_i\right]}\,. \tag{E.36}$$

The integration over the momentum components p_2, p_3 has the following structure:

$$\frac{1}{2\pi} \int_{-\pi}^{\pi} dp\, e^{2\alpha\cos p} = \frac{1}{\pi} \int_0^{\pi} dp\, e^{2\alpha\cos p} = I_0(2\alpha) \tag{E.37}$$

where I_0 is a modified Bessel function. Back to our computation, we change variable $\alpha = x/2$ and we arrive to the final expression

$$\begin{aligned} B_\infty^{(0)} = \frac{1}{L_0} \sum_{n_0=0}^{L_0/a-1} \frac{1}{2} \int_0^{+\infty} dx \Bigg\{ & \left[e^{-x} I_0(x)\right]^2 \\ & \times \int_{-\pi}^{\pi} \frac{dp_1}{2\pi}\, e^{x[\cos(a\tilde{p}_0 - \xi a p_1) + \cos(a p_1) - 2]} \Bigg\}\,, \end{aligned} \tag{E.38}$$

where for definiteness we inserted the proper powers of the lattice spacing a. In this expression the momentum integral over p_1 and the integral over x still need to be computed numerically, but the final result is exactly in infinite volume. Note that in the $\xi = 0$ case the integral $\int dp_1$ "collapses" in one extra factor of $[e^{-x} I_0(x)]$, as expected since the symmetry in the three spatial directions is restored.

E.4.2 Analytic infinite volume of $B_\mu^{(3)}$

Using the same conventions of the previous Subsection E.4.1, we write the infinite volume limit of $B_\mu^{(3)}$ as follows:

$$B_{\mu,\infty}^{(3)} \equiv \frac{1}{L_0} \sum_{n_0} \int_{-\pi}^{\pi} \frac{d^3\boldsymbol{p}}{(2\pi)^3} \frac{\cos p_\mu}{8 - 2\left[\cos(\tilde{p}_0 - \xi p_1) + \sum_i \cos p_i\right]}\,. \tag{E.39}$$

We focus separately on the four components $\mu = 0, 1, 2, 3$. $B_{0,\infty}^{(3)}$ and $B_{1,\infty}^{(3)}$ can be computed in full analogy to what we did for $B_\infty^{(0)}$. The results are

$$\begin{aligned} B_{0,\infty}^{(3)} = \frac{1}{L_0} \sum_{n_0=0}^{L_0/a-1} \frac{1}{2} \int_0^{+\infty} dx \Bigg\{ & \left[e^{-x} I_0(x)\right]^2 \\ & \times \int_{-\pi}^{\pi} \frac{dp_1}{2\pi}\, \cos(a\tilde{p}_0 - \xi a p_1)\, e^{x[\cos(a\tilde{p}_0 - \xi a p_1) + \cos(a p_1) - 2]} \Bigg\}\,, \end{aligned} \tag{E.40}$$

$$B_{1,\infty}^{(3)} = \frac{1}{L_0} \sum_{n_0=0}^{L_0/a-1} \frac{1}{2} \int_0^{+\infty} dx \left\{ \left[e^{-x} I_0(x) \right]^2 \right. \\ \left. \times \int_{-\pi}^{\pi} \frac{dp_1}{2\pi} \cos(ap_1)\, e^{x[\cos(a\tilde{p}_0 - \xi a p_1) + \cos(ap_1) - 2]} \right\}, \tag{E.41}$$

where we inserted the proper powers of the lattice spacing.

For the other two components $B_{2,\infty}^{(3)}$ and $B_{3,\infty}^{(3)}$ the calculation is similar: after using the Schwinger representation (E.35) and change variable $\alpha = x/2$, we have to compute the momentum integral

$$\int_{-\pi}^{\pi} dp_i \, \cos p_i \, e^{x(\cos p_i - 1)} = e^{-x} \frac{d}{dx} I_0(x) = e^{-x} I_1(x) \,, \tag{E.42}$$

where $i = 2, 3$ (but the result is the same). Inserting the proper powers of the lattice spacing we finally get

$$B_{2,\infty}^{(3)} = B_{3,\infty}^{(3)} = \frac{1}{L_0} \sum_{n_0=0}^{L_0/a-1} \frac{1}{2} \int_0^{+\infty} dx \left\{ \left[e^{-x} I_0(x) \right] \left[e^{-x} I_1(x) \right] \right. \\ \left. \times \int_{-\pi}^{\pi} \frac{dp_1}{2\pi} \, e^{x[\cos(a\tilde{p}_0 - \xi a p_1) + \cos(ap_1) - 2]} \right\}. \tag{E.43}$$

The integrals over the momentum $\int dp_1$ and over the auxiliary variable $\int dx$ can be computed numerically.

E.4.3 Analytic infinite volume of $s^{G(0)}$

The tree-level gluonic component of the entropy density is given in equation (4.40) as the discrete derivative in the shift of the tree-level gluonic component of the free-energy density, $f^{G(0)}$. The latter is given in equation (E.22) and the computation of its infinite volume limit is similar to the computations for $B_{\infty}^{(0)}$ and $B_{\mu,\infty}^{(3)}$, although slightly more involved because of the logarithm in the integrand function. Adopting the usual conventions of Subsection E.4.1 we define the infinite spatial volume integral

$$f_{\infty}^{G(0)} \equiv \frac{1}{L_0} \sum_{n_0} \int_{-\pi}^{\pi} \frac{d^3\boldsymbol{p}}{(2\pi)^3} \ln \left(8 - 2\cos(\tilde{p}_0 - \xi p_1) - 2 \sum_i \cos p_i \right) . \tag{E.44}$$

We start with the following one-dimensional integral prototype,

$$\int_{-\pi}^{\pi} \frac{dp}{2\pi} \ln \left(M - 2\cos p \right) = \frac{1}{\pi} \int_0^{\pi} dp \, \ln \left(M - 2\cos p \right) , \tag{E.45}$$

where M is a constant with respect to p. Integrating by parts, using the Schwinger representation and integrating again by parts it is possible to show that

$$\int_{-\pi}^{\pi} \frac{dp}{2\pi} \ln \left(M - 2\cos p \right) = \ln M + \int_0^{\infty} dx \, \frac{1}{x} e^{-xM/2} \left[1 - I_0(x) \right] . \tag{E.46}$$

Our integral (E.43) is a multidimensional version of the prototype (E.45), with three nested integrations over the spatial components of the momentum. We start from the integral in dp_3, and we define

$$M_3 = 8 - 2\cos(\tilde{p}_0 - \xi p_1) - 2\cos p_1 - 2\cos p_2 \tag{E.47}$$

which is constant with respect to the integration over the third component of the momentum. From equation (E.46) we immediately get

$$f_\infty^{G(0)} = \frac{1}{L_0}\sum_{n_0}\int_{-\pi}^{\pi}\frac{dp_1 dp_2}{(2\pi)^2}\left\{\ln M_3 + \int_0^\infty dx\,\frac{1}{x}e^{-xM_3/2}\left[1 - I_0(x)\right]\,.\right\} \tag{E.48}$$

Proceeding iteratively, we focus on the dp_2 integral and we define

$$M_2 = 8 - 2\cos(\tilde{p}_0 - \xi p_1) - 2\cos p_1 \tag{E.49}$$

so that $M_3 = M_2 - 2\cos p_2$. The first piece of (E.48) in terms of M_2 and p_2 is again the integral prototype, while in the second another factor of the Bessel function $I_0(x)$ emerges. In conclusion, the final result is

$$\begin{aligned} f_\infty^{G(0)} = \frac{1}{L_0}\sum_{n_0=0}^{L_0/a-1}\Bigg\{ & \int_{-\pi}^{\pi}\frac{dp_1}{2\pi}\,\ln\left[8 - 2\cos(a\tilde{p}_0 - \xi a p_1) - 2\cos(a p_1)\right] \\ & + \int_0^{+\infty} dx\,\frac{1}{x}e^{-2x}\left[1 - I_0^2(x)\right]\int_{-\pi}^{\pi}\frac{dp_1}{2\pi}\,e^{x[\cos(a\tilde{p}_0 - \xi a p_1) + \cos(a p_1) - 2]}\Bigg\} \end{aligned} \tag{E.50}$$

where we introduced the proper powers of the lattice spacing. The integrals $\int dp_1$ and $\int dx$ can be computed numerically.

One may be worried that the $\sim 1/x$ in the second integral spoils the convergence near the $x = 0$ integral boundary. We thus study the $x \to 0$ limit of the integrand function. The relevant leading quantity is

$$\frac{1 - I_0^2(x)}{x} = \frac{[1 - I_0(x)][1 + I_0(x)]}{x} \approx -\frac{1}{2}x + \mathrm{O}(x^3) \tag{E.51}$$

where we used the $x \to 0$ Taylor expansion of the Bessel function:

$$I_0(x) \approx 1 + \frac{1}{4}x^2 + \mathrm{O}(x^4)\,. \tag{E.52}$$

Therefore the $\int dx$ does not diverge for $x \to 0$. However, in a numerical computation the $\sim 1/x$ may give rise to numerical instabilities. A solution could be to regularize the integral by splitting

$$\int_0^{+\infty} dx = \int_0^{\varepsilon} dx + \int_\varepsilon^{+\infty} dx\,, \tag{E.53}$$

and use the Taylor expansion of the integrand function in the $[0, \varepsilon]$ integral. It must be said that if the numerical integration is carried out with a Gaussian-type quadrature then the integrand function is not evaluated at the boundaries and the numerical problem is circumvented. Using this result we can compute the related entropy $s^{G(0)}$. Results for values of L_0/a relevant to our study are reported in Table 4.6.

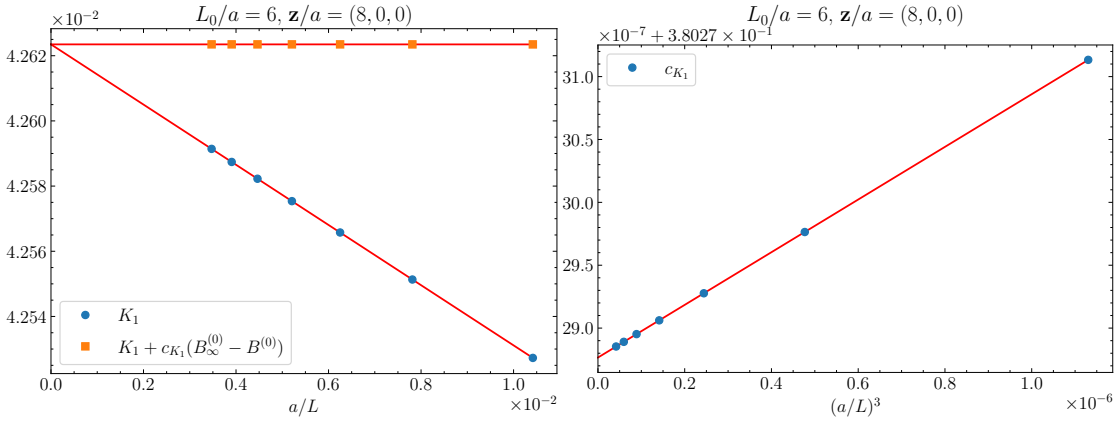

Figure E.1: Left: Infinite volume extrapolation of the integral K_1 at given lattice parameters. The comparison with the subtracted case is shown. The former is fitted linearly in a/L, the latter in $(a/L)^3$. Right: Infinite volume extrapolation for the subtraction coefficient c_{K_1}.

E.4.4 Infinite volume extrapolation of $s^{F(0)}$

The tree-level fermionic entropy density in lattice perturbation theory is defined in equation (4.41) as the derivative in the shift of the tree-level fermionic free-energy $f^{F(0)}$, eq. (E.22). We take the infinite volume limit by extrapolation. At fixed L_0/a, we compute numerically $f^{F(0)}$ at two shifts and combine them so to obtain $s^{F(0)}$. We fix the lattice parameters as described in 4.3. We repeat the computation for increasing values of L/a which is taken to be the same in all the special directions, from $L/a = 96$ to $L/a = 288$. The convergence at infinite volume is very fast: this is expected because fermions at finite temperature have a mass gap $\propto \pi T$ and finite-volume effects are exponentially suppressed with $\sim TL$ [59]. The infinite volume values reported in Table 4.6 are the ones at the largest volume.

E.4.5 Infinite volume extrapolation of $s^{G(1)}$

The 1-loop gluonic contribution to the entropy density is given in equation (4.42) in terms of the discrete derivative in the shift of the free-energy components $f^{G(1,N_c)}$ and $f^{G(1,\frac{1}{N_c})}$, shown in equations (E.23) and (E.24). The latter can be computed analytically in the thermodynamic limit, as well as part of $f^{G(1,N_c)}$, using the results of Subsections E.4.1, E.4.2. However the integrals K_1, K_2 defined in eqs. E.25, E.26 and appearing in $f^{G(1,N_c)}$ have to be extrapolated to infinite volume, as we discuss in the following. For definiteness, we adopt the choice of parameters relevant for our study and described in Section 4.3.

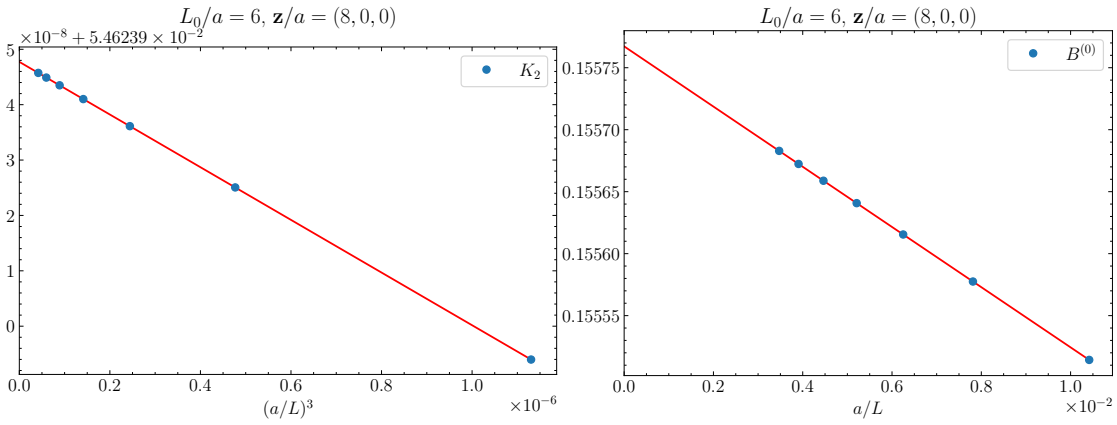

(a) (b)

Figure E.2: Left: Infinite volume extrapolation of the integral K_2. Right: Infinite volume extrapolation of the integral $B^{(0)}$.

Infinite volume limit of K_1, K_2

To start with, we may try to naively extrapolate in the $a/L \to 0$ limit the two integrals. The left panel of Figure E.1 shows (blue circle markers) the infinite volume extrapolation for K_1, at the indicated lattice parameters. The volumes range between spatial sizes $L/a = 96$ and $L/a = 288$. The convergence to thermodynamic limit is as slow as $\sim a/L$. On the contrary, from Figure E.2a we see that K_2 approaches the infinite volume limit with the faster power $\sim (a/L)^3$, so that for all practical purposes we can take the value at the largest lattice size $L/a = 288$ as the infinite volume result. The slow convergence of K_1 can be traced back to the fact that in its integrand function, see eq. (E.25), the powers of momenta from the gluon propagators are not all balanced by the powers of momenta in the numerator (compare for instance with K_2 in eq. (E.26), where this balance occurs). Therefore whenever the unbalanced momentum k goes to zero the integral has the effective behaviour

$$K_1 \sim \int_{k_\xi} \frac{1}{D_G(k)} = B^{(0)}\,, \quad k \to 0\,,\, p, q \neq 0 \tag{E.54}$$

whose approach to the infinite volume limit is $\sim a/L$, see Figure E.2b. This observation gives us the handle to speed up the convergence. We replace K_1 with the subtracted integral

$$\begin{aligned} K_1 \to & K_1 - c_{K_1} B^{(0)} + c_{K_1} B^{(0)}_\infty \\ & = \int_{p_\xi; q_\xi; k_\xi} \left[\frac{\bar{\delta}(p+q+k) \sum_\mu \hat{p}_\mu^2 \, \hat{q}_\mu^2}{D_G(p) D_G(q) D_G(k)} - \frac{c_{K_1}}{D_G(k)} \right] + c_{K_2} B^{(0)}_\infty \,, \end{aligned} \tag{E.55}$$

where c_{K_1} is the residual at the pole $1/D_G(k)$ of the integrand function when $k \to 0$, that is on the momenta hyperplane $p + q = 0$ constrained by the delta function:

$$c_{K_1} = \int_{p_\xi} \frac{\sum_\mu \hat{p}_\mu^4}{D_G^2(p)} \,. \tag{E.56}$$

This coefficient is easily computed numerically, see the right panel of Figure E.1. The expected effect is that the $\sim a/L$ volume effects are removed from K_1, so that the subtracted integral converges to the infinite volume limit faster. Then, the subtracted term can be added in the infinite volume by computing $B_\infty^{(0)}$. The left panel of Figure E.1 shows the comparison of K_1 with its subtracted version (E.55)(orange square markers). The scaling of the latter is $\sim (a/L)^3$, so that its finite volume effects are negligible compared with the not-subtracted integral. In practice we can just use the result at the larger lattice $L/a = 288$ as infinite volume result. We repeat the whole procedure at the two shifts required for the computation of $s^{G(1)}$. The resulting values are reported in Table 4.6. In conclusion, we notice that the large finite volume effects $\sim a/L$ do not cancel when we take the derivative in the shift, therefore the described procedure is necessary also for the infinite volume limit of the entropy density.

E.4.6 Infinite volume extrapolation of $s^{F(1)}$

This contribution is defined as the discrete derivative of the fermionic 1-loop terms of the free-energy density, see equation (4.43). The building blocks are the terms $f^{F(1,N_f)}$, $\mathcal{F}^{F1}$ and $\mathcal{F}^{F2}$, whose expressions can be found in equations (E.28), (E.29) and (E.30) respectively. In the following we consider separately the infinite volume computation of these terms. The infinite volume values of $s^{F(1)}$, relevant for our purposes, are reported in Table 4.6.

Infinite volume limit of $f^{F(1)}$

This term is given in equation (E.28). We can express it analytically in infinite volume but for the integral

$$\begin{aligned} I_f = \int_{q_\xi; p_\xi; k_\xi} \frac{\bar{\delta}(p-q-k)}{D_G(q) D_F(p) D_F(k)} \Bigg[& a m_0(k) \sum_\sigma \bar{r}_\sigma \bar{p}_\sigma + a m_0(p) \sum_\sigma \bar{k}_\sigma \bar{r}_\sigma \\ & - m_0(k) m_0(p) \sum_\sigma \mathrm{c}_\sigma(r) + \sum_\sigma \bar{p}_\sigma \bar{k}_\sigma \left(\mathrm{c}_\sigma(r) - 3\right) \Bigg] \end{aligned} \tag{E.57}$$

which has to be extrapolated to the thermodynamic limit. Working as for the integral K_1 in Subsection E.4.5, we first note that a naive infinite volume extrapolation is plagued by $\sim a/L$ finite volume effects, see the blue circle data in the lest panel of Figure E.3. We note that in the $q \to 0$ limit the integrand function in (E.57) behaves like $\sim 1/D_G(q)$. This suggests to replace I_f with the subtracted integral

$$I_f \to I_f - c_{I_f} B^{(0)} + c_{I_f} B_\infty^{(0)} \,, \tag{E.58}$$

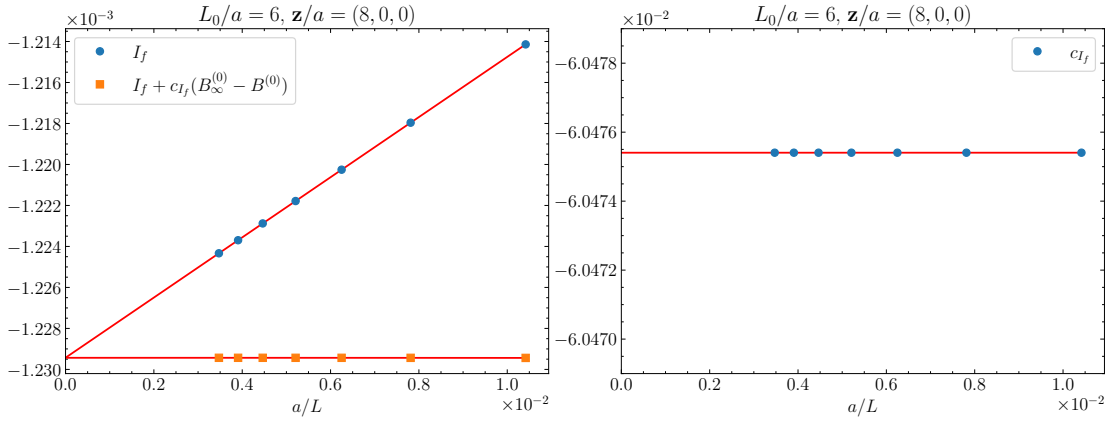

Figure E.3: Left: Infinite volume extrapolation of the integral I_f. The comparison with the subtracted case is shown. The former is fitted linearly in a/L, the latter in $(a/L)^3$. Right: Infinite volume extrapolation for the subtraction coefficient c_{I_f}.

where the coefficient c_{I_f} is the residual at the pole $1/D_G(q)$ of I_f, on the momentum hyperplane $q = p - k = 0$:

$$c_{I_f} = \int_{p_\xi} \frac{1}{D_F(p)^2} \left[2am_0(p) \sum_\sigma \overline{(2p)}_\sigma \overline{p}_\sigma - m_0^2(p) \sum_\sigma \mathrm{c}_\sigma(2p) + \sum_\sigma \overline{p}_\sigma^2 \left(\mathrm{c}_\sigma(2p) - 3 \right) \right] . \tag{E.59}$$

This integral can be easily computed numerically and its finite volume effects are exponentially suppressed and negligible (right panel of Figure E.3). The subtraction (E.58) effectively removes the $\sim a/L$ finite volume effects from I_f, and the convergence to the thermodynamic limit becomes as fast as $\sim (a/L)^3$. We see the subtracted data in the left panel of Figure E.3, orange square markers. We can safely take the value at the largest lattice as the infinite volume limit.

Infinite volume limit of $\mathcal{F}^{F1}$, $\mathcal{F}^{F2}$

These integrals need to be computed numerically. Following the discussion we did so far, we expect that the improvement terms $\mathcal{F}^{F1}$ and $\mathcal{F}^{F2}$ in equations (E.29) and (E.30) approach the infinite volume limit with corrections of the order $\sim (a/L)^3$, since the momentum of the gluon propagator is balanced at the numerator. The data actually show this behaviour, see Figure (E.4). We take the value at the largest lattice, $L/a = 288$, as an estimation of the infinite volume limit.

Infinite volume limit of the mass counterterm

We compute numerically the mass counterterm in equation (E.31) at increasing values of the lattice volume, with sizes from $L/a = 96$ to $L/a = 288$. The finite-volume effects are exponentially suppressed. We quote the value at the largest volume as an estimation of the infinite volume result.

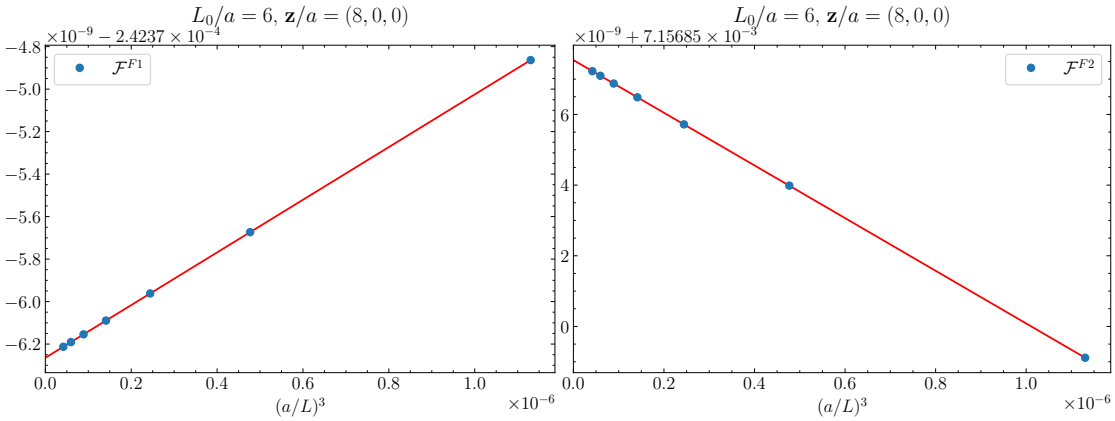

Figure E.4: Left: Infinite volume extrapolation of the integral $\mathcal{F}^{F1}$. Right: Infinite volume extrapolation of the integral $\mathcal{F}^{F2}$.

Appendix F

Technical details on the computation of the QCD entropy density

F.1 Gaussian quadrature

We collect in this Appendix some relevant theoretical aspects of the Gaussian quadrature.

F.1.1 The formula

Given the definite integral

$$I_{[-1,1]}[f] \equiv \int_{-1}^{1} dx\, f(x) \tag{F.1}$$

the n-point *Gaussian quadrature* approximates it with the sum

$$I_{[-1,1]}[f] \approx \sum_{i=1}^{n} \omega_i^{(n)} f(r_i^{(n)}) \tag{F.2}$$

and it is exact if f is a polynomial of degree $\leq 2n-1$. The $r_i^{(n)}$, $i = 1, ..., n$ are the roots of the n-th Legendre polynomial $P_n(x)$, while the coefficients $\omega_i^{(n)}$ are given by

$$\omega_i^{(n)} = \frac{2}{\left[1 - (r_i^{(n)})^2\right] \left[P_n'(r_i^{(n)})\right]^2} \tag{F.3}$$

The Legendre polynomials can be obtained from the recursion

$$n\, P_n(x) = 2n\, x\, P_{n-1}(x) - (n-1)\, P_{n-2}(x)\,, \quad n \geq 2 \tag{F.4}$$

with starting conditions $P_0(x) = 1$, $P_1(x) = x$. The set of polynomials generated in this way satisfies the orthogonality relation

$$\int_{-1}^{1} dx\, P_m(x) P_n(x) = 0 \quad \text{if } n \neq m \tag{F.5}$$

We can generalize to definite integrals in the generic interval $[a, b]$ as follows. We consider the change of variable

$$x = \frac{b-a}{2}\, y + \frac{b+a}{2}, \quad y \in [-1, 1] \to x \in [a, b] \tag{F.6}$$

which allows us to cast the integral on $[a, b]$ to an integral on the standard domain:

$$I_{[a,b]}[f] \equiv \int_a^b dx\, f(x) = \frac{b-a}{2} \int_{-1}^1 dy\, f\left(\frac{b-a}{2}\, y + \frac{b+a}{2}\right) \tag{F.7}$$

We can finally apply equation (F.2) to the last integral in this chain of equalities:

$$I_{[a,b]}[f] \approx \sum_{i=1}^n \omega_i^{(a,b,n)} f(x_i^{(a,b,n)}) \tag{F.8}$$

where

$$\omega_i^{(a,b,n)} = \frac{b-a}{2}\, \omega_i^{(n)}\,, \quad x_i^{(a,b,n)} = \frac{b-a}{2}\, r_i^{(n)} + \frac{b+a}{2} \tag{F.9}$$

are the weights and the sample points for the approximation of the integral in a generic bounded interval.

F.1.2 Accuracy of the Gaussian quadrature

We give some theoretical ground on which the Gaussian quadrature is founded.

Lagrange polynomials

Given n points x_0, ..., x_{n-1}, we define the *Lagrange polynomials* as follows:

$$l_j^{(n-1)}(x) = \prod_{\substack{0 \le i \le n-1 \\ i \ne j}} \frac{x - x_i}{x_j - x_i}\,, \quad j = 0, ..., n-1\,. \tag{F.10}$$

Note that the Lagrange polynomials have degree $n-1$. They satisfy $l_j(x_k) = \delta_{jk}$, therefore they can be used as a basis for expanding polynomials of degree $< n$ given their values at the points x_0, ..., x_{n-1}.

Example. We consider three points x_0, x_1, x_2, thus $n = 3$. The associated Lagrange polynomials are

$$l_0^{(2)}(x) = \frac{x-x_1}{x_0-x_1}\frac{x-x_2}{x_0-x_2}\,, \quad l_1^{(2)}(x) = \frac{x-x_0}{x_1-x_0}\frac{x-x_2}{x_1-x_2}\,, \quad l_2^{(2)}(x) = \frac{x-x_0}{x_2-x_0}\frac{x-x_1}{x_2-x_1}\,. \tag{F.11}$$

□

Gaussian quadrature theorem

We consider a family of orthogonal polynomials $\{L\}$ in the interval $[a, b]$ with weight function ω:

$$\int_a^b dx\, \omega(x) L_m(x) L_n(x) = c_m \delta_{mn}\,. \tag{F.12}$$

We call $r_0, ..., r_{n-1}$ the roots of the polynomial L_n, which has degree n.

Given a polynomial P of degree $< 2n$, it holds that

$$\int_a^b dx\, \omega(x) P(x) = \sum_{j=0}^{n-1} \omega_j P(r_j)\,, \quad \omega_j = \int_a^b dx\, \omega(x) l_j^{(n-1)}(x)\,, \tag{F.13}$$

where $l_j^{(n-1)}$ are the Legendre polynomials associated to the points $r_0, ..., r_{n-1}$.

Proof. We first assume that $\deg P < n$. For $x \in [a, b]$ we can expand the polynomial in the Lagrange basis built with the n roots $r_0, ..., r_{n-1}$ of L_n:

$$P(x) = \sum_{j=0}^{n-1} P(r_j) l_j^{(n-1)}(x)\,. \tag{F.14}$$

Then it is immediate to prove that

$$\int_a^b dx\, \omega(x) P(x) = \sum_{j=0}^{n-1} P(r_j) \int_a^b dx\, \omega(x) l_j^{(n-1)}(x) = \sum_{j=0}^{n-1} \omega_j P(r_j)\,. \tag{F.15}$$

We move to the case $n \leq \deg P < 2n$. We rewrite the polynomial as follows,

$$P(x) = Q(x) L_n(x) + R(x)\,, \tag{F.16}$$

and the integral becomes

$$\int_a^b dx\, \omega(x) P(x) = \int_a^b dx\, \omega(x) Q(x) L_n(x) + \int_a^b dx\, \omega(x) R(x)\,. \tag{F.17}$$

Since $\deg Q < n$, we can expand Q in the basis $\{L\}$ without the element L_n. The first integral thus vanishes for the orthogonality condition (F.12).
Since $\deg R < n$, we can expand it in the same Legendre basis as we did before for P:

$$\int_a^b dx\, \omega(x) R(x) = \sum_{j=0}^{n-1} \omega_j R(r_j)\,. \tag{F.18}$$

However, $P(r_j) = Q(r_j) L_n(r_j) + R(r_j) = R(r_j)$ because r_j is a root of L_n.
We conclude that equation (F.13) holds for any polynomial P with $\deg P < 2n$. □

Polynomial approximation of a function

Let's consider a function $f(x)$, $x \in [a,b]$, and choose n points $x_0, ..., x_{n-1} \in [a,b]$. We introduce a polynomial P that interpolates the function in these points: $P(x_i) = f(x_i)$ for $i = 0, ..., n-1$. Then, $\forall x \in [a,b]$ there exists a point $\xi(x) \in [a,b]$ such that

$$f(x) - P(x) = \frac{1}{n!} f^{(n)}(\xi(x)) \prod_{i=0}^{n-1} (x - x_i) \tag{F.19}$$

where $f^{(n)}$ is the n-th derivative of f.

Proof. We pick a value $\tilde{x} \in [a,b]$ and we define the function

$$g(x) \equiv f(x) - P(x) - Q(x) \frac{f(\tilde{x}) - P(\tilde{x})}{Q(\tilde{x})}\,, \quad Q(x) = \prod_{i=0}^{n-1} (x - x_i)\,. \tag{F.20}$$

The function $g(x)$ has $n+1$ zeros, at the points

$$\tilde{x}, x_0, ..., x_{n-1} \in [a,b]\,. \tag{F.21}$$

Assuming f (and thus g) to be enough differentiable, Rolle's theorem guarantees that its k-th derivative has at least $n+1-k$ roots in $[a,b]$. Therefore the n-th derivative has one root only, let's call it $\xi(\tilde{x}) \in [a,b]$. By differentiating g n times and evaluating in $\xi(\tilde{x})$ we get

$$0 = g^{(n)}(\xi(\tilde{x})) = f^{(n)}(\xi(\tilde{x})) - n!\, \frac{f(\tilde{x}) - P(\tilde{x})}{Q(\tilde{x})}\,. \tag{F.22}$$

Dropping the $\sim$ and solving for $f(x) - P(x)$ leads to equation (F.19). □

Gaussian quadrature of a function

The quadrature theorem tells that with the n roots of a polynomial L_n belonging to some orthogonal basis $\{L\}$ we can compute exactly the integral of a polynomial with degree $\deg P < 2n$.

The n-th order Gaussian quadrature can be used for a generic function f too, as follows:

- interpolate the function f with a polynomial P of degree $< 2n$, such that

  $$P(r_i) = f(r_i)\,, \quad i = 0, ..., n-1\,, \quad r_i \text{ roots of } L_n\,. \tag{F.23}$$

  Note that the polynomial is in general not uniquely determined, because the samples are in principle less than its degree.

- Integrate the polynomial $P(x)$ using Gaussian quadrature. This requires to know the polynomial only at the points r_i.

The polynomial interpolation of the function introduces approximation errors in the Gaussian quadrature of f, with respect to the exact integral. In order to estimate the error we have to reload the previous theorem to the present case, as follows.

Given a polynomial P of degree $\deg P < 2n$ which interpolates a function f in n sample points $x_0, ..., x_{n-1} \in [a, b]$, the error on the approximation is

$$\forall x \in [a,b] \quad \exists \xi(x) \in [a,b] \quad | \\ f(x) - P(x) = \frac{1}{(2n)!} f^{(2n)}(\xi(x)) Q^2(x)\,, \quad Q(x) = \prod_{i=0}^{n-1} (x - x_i)\,. \tag{F.24}$$

Proof. The proof is similar to the previous one. We first observe that the definition (F.20) does not work now, because the polynomial P has order up to $2n$ and thus the n-th derivative of g may not vanish.

We build g so that it has $2n + 1$ roots by taking

$$g(x) \equiv f(x) - P(x) - Q^2(x) \frac{f(\tilde{x}) - P(\tilde{x})}{Q^2(\tilde{x})} \tag{F.25}$$

where $\tilde{x} \in [a, b]$. We now take the $2n$-derivative of g and call $\xi(\tilde{x}) \in [a, b]$ the root of $g^{(2n)}$ in the interval, whose existence is guaranteed by Rolle's theorem:

$$0 = f^{(2n)}(\xi(\tilde{x})) - (2n)!\, \frac{f(\tilde{x}) - P(\tilde{x})}{Q^2(\tilde{x})} \tag{F.26}$$

Equation (F.24) is obtained by dropping $\sim$ and solving for $f(x) - P(x)$. □

A special case of this theorem is when we take the n sample points to be the roots $r_0, ..., r_{n-1}$ of the n-th order orthogonal polynomial L_n defined in the interval $[a, b]$ with weight function ω, see equation (F.12). The approximation formula thus reads

$$f(x) = P(x) + \frac{1}{(2n)!} f^{(2n)}(\xi(x)) L_n^2(x) \tag{F.27}$$

for some $\xi(x) \in [a, b]$. The polynomial P has degree $\deg P < 2n$ and interpolates f in the roots L_n.

The n-order Gaussian quadrature allows to approximate the following integral of f,

$$\int_a^b dx\, \omega(x) f(x) = \sum_{i=0}^{n-1} \omega_i f(r_i) + E_n^G[f]\,, \tag{F.28}$$

where we inserted equation (F.27) and we used the Gaussian quadrature for a polynomial, equation (F.13). The error on the estimation of the n-th order Gaussian quadrature is

$$E_n^G[f] = \frac{1}{(2n)!} \int_a^b dx\, \omega(x) f^{(2n)}(\xi(x)) L_n^2(x)\,. \tag{F.29}$$

In our case, we choose the Legendre polynomials as orthogonal basis. They are defined in the interval $[-1, 1]$ with weight function $\omega(x) = 1$. By a change of variable, it is possible to extend the quadrature to any compact interval.

F.2 Perturbative exploration

In this Section we report the results of the preliminary exploration in lattice perturbation theory at tree-level for the computation of the mass integral χ. These studies served as a guideline for the non-perturbative computation. In particular, the choice of the Gaussian quadratures were inspired from the tree-level results. At this order in perturbation theory we can calculate χ exactly through the shift derivative of the fermionic free-energy at tree-level (4.37). We call it $\tilde{\chi}^{(0)}$:

$$\tilde{\chi}^{(0)}/T^3 = N_c N_f \, \frac{1+\boldsymbol{\xi}^2}{\xi_k} \frac{1}{T^4} \frac{\Delta}{\Delta \xi_k} f^{F(0)} \,. \tag{F.30}$$

However we can also compute it emulating what we do non-perturbatively, that is through the integral in the quark mass of the shift-derivative of the chiral condensate at tree-level (see Section 4.5):

$$\chi^{(0)}/T^3 = -\frac{1+\boldsymbol{\xi}^2}{\xi_k} \frac{1}{T} \int_0^\infty d\widetilde{m}_q \, \frac{\Delta}{\Delta \xi_k} \langle \overline{\psi}\psi \rangle^{(0)}_{\boldsymbol{\xi}, \widetilde{m}_q} \,, \tag{F.31}$$

where $\widetilde{m}_q = m_q/T$ and m_q is the tree-level subtracted bare quark mass (E.17). We can thus study the bounty of the Gaussian quadrature approximation applied to (F.31) by comparing it to the exact value from equation (F.30), at given L_0/a. The tree-level fermionic free energy (4.37) is a purely fermionic integral, and as discussed in Section E.4 its finite volume effects are exponentially suppressed. The same holds for the chiral condensate at tree-level, which is related to the derivative in the bare mass of the free-energy density (E.31):

$$\left\langle \overline{\psi}\psi \right\rangle^{(0)} = -4 N_c N_f F^{(8)} \,. \tag{F.32}$$

We can thus safely work in finite volume with spatial sizes $L/a = 144$. We start from the plot of the integrand function sampled at tree-level, see Figure F.1. The very smooth dependence on the subtracted mass $\widetilde{m}_q$ makes us confident that the polynomial reconstruction underlying the Gaussian quadrature will work excellently. The mild peaked structure suggests to split the integration in three intervals: the peak itself $\chi^{(0)}_{\text{peak}}$, which gives the bulk of the area, the tail $\chi^{(0)}_{\text{tail}}$ up to some conveniently chosen value of the mass, and a residual term $\chi^{(0)}_{\text{res}}$ to estimate the contribution from the asymptotic behaviour at large mass. This last term is integrated in the hopping parameter κ, so that the integration interval is compact. We call $\widetilde{m}_1$, $\widetilde{m}_2$ the two masses that split the integration interval. We choose them so that $\sim 80\%$ of the integral falls in $\chi^{(0)}_{\text{peak}}$, $\sim 20\%$ is given by $\chi^{(0)}_{\text{tail}}$ and the residue $\chi^{(0)}_{\text{res}}$ is of the order of less than one sigma in the target relative error of $\sim 0.5\%$ on the non-perturbative integral. Note that towards the continuum limit the integrand function appears to go to zero faster at large mass, which means that $\chi^{(0)}_{\text{res}}$ becomes less and less important. Table F.1 shows the contributions at tree-level computed as in eq. (F.30), and the chosen values for the split masses. The mass $\widetilde{m}_1 = 5.0$ is common to all the lattice resolutions, while $\widetilde{m}_2 = 35.0$ for $L_0/a = 4$ and $\widetilde{m}_2 = 20.0$ for

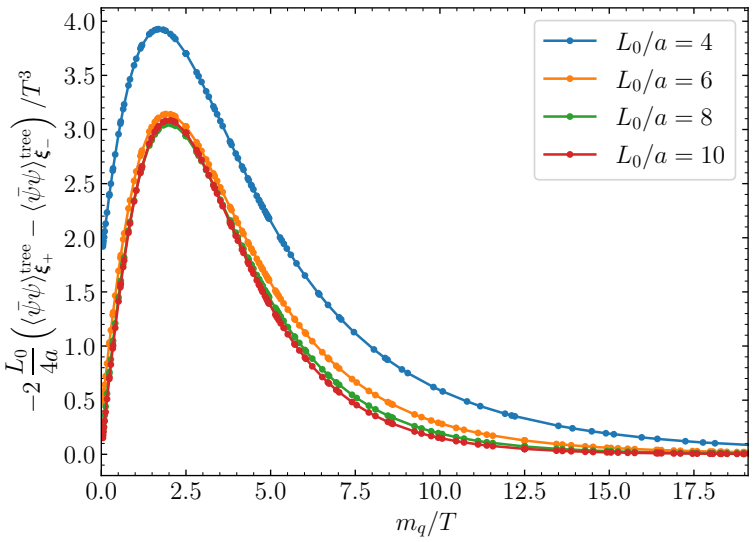

Figure F.1: Integrand function of χ at tree-level in lattice perturbation theory. The function has been sampled in many points and then interpolated.

L_0/a	$\tilde{\chi}^{(0)}_{\rm peak}/T^3$	$\widetilde{m}_1$	$\tilde{\chi}^{(0)}_{\rm tail}/T^3$	$\widetilde{m}_2$	$\tilde{\chi}^{(0)}_{\rm res}/T^3$	$\tilde{\chi}^{(0)}/T^3$	$0.5\%\,\tilde{\chi}^{(0)}/T^3$
4	15.938	5.0	8.755	35.0	0.067	24.760	0.124
6	11.915	5.0	4.666	20.0	0.066	16.647	0.083
8	11.200	5.0	3.595	20.0	0.017	14.812	0.074
10	11.155	5.0	3.142	20.0	0.007	14.304	0.072

Table F.1: Contributions to the mass integral χ at tree-level in lattice perturbation theory. The computation is carried out with the derivative in the shift of the tree-level fermionic free-energy.

$L_0/a = 6, 8, 10$ to take into account the slower asymptotic decrease at large mass of the coarsest lattice. For comparison, the table shows the 0.5% of the central value in lattice perturbation theory, as an estimation for the target non-perturbative error. As discussed, the residual term is half sigma for $L_0/a = 4$, and it drops to $\sim 1/10$ sigma at $L_0/a = 10$. We are left with the choice of the order of the three Gaussian quadratures. This is related to the number of points where the integrand function has to be sampled. We explored different setups and at the end we opted for a total of 20 points, 10 of which for the peak and 7 and 3 for the tail and residue respectively. In table F.2 we see the relative error on this Gauss approximation with respect to the exact value. The systematics introduced by the Gaussian quadratures is completely negligible with respect to the target accuracy $\sim 0.5\%$ on the integral.

L_0/a	$\chi^{(0)}/T^3$	$\lvert\tilde{\chi}^{(0)} - \chi^{(0)}\rvert/\tilde{\chi}^{(0)}$ (%)	$\tilde{\chi}^{(0)}/T^3$
4	24.76028	0.002	24.75990
6	16.63858	0.050	16.64685
8	14.80506	0.047	14.81204
10	14.29978	0.032	14.30431

Table F.2: Second column: integral χ computed with Gaussian quadratures at tree-level in lattice perturbation theory. To be compared with the last column, where the same quantity is computed as in equation (F.30). Third column: relative percentile systematic error of the quadrature. To be compared with the target accuracy $\sim 0.5\%$.

F.3 Bare parameters and collected statistics

Table F.4 reports the values of the bare couplings $g_0^2 = 6/\beta$ that were simulated for the computation of the Gauss quadratures for the determination of s_∞ in eq. (4.16). The spatial volume of the simulations is $L/a = 144$. At each value of L_0/a and g_0^2 we generated two Monte Carlo streams at the two shifts $\boldsymbol{\xi}_+$, $\boldsymbol{\xi}_-$ of eq. (4.23). The observable of interest from these simulations is the gauge action S^G, and in the Table F.4 the number of measurements at the two shifts is also reported.

In full QCD simulations the main observable is the chiral condensate $\langle\overline{\psi}\psi\rangle$, for the computation of the integral χ in eq. (4.16). The analogous table for QCD simulations would have 40 entries at each of the 36 couples of L_0/a, β of Table F.3, and thus would be unpractical. However, at given couple L_0/a, g_0^2 the simulated values of the hopping parameter κ can be uniquely computed with the Gauss quadrature scheme described in Table 4.4 and related main text. Then, the number of measurements of the chiral condensate is given by the optimized statistics in Table F.8 and it is the same at the two shifts. As the temperature decreases, we incremented the statistics up to a factor 2 at T_8, so to keep roughly constant the target relative error of Table F.8.

F.4 Systematic effects from the quadrature

We checked the systematics induced by the numerical Gaussian quadrature using the Gauss-Kronrod rule. This quadrature improves the precision of a Gaussian quadrature by adding points to the already evaluated Gauss points, although the gain in precision is less than a pure Gaussian quadrature with more points. On the other end, a higher order Gaussian quadrature would require the re-evaluation of all the points, which is more expensive. Given the n-th order Gaussian quadrature based on Lagrange polynomials, the related Kronrod rule adds $n+1$ points and it is exact for polynomials up to degree $3n+1$ if n is even, $3n+2$ if n is odd [131].

We use preliminary data at bare parameters 6×48^3, $\beta = 8.8727$. We focus on the computation of the peak part of the integral, in the interval of bare mass $am_0 \in [am_{\rm cr}, 0.5]$. We check the consistency of a $n = 5$ Gaussian quadrature with a $n = 5 + 6$ Gauss-Kronrod quadrature, which requires the numerical determination of 6 extra points.

T	L_0/a	β	$\kappa_{\rm cr}^{(W)}$	$c_{\rm sw}^{(W)}$
T_0	4	8.7325	0.131887597685602	1.224666388699756
	6	8.9950	0.131885781718599	1.214293680665697
T_1	4	8.3033	0.132316223701646	1.244443949720750
	6	8.5403	0.132336064110711	1.233045285565058
	8	8.7325	0.132133744093735	1.224666388699756
	10	8.8727	0.131984877002653	1.218983546266290
T_2	4	7.9794	0.132672230374640	1.262303345977765
	6	8.2170	0.132690343212428	1.248924515099129
	8	8.4044	0.132476707113024	1.239426196162344
	10	8.5534	0.132305706323476	1.232451001338001
T_3	4	7.6713	0.133039441274476	1.282333503658225
	6	7.9091	0.133057201010874	1.266585617959733
	8	8.0929	0.132831173856378	1.255711356539447
	10	8.2485	0.132638399517155	1.247267216254281
T_4	4	7.3534	0.133449711446233	1.307002958449583
	6	7.5909	0.133469338865844	1.288146969458134
	8	7.7723	0.133228362183550	1.275393611340024
	10	7.9322	0.133013578229002	1.265160978064686
T_5	4	7.0250	0.133908723921720	1.338089264736139
	6	7.2618	0.133933679858703	1.315030958783770
	8	7.4424	0.133674531074371	1.299622821237046
	10	7.6042	0.133438165920285	1.287166774665371
T_6	4	6.7079	0.134386271436463	1.375352693193284
	6	6.9433	0.134421953633166	1.346919223092444
	8	7.1254	0.134141768774467	1.327878356622864
	10	7.2855	0.133888442235086	1.312909828079458
T_7	4	6.3719	0.134926677491050	1.425561566301377
	6	6.6050	0.134982857878749	1.389385004928746
	8	6.7915	0.134676613758678	1.364706438701718
	10	6.9453	0.134412950133538	1.346697162567041
T_8	4	6.0433	0.135481632961481	1.489790983990814
	6	6.2735	0.135571353236717	1.442967721668930
	8	6.4680	0.135236172024848	1.409845308468962
	10	6.6096	0.134976206524104	1.388734449325687

Table F.3: Lines of constant physics for simulations performed with the Wilson plaquette action, and $N_f = 3$ flavours of O(a)-improved Wilson fermions. At each temperature the values of L_0/a and bare coupling $\beta = 6/g_0^2$ are reported, together with the critical hopping parameter $\kappa_{\rm cr}$ and the improvement coefficient $c_{\rm sw}$ for the Sheikholeslami-Wohlert term in the lattice action.

	$L_0/a = 4$			$L_0/a = 6$			$L_0/a = 8$			$L_/a = 10$		
	β	$\boldsymbol{\xi}_-$	$\boldsymbol{\xi}_+$	β	$\boldsymbol{\xi}_-$	$\boldsymbol{\xi}_+$	β	$\boldsymbol{\xi}_-$	$\boldsymbol{\xi}_+$	β	$\boldsymbol{\xi}_-$	$\boldsymbol{\xi}_+$
start	30.0000	5648	4057									
	15.0000	1734	1829	15.0000	4314	4442	15.0000	42944	30249	15.0000	31539	31627
	13.9517	1083	1095	13.9517	1856	2035	13.9517	25631	25339	13.9517	34320	33560
start	11.2500	3036	3052	11.2500	2412	2513	11.2500	28930	30007	11.2500	15356	15963
	9.4249	3115	3104	9.4249	1486	1530	9.4249	21371	21709	9.4249	15932	16353
	8.9690	3094	2721									
T_0	8.8642	3118	3026	8.9975	2270	1787						
	8.7618	3098	3026									
	8.9157	1725	1680	8.9457	2546	2100	8.9690	8047	6338	8.9855	8497	10122
T_1	8.6376	1682	1646	8.7641	3151	3159	8.8642	8108	7958	8.9359	9922	10828
	8.3764	2061	1993	8.5897	2568	2589	8.7618	6053	6839	8.8869	9475	9449
	8.9157	2934	3064	8.5026	4453	4141	8.6942	7201	7331	8.8355	8270	8916
T_2	8.6376	2850	2967	8.3755	4900	4966	8.5653	9387	7149	8.7101	7933	8946
	8.3764	2981	2972	8.2522	2470	2454	8.4401	7337	7375	8.5882	8444	9431
	8.2655	2064	2009	8.1811	2597	4103	8.3681	10827	10709	8.5179	8571	9623
T_3	8.1381	2103	2060	8.0601	3210	3223	8.2457	10669	7397	8.3982	8653	9213
	8.0146	2038	2069	7.9426	2598	2607	8.1268	10452	10716	8.2818	8631	9546
	7.3149	1236	1223	7.8719	1218	2525	8.0555	9235	9001	8.2116	8245	6943
T_4	7.1854	2380	2327	7.7467	2417	2457	7.9294	10595	13126	8.0873	8509	9765
	7.0605	1232	1235	7.6255	1181	1189	7.8072	8998	10287	7.9666	8678	9686
	6.9878	1326	1310	7.5523	1036	1181	7.7337	8451	7935	7.8938	8676	9771
T_5	6.8628	2649	2575	7.4227	1708	2020	7.6038	5111	5885	7.7647	8760	9710
	6.7422	1321	1324	7.2975	1997	1034	7.4782	8054	6391	7.6398	8749	9599
	6.6683	1226	1213	7.2245	1330	1327	7.4053	10428	10594	7.5669	8811	8716
T_6	6.5356	2359	2292	7.0990	2539	2617	7.2805	10504	10442	7.4414	8856	9981
	6.4081	1224	1225	6.9778	1315	1209	7.1598	10867	10667	7.3201	8854	7909
	6.6913	1544	1527	6.9267	1230	1273	7.1090	11175	11058	7.2688	8876	9974
	6.6273	2667	2619	6.8622	2357	2920	7.0455	11205	12196	7.2041	5943	10005
T_7	6.5356	1784	1753	6.7699	2247	1485	6.9544	11232	12225	7.1113	4506	5067
	6.4464	2580	2656	6.6801	1865	1944	6.8657	11235	10746	7.0210	8927	10052
	6.3869	1493	1554	6.6201	1264	535	6.8065	11251	11160	6.9605	5362	8912
	6.3557	1840	1884	6.5887	2749	1736	6.7756	2384	2364	6.9288	6249	7127
	6.2929	1930	1895	6.5254	3483	1547	6.7140	2374	2359	6.8648	6236	7147
T_8	6.2033	2455	2381	6.4350	2759	2224	6.6258	2385	2298	6.7733	6311	7168
	6.1161	1866	1923	6.3470	2827	3465	6.5399	1982	2368	6.6842	6306	7189
	6.0580	1276	1248	6.2883	2751	3476	6.4825	2113	2379	6.6246	6277	7112

Table F.4: First column: values of $\beta = 6/g_0^2$ where $\langle S^G \rangle$ is sampled in pure gauge. Second and third columns: number of measurements at the two shifts of the observable. Rows are separated according to the quadrature scheme of Table 4.2. The same structure for all the L_0/a.

k	quad	nms	integrand	interp
0.13180	GK	500	4.10(32)	2.0(3)
0.13085	G	500	12.54(29)	
0.12902	GK	500	25.16(27)	25.43(24)
0.12651	G	500	31.68(21)	
0.12363	GK	500	29.30(24)	29.25(22)
0.12066	G	500	22.51(22)	
0.11783	GK	500	16.24(17)	16.14(19)
0.11532	G	500	11.89(16)	
0.11332	GK	500	9.01(14)	9.19(15)
0.11194	G	500	7.26(15)	
0.11125	GK	500	6.54(13)	6.12(17)

Table F.5: Exploratory results for 6×48^3, $\beta = 8.8727$. The last column shows the values, at the Kronrod points, obtained from the Lagrange interpolation of the Gauss points. The Kronrod points in the first and last rows are outside the interval of definition of the Gaussian quadrature.

quad	value
G	13.655(69)
GK	13.679(49)
diff	0.024(50)

Table F.6: Comparison between the integral computed with Gaussian quadrature and Gauss-Kronrod quadrature. The data used are the ones in Table F.5. The last row contains the correlated difference of the two integrals.

The resulting quadrature is exact for polynomials of order ≤ 17. The numerical values are stored in Table F.5, where we denote by G the original Gauss points, and with GK the added Gauss-Kronrod points. The number of measurements per point is reported. The Gauss rule we use relies on approximating the integrand function with Lagrange polynomials. The reconstruction of the integrand function is robust if the Lagrange interpolation of the Gauss points can predict the position of some other points, such as the Kronrod points. The last column of Table F.5 stores the values of the integrand function at the Kronrod points obtained from the interpolation as described above. We see that, within the interval of the Gauss points (i.e. excluding the first and last rows), the interpolated values are in perfect agreement with the numerical Kronrod values. The points and the Lagrange interpolation are shown in Figure F.2. The direct check of the integration is in Table F.6, where the integrals computed with the Gauss and Gauss-Kronrod quadratures are compared. The correlated difference is compatible to zero, and it is half of the smallest sigma. Since in the final simulations we estimate the peak with a $n = 10$ quadrature, we expect this difference to become negligible.

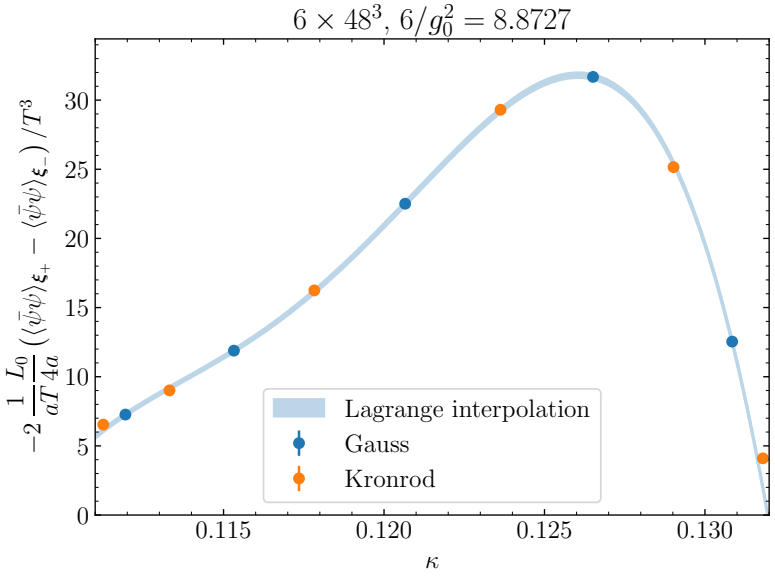

Figure F.2: 6×48^3, $\beta = 8.8727$. Integrand function for the mass integral. The points are labelled as Gauss or Kronrod. Errorbars are smaller than markers. The Lagrange interpolation of the Gauss points is shown.

F.5 Simulation details

We have simulated lattice QCD using the HMC algorithm, see also Section 3.7. Our code is based on the package `openQCD-1.6` [99], modified for including shifted boundary conditions. We employed even-odd preconditioning for all the $N_f = 3$ flavors [97]. The strange quark has been included with the RHMC algorithm. The solution of the Dirac equation in the molecular dynamics trajectory was performed with a standard conjugate gradient with chronological inversion. In the following, we focus on the thermalization procedure of our ensembles. We discuss the parameters of the algorithm in the dedicated Section F.6.

Simulations at each set of bare parameters $\{L_0/a,\, g_0^2,\, \kappa,\, \boldsymbol{\xi}\}$ were first generated on lattices with spatial extensions $L/a = 48$, with a statistics of 500-1000 trajectories of 2 MDUs each. We proceeded from high to low temperatures, and the last configuration of each ensemble was used as starting point for the ensemble at the same shift and closest hopping parameter at the next lower temperature. These small volume runs served both as a thermalization for larger volumes, and for checks on the algorithm performance. At selected values of the bare mass we measured the spectral range of the Dirac operator, which is needed for the optimal tuning of the Hasenbusch masses and of the RHMC. We always monitored the components of the Energy-Momentum tensor as well as the Monte Carlo history of the Wilson-flowed plaquette and topological charge. In our simulations we also paid attention to the phase of the Polyakov loop measured on the generated gauge configurations especially at large bare quark mass, where the theory is sensible to

the $\mathbb{Z}_3$ center symmetry.

The target lattices with $L/a = 144$ were generated by tripling the $L/a = 48$ ones in the spatial directions, after checking that the starting small volume configuration was in the trivial topology sector and had null Polyakov phase. At the lowest temperatures and largest masses, where the topological activity is less suppressed, we further refined the thermalization procedure considering two steps: from $L/a = 24$ lattices to $L/a = 72$ ones and finally to the target volume by duplicating the spatial directions. This allowed us, in the last step, to anti-periodically extend the $L/a = 72$ lattice to the $L/a = 144$ so to start with exactly zero topology on the target lattice. We finally measured our observables on the $L/a = 144$ lattices after 50-100 trajectories of thermalization. The same checks on Energy-Momentum tensor, topology, plaquette and Polyakov loop were performed on the final ensembles too.

F.6 Tuning of the HMC

In the following we describe our algorithmic choices to optimize the QCD simulations. See Table F.7 for a schematic summary. We performed the tuning of the simulation parameters on 6×48^3 lattices at the inverse bare coupling $\beta = 8.8727$, and for forward shift $\boldsymbol{z}/a = (8, 0, 0)$. We started from a high-mass (low-κ) ensemble and we progressively decreased the bare mass. At the different values of hopping parameter κ we tried many algorithmic setups. We defined a performance estimator given by the ratio of the computational time over acceptance rate: the best algorithm is the one that minimizes this estimator (with a lower bound of $\sim 90\%$ on the acceptance). We also monitored the spectrum of the Dirac operator so to optimally tune the Hasenbusch twisted-masses and the RHMC. In particular as the quark masses decrease the spectrum shifts downwards: the interval for the rational approximation has to be accordingly tuned, and the number of poles increased to keep the approximation error under control.

We start from small values of the hopping parameter and describe how the algorithm becomes progressively more and more elaborate towards the chiral limit. At the smallest values of hopping parameter, we used a plain 2-level algorithm where the gauge force is at the finest level and the fermionic forces at the coarsest. These included the contributions from the light doublet and from the RHMC for the strange quark. Both levels have been integrated with a 4^{th} order Omelyan-Mryglod-Folk scheme [123], the finer with 1 step and the coarser with a tunable number of steps. By looking at the performance estimator and the acceptance, we saw that the Hasenbusch preconditioning of the light doubled determinant is not required up to $\kappa \sim 0.1$. In the interval $0.10 \lesssim \kappa \lesssim 0.12$ this simple algorithm has been refined with one Hasenbusch twisted-mass chosen as suggested in [74]. For $\kappa \gtrsim 0.12$, we opted for a frequency splitting of the RHMC in two terms, and we added a third integration level to profit from the hierarchy of the two contributions. The outermost level has been integrated with a 2^{nd} order Omelyan scheme with a tunable number of steps, while the two finer levels with 1 step. More refined algorithms were not competitive up to $\kappa \gtrsim 0.126$, where we further split the light determinant with one extra Hasenbusch twisted-mass. We tried many setups, including a generalization of the rule

level	integrator	$\kappa < 0.098$	$0.098 < \kappa < 0.120$	$0.120 < \kappa < 0.126$	$\kappa > 0.126$
0	OMF4	G	G	G	G
1	OMF4	L[0] S[1, d]	L[0, μ_0] L[μ_0] S[1, d]	L[0, μ_0] L[μ_0] S[1, 5]	L[0, μ_1] L[μ_1, μ_2] L[μ_2] S[1, 5]
2	OMF2			S[5, d]	S[5, d]
algorithm		A0	A1	A2	A3

Table F.7: Algorithms used to simulate QCD for increasing κ (decreasing quark mass). Capital G denotes the gauge force. Capital L denotes the (frequency-split) light quark force, with the relative Hasenbusch twisted-masses in square brackets. Capital S is the (frequency-split) strange quark force, with the associated RHMC poles in square brackets (d is the degree of the rational approximation). See main text for details.

proposed in [74] to the two twisted-mass case. At the end we found that two twisted-masses equally spaced in the spectrum of the Dirac operator was a valuable choice in terms of performance. In all the chosen integration schemes for the molecular dynamics, the coarsest level has been discretized with a number of steps increasing from 7 to 15 for decreasing bare mass and temperature.

F.6.1 Choice of Hasenbusch and RHMC parameters

We describe the tuning of the Hasenbusch and RHMC parameters as the bare quark mass changes. We follow the notation of Table F.7. At given bare lattice parameters $(L_0/a, g_0^2, \boldsymbol{\xi}, \kappa)$, we call $r_{a,m}$ and $r_{b,m}$ the measured spectrum of the Dirac operator. These measurements has been performed on gauge configurations produced under some guessed values of the parameters. Then, we chose the optimized Hasenbusch twisted-masses as

$$\mu_i = \begin{cases} \sqrt{r_{a,m} \cdot r_{b,m}} & i = 0 \\ r_{a,m} + \frac{1}{3}(r_{b,m} - r_{a,m}) & i = 1 \\ r_{b,m} - \frac{1}{3}(r_{b,m} - r_{a,m}) & i = 2\,. \end{cases} \tag{F.33}$$

The $i = 0$ case of algorithms A1, A2 has been chosen as prescribed in [74], so that the pseudofermion propagator split in two operators with the same condition number. The values μ_1, μ_2 were used in the algorithm A3 and they are equally spaced in the spectral range $[r_{a,m}, r_{b,m}]$.

In the RHMC algorithm we have to specify the interval $[r_a, r_b]$ and the degree of the rational approximation d, which is also the number of poles of the rational function. We chose

$$r_a = 0.7 \cdot r_{a,m} \quad r_b = 1.2 \cdot r_{b,m} \tag{F.34}$$

so that the measured spectrum was safely contained in the approximation interval. We

tuned the degree d so to make the approximation error smaller than a chosen threshold,

$$12V\delta^2 \lesssim 10^{-5}\,, \tag{F.35}$$

where δ is the maximum theoretical error of equation (3.96) and the factor $12V$ counts the fermionic degrees of freedom. In our simulations, d ranged between 3 and 10.

At given L_0/a and g_0^2 we had to tune the parameters for all the values of κ needed for the Gauss quadratures. Instead of measuring the Dirac spectrum at all κ, we simplified the work by noticing that, roughly speaking, when the mass changes the spectrum of the Dirac operator gets shifted of the same amount. Therefore if the spectrum is known at some reference value $\tilde{\kappa}$, a reasonable guess of the spectrum at another value can be obtained by shifting it of the difference of the respective bare masses,

$$r_{a,m}(\kappa) = r_{a,m}(\tilde{\kappa}) + \Delta a m_0\,, \quad r_{b,m}(\kappa) = r_{b,m}(\tilde{\kappa}) + \Delta a m_0\,, \tag{F.36}$$

where the mass shift amounts to

$$\Delta a m_0 = \frac{1}{2\kappa} - \frac{1}{2\tilde{\kappa}}\,. \tag{F.37}$$

In practice, at given L_0/a and g_0^2, we measured the spectrum at some selected values of κ starting from the highest value (lightest quark mass), and we predicted the spectrum at the other values of hopping parameter using equation (F.36).

F.7 Random sources

On the lattice, we consider the one-point function

$$a^3\langle\overline{\psi}\Gamma\psi\rangle = -\frac{\int DU\ \det D\, a^{-1}\mathrm{Tr}\,\{\Gamma S\}\ e^{-S^G}}{\int DU\ \det D\, e^{-S^G}} = -a^{-1}\langle\mathrm{Tr}\,\{\Gamma S\}\rangle_U\,, \tag{F.38}$$

where in the second step we performed the analytical integration over Grassmann variables, and in the last step we defined the expectation value on the gauge field $\langle\cdot\rangle_U$. The operator S is the quark propagator, and the matrix Γ stands for any possible spinor and/or flavour structure of the local field. In numerical simulations, for each gauge configuration we have to compute the trace

$$\mathrm{Tr}\,\{\Gamma S\} = \sum_x \mathrm{tr}\,\{\Gamma S(x,x)\}\ , \tag{F.39}$$

whose direct evaluation is very demanding from the computational point of view. The trace can also be estimated stochastically, as reviewed for instance in [66]. We introduce a set of random auxiliary fields called *random sources*, obeying the relation

$$\langle\overline{\eta}^i_\alpha\,\eta^j_\beta\rangle_\eta = \delta^{ij}\delta_{\alpha\beta}\,, \tag{F.40}$$

where α,β are collective labels for all the possible indices (in particular spinor, colour and spacetime) and i,j label the random source "configuration". The expectation value

$\langle\cdot\rangle_\eta$ is taken with respect to the probability distribution of the random sources. It is straightforward to prove that

$$\langle\overline{\eta}\,\Gamma S\,\eta\rangle_\eta = \mathrm{Tr}\,\{\Gamma S\}\ , \tag{F.41}$$

and if we consider a finite set of N_s random sources, a valid stochastic estimator of the trace is

$$\mathrm{Tr}\,\{\Gamma S\} \approx \mathcal{O}[U,\overline{\eta},\eta] \equiv \frac{1}{N_s}\sum_{i=1}^{N_s}\overline{\eta}^i_\alpha(\Gamma S)_{\alpha\beta}\eta^i_\beta \tag{F.42}$$

where we explicitly wrote the index contractions (repeated letters are summed). Therefore, at fixed gauge configuration we can estimate the trace by sampling N_s random sources and using equation (F.42). The variance of the stochastic estimator (F.42) contains an effect due to the random sources, in addition to the usual noise from the gauge configurations. The computation of this variance involves the 4-point function of the random sources. We thus specialize to U(1) random sources, which is the choice for our simulations., and the 4-point function reads [87]

$$\left\langle\overline{\eta}_\alpha\eta_\beta\overline{\eta}_\gamma\eta_\delta\right\rangle_\eta = \delta_{\alpha\beta}\delta_{\gamma\delta} + \delta_{\alpha\delta}\delta_{\beta\gamma} - \delta_{\alpha\beta\gamma\delta}\,. \tag{F.43}$$

The variance of our estimator is

$$\mathrm{var}\,[\mathcal{O}] = \langle\langle\mathcal{O}^2\rangle_\eta\rangle_U - \langle\langle\mathcal{O}\rangle_\eta\rangle^2_U \tag{F.44}$$

where we explicitly indicate the nature of the expectation value, i.e. over random sources and over gauge configurations. This gives

$$\begin{aligned}\mathrm{var}\,[\mathcal{O}] = \Big\langle\Big\langle\frac{1}{N_s^2}\sum_{i,j}\overline{\eta}^i_\alpha(\Gamma S)_{\alpha\beta}\eta^i_\beta\,\overline{\eta}^j_\gamma(\Gamma S)_{\gamma\delta}\eta^j_\delta\Big\rangle_\eta\Big\rangle_U \\ - \Big\langle\Big\langle\frac{1}{N_s}\sum_i\overline{\eta}^i_\alpha(\Gamma S)_{\alpha\beta}\eta^i_\beta\Big\rangle_\eta\Big\rangle^2_U\,,\end{aligned} \tag{F.45}$$

and after computing the contractions we get

$$\mathrm{var}\,[\mathcal{O}] = \mathrm{var}\,[\mathcal{O}]_U + \frac{1}{N_s}\mathrm{var}\,[\mathcal{O}]_\eta \tag{F.46}$$

where we separated the two contributions coming respectively from the gauge noise and the random sources noise:

$$\mathrm{var}\,[\mathcal{O}]_U = \left\langle\mathrm{Tr}^2\{\Gamma S\}\right\rangle_U - \langle\mathrm{Tr}\,\{\Gamma S\}\rangle^2_U\,, \tag{F.47}$$

$$\mathrm{var}\,[\mathcal{O}]_\eta = \left\langle\mathrm{Tr}\left\{(\Gamma S)^2\right\}\right\rangle_U - \Big\langle\sum_\alpha[(\Gamma S)_{aa}]^2\Big\rangle_U\,. \tag{F.48}$$

Notice that, given a matrix M, $\mathrm{Tr}\left\{M^2\right\} = \sum_{\alpha\beta}M_{\alpha\beta}M_{ba} \neq \sum_\alpha(M_{\alpha\alpha})^2$. Equation (F.46) shows that, in addition to the usual variance, the random sources give a contribution that

is suppressed with their number N_s. In practice, N_s is tuned so that the variance from the sources is subdominant compared to gauge variance.

It may be useful to disentangle the two contributions so to have control on them separately. In equation (F.45) the variance contribution from the random sources comes entirely from the 4-point function of the sources themselves, as well as the connected part $\left\langle \mathrm{Tr}^2\{\Gamma S\}\right\rangle_U$ of the gauge variance. We observe that, if we consider two independent sets of noise sources $\overline{\eta}, \eta$ and $\overline{\phi}, \phi$, we can define two independent observables $\mathcal{P}[U, \overline{\eta}, \eta]$ and $\mathcal{Q}[U, \overline{\phi}, \phi]$ as in equation (F.42). Then, the quantity

$$\left\langle \langle \mathcal{P}\mathcal{Q}\rangle_{\eta,\phi}\right\rangle_U = \left\langle \mathrm{Tr}^2\{\Gamma S\}\right\rangle_U \tag{F.49}$$

involves 2-point functions only of the random sources, leading to the desired connected part of the gauge variance without the sources terms. In practice, since each noise source is independent from the others, we can split the noise sources in two sets (the first half and the second half, say) and average them separately. The disconnected part of the gauge variance can be computed in the standard way. This procedure, known as *diluition*, allows to compute the gauge variance alone. The variance of the sources is then obtained by subtraction from the full result.

F.8 Variance reduction

On a gauge configuration, we estimate the chiral condensate by computing stochastically the trace of the propagator as discussed in Appendix F.7. Calling $\overline{\eta}, \eta$ the U(1) random sources, the estimator reads

$$\mathcal{O}[U, \eta] = \frac{1}{N_s}\sum_{i=1}^{N_s}\sum_x \overline{\eta}^i(x) S[U] \eta^i(x)\,, \tag{F.50}$$

where $S = (D + M_0)^{-1}$ is the quark propagator and N_s is the number of random sources generated for the estimation. The gauge and random sources components of the variance of $\mathcal{O}$ can be written using equations (F.47), (F.48),

$$\mathrm{var}\left[\mathcal{O}\right]_U = \left\langle \mathrm{Tr}^2\{S\}\right\rangle_U - \left\langle \mathrm{Tr}\,\{S\}\right\rangle_U^2\,, \tag{F.51}$$

$$\mathrm{var}\left[\mathcal{O}\right]_\eta = \left\langle \mathrm{Tr}\left\{S^2\right\}\right\rangle_U - \left\langle \sum_\alpha (S_{\alpha\alpha})^2\right\rangle_U\,, \tag{F.52}$$

and in the last equation the index α runs over all the indices of the quark propagator: spacetime, flavour, spin and colour. Since we have to compute the chiral condensate at large masses, that is small hopping parameter κ, the hopping expansion of these quantities may shed some light on their behaviour in this regime. The computation can be found in Subsection F.8.1. At leading order the variances scale as follows:

$$\mathrm{var}\left[\mathcal{O}\right]_U \sim \kappa^6\,, \quad \mathrm{var}\left[\mathcal{O}\right]_\eta \sim \kappa^4\,, \quad \kappa \to 0\,, \tag{F.53}$$

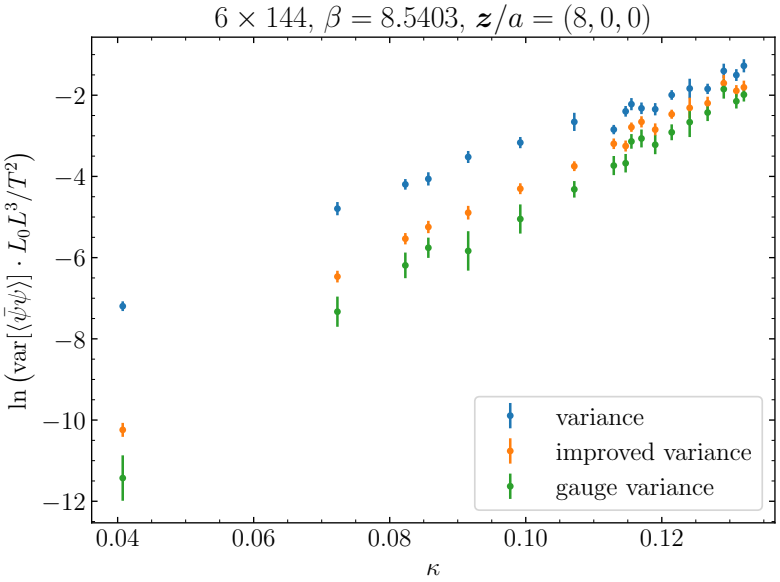

Figure F.3: Behaviour of the variance of the chiral condensate on a representative ensemble. The variance, improved variance (i.e. hopping subtracted) and the gauge variance only are compared for several values of the hopping parameter κ.

meaning that the decreasing of the variance from random sources is slower than the gauge variance, by a factor κ^2. Naively, this slower decreasing may be compensated by increasing the number of sources as $N_s \propto \kappa^2$, even though this makes the computation more and more demanding as $\kappa \to 0$. Instead, following [66] we consider an improved version of the estimator,

$$\mathcal{O}[U,\eta] \to \widetilde{\mathcal{O}}[U,\eta] = \frac{1}{N_s}\sum_{i=1}^{N_s}\sum_{x}\overline{\eta}^i(x)\Big(S[U] + 4\kappa^2 a^2 H[U]\Big)\eta^i(x)\,, \tag{F.54}$$

where we subtracted the leading order in the hopping expansion of the quark propagator. The operator H contains the hopping and improvement parts of the O(a)-improved Wilson-Dirac operator, and its expression is given in Subsection F.8.1. The central value of the estimator is not affected because the operator H is traceless. However, the subtraction has the effect of removing the leading terms in the hopping expansion of the random sources variance, so that the whole variance of the improved operator scales as $\mathrm{var}[\widetilde{\mathcal{O}}] \sim \kappa^6$ for $\kappa \to 0$. The effect of the improvement can be seen in Figure F.3. On a representative set of data at different κ, we show the variance of the chiral condensate in comparison with the variance of the hopping-improved estimator as functions of the hopping parameter. The variance of the improved estimator is smaller in the whole interval of κ. As expected, the gain is particularly evident at the smallest values of hopping parameter, where the variance is reduced by more than one order of magnitude. For reference we also compare with the gauge variance, extracted by diluition (see Appendix F.7).

In conclusion, since we are ultimately interested in the computation of the mass integral χ, see eq. (4.32), it is also relevant to notice that the signal of the integrand function at small hopping parameter scales as

$$\left\langle \overline{\psi}\psi \right\rangle_{\boldsymbol{\xi}_+} - \left\langle \overline{\psi}\psi \right\rangle_{\boldsymbol{\xi}_-} \sim \kappa^3 \,, \quad \kappa \to 0 \,. \tag{F.55}$$

Therefore, its signal-to-noise ratio using the hopping-subtracted chiral condensate is constant in the large mass limit.

F.8.1 Hopping parameter expansion

We compute here the large mass (hopping) expansion of the variance of the chiral condensate. For convenience we rewrite the fermionic O(a)-improved Wilson-Dirac action as

$$S^F = a^4 \sum_x \overline{\psi}(H+M)\psi \,, \quad H = D_H + aD_{\rm sw} \,, \tag{F.56}$$

where we defined the hopping term

$$D_H\psi(x) \equiv \frac{1}{2a}\sum_\mu \Big[(\gamma_\mu - 1)U_\mu(x)\psi(x+a\hat{\mu}) - (\gamma_\mu+1)U^\dagger_\mu(x-a\hat{\mu})\psi(x-a\hat{\mu})\Big] \tag{F.57}$$

and the parameter $M \equiv M_0 + 4/a$ contains the bare quark mass. In this notation the usual O(a)-improved Wilson-Dirac operator is

$$D + M_0 = H + M = D_H + aD_{\rm sw} + M_0 + 4/a \,. \tag{F.58}$$

We expand the quark propagator for $M \to \infty$:

$$\begin{aligned} S_{\alpha\beta} &= \left(\frac{1}{H+M}\right)_{\alpha\beta} = \left(\frac{1}{M(1+H/M)}\right)_{\alpha\beta} \\ &= \frac{1}{M}\left(\delta_{\alpha\beta} - \frac{H_{\alpha\beta}}{M} + \frac{(H^2)_{\alpha\beta}}{M^2} - \frac{(H^3)_{\alpha\beta}}{M^3} + \frac{(H^4)_{\alpha\beta}}{M^4} + \mathrm{O}(M^{-5})\right) . \end{aligned} \tag{F.59}$$

The labels α, β stand for any index attached to the operator. We also introduce the convenient notation

$$T_n \equiv \mathrm{Tr}\,\{H^n\} = \sum_\alpha (H^n)_{\alpha\alpha} \tag{F.60}$$

for the trace of the n-th power of the operator H.

We now discuss the large mass expansion of the gauge and random sources variances of equations (F.51), (F.52). We compute separately the various ingredients.

$$\mathrm{Tr}\,\{S\} = \frac{1}{M}\left(T_0 + \frac{1}{M^2}T_2 - \frac{1}{M^3}T_3 + \frac{1}{M^4}T_4 + \mathrm{O(M^{-5})}\right) \tag{F.61}$$

$$\left\langle \mathrm{Tr}^2\{S\}\right\rangle_U = \frac{1}{M^2}\left[T_0^2 + \frac{2}{M^2}T_0\langle T_2\rangle_U - \frac{2}{M^3}T_0\langle T_3\rangle_U \right. \\ \left. + \frac{1}{M^4}\left(2T_0\langle T_4\rangle_U + \left\langle T_2^2\right\rangle_U\right) + \mathrm{O}(M^{-5})\right] \quad \text{(F.62)}$$

$$\langle \mathrm{Tr}\,\{S\}\rangle_U^2 = \frac{1}{M^2}\left[T_0^2 + \frac{2}{M^2}T_0\langle T_2\rangle_U - \frac{2}{M^3}T_0\langle T_3\rangle_U \right. \\ \left. + \frac{1}{M^4}\left(2T_0\langle T_4\rangle_U + \langle T_2\rangle_U^2\right) + \mathrm{O}(M^{-5})\right] \quad \text{(F.63)}$$

Then the gauge variance at leading order is

$$\begin{aligned} \mathrm{var}\,[\mathcal{O}]_U &= \left\langle \mathrm{Tr}^2\{S\}\right\rangle_U - \langle \mathrm{Tr}\,\{S\}\rangle_U^2 \\ &= \frac{1}{M^6}\left(\left\langle T_2^2\right\rangle_U - \langle T_2\rangle_U^2\right) + \mathrm{O}(M^{-7})\,. \end{aligned} \quad \text{(F.64)}$$

For the variance of the random sources we need

$$\left\langle \mathrm{Tr}\left\{S^2\right\}\right\rangle_U = \frac{1}{M^2}\left[T_0 + \frac{3}{M^2}\langle T_2\rangle_U - \frac{4}{M^3}\langle T_3\rangle_U + \frac{5}{M^4}\langle T_4\rangle_U + \mathrm{O}(M^{-5})\right] \quad \text{(F.65)}$$

and

$$\left\langle \sum_\alpha (S_{\alpha\alpha})^2\right\rangle_U = \frac{1}{M^2}\left[T_0 + \frac{1}{M^2}\left(\left\langle \sum_\alpha (H_{\alpha\alpha})^2\right\rangle_U + 2\langle T_2\rangle_U\right) + \mathrm{O}(M^{-3})\right] \quad \text{(F.66)}$$

The random source variance reads

$$\begin{aligned} \mathrm{var}\,[\mathcal{O}]_\eta &= \left\langle \mathrm{Tr}\left\{S^2\right\}\right\rangle_U - \left\langle \sum_\alpha (S_{\alpha\alpha})^2\right\rangle_U \\ &= \frac{1}{M^4}\left(\langle T_2\rangle_U - \left\langle \sum_\alpha (H_{\alpha\alpha})^2\right\rangle_U\right) + \mathrm{O}(M^{-5}) \end{aligned} \quad \text{(F.67)}$$

In terms of the hopping parameter, the gauge variance (F.64) decreases with $\sim \kappa^6$ as $\kappa \to 0$, while the random sources variance with the slower power $\sim \kappa^4$.

Hopping subtraction

We introduce the (generalized) improved estimator for the chiral condensate,

$$\widetilde{\mathcal{O}}[U,\eta] = \frac{1}{N_s}\sum_{i=1}^{N_s}\sum_x \eta^{i\dagger}(x)\,\widetilde{S}\,\eta^i(x)\,, \quad \text{(F.68)}$$

where $\widetilde{S}$ is the subtracted propagator

$$\widetilde{S} \equiv S - \frac{1}{M}\left(1 - c_0 - \frac{1-c_1}{M}H\right) \quad \text{(F.69)}$$

and c_0, c_1 are tunable parameters. Its large mass expansion is

$$\widetilde{S}_{\alpha\beta} = \frac{1}{M}\left(c_0\delta_{\alpha\beta} - c_1\frac{H_{\alpha\beta}}{M} + \frac{(H^2)_{\alpha\beta}}{M^2} - \frac{(H^3)_{\alpha\beta}}{M^3} + \frac{(H^4)_{\alpha\beta}}{M^4} + \mathrm{O}(M^{-5})\right). \tag{F.70}$$

The gauge part of the variance of $\widetilde{O}$ coincides with the one of the unimproved operator for any value of c_0, c_1:

$$\mathrm{var}[\widetilde{O}]_U = \mathrm{var}\,[O]_U\,. \tag{F.71}$$

Instead, the random sources variance is

$$\begin{aligned}
\mathrm{var}[\widetilde{O}]_\eta &= \Big\langle \mathrm{Tr}\{\widetilde{S}^2\}\Big\rangle_U - \Big\langle \sum_\alpha (\widetilde{S}_{\alpha\alpha})^2\Big\rangle_U \\
&= \frac{c_1^2}{M^4}\Big[\langle T_2\rangle_U - \Big\langle \sum_\alpha (H_{\alpha\alpha})^2\Big\rangle_U\Big] \\
&- \frac{2c_1}{M^5}\Big[\langle T_3\rangle_U - \Big\langle \sum_\alpha H_{\alpha\alpha}(H^2)_{\alpha\alpha}\Big\rangle_U\Big] \\
&+ \frac{1}{M^6}\Big[2c_1\Big(\langle T_4\rangle_U - \Big\langle \sum_\alpha H_{\alpha\alpha}(H^3)_{\alpha\alpha}\Big\rangle_U\Big) \\
&\qquad + \langle T_4\rangle_U - \sum_\alpha (H^2)_{\alpha\alpha}(H^2)_{\alpha\alpha}\Big] \\
&+ \mathrm{O}(M^{-7})\,.
\end{aligned} \tag{F.72}$$

If we choose $c_1 = 0$, both the $\sim M^{-4}$ and $\sim M^{-5}$ orders disappear and $\sim M^{-6}$ becomes the leading power, as for the gauge variance. This result does not depend on the coefficient c_0, and we set it to $c_0 = 1$ so that the central value of the subtracted operator coincides with the unimproved one. The final definition of the subtracted propagator is thus

$$\widetilde{S} = S + 4\kappa^2 a^2 H \tag{F.73}$$

where for definiteness we used the hopping parameter $\kappa = 1/(2aM)$.

F.9 Optimization of the statistics

In this Section we describe the optimization procedure we developed to minimize the computational cost for the numerical determination of the integral in the mass χ. The Gauss quadrature estimates the integral by a linear combination of samples of the integrand function, weighted by prescribed coefficients, see eq. (4.32). These coefficients have symmetric values in the integration interval, with the minima at the boundaries and the maximum in the middle. In our case the integrand function is sampled from lattice simulations, and therefore the sample points are known with a statistical error. The error squared of the estimated integral χ is the linear combination of the errors squared of the

sample points, weighted by the square of the Gauss quadrature coefficients. This establishes a hierarchy among the samples, with the points in the middle of the integration range contributing more to the error on χ than the points near the boundaries.

However, there are other hierarchies that should be taken into account. The computational time widely changes with κ, so that it may be preferable to produce more data at small values of the hopping parameter. On the other side, the bulk of the contribution to the integral comes from lower values of κ. In addition the variance of the chiral condensate decreases with the hopping parameter, see Figure F.3. Furthermore it may be convenient to change the number of random sources with κ. On top of all that, a lower bound comes from the fact that every point should be sampled enough for the statistical analysis to be meaningful.

To take into account all these effects we set up an optimization problem: at given L_0/a and g_0^2 we look for the number of trajectories and random sources for each point of the Gauss quadrature, so that the total computational cost for estimating the integral is minimized under the condition that the target relative error on the integral σ_χ/χ is fixed. This problem can be solved in closed form using Lagrange multipliers, see the next Section F.9.1 for further details. The results are reported in Table F.8. We choose a target relative accuracy for the integral in the bare mass of 0.5% at $L_0/a = 4, 6, 8$ and 1.0% at $L_0/a = 10$. In practice, for simplicity we fix a flat statistics for $L_0/a = 4, 6$ and use the optimization for the two finest lattices. At each point of the Gauss quadratures is associated one row of the table, where the number of trajectories to be generated is reported (the bare quark mass increases from top to bottom). The number of trajectories within each quadrature χ_{peak}, χ_{tail}, χ_{res} is almost symmetric with respect to the middle of the interval, as expected since the Gaussian weights are symmetric. The mild breaking of this pattern is due to the emerging of other effects such as the decreasing of the variance of the chiral condensate with κ, which tends to cluster the statistics at higher values of the hopping parameter as it is evident in χ_{res}. The quoted statistics in Table F.8 is used for both shifts.

The number of random sources turns out to depend much more mildly on κ, and thus for convenience we fix it to $N_s = 100$ for all the simulations. This tuning was performed using the data at the temperature T_1, combining the results at the two shifts. For the other temperatures we consider the same optimized statistics and scale it from temperature to temperature according to the resulting relative precision on χ.

F.9.1 Minimization of the cost

Given the target relative error σ_{target} on the integral in the mass χ at given L_0/a and g_0^2, we would like to tune the number of trajectories per integrand point, and the number of random sources per trajectory so to minimize the computational cost. This can be

	$L_0/a = 4$	$L_0/a = 6$	$L_0/a = 8$	$L_0/a = 10$
σ_χ/χ	0.5%	0.5%	0.5%	1.0%
χ_{peak}	50	100	50	50
	50	100	150	100
	50	100	150	100
	50	100	200	200
	50	100	150	250
	50	100	150	250
	50	100	150	200
	50	100	150	150
	50	100	100	100
	50	100	50	50
χ_{tail}	50	100	250	300
	50	100	400	600
	50	100	450	700
	50	100	400	700
	50	100	300	500
	50	100	150	350
	50	100	150	150
χ_{res}	50	100	1400	2400
	50	100	1200	2100
	50	100	150	300

Table F.8: Number of measurements for each L_0/a optimized to obtain the target relative accuracy on χ reported in the first row at the temperature T_1 and $L/a = 144$. Each row corresponds to one Gauss point where the integrand function of χ has to be sampled. The bare mass increases from top to bottom.

achieved by solving the constrained minimization problem

$$\begin{cases} N_j^g, N_j^s : \sum_{j=1}^{n_G} N_j^g \left(t_j^g + N_j^s t_j^s \right) & \text{is minimized} \\ \sum_{j=1}^{n_G} \frac{\omega_j^2 2\tau_j}{N_j^g} \left(v_j^g + \frac{1}{N_j^s} v_j^s \right) = \sigma_{target}^2 \end{cases} \tag{F.74}$$

where the index $i = 1, 2, ..., n_G$ labels all the Gauss points for the quadrature of χ. Specifically, in our case $n_G = 20$. The first equation is the total computational cost, while the second is the total variance of χ fixed to a prescribed target value. At the i-th point of the quadrature, the other quantities are as follows:

- N_i^g is the number of measurements (gauge configurations),
- N_i^s is the number of random sources per trajectory,
- t_i^g is the computational time (in ch) for one HMC update of the gauge configuration (sum of shift forward and backward),
- t_i^s is the computational time (in ch) for processing one random source (sum of shift forward and backward),
- ω_i is the Gauss quadrature weight,
- v_i^g is the gauge variance,
- v_i^s is the random sources variance,
- τ_i is the integrated autocorrelation time (max between forward and backward), measured with the Gamma method 3.7.2.

This problem can be solved using Lagrange multipliers. We call λ the Lagrange parameter. The unknown variables are the N_i^g and N_i^s, while all the other quantities are assumed to be known (usually from some preliminary ensembles, or from the thermalization). We get the system

$$\begin{cases} t_i^g + N_i^s t_i^s - \lambda \frac{\omega_i^2}{(N_i^g)^2} \left(v_i^g + \frac{1}{N_i^s} v_i^s \right) 2\tau_i = 0 \\ N_i^g t_i^s - \lambda \frac{\omega_i^2}{N_i^g (N_i^s)^2} v_i^s 2\tau_i = 0 \\ \sum_{j=1}^{n_G} \frac{\omega_j^2 2\tau_j}{N_j^g} \left(v_j^g + \frac{1}{N_j^s} v_j^s \right) = \sigma_{target}^2 \,. \end{cases} \tag{F.75}$$

We solve the first two equations in λ, and by equating the results we get the condition on the number of sources:

$$N_i^s = \sqrt{\frac{t_i^g \, v_i^s}{t_i^s \, v_i^g}} \equiv N_i^{s,*} \,, \quad 1, ..., n_G \,. \tag{F.76}$$

These numbers do not depend on ω_i, τ_i and N_i^g, as we may expect. The scaling of N_i^s with the computational times and the variances is such that more sources are produced when the cost of the gauge configuration is high compared to the gain in the variance. If we substitute back in λ, we get

$$\lambda = \frac{t_i^*(N_i^g)^2}{\omega_i^2 v_i^* \, 2\tau_i} \tag{F.77}$$

where we also defined the source-optimized computational time and variance

$$t_i^* \equiv t_i^g + N_i^{s,*} t_i^s \,, \quad v_i^* \equiv v_i^g + \frac{1}{N_i^{s,*}} v_i^s \,. \tag{F.78}$$

If we consider λ at two indices i, j we get $n_G - 1$ independent constraints, leading to

$$N_j^g = N_i^g \sqrt{\frac{\omega_j^2}{\omega_i^2} \frac{v_j^* \, 2\tau_j}{v_i^* \, 2\tau_i} \frac{t_i^*}{t_j^*}} \tag{F.79}$$

If we replace in the third equation of (F.75), and we also replace the optimized value $N_j^s = N_j^{s,*}$ of eq. (F.76), we finally get

$$N_i = \frac{1}{\sigma_{target}^2} \sqrt{\frac{\omega_i^2 \, v_i^* \, 2\tau_i}{t_i^*}} \sum_{j=1}^{n_G} \sqrt{\omega_j^2 \, t_j^* \, v_j^* \, 2\tau_j} \,, \quad i = 1, ..., n_G \,. \tag{F.80}$$

This formula suggests the number of measurements (with optimized random sources) per Gauss point such that the target error on the quadrature is reached at the minimum computational effort. The optimization requires some input data: the computational times, the gauge and sources variances, the autocorrelation times. The target error σ_{target} itself is better constrained if an estimation of the integral χ is available. The procedure is thus the following:

1. we generate some exploratory ensembles with a guessed number of trajectories per point (flat statistics, say), and with a reasonable number of random sources per trajectory. In this way the integral χ can be estimated, as well as the computational times per trajectory t_i^g, t_i^s, the variances v_i^g, v_i^s and the autocorrelation times τ_i for a known number of measurements.

2. Using the estimated central value of the integral, and the target relative accuracy, the target absolute error σ_{target} on χ can be determined.

3. Finally, equations (F.76) and (F.80) give the optimized statistics.

F.9.2 Optimization at work

The chosen showcase for the optimization is the 8×144^3 lattice at T_1. Computational times, variances and autocorrelations were first measured on the thermalization ensembles

κ	N_i^s opt	N^g flat	N_i^g opt
0.13193	53.7(16)	489	47
0.13110	54.9(20)	489	132
0.12971	57.0(12)	489	172
0.12790	62.5(14)	489	199
0.12588	70.7(23)	489	189
0.12383	74.5(24)	489	176
0.12193	82.5(28)	489	168
0.12033	84(3)	489	134
0.11916	72.5(25)	489	107
0.11848	77(3)	489	39
0.11738	75.6(20)	489	231
0.11371	83.6(23)	489	428
0.10823	98(3)	489	461
0.10227	103(3)	489	422
0.09694	103(3)	489	331
0.09293	113(6)	489	178
0.09061	111(6)	489	108
0.07991	107(3)	489	1465
0.04503	112(4)	489	1237
0.01015	98(4)	489	190
total time (Mch)		8.84	3.88

Table F.9: Optimized number of random sources and trajectories for a target error on χ of $\sim 0.5\%$ on a 8×144^3 lattice at temperature T_1. The comparison with the corresponding flat statistics case is shown.

at volume 8×48^3. We then imposed a target accuracy of 0.5% on the mass integral, and obtained the optimized numbers of random sources and trajectories per value of the hopping parameter κ. Finally we rescaled these numbers by the volume factor $(48/144)^3$ and, taking into account a $\sim 20\%$ increase of computing time due to the scaling of the algorithm and parallelization with the system size, we obtained the optimized numbers shown in table Table F.9 for the target lattice volume. For comparison we also computed the number of trajectories in case a flat-statistics approach is chosen, given the optimized number of random sources. The number N^g_{flat} is common to all values of κ and is implicitly defined by

$$\frac{1}{N^g_{\text{flat}}} \sum_{i=1}^{n_G} \omega_i^2 2\tau_i \left(v_i^g + \frac{1}{N_i^{s,*}} v_i^s \right) = \sigma^2_{target} \,. \tag{F.81}$$

We can see the optimization at work in the last line of Table F.9. We computed the the total computational time in the two cases using the average time per trajectory in actual simulations of 8×144^3 lattices. The cost of the optimized case is roughly a half compared to the naive, flat-statistics case. From Table F.9 we also see that, while the optimized numbers of trajectories change widely with κ, the number of random sources is roughy of the order of ~ 100 at all hopping parameters. For simplicitly we decided to fix the number of sources to 100 at all bare parameters, and to round the number of trajectories consequently. The final optimized numbers are listed in Table F.8 for the resolutions L_0/a we consider in our study. Actually we used the optimization only for $L_0/a = 8, 10$ because simulations at $L_0/a = 4, 6$ are cheap enough for the simpler, flat-statistics choice to be competitive.

F.9.3 Lagrange multipliers

The Lagrange multipliers are used to minimize a function $f(x)$, $x \in \mathbb{R}^d$, under a constraint of the form $g(x) = 0$. We define the Lagrangian

$$\mathcal{L}(x, \lambda) = f(x) + \lambda g(x) \,, \tag{F.82}$$

and the function f is minimized on the stationary points of this Lagrangian:

$$\begin{cases} \partial_{x_i} \mathcal{L}(x, \lambda) = 0 \,, \quad i = 1, ..., d \\ \partial_\lambda \mathcal{L}(x, \lambda) = 0 \,. \end{cases} \tag{F.83}$$

Notice that the second equation is the constraint itself.

F.10 Continuum limit

We collect here the tables with all the fit parameters considered for the extrapolation to the continuum limit of the entropy density. Table F.10 contains the continuum limits p_0–p_8 for all the relevant fits we performed on the numerical data. Table F.11 contains the related fit coefficients for the parametrization of the cutoff effects.

id	dataset	p_0	p_1	p_2	p_3	p_4	p_5	p_6	p_7	p_8	χ^2	d.o.f
0	A	20.140(16)	20.103(18)	20.063(19)	20.024(21)	19.986(23)	19.913(26)	19.850(30)	19.765(35)	19.642(58)	17.192	23
1	A	20.136(33)	20.100(30)	20.061(28)	20.022(27)	19.985(25)	19.913(26)	19.852(35)	19.771(56)	19.646(67)	17.177	22
2	4I	20.159(39)	20.093(30)	20.098(31)	20.007(35)	19.982(35)	19.908(37)	19.846(40)	19.784(48)	19.647(60)	14.034	23
3	4I	20.152(49)	20.088(39)	20.094(37)	20.004(38)	19.980(36)	19.909(37)	19.850(44)	19.794(64)	19.658(77)	13.983	22
4	A	20.220(53)	20.195(60)	20.165(67)	20.136(74)	20.112(82)	20.055(93)	20.01(11)	19.95(12)	19.87(15)	14.647	22
5	A	20.18(12)	20.16(12)	20.13(11)	20.11(11)	20.09(10)	20.046(97)	20.02(11)	19.99(16)	19.95(26)	14.485	20
6	4I	20.242(65)	20.186(65)	20.200(71)	20.119(78)	20.108(86)	20.052(97)	20.01(11)	19.97(13)	19.88(15)	11.472	22
7	4I	20.21(13)	20.15(12)	20.17(12)	20.09(11)	20.09(10)	20.04(10)	20.01(11)	20.00(16)	19.94(26)	11.357	20
8	N4	20.230(63)	20.139(52)	20.184(54)	20.057(60)	20.050(64)	19.987(71)	19.932(76)	19.908(91)	19.78(11)	9.127	15
9	N4	20.20(10)	20.115(83)	20.163(79)	20.039(77)	20.037(73)	19.981(73)	19.936(77)	19.93(11)	19.83(17)	8.998	14

Table F.10: Summary of the continuum limit extrapolations for the entropy s/T^3 for 10 different fit functions. The first column contains the id of the fit. The second column indicates the dataset used: A for all the data, 4I for all the data with errors on $L_0/a = 4$ points enlarged to the errors of $L_0/a = 6$ points, N4 for $L_0/a = 6, 8, 10$ data only. Columns labelled with p_i contain the continuum limit parameter of the fit, see equation 4.46 for the fit function. The last two columns contain the χ^2 and the number of degrees of freedom of the fit.

	id0	id1	id2	id3	id4	id5	id6	id7	id8	id9
p_{23}	-2.48(23)	-2.1(28)	-2.55(33)	-1.7(40)	-9.4(44)	8(46)	-9.6(44)	6(47)	-4.5(13)	1(14)
p_{24}		-0.3(23)		-0.7(33)		-14(37)		-13(37)		-4(11)
p_{33}					23(14)	-37(150)	23(15)	-29(155)		
p_{34}						48(120)		42(123)		

Table F.11: Summary of the fit parameters for the cutoff effects, see equation 4.46 for the fit function. This table is matched to the one above through the id of the fits.

$c_{00} = 10.14328$	$c_{01} = 6.56528$	$c_{02} = 6.10007$
$c_{03} = 5.53266$	$c_{04} = 4.84359$	$c_{05} = 3.58625$
$c_{06} = 1.47970$	$c_{07} = -1.78790$	$c_{08} = -6.91749$
$c_{11} = 6.88316$	$c_{12} = 5.36563$	$c_{13} = 4.92258$
$c_{14} = 4.39836$	$c_{15} = 3.41327$	$c_{16} = 1.69967$
$c_{17} = -0.91015$	$c_{18} = -5.07463$	$c_{22} = 6.26307$
$c_{23} = 4.70072$	$c_{24} = 4.28437$	$c_{25} = 3.47033$
$c_{26} = 1.98627$	$c_{27} = -0.22396$	$c_{28} = -3.82206$
$c_{33} = 5.90892$	$c_{34} = 4.14999$	$c_{35} = 3.54695$
$c_{36} = 2.34539$	$c_{37} = 0.62760$	$c_{38} = -2.27333$
$c_{44} = 5.38179$	$c_{45} = 3.73862$	$c_{46} = 2.91580$
$c_{47} = 1.86685$	$c_{48} = -0.09793$	$c_{55} = 5.28125$
$c_{56} = 3.67951$	$c_{57} = 3.70483$	$c_{58} = 3.26356$
$c_{66} = 5.86791$	$c_{67} = 5.84762$	$c_{68} = 7.55016$
$c_{77} = 12.03381$	$c_{78} = 15.22651$	$c_{88} = 28.92183$

Table F.12: Covariance matrix for the continuum extrapolated values of the entropy density, according to fit id9 (see Table 4.8). The coefficient c_{ij} gives the covariance of the parameters p_i, p_j. Values are multiplied by 10^3.

F.11 Systematic effects from topology

It is well known that lattice QCD simulations with periodic boundary conditions at fine lattice spacing suffer from topology freezing [47, 137, 4]. Consequently, either a setup is chosen where all topological sectors can be sampled (e.g. open boundary conditions [101]), or one should be in the circumstance where topology does not matter.

In our interval of temperatures $1\,\mathrm{GeV} \lesssim T \lesssim 100\,\mathrm{GeV}$ the $Q = 0$ sector of the QCD phase space gives by far the dominant contribution to the path integral. The strong suppression of the topological susceptibility at high temperatures is predicted by the instanton model approximation, see eqs. (2.24), (2.23), and has been numerically explored [58, 20]. For all practical purposes, we can in principle restrict our study to the trivial topology sector. We may thus consider all our formulas with the zero topology condition $\delta_{Q,0}$ enforced in the path integral. This propagates to our main observables, the expectation value of the Wilson plaquette action measured in the pure gauge theory and the chiral condensate measured in QCD:

$$\left\langle S^G \right\rangle^{\mathrm{YM}}_{Q=0} = \frac{\left\langle \delta_{Q,0}\, S^G \right\rangle^{\mathrm{YM}}}{\left\langle \delta_{Q,0} \right\rangle^{\mathrm{YM}}}\,, \quad \left\langle \overline{\psi}\psi \right\rangle_{Q=0} = \frac{\left\langle \delta_{Q,0}\, \overline{\psi}\psi \right\rangle}{\left\langle \delta_{Q,0} \right\rangle}\,. \tag{F.84}$$

The computation of the integral χ requires, at given L_0/a and g_0^2, simulations in QCD with increasing bare quark mass. At large masses, quarks contribute less and less to the dynamics and thus the theory behaves more and more as the pure gauge theory (at the bare parameters of QCD), and the topological susceptibility is expected to be less suppressed compared to QCD near the chiral limit. This is true in particular for the pure

gauge simulations where we measure $\langle S^G \rangle$, which should be meant as QCD simulations in the limit of infinite bare quark mass.

The effect is that in some (few) of our ensembles topology do fluctuate, at the point that the zero topology projection eq. (F.84) cannot be enforced efficiently in terms of accumulated statistics. Actually pure gauge simulations show some topological activity only at the two lowest temperatures T_7, T_8 considered in this study, while QCD simulations at T_8 only and at the largest values of bare quark mass. In both cases, only the lattice resolutions $L_0/a = 4, 6$ are affected.

As an alternative solution, we can verify that the correlation between topology and our observables is negligible within the statistical accuracy. If this is the case, we can include in the analysis samples from non-zero topological sectors without introducing any systematics in the results. In the following we report on the detailed investigation of the effects of topology on our observables. The outcome of these studies is that any effect from sampling non-trivial topological sectors is negligible within our statistical accuracy. Therefore, at the lowest temperatures and largest bare masses, we could sample on all configurations without worrying about the topological activity of the system.

F.11.1 Correlation with Q

We would like to estimate the effect of the topological activity on our main observables. To this purpose we introduce, in continuum QCD and in the large volume limit, the fixed topology partition function [24],

$$\mathcal{Z}_Q = \mathcal{Z} \sqrt{\frac{2\pi}{\langle Q^2 \rangle}} \exp\left\{ -\frac{Q^2}{2\langle Q^2 \rangle} \right\} (1 + \mathrm{O}(1/V)) \tag{F.85}$$

where $\mathcal{Z}$ denotes the usual partition function including all topological sectors. This relation can be used to derive the effect on spectral quantities due to the projection in a topological sector. By deriving both sides with respect to the bare coupling g_0^2 we get

$$\langle S^G \rangle_Q = \langle S^G \rangle + \frac{1}{2} \frac{\langle S^G Q^2 \rangle_c}{\chi_t L_0 V} \left(1 - \frac{Q^2}{\chi_t L_0 V} \right) + \mathrm{O}\left(\frac{1}{L_0 V} \right) . \tag{F.86}$$

If we similarly differentiate eq. (F.85) with respect to the bare quark mass we get the analogous relation for the chiral condensate,

$$\langle \overline{\psi}\psi \rangle_Q = \langle \overline{\psi}\psi \rangle - \frac{1}{2} \frac{\langle \overline{\psi}\psi Q^2 \rangle_c}{\chi_t L_0 V} \left(1 - \frac{Q^2}{\chi_t L_0 V} \right) + \mathrm{O}\left(\frac{1}{L_0 V} \right) . \tag{F.87}$$

On the left hand sides, the gauge action and chiral condensate are evaluated at fixed topology Q while on the right the expectation value is over all the topological sectors. These equations state that the magnitude of the impact of topology on $\langle S^G \rangle$ and $\langle \overline{\psi}\psi \rangle$ is related to their connected correlation function with the square of the topological charge, and it is suppressed as $\chi_t V$ which is the variance of the topological charge distribution.

F.11.2 Topological effects from Dirac spectrum

The chiral condensate can be explicitly written as

$$\langle\overline{\psi}\psi\rangle = \frac{1}{L_0V}\big\langle \mathrm{Tr}\left\{(D+m)^{-1}\right\}\big\rangle_U\,, \tag{F.88}$$

where the trace is over all indices including spacetime, and $\langle\cdot\rangle_U$ is defined on the path integral after the integration of fermionic fields. Calling λ the eigenvalues of the Dirac operator D, we have

$$\mathrm{Tr}\left\{(D+m)^{-1}\right\} = \sum_\lambda \frac{1}{\lambda+m} = \frac{n_+-n_-}{m} + \sum_{\lambda\neq 0}\frac{1}{\lambda+m}\,, \tag{F.89}$$

where in the second step we isolated the zero modes of the Dirac operator, which have definite chirality: $n_\pm$ is the number of zero modes with positive (negative) chirality. Assuming that either $n_+\neq 0$ or $n_-\neq 0$ (a conjecture called *absence of fine tuning*), then $n_+-n_- = |Q|$ as a consequence of the index theorem. We get

$$\langle\overline{\psi}\psi\rangle = \frac{\langle|Q|\rangle_U}{mL_0V} + \frac{1}{L_0V}\Big\langle\sum_{\lambda\neq 0}\frac{1}{\lambda+m}\Big\rangle_U \tag{F.90}$$

The bulk of the topology dependence comes from the first term. If we take the difference of this quantity with the same quantity projected in the trivial topological sector, the second term mostly cancels. Furthermore, in the large volume limit the topological charge distribution is Gaussian and $\langle|Q|\rangle_U \sim \sqrt{L_0V\chi_t}$ so that

$$\langle\overline{\psi}\psi\rangle - \langle\overline{\psi}\psi\rangle_{Q=0} \approx \frac{\sqrt{\chi_t}}{m\sqrt{L_0V}} + \mathrm{O}\left(\frac{1}{L_0V}\right) \tag{F.91}$$

This equation reveals that the correlation of the chiral condensate with the topological sector is suppressed with one power of the quark mass. This is reassuring because we expect topology to be more active at large masses [1]. However, it must be said that equation (F.91) has been derived under many assumptions, one above all the fact that the Dirac operator respects chiral symmetry, which is not true in our simulations with Wilson fermions. Therefore any conclusion from equation (F.91) cannot be more than an indicative guideline.

F.11.3 Numerical checks

Equations (F.87) and (F.91) suggest that the effects of topology on the chiral condensate are suppressed both with the quark mass and the volume. In order to check this behaviour we measured the chiral condensate on a long Monte Carlo history produced in quenched

[1] The volume and mass suppressions predicted by equations (F.91) and (F.87) are apparently different. However, in equation (F.91) we are not considering the implicit dependence of the topological susceptibility on the quark mass, in the large mass limit.

κ	$\lvert\Delta Q\rvert = 1$	$\lvert\Delta Q\rvert = 2$	$\lvert\Delta Q\rvert = 3$	$\lvert\Delta Q\rvert = 4$
0.10100	0.002(6)	0.026(8)	0.043(12)	0.044(19)
0.08354	0.0011(29)	0.012(4)	0.020(5)	0.019(8)
0.04136	0.4(6)	2.8(8)	4.6(11)	4.3(18)
0.00932	0.10(13)	0.60(17)	0.97(23)	0.9(4)
nms	11022	4310	1526	622

(a) Data from lattice 6×48^3, $\boldsymbol{z}/a = (8, 0, 0)$, quenched. Estimates of the effect of topology on the integrand function for the mass integral χ. The $Q = 0$ sector is sampled with 7552 points.

κ	$\lvert\Delta Q\rvert = 1$	$\lvert\Delta Q\rvert = 2$	$\lvert\Delta Q\rvert = 3$	$\lvert\Delta Q\rvert = 4$
0.10100	0.0075(29)	0.002(3)	0.007(4)	0.005(4)
0.08354	0.0035(13)	0.0009(15)	0.0034(17)	0.0024(18)
0.04136	0.8(3)	0.2(3)	0.8(4)	0.6(4)
0.00932	0.17(7)	0.05(7)	0.18(8)	0.12(9)
nms	2421	2408	2007	1398

(b) Data from lattice 6×96^3, $\boldsymbol{z}/a = (8, 0, 0)$, quenched. Estimates of the effect of topology on the integrand function for the mass integral χ. The $Q = 0$ sector is sampled with 1334 points.

Table F.13

QCD, on a 6×48^3 lattice at bare parameters of T_8. On each configuration, we measured the topological charge at fixed Wilson flow time t_{wf} [109], such that

$$T\sqrt{8t_{\text{wf}}} = c\,, \quad T = 1/(L_0\sqrt{2})\,, \quad c = 1/\sqrt{10} \approx 0.316\,. \tag{F.92}$$

The chiral condensate was computed by setting the valence quark hopping parameter at some selected values in the interval $0.009 \lesssim \kappa \lesssim 0.1$. On this ensemble we then computed the discrepancy

$$\langle\overline{\psi}\psi\rangle_{|Q|} - \langle\overline{\psi}\psi\rangle_{Q=0} \tag{F.93}$$

considering the most sampled topological sectors. The related discrepancies on the integrand function for the mass integral χ are reported in Table F.13a. To obtain these numbers we considered the worst case where the effects at the two shifts add up. The table reports the number of configurations that occurred at the different topological sectors considered for the study. The trend along the rows (that is, for increasing topological charge) is compatible with an increasing of the topological effect on the integrand function, although less statistics is available at large $|\Delta Q|$. The trend along columns (that is, for decreasing κ) is more difficult to interpret because both the quark mass and the topological susceptibility increase, see also Table F.14. From equation (F.91), we expect a (partial) compensation between the two.

It is interesting to compare the deviations in Table F.13a to the values of the integrand function corresponding to the same κ in Table F.14, containing (full QCD) data for the quadrature of the mass integral. The largest impact occurs at $\kappa = 0.041$ and $|\Delta Q| = 4$, where the effect due to topology is $\sim 2\sigma$ of the integrand function (even though the

		all Q sectors			$Q=0$ only	
κ	ω Gauss	nms	$\chi_t/T^4 \times 10^3$	integrand	nms	integrand
0.13529	0.167	1000	0.01281(56)	0.804(53)	1000	0.804(53)
0.13413	0.374	1000	0.01273(56)	2.705(51)	1000	2.705(51)
0.13219	0.548	1000	0.01524(69)	4.424(47)	1000	4.424(47)
0.12970	0.673	1070	0.01576(75)	4.762(49)	1070	4.762(49)
0.12694	0.739	1000	0.01873(87)	3.779(39)	1000	3.779(39)
0.12417	0.739	1000	0.02005(96)	2.567(35)	1000	2.567(35)
0.12164	0.673	1000	0.0230(10)	1.821(27)	1000	1.821(27)
0.11953	0.548	1000	0.0243(13)	1.370(26)	1000	1.370(26)
0.11799	0.374	1000	0.0256(16)	1.041(22)	1000	1.041(22)
0.11711	0.167	1000	0.0281(21)	0.929(25)	1000	0.929(25)
0.11529	1.285	1000	0.0279(14)	0.678(24)	999	0.677(24)
0.10925	2.706	1000	0.0291(14)	0.282(17)	999	0.282(17)
0.10100	3.509	1000	0.0446(45)	0.095(12)	999	0.095(12)
0.09307	3.509	1500	0.71(54)	0.0435(70)	1404	0.0409(72)
0.08702	2.706	1500	0.22(12)	0.0316(52)	1472	0.0309(53)
0.08354	1.285	1500	1.78(23)	0.0268(43)	1120	0.0228(56)
0.07339	0.023	1000	0.139(30)	14.1(2.9)	941	15.3(2.9)
0.04136	0.037	1000	2.07(31)	11.1(1.4)	612	9.8(2.2)
0.00932	0.023	1000	9.3(3.5)	2.40(30)	454	2.55(55)
mass integral χ/T^4			17.01(13)			16.98(14)

Table F.14: Data from 6×48^3 lattices, temperature T_8. First column: points for the Gauss quadrature at these bare parameters. Second column: Gauss weights for the quadrature. Third, fourth, fifth columns: number of measurements, topological susceptibility and integrand function considering all the sampled topological sectors. Sixth and seventh columns: number of measurements and integrand function considering data at $Q = 0$ only. Last row: comparison of integrals computed with and without $Q = 0$ projection.

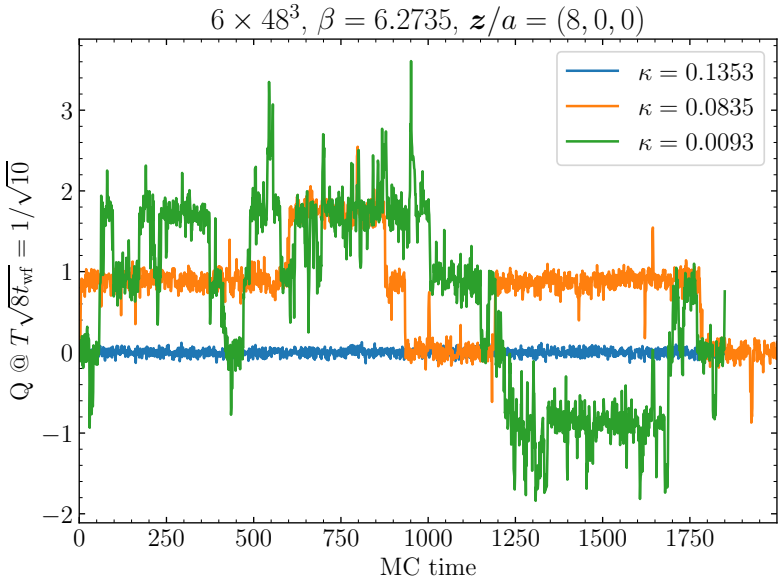

Figure F.4: Monte Carlo history of the topological charge at selected values of κ.

uncertainty is large). Despite these effects, we see from the last row of Table F.14 that the impact of the $Q = 0$ projection on the full integral is well below 1σ, while its relative error is comparable to the $\sim 0.5\%$ target accuracy.

Table F.13b is analogous to Table F.13b, but data are produced on a 6×96^3 lattice. The statistics was tuned so to have a comparable accuracy on the chiral condensate. The data in the two Tables are compatible with a suppression of the topological effects with the volume. Comparing data from Tables F.13b and F.14 we see that the worst case is $\kappa = 0.041$, $|\Delta Q| = 3$, whose impact is less than $\sim 0.5\sigma$ of the integrand function. This makes us confident that at the target volume, that is as large as $L/a = 144$ in the three spatial directions, the effects of topology on the integrand function are definitely subdominant within our statistical accuracy.

In conclusion, in Figure F.4 we report the Monte Carlo the history of the topological charge at some values of hopping parameter, measured on selected ensembles. As expected, the topological susceptibility increases with the mass and thus more and more non-trivial topological sectors are sampled. Figure F.5 shows the Monte Carlo history of the plaquette and the tree-level subtracted chiral condensate compared to the topological charge, at the largest mass of Figure F.4. This plot shows qualitatively that no relevant correlation is present between the observables and the topological sectors.

F.12 Finite volume effects

We report on the tests we performed to check that finite volume effects on the entropy density are negligible within our statistical accuracy. The entropy density is proportional to the 1-point function $\langle T_{0k} \rangle_{\boldsymbol{\xi}}$ of the QCD Energy-Momentum tensor (EMT) measured

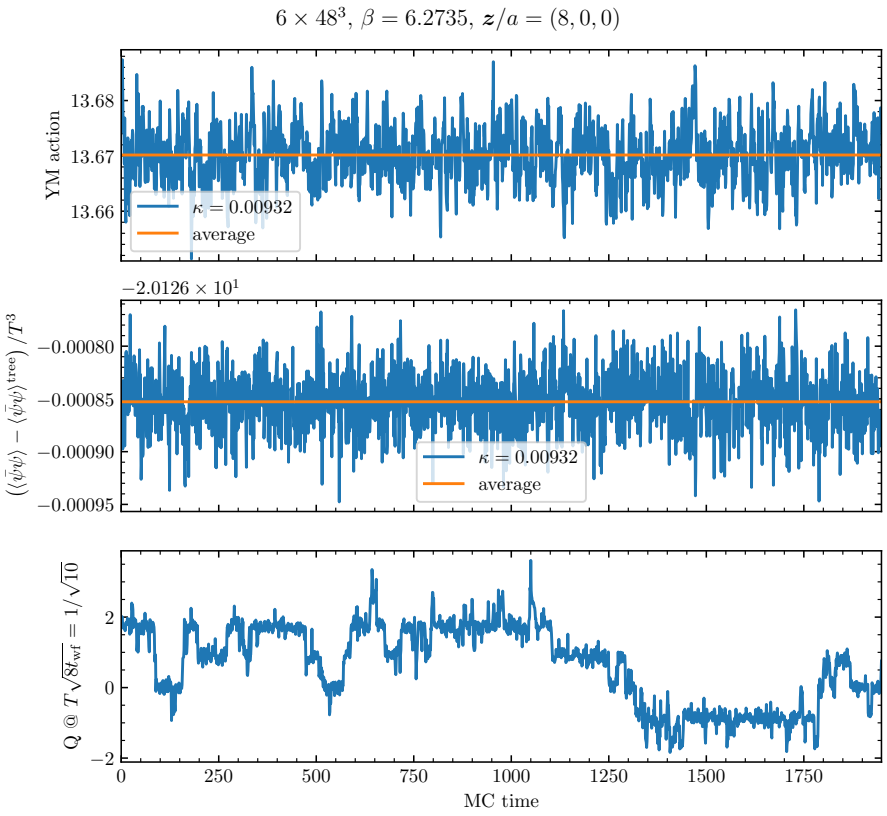

Figure F.5: Monte Carlo history of the plaquette and tree-level subtracted chiral condensate, compared to the history of the topological charge.

T	L/a	$\langle T_{01}^{G,\{6\}} \rangle_{\boldsymbol{\xi}} / T^4$	$\langle T_{01}^{F,\{6\}} \rangle_{\boldsymbol{\xi}} / T^4$	s/T^3
T_1	144	-2.802(17)	-6.3058(59)	19.763(48)
	288	-2.791(14)	-6.3175(60)	19.759(38)
T_8	144	-2.373(23)	-5.8475(98)	18.238(64)
	288	-2.361(19)	-5.867(10)	18.245(62)

Table F.15: Results for the bare EMT components, and for the entropy density obtained from the perturbatively renormalized EMT. We consider two temperatures and two values of the spatial volume, and $L_0/a = 6$.

in the moving frame, see equation (2.17). On the lattice the EMT requires a finite renormalization because the regularization breaks the SO(4) symmetry to its discrete hypercubic subgroup. At given L_0/a and g_0^2 we write the lattice entropy density as

$$\frac{s}{T^3} = -\frac{1+\boldsymbol{\xi}^2}{\xi_k} \frac{1}{T^4} \langle T_{0k}^{R,\{6\}} \rangle_{\boldsymbol{\xi}} \,, \tag{F.94}$$

where on the right appears the renormalized lattice EMT in the sextet representation of the hypercubic group [33]:

$$T_{\mu\nu}^{R,\{6\}} = Z_G^{\{6\}}(g_0^2)\, T_{\mu\nu}^{G,\{6\}} + Z_F^{\{6\}}(g_0^2)\, T_{\mu\nu}^{F,\{6\}} \,. \tag{F.95}$$

The conventions for the EMT can be found in Appendix B. Finite volume effects for the entropy can thus be directly estimated by measuring the relevant 1-point functions of the EMT at some selected bare parameters, on lattices with different spatial volumes. This circumvents the very expensive computation of the free energy along the line of Chapter 4 on a larger physical volume. The two finite renormalization constants are not known yet non-perturbatively, even though there is some work in progress in this direction [23] (see also Section 5.3). However, in order to study the finite volume effects we may use the 1-loop results in lattice perturbation theory [31, 42].

We proceeded as follows. At the bare parameters of T_1, T_8 and lattice resolution $L_0/a = 6$ we measured the two one-point functions appearing in (F.95) in lattice QCD simulations at $L/a = 144$ and $L/a = 288$, and shift $\boldsymbol{\xi} = (1, 0, 0)$. Then, we computed the entropy density at the two volumes using equation (F.94) and the perturbative renormalization constants. The results are collected in Table F.15, where we show the bare matrix elements of the EMT and the entropy density obtained from the perturbative renormalization of the tensor. For the check to be significant, we collected enough statistics so that the relative accuracy on the entropy density is comparable to the accuracy of the fully non-perturbative values in Table 4.7. At both temperatures T_1 and T_8, the gluonic 1-point functions at two volumes are compatible within ~ 0.5 combined sigma, while the fermionic components within ~ 1.4 combined sigma. However, when they are combined together for estimating the entropy density, we see that the values at two volumes are in perfect agreement, with a deviation smaller than ~ 0.1 combined sigma.

Appendix G

Technical details on the non-perturbative renormalization of composite operators

G.1 Perturbative computation of Z_V

In this Appendix we discuss the computation of $\langle V_\mu^l \rangle$ and $\langle V_\mu^c \rangle$ at $\mathrm{O}(g_0^2)$ in lattice perturbation theory. We present here only the relevant expressions, while for the details of our conventions and notation we refer readers to Appendix E and to Ref. [42]: in particular, the results of the calculation for the conserved flavour-singlet vector current can be found in Appendix G of that reference. The computation is carried out in the presence of shifted boundary conditions and of a twist fermion phase for a generic number of colours, N_c, and of quark flavours, N_f. We write the expectation value of the local current as follows

$$\langle V_\mu^l \rangle = \mathcal{V}_\mu^{l,(0)} + g_0^2 \, \mathcal{V}_\mu^{l,(1)} \, , \tag{G.1}$$

where the tree-level value is given by

$$\mathcal{V}_\mu^{l,(0)} = 4iN_cN_f \frac{aF_\mu^{(5)} + \sum_\sigma F_{\mu\sigma}^{(4)}}{(am_0+4)} \, . \tag{G.2}$$

The definitions of the integrals $F_\mu^{(5)}$, $F_{\mu\nu}^{(4)}$ and of similar ones that appear below can be found in Appendix E. The $\mathrm{O}(g_0^2)$ contribution can be written as the sum of three terms,

$$\mathcal{V}_\mu^{l,(1)} = i(N_c^2-1)N_f \left\{ \mathcal{V}_\mu^{l,1} + \mathcal{V}_\mu^{l,2} + \mathcal{V}_\mu^{l,3} \right\} \, , \tag{G.3}$$

whose expressions are

$$\mathcal{V}_\mu^{l,1} = aB^{(0)} \left\{ \frac{a^2F_\mu^{(5)} + \sum_\sigma aF_{\mu\sigma}^{(4)}}{(am_0+4)} - 2\left(aF_\mu^{(7)} + \sum_\sigma F_{\mu\sigma}^{(6)} \right) \right\} \, , \tag{G.4}$$

$$\mathcal{V}_\mu^{l,2} = -4 \int_{q_{\boldsymbol{\xi}};p_{\boldsymbol{\xi},\theta};k_{\boldsymbol{\xi},\theta}} \frac{\bar{\delta}(p-q-k)}{D_G(q)D_F^2(k)D_F(p)} \times \tag{G.5}$$
$$\bar{k}_\mu \Bigg\{ m_0(p)m_0(k) \sum_\sigma \mathrm{c}_\sigma(r) - a \sum_\sigma \Big\{ \bar{r}_\sigma \Big[m_0(k)\bar{p}_\sigma + m_0(p)\bar{k}_\sigma \Big] \Big\}$$
$$+ \sum_\sigma \Big\{ \bar{p}_\sigma \bar{k}_\sigma \Big[3 - \mathrm{c}_\sigma(r) \Big] \Big\} \Bigg\} ,$$

$$\mathcal{V}_\mu^{l,3} = -2 \int_{q_{\boldsymbol{\xi}};p_{\boldsymbol{\xi},\theta};k_{\boldsymbol{\xi},\theta}} \frac{\left[\bar{p}_\mu \left(\mathrm{c}_\mu(r) - 3\right) + a m_0(p) \bar{r}_\mu\right]}{D_G(q)D_F(p)D_F(k)} \, \bar{\delta}(p-q-k) \, , \tag{G.6}$$

and we have defined $r = p + k$.

The Sheikholeslami-Wohlert term for the O(a)-improvement of the action adds two contributions to the O(g_0^2) coefficient,

$$\mathcal{V}_\mu^{l,(1)} \longrightarrow \mathcal{V}_\mu^{l,(1)} + i(N_c^2 - 1)N_f \left\{ \mathcal{V}_\mu^{l,4} + \mathcal{V}_\mu^{l,5} \right\} \, , \tag{G.7}$$

which are given by

$$\mathcal{V}_\mu^{l,4} = a c_{\mathrm{sw}} \int_{q_{\boldsymbol{\xi}};p_{\boldsymbol{\xi},\theta};k_{\boldsymbol{\xi},\theta}} \frac{\bar{\delta}(p-q-k)}{D_G(q)D_F^2(k)D_F(p)} \times \tag{G.8}$$
$$\Bigg\{ 2\bar{k}_\mu \Bigg\{ a \sum_{\sigma\rho} \Big\{ \bar{q}_\sigma (\bar{k}_\sigma \bar{p}_\rho - \bar{p}_\sigma \bar{k}_\rho) \big(\bar{p}_\rho + \bar{k}_\rho \big) \Big\}$$
$$+ \sum_\sigma \Big\{ \bar{q}_\sigma \big[m_0(k)\bar{p}_\sigma - m_0(p)\bar{k}_\sigma \big] \sum_{\rho \neq \sigma} \big[\mathrm{c}_\rho(p) + \mathrm{c}_\rho(k) \big] \Big\} \Bigg\}$$
$$+ D_F(k) \Bigg\{ a \big(\bar{p}_\mu + \bar{k}_\mu \big) \sum_\sigma \bar{q}_\sigma \bar{p}_\sigma + \bar{q}_\mu \Big[m_0(p) \sum_{\sigma \neq \mu} \Big(\mathrm{c}_\sigma(p) + \mathrm{c}_\sigma(k) \Big)$$
$$- a \sum_\sigma \bar{p}_\sigma \big(\bar{p}_\sigma + \bar{k}_\sigma \big) \Big] \Bigg\} \Bigg\} ,$$

$$\mathcal{V}_\mu^{l,5} = \frac{a^2 c_{\rm sw}^2}{4} \int_{q_{\boldsymbol{\xi}};p_{\boldsymbol{\xi},\theta};k_{\boldsymbol{\xi},\theta}} \frac{\bar{\delta}(p-q-k)}{D_G(q) D_F^2(k) D_F(p)} \times \tag{G.9}$$

$$\Bigg\{ 2\bar{k}_\mu \Bigg\{ 2 \sum_\sigma \bar{q}_\sigma^2 \sum_\rho \bar{p}_\rho \bar{k}_\rho \big(1 + \mathrm{c}_\rho(q)\big)$$

$$+ 2 \sum_\sigma \bar{k}_\sigma \bar{q}_\sigma \sum_\rho \bar{q}_\rho \bar{p}_\rho \Big(2 - \mathrm{c}_\sigma(q) + \sum_{\lambda \neq \rho} \mathrm{c}_\lambda(q)\Big)$$

$$- \Big[\sum_\sigma \bar{p}_\sigma \bar{k}_\sigma - m_0(k) m_0(p) \Big] \Big[\sum_\rho \bar{q}_\rho^2 \Big(3 + \sum_{\lambda \neq \rho} \mathrm{c}_\lambda(q)\Big) \Big] \Bigg\}$$

$$+ D_F(k) \Bigg\{ \bar{p}_\mu \sum_\sigma \Big[\bar{q}_\sigma^2 \Big(1 - 2\mathrm{c}_\mu(q) + \sum_{\rho \neq \sigma} \mathrm{c}_\rho(q)\Big)\Big]$$

$$- 2\bar{q}_\mu \sum_\sigma \Big[\bar{p}_\sigma \bar{q}_\sigma \Big(2 - \mathrm{c}_\mu(q) + \sum_{\rho \neq \sigma} \mathrm{c}_\rho(q)\Big)\Big] \Bigg\} \Bigg\} \, .$$

The critical mass at $\mathrm{O}(g_0^2)$ is given in Appendix E.2. The 1-loop term generates one extra contribution to the expectation value of the vector current which reads

$$\mathcal{V}_\mu^{l,(0)} \longrightarrow \mathcal{V}_\mu^{l,(0)} + \frac{\partial \mathcal{V}_\mu^{l,(0)}}{\partial m_0}\Big|_{m_0 = m_{\rm cr}^{(0)} = 0} m_{\rm cr}^{(1)} g_0^2 \, , \tag{G.10}$$

where

$$\frac{\partial \mathcal{V}_\mu^{l,(0)}}{\partial m_0} = -8 i N_c N_f \frac{a F_\mu^{(7)} + \sum_\sigma F_{\mu\sigma}^{(6)}}{(a m_0 + 4)} \, . \tag{G.11}$$

Based on the above results and those discussed in Ref. [42] for the conserved vector current, we have computed the perturbative expansion of Z_V at $\mathrm{O}(g_0^2)$ in infinite spatial volume, see eq. (5.15). We report in the following the results for the tree-level and 1-loop coefficients $Z_V^{(0)}$, $Z_V^{(1)}$. We write the latter as follows:

$$Z_V^{(1)} = Z_V^{(1,0)} + Z_V^{(1,1)} c_{\rm sw} + Z_V^{(1,2)} c_{\rm sw}^2 . \tag{G.12}$$

The coefficients $Z_V^{(0)}$, $Z_V^{(1,0)}$, ..., $Z_V^{(1,2)}$ depend on the extension of the compact direction L_0/a because of discretization effects. Their numerical values at $\theta_0 = \pi/6$ with shift $\boldsymbol{\xi} = (1,0,0)$ are collected in Table G.1 for several values of L_0/a. These are the coefficients to be used in eq. (5.17) to improve the non-perturbative results presented in Subsection 5.2.4. The values in the Table G.1 suggest also that, at least at this order in perturbation theory, discretization errors for Z_V are tiny for the larger temporal extensions.

L_0/a	$Z_V^{(0)}$	$Z_V^{(1,0)}$	$Z_V^{(1,1)}$	$Z_V^{(1,2)}$
4	1.112904	-0.071406	0.012116	0.001336
6	1.021530	-0.067500	0.014571	0.001616
8	1.005285	-0.066005	0.015062	0.001689
10	1.001882	-0.065592	0.015097	0.001708

Table G.1: Values of $Z_V^{(0)}$, ..., $Z_V^{(1,2)}$ at $\theta_0 = \pi/6$ and $\boldsymbol{\xi} = (1,0,0)$ for several values of L_0/a. The numerical values have been rounded at the level of 10^{-6}.

G.2 Renormalization constants

We collect here the explicit solutions of the master equation (5.26) for the sextet renormalization constants. It is convenient to define the following differences,

$$\Delta_{0k}^{G,\{6\}} = \langle T_{0k}^{G,\{6\}} \rangle_{\boldsymbol{\xi},\theta_0^B} - \langle T_{0k}^{G,\{6\}} \rangle_{\boldsymbol{\xi},\theta_0^A} , \tag{G.13}$$

$$\Delta_{0k}^{F,\{6\}} = \langle T_{0k}^{F,\{6\}} \rangle_{\boldsymbol{\xi},\theta_0^B} - \langle T_{0k}^{F,\{6\}} \rangle_{\boldsymbol{\xi},\theta_0^A} , \tag{G.14}$$

while the determinant of the matrix in the master equation (5.26) reads

$$\begin{aligned} D_{0k}^{\{6\}} &= \langle T_{0k}^{G,\{6\}} \rangle_{\boldsymbol{\xi},\theta_0^A} \langle T_{0k}^{F,\{6\}} \rangle_{\boldsymbol{\xi},\theta_0^B} - \langle T_{0k}^{F,\{6\}} \rangle_{\boldsymbol{\xi},\theta_0^A} \langle T_{0k}^{G,\{6\}} \rangle_{\boldsymbol{\xi},\theta_0^B} \\ &= \langle T_{0k}^{G,\{6\}} \rangle_{\boldsymbol{\xi},\theta_0^A} \Delta_{0k}^{F,\{6\}} - \langle T_{0k}^{F,\{6\}} \rangle_{\boldsymbol{\xi},\theta_0^A} \Delta_{0k}^{G,\{6\}} . \end{aligned} \tag{G.15}$$

Then, the solution of the system for the sextet gluonic renormalization constant $Z_G^{\{6\}}$ may be put in the following form,

$$Z_G^{\{6\}} = -\frac{1}{\langle T_{0k}^{G,\{6\}} \rangle_{\boldsymbol{\xi},\theta_0^A}} \left(\frac{\Delta f_{\boldsymbol{\xi},\theta_0^A}}{\Delta \xi_k} + \frac{\langle T_{0k}^{F,\{6\}} \rangle_{\boldsymbol{\xi},\theta_0^A} \mathcal{V}_{0,k}^{AB}}{\Delta_{0k}^{F,\{6\}}} \right) \left(1 + \frac{\langle T_{0k}^{F,\{6\}} \rangle_{\boldsymbol{\xi},\theta_0^A} \Delta_{0k}^{G,\{6\}}}{D_{0k}^{\{6\}}} \right) , \tag{G.16}$$

while the sextet fermionic $Z_F^{\{6\}}$ reads

$$Z_F^{\{6\}} = \frac{\mathcal{V}_{0,k}^{AB}}{\Delta_{0k}^{F,\{6\}}} + \frac{\Delta_{0k}^{G,\{6\}}}{D_{0k}^{\{6\}}} \left(\frac{\Delta f_{\boldsymbol{\xi},\theta_0^A}}{\Delta \xi_k} + \frac{\langle T_{0k}^{F,\{6\}} \rangle_{\boldsymbol{\xi},\theta_0^A} \mathcal{V}_{0,k}^{AB}}{\Delta_{0k}^{F,\{6\}}} \right) . \tag{G.17}$$

The expressions for the triplet renormalization constants $Z_G^{\{3\}}$, $Z_F^{\{3\}}$ can be similarly derived exploiting equation (5.27).

G.3 Simulation details

In our simulations of $N_f = 3$ O(a)-improved Wilson fermions we used the package `openQCD-1.6` [99] modified for including shifted boundary conditions. We simulated

the up and down quark doublet with an optimized twisted-mass Hasenbusch preconditioning [75, 101] for the quark determinant. This determinant was factorized into three components using twisted mass values of $a\mu = 0.0$, 0.1 and 1.0. For the strange quark we adopted the RHMC algorithm [86, 36], optimizing the frequency splitting of the rational approximation with two distinct contributions. All the flavours were even-odd preconditioned. The integration of the molecular dynamics equations has been performed with a three-level integration scheme. The gauge force have been integrated at the finest level using a 4th-order Omelyan-Mryglod-Folk (OMF4) [123] integrator with a step size of 1, while the fermionic forces were integrated at the two coarser levels. At the finest of these levels, we again used an OMF4 integrator with a step size of 1, while at the coarsest level, we employed a 2nd-order OMF integrator with a step size ranging from 7 to 9. Along the molecular dynamics evolution the Dirac equation has been solved using a standard conjugate gradient method with chronological inversion. Each trajectory has been chosen to be 2 Molecular Dynamics Units long for all lattices.

Bibliography

[1] C. Abel et al. "Measurement of the Permanent Electric Dipole Moment of the Neutron". In: *Phys. Rev. Lett.* 124.8 (2020), p. 081803. DOI: 10.1103/PhysRevLett.124.081803. arXiv: 2001.11966 [hep-ex].

[2] Shreyasi Acharya et al. "Two-particle transverse momentum correlations in pp and p-Pb collisions at LHC energies". In: *Phys. Rev. C* 107.5 (2023), p. 054617. DOI: 10.1103/PhysRevC.107.054617. arXiv: 2211.08979 [nucl-ex].

[3] Stephen L. Adler. "Overrelaxation Algorithms for Lattice Field Theories". In: *Phys. Rev. D* 37 (1988), p. 458. DOI: 10.1103/PhysRevD.37.458.

[4] B. Alles et al. "Hybrid Monte Carlo and topological modes of full QCD". In: *Phys. Lett. B* 389 (1996), pp. 107–111. DOI: 10.1016/S0370-2693(96)01247-6. arXiv: hep-lat/9607049.

[5] Pau Amaro-Seoane et al. "Laser Interferometer Space Antenna". In: (Feb. 2017). arXiv: 1702.00786 [astro-ph.IM].

[6] S. Aoki et al. "Precise determination of the strong coupling constant in $N_f = 2{+}1$ lattice QCD with the Schrodinger functional scheme". In: *JHEP* 10 (2009), p. 053. DOI: 10.1088/1126-6708/2009/10/053. arXiv: 0906.3906 [hep-lat].

[7] Thomas Appelquist and Robert D. Pisarski. "High-Temperature Yang-Mills Theories and Three-Dimensional Quantum Chromodynamics". In: *Phys. Rev. D* 23 (1981), p. 2305. DOI: 10.1103/PhysRevD.23.2305.

[8] Peter Brockway Arnold and Cheng-xing Zhai. "The Three loop free energy for high temperature QED and QCD with fermions". In: *Phys. Rev. D* 51 (1995), pp. 1906–1918. DOI: 10.1103/PhysRevD.51.1906. arXiv: hep-ph/9410360.

[9] Alexander Aryshev et al. "The International Linear Collider: Report to Snowmass 2021". In: (Mar. 2022). arXiv: 2203.07622 [physics.acc-ph].

[10] Andreas Athenodorou et al. "Topological susceptibility of $\mathrm{N}_f = 2 + 1$ QCD from staggered fermions spectral projectors at high temperatures". In: *JHEP* 10 (2022), p. 197. DOI: 10.1007/JHEP10(2022)197. arXiv: 2208.08921 [hep-lat].

[11] P. A. Baikov, K. G. Chetyrkin, and J. H. Kühn. "Five-Loop Running of the QCD coupling constant". In: *Phys. Rev. Lett.* 118.8 (2017), p. 082002. DOI: 10.1103/PhysRevLett.118.082002. arXiv: 1606.08659 [hep-ph].

[12] Tom Banks and A. Casher. "Chiral Symmetry Breaking in Confining Theories". In: *Nucl. Phys. B* 169 (1980), pp. 103–125. DOI: 10.1016/0550-3213(80)90255-2.

[13] A. Bazavov et al. "Equation of state in (2+1)-flavor QCD". In: *Phys. Rev. D* 90 (2014), p. 094503. DOI: 10.1103/PhysRevD.90.094503. arXiv: 1407.6387 [hep-lat].

[14] A. Bazavov et al. "The chiral transition and $U(1)_A$ symmetry restoration from lattice QCD using Domain Wall Fermions". In: *Phys. Rev. D* 86 (2012), p. 094503. DOI: 10.1103/PhysRevD.86.094503. arXiv: 1205.3535 [hep-lat].

[15] A. Bazavov, P. Petreczky, and J. H. Weber. "Equation of State in 2+1 Flavor QCD at High Temperatures". In: *Phys. Rev. D* 97.1 (2018), p. 014510. DOI: 10.1103/PhysRevD.97.014510. arXiv: 1710.05024 [hep-lat].

[16] A. A. Belavin et al. "Pseudoparticle Solutions of the Yang-Mills Equations". In: *Phys. Lett. B* 59 (1975). Ed. by J. C. Taylor, pp. 85–87. DOI: 10.1016/0370-2693(75)90163-X.

[17] Tanmoy Bhattacharya et al. "Improved bilinears in lattice QCD with non-degenerate quarks". In: *Phys. Rev. D* 73 (2006), p. 034504. DOI: 10.1103/PhysRevD.73.034504. arXiv: hep-lat/0511014.

[18] Tanmoy Bhattacharya et al. "Nonperturbative renormalization constants using Ward identities". In: *Phys. Lett. B* 461 (1999), pp. 79–88. DOI: 10.1016/S0370-2693(99)00796-0. arXiv: hep-lat/9904011.

[19] Marco Bochicchio et al. "Chiral Symmetry on the Lattice with Wilson Fermions". In: *Nucl. Phys. B* 262 (1985), p. 331. DOI: 10.1016/0550-3213(85)90290-1.

[20] Sz. Borsanyi et al. "Calculation of the axion mass based on high-temperature lattice quantum chromodynamics". In: *Nature* 539.7627 (2016), pp. 69–71. DOI: 10.1038/nature20115. arXiv: 1606.07494 [hep-lat].

[21] Szabocls Borsanyi et al. "Full result for the QCD equation of state with 2+1 flavors". In: *Phys. Lett. B* 730 (2014), pp. 99–104. DOI: 10.1016/j.physletb.2014.01.007. arXiv: 1309.5258 [hep-lat].

[22] Matteo Bresciani et al. "Non-perturbative renormalization of the QCD flavour-singlet local vector current". In: *Phys. Lett. B* 835 (2022), p. 137579. DOI: 10.1016/j.physletb.2022.137579. arXiv: 2203.14754 [hep-lat].

[23] Matteo Bresciani et al. "Progresses on high-temperature QCD: Equation of State and energy-momentum tensor". In: *PoS* LATTICE2023 (2024), p. 192. DOI: 10.22323/1.453.0192. arXiv: 2312.11009 [hep-lat].

[24] R. Brower et al. "QCD at fixed topology". In: *Phys. Lett. B* 560 (2003), pp. 64–74. DOI: 10.1016/S0370-2693(03)00369-1. arXiv: hep-lat/0302005.

[25] Mattia Bruno et al. "QCD Coupling from a Nonperturbative Determination of the Three-Flavor Λ Parameter". In: *Phys. Rev. Lett.* 119.10 (2017), p. 102001. DOI: 10.1103/PhysRevLett.119.102001. arXiv: 1706.03821 [hep-lat].

[26] N. Cabibbo and E. Marinari. "A New Method for Updating SU(N) Matrices in Computer Simulations of Gauge Theories". In: *Phys. Lett. B* 119 (1982), pp. 387–390. DOI: 10.1016/0370-2693(82)90696-7.

[27] Curtis G. Callan Jr. "Broken scale invariance in scalar field theory". In: *Phys. Rev. D* 2 (1970), pp. 1541–1547. DOI: 10.1103/PhysRevD.2.1541.

[28] Isabel Campos et al. "Non-perturbative quark mass renormalisation and running in $N_f = 3$ QCD". In: *Eur. Phys. J. C* 78.5 (2018), p. 387. DOI: 10.1140/epjc/s10052-018-5870-5. arXiv: 1802.05243 [hep-lat].

[29] Stefano Capitani et al. "Non-perturbative quark mass renormalization in quenched lattice QCD". In: *Nucl. Phys. B* 544 (1999). [Erratum: Nucl.Phys.B 582, 762–762 (2000)], pp. 669–698. DOI: 10.1016/S0550-3213(98)00857-8. arXiv: hep-lat/9810063.

[30] Sergio Caracciolo, Pietro Menotti, and Andrea Pelissetto. "Analytic determination at one loop of the energy momentum tensor for lattice QCD". In: *Phys. Lett. B* 260 (1991), pp. 401–406. DOI: 10.1016/0370-2693(91)91632-6.

[31] Sergio Caracciolo, Pietro Menotti, and Andrea Pelissetto. "One loop analytic computation of the energy momentum tensor for lattice gauge theories". In: *Nucl. Phys. B* 375 (1992), pp. 195–239. DOI: 10.1016/0550-3213(92)90339-D.

[32] Sergio Caracciolo et al. "Renormalization of the Energy Momentum Tensor and the Trace Anomaly in Lattice QED". In: *Phys. Lett. B* 228 (1989), pp. 375–378. DOI: 10.1016/0370-2693(89)91562-1.

[33] Sergio Caracciolo et al. "The Energy Momentum Tensor for Lattice Gauge Theories". In: *Annals Phys.* 197 (1990), p. 119. DOI: 10.1016/0003-4916(90)90203-Z.

[34] Scott Chapman. "A New dimensionally reduced effective action for QCD at high temperature". In: *Phys. Rev. D* 50 (1994), pp. 5308–5313. DOI: 10.1103/PhysRevD.50.5308. arXiv: hep-ph/9407313.

[35] S. A. Chin. "Transition to Hot Quark Matter in Relativistic Heavy Ion Collision". In: *Phys. Lett. B* 78 (1978), pp. 552–555. DOI: 10.1016/0370-2693(78)90637-8.

[36] M. A. Clark and A. D. Kennedy. "The RHMC algorithm for two flavors of dynamical staggered fermions". In: *Nucl. Phys. B Proc. Suppl.* 129 (2004). Ed. by S. Aoki et al., pp. 850–852. DOI: 10.1016/S0920-5632(03)02732-4. arXiv: hep-lat/0309084.

[37] ALPHA collaboration. *Simulating the QCD Schrodinger Functional with three massless quark flavors.* Internal notes, in preparation for publication.

[38] M. Creutz. "Monte Carlo Study of Quantized SU(2) Gauge Theory". In: *Phys. Rev. D* 21 (1980), pp. 2308–2315. DOI: 10.1103/PhysRevD.21.2308.

[39] Michael Creutz. "Confinement and the Critical Dimensionality of Space-Time". In: *Phys. Rev. Lett.* 43 (1979). [Erratum: Phys.Rev.Lett. 43, 890 (1979)], pp. 553–556. DOI: 10.1103/PhysRevLett.43.553.

[40] Francesca Cuteri, Owe Philipsen, and Alessandro Sciarra. "On the order of the QCD chiral phase transition for different numbers of quark flavours". In: *JHEP* 11 (2021), p. 141. DOI: 10.1007/JHEP11(2021)141. arXiv: 2107.12739 [hep-lat].

[41] Mattia Dalla Brida. "Past, present, and future of precision determinations of the QCD parameters from lattice QCD". In: *Eur. Phys. J. A* 57.2 (2021), p. 66. DOI: 10.1140/epja/s10050-021-00381-3. arXiv: 2012.01232 [hep-lat].

[42] Mattia Dalla Brida, Leonardo Giusti, and Michele Pepe. "Non-perturbative definition of the QCD energy-momentum tensor on the lattice". In: *JHEP* 04 (2020), p. 043. DOI: 10.1007/JHEP04(2020)043. arXiv: 2002.06897 [hep-lat].

[43] Mattia Dalla Brida, Leonardo Giusti, and Michele Pepe. "QCD in a moving frame: an exploratory study". In: *EPJ Web Conf.* 175 (2018). Ed. by M. Della Morte et al., p. 14012. DOI: 10.1051/epjconf/201817514012. arXiv: 1710.09219 [hep-lat].

[44] Mattia Dalla Brida et al. "A non-perturbative exploration of the high energy regime in $N_{\mathrm{f}} = 3$ QCD". In: *Eur. Phys. J. C* 78.5 (2018), p. 372. DOI: 10.1140/epjc/s10052-018-5838-5. arXiv: 1803.10230 [hep-lat].

[45] Mattia Dalla Brida et al. "Determination of the QCD Λ-parameter and the accuracy of perturbation theory at high energies". In: *Phys. Rev. Lett.* 117.18 (2016), p. 182001. DOI: 10.1103/PhysRevLett.117.182001. arXiv: 1604.06193 [hep-ph].

[46] Mattia Dalla Brida et al. "Non-perturbative thermal QCD at all temperatures: the case of mesonic screening masses". In: *JHEP* 04 (2022), p. 034. DOI: 10.1007/JHEP04(2022)034. arXiv: 2112.05427 [hep-lat].

[47] Luigi Del Debbio, Gian Mario Manca, and Ettore Vicari. "Critical slowing down of topological modes". In: *Phys. Lett. B* 594 (2004), pp. 315–323. DOI: 10.1016/j.physletb.2004.05.038. arXiv: hep-lat/0403001.

[48] S. Duane et al. "Hybrid Monte Carlo". In: *Phys. Lett. B* 195 (1987), pp. 216–222. DOI: 10.1016/0370-2693(87)91197-X.

[49] Georg P. Engel et al. "Chiral Symmetry Breaking in QCD with Two Light Flavors". In: *Phys. Rev. Lett.* 114.11 (2015), p. 112001. DOI: 10.1103/PhysRevLett.114.112001. arXiv: 1406.4987 [hep-ph].

[50] L. D. Faddeev and V. N. Popov. "Feynman Diagrams for the Yang-Mills Field". In: *Phys. Lett. B* 25 (1967). Ed. by Jong-Ping Hsu and D. Fine, pp. 29–30. DOI: 10.1016/0370-2693(67)90067-6.

[51] D. Friedan. "A PROOF OF THE NIELSEN-NINOMIYA THEOREM". In: *Commun. Math. Phys.* 85 (1982), pp. 481–490. DOI: 10.1007/BF01403500.

[52] E. Gabrielli et al. "Renormalization of lattice two fermion operators with improved nearest neighbor action". In: *Nucl. Phys. B* 362 (1991), pp. 475–486. DOI: 10.1016/0550-3213(91)90569-J.

[53] Christof Gattringer and Christian B. Lang. *Quantum chromodynamics on the lattice*. Vol. 788. Berlin: Springer, 2010. DOI: 10.1007/978-3-642-01850-3.

[54] Murray Gell-Mann and F. E. Low. "Quantum electrodynamics at small distances". In: *Phys. Rev.* 95 (1954), pp. 1300–1312. DOI: 10.1103/PhysRev.95.1300.

[55] Murray Gell-Mann, R. J. Oakes, and B. Renner. "Behavior of current divergences under SU(3) x SU(3)". In: *Phys. Rev.* 175 (1968), pp. 2195–2199. DOI: 10.1103/PhysRev.175.2195.

[56] Paul H. Ginsparg and Kenneth G. Wilson. "A Remnant of Chiral Symmetry on the Lattice". In: *Phys. Rev. D* 25 (1982), p. 2649. DOI: 10.1103/PhysRevD.25.2649.

[57] Leonardo Giusti and Martin Luscher. "Chiral symmetry breaking and the Banks-Casher relation in lattice QCD with Wilson quarks". In: *JHEP* 03 (2009), p. 013. DOI: 10.1088/1126-6708/2009/03/013. arXiv: 0812.3638 [hep-lat].

[58] Leonardo Giusti and Martin Lüscher. "Topological susceptibility at $T > T_c$ from master-field simulations of the SU(3) gauge theory". In: *Eur. Phys. J. C* 79.3 (2019), p. 207. DOI: 10.1140/epjc/s10052-019-6706-7. arXiv: 1812.02062 [hep-lat].

[59] Leonardo Giusti and Harvey B. Meyer. "Implications of Poincare symmetry for thermal field theories in finite-volume". In: *JHEP* 01 (2013), p. 140. DOI: 10.1007/JHEP01(2013)140. arXiv: 1211.6669 [hep-lat].

[60] Leonardo Giusti and Harvey B. Meyer. "Thermal momentum distribution from path integrals with shifted boundary conditions". In: *Phys. Rev. Lett.* 106 (2011), p. 131601. DOI: 10.1103/PhysRevLett.106.131601. arXiv: 1011.2727 [hep-lat].

[61] Leonardo Giusti and Michele Pepe. "Energy-momentum tensor on the lattice: Non-perturbative renormalization in Yang-Mills theory". In: *Phys. Rev. D* 91 (2015), p. 114504. DOI: 10.1103/PhysRevD.91.114504. arXiv: 1503.07042 [hep-lat].

[62] Leonardo Giusti and Michele Pepe. "Equation of state of the SU(3) Yang–Mills theory: A precise determination from a moving frame". In: *Phys. Lett. B* 769 (2017), pp. 385–390. DOI: 10.1016/j.physletb.2017.04.001. arXiv: 1612.00265 [hep-lat].

[63] Leonardo Giusti, Silvano Petrarca, and Bruno Taglienti. "Theta dependence of the vacuum energy in the SU(3) gauge theory from the lattice". In: *Phys. Rev. D* 76 (2007), p. 094510. DOI: 10.1103/PhysRevD.76.094510. arXiv: 0705.2352 [hep-th].

[64] Leonardo Giusti et al. "Baryonic screening masses in QCD at high temperature". In: *Phys. Lett. B* 855 (2024), p. 138799. DOI: 10.1016/j.physletb.2024.138799. arXiv: 2405.04182 [hep-lat].

[65] Leonardo Giusti et al. "Baryonic thermal screening mass at NLO". In: *JHEP* 06 (2024), p. 205. DOI: 10.1007/JHEP06(2024)205. arXiv: 2405.03975 [hep-ph].

[66] Leonardo Giusti et al. "Frequency-splitting estimators of single-propagator traces". In: *Eur. Phys. J. C* 79.7 (2019), p. 586. DOI: 10.1140/epjc/s10052-019-7049-0. arXiv: 1903.10447 [hep-lat].

[67] Jeffrey Goldstone, Abdus Salam, and Steven Weinberg. "Broken Symmetries". In: *Phys. Rev.* 127 (1962), pp. 965–970. DOI: 10.1103/PhysRev.127.965.

[68] Giovanni Grilli di Cortona et al. "The QCD axion, precisely". In: *JHEP* 01 (2016), p. 034. DOI: 10.1007/JHEP01(2016)034. arXiv: 1511.02867 [hep-ph].

[69] David J. Gross and Frank Wilczek. "Ultraviolet Behavior of Nonabelian Gauge Theories". In: *Phys. Rev. Lett.* 30 (1973). Ed. by J. C. Taylor, pp. 1343–1346. DOI: 10.1103/PhysRevLett.30.1343.

[70] Particle Data Group et al. "Review of Particle Physics". In: *Progress of Theoretical and Experimental Physics* 2022.8 (Aug. 2022), p. 083C01. DOI: 10.1093/ptep/ptac097. URL: https://doi.org/10.1093/ptep/ptac097.

[71] Miklos Gyulassy and Larry McLerran. "New forms of QCD matter discovered at RHIC". In: *Nucl. Phys. A* 750 (2005). Ed. by D. Rischke and G. Levin, pp. 30–63. DOI: 10.1016/j.nuclphysa.2004.10.034. arXiv: nucl-th/0405013.

[72] Najmul Haque et al. "Three-loop HTLpt thermodynamics at finite temperature and chemical potential". In: *JHEP* 05 (2014), p. 027. DOI: 10.1007/JHEP05(2014)027. arXiv: 1402.6907 [hep-ph].

[73] A. Hart, M. Laine, and O. Philipsen. "Static correlation lengths in QCD at high temperatures and finite densities". In: *Nucl. Phys. B* 586 (2000), pp. 443–474. DOI: 10.1016/S0550-3213(00)00418-1. arXiv: hep-ph/0004060.

[74] M. Hasenbusch and K. Jansen. "Speeding up lattice QCD simulations with clover improved Wilson fermions". In: *Nucl. Phys. B* 659 (2003), pp. 299–320. DOI: 10.1016/S0550-3213(03)00227-X. arXiv: hep-lat/0211042.

[75] Martin Hasenbusch. "Speeding up the hybrid Monte Carlo algorithm for dynamical fermions". In: *Phys. Lett. B* 519 (2001), pp. 177–182. DOI: 10.1016/S0370-2693(01)01102-9. arXiv: hep-lat/0107019.

[76] W. K. Hastings. "Monte Carlo Sampling Methods Using Markov Chains and Their Applications". In: *Biometrika* 57 (1970), pp. 97–109. DOI: 10.1093/biomet/57.1.97.

[77] Jochen Heitger, Fabian Joswig, and Anastassios Vladikas. "Ward identity determination of Z_S/Z_P for $N_f = 3$ lattice QCD in a Schrödinger functional setup". In: *Eur. Phys. J. C* 80.8 (2020), p. 765. DOI: 10.1140/epjc/s10052-020-8266-2. arXiv: 2005.01352 [hep-lat].

[78] Pilar Hernandez, Karl Jansen, and Martin Luscher. "Locality properties of Neuberger's lattice Dirac operator". In: *Nucl. Phys. B* 552 (1999), pp. 363–378. DOI: 10.1016/S0550-3213(99)00213-8. arXiv: hep-lat/9808010.

[79] A. Hietanen et al. "Plaquette expectation value and gluon condensate in three dimensions". In: *JHEP* 01 (2005), p. 013. DOI: 10.1088/1126-6708/2005/01/013. arXiv: hep-lat/0412008.

[80] Nikolai Husung, Peter Marquard, and Rainer Sommer. "The asymptotic approach to the continuum of lattice QCD spectral observables". In: *Phys. Lett. B* 829 (2022), p. 137069. DOI: 10.1016/j.physletb.2022.137069. arXiv: 2111.02347 [hep-lat].

[81] Karl Jansen and Rainer Sommer. "O(a) improvement of lattice QCD with two flavors of Wilson quarks". In: *Nucl. Phys. B* 530 (1998). [Erratum: Nucl.Phys.B 643, 517–518 (2002)], pp. 185–203. DOI: 10.1016/S0550-3213(98)00396-4. arXiv: hep-lat/9803017.

[82] K. Kajantie et al. "The Pressure of hot QCD up to g6 ln(1/g)". In: *Phys. Rev. D* 67 (2003), p. 105008. DOI: 10.1103/PhysRevD.67.105008. arXiv: hep-ph/0211321.

[83] Joseph I. Kapusta. "Quantum Chromodynamics at High Temperature". In: *Nucl. Phys. B* 148 (1979), pp. 461–498. DOI: 10.1016/0550-3213(79)90146-9.

[84] F. Karsch, K. Redlich, and A. Tawfik. "Hadron resonance mass spectrum and lattice QCD thermodynamics". In: *Eur. Phys. J. C* 29 (2003), pp. 549–556. DOI: 10.1140/epjc/s2003-01228-y. arXiv: hep-ph/0303108.

[85] S. Kawamura. "Space gravitational wave antenna DECIGO and B-DECIGO". In: *16th Marcel Grossmann Meeting on Recent Developments in Theoretical and Experimental General Relativity, Astrophysics and Relativistic Field Theories*. 2023. DOI: 10.1142/9789811269776_0267.

[86] A. D. Kennedy, Ivan Horvath, and Stefan Sint. "A New exact method for dynamical fermion computations with nonlocal actions". In: *Nucl. Phys. B Proc. Suppl.* 73 (1999). Ed. by Thomas A. DeGrand et al., pp. 834–836. DOI: 10.1016/S0920-5632(99)85217-7. arXiv: hep-lat/9809092.

[87] Francesco Knechtli, Michael Günther, and Michael Peardon. *Lattice Quantum Chromodynamics: Practical Essentials*. SpringerBriefs in Physics. Springer, 2017. DOI: 10.1007/978-94-024-0999-4.

[88] Stefan Kurth. "The Renormalized quark mass in the Schrodinger functional of lattice QCD: A One loop calculation with a nonvanishing background field". Other thesis. Nov. 2002. arXiv: hep-lat/0211011.

[89] Mikko Laine and York Schroder. "Quark mass thresholds in QCD thermodynamics". In: *Phys. Rev. D* 73 (2006), p. 085009. DOI: 10.1103/PhysRevD.73.085009. arXiv: hep-ph/0603048.

[90] Mikko Laine and Aleksi Vuorinen. *Basics of Thermal Field Theory*. Vol. 925. Springer, 2016. DOI: 10.1007/978-3-319-31933-9. arXiv: 1701.01554 [hep-ph].

[91] L. D. Landau and E. M. Lifschits. *Course of theoretical physics X: physical kinetics*. Oxford U.K.: Butterworth-Heinemann, 1981.

[92] L. D. Landau and E. M. Lifschits. *The Classical Theory of Fields*. Vol. Volume 2. Course of Theoretical Physics. Oxford: Pergamon Press, 1975.

[93] Davide Laudicina et al. "QCD mesonic screening masses and restoration of chiral symmetry at high T". In: *PoS* LATTICE2022 (2023), p. 182. DOI: 10.22323/1.430.0182. arXiv: 2212.02167 [hep-lat].

[94] Andrei D. Linde. "Infrared Problem in Thermodynamics of the Yang-Mills Gas". In: *Phys. Lett. B* 96 (1980), pp. 289–292. DOI: 10.1016/0370-2693(80)90769-8.

[95] M. Luscher and P. Weisz. "O(a) improvement of the axial current in lattice QCD to one loop order of perturbation theory". In: *Nucl. Phys. B* 479 (1996), pp. 429–458. DOI: 10.1016/0550-3213(96)00448-8. arXiv: hep-lat/9606016.

[96] Martin Luscher. "Advanced lattice QCD". In: *Les Houches Summer School in Theoretical Physics, Session 68: Probing the Standard Model of Particle Interactions*. Feb. 1998, pp. 229–280. arXiv: hep-lat/9802029.

[97] Martin Luscher. "Computational Strategies in Lattice QCD". In: *Les Houches Summer School: Session 93: Modern perspectives in lattice QCD: Quantum field theory and high performance computing*. Feb. 2010, pp. 331–399. arXiv: 1002.4232 [hep-lat].

[98] Martin Luscher. "Exact chiral symmetry on the lattice and the Ginsparg-Wilson relation". In: *Phys. Lett. B* 428 (1998), pp. 342–345. DOI: 10.1016/S0370-2693(98)00423-7. arXiv: hep-lat/9802011.

[99] Martin Luscher. *openQCD: Simulation programs for lattice QCD*. URL: https://luscher.web.cern.ch/luscher/openQCD.

[100] Martin Luscher and Filippo Palombi. "Fluctuations and reweighting of the quark determinant on large lattices". In: *PoS* LATTICE2008 (2008). Ed. by Christopher Aubin et al., p. 049. DOI: 10.22323/1.066.0049. arXiv: 0810.0946 [hep-lat].

[101] Martin Luscher and Stefan Schaefer. "Lattice QCD with open boundary conditions and twisted-mass reweighting". In: *Comput. Phys. Commun.* 184 (2013), pp. 519–528. DOI: 10.1016/j.cpc.2012.10.003. arXiv: 1206.2809 [hep-lat].

[102] Martin Luscher and Peter Weisz. "Coordinate space methods for the evaluation of Feynman diagrams in lattice field theories". In: *Nucl. Phys. B* 445 (1995), pp. 429–450. DOI: 10.1016/0550-3213(95)00185-U. arXiv: hep-lat/9502017.

[103] Martin Luscher, Peter Weisz, and Ulli Wolff. "A Numerical method to compute the running coupling in asymptotically free theories". In: *Nucl. Phys. B* 359 (1991), pp. 221–243. DOI: 10.1016/0550-3213(91)90298-C.

[104] Martin Luscher et al. "A Precise determination of the running coupling in the SU(3) Yang-Mills theory". In: *Nucl. Phys. B* 413 (1994), pp. 481–502. DOI: 10.1016/0550-3213(94)90629-7. arXiv: hep-lat/9309005.

[105] Martin Luscher et al. "Chiral symmetry and O(a) improvement in lattice QCD". In: *Nucl. Phys. B* 478 (1996), pp. 365–400. DOI: 10.1016/0550-3213(96)00378-1. arXiv: hep-lat/9605038.

[106] Martin Luscher et al. "Nonperturbative determination of the axial current normalization constant in O(a) improved lattice QCD". In: *Nucl. Phys. B* 491 (1997), pp. 344–364. DOI: 10.1016/S0550-3213(97)00087-4. arXiv: hep-lat/9611015.

[107] Martin Luscher et al. "Nonperturbative O(a) improvement of lattice QCD". In: *Nucl. Phys. B* 491 (1997), pp. 323–343. DOI: 10.1016/S0550-3213(97)00080-1. arXiv: hep-lat/9609035.

[108] Martin Luscher et al. "The Schrödinger functional: A Renormalizable probe for nonAbelian gauge theories". In: *Nucl. Phys. B* 384 (1992), pp. 168–228. DOI: 10.1016/0550-3213(92)90466-O. arXiv: hep-lat/9207009.

[109] Martin Lüscher. "Properties and uses of the Wilson flow in lattice QCD". In: *JHEP* 08 (2010). [Erratum: JHEP 03, 092 (2014)], p. 071. DOI: 10.1007/JHEP08(2010)071. arXiv: 1006.4518 [hep-lat].

[110] Martin Lüscher. "Step scaling and the Yang-Mills gradient flow". In: *JHEP* 06 (2014), p. 105. DOI: 10.1007/JHEP06(2014)105. arXiv: 1404.5930 [hep-lat].

[111] L. Maiani and G. Martinelli. "Current Algebra and Quark Masses from a Monte Carlo Simulation with Wilson Fermions". In: *Phys. Lett. B* 178 (1986), pp. 265–271. DOI: 10.1016/0370-2693(86)91508-X.

[112] G. Martinelli et al. "Nonperturbative renormalization of two quark operators with an improved lattice fermion action". In: *Phys. Lett. B* 311 (1993). [Erratum: Phys.Lett.B 317, 660 (1993)], pp. 241–248. DOI: 10.1016/0370-2693(93)90562-V.

[113] N. Metropolis et al. "Equation of state calculations by fast computing machines". In: *J. Chem. Phys.* 21 (1953), pp. 1087–1092. DOI: 10.1063/1.1699114.

[114] Harvey B. Meyer. "Transport Properties of the Quark-Gluon Plasma: A Lattice QCD Perspective". In: *Eur. Phys. J. A* 47 (2011), p. 86. DOI: 10.1140/epja/i2011-11086-3. arXiv: 1104.3708 [hep-lat].

[115] I. Montvay and G. Munster. *Quantum fields on a lattice*. Cambridge Monographs on Mathematical Physics. Cambridge University Press, Mar. 1997. DOI: 10.1017/CBO9780511470783.

[116] Guy D. Moore and Niels Schlusser. "Full O(a) improvement in electrostatic QCD". In: *Phys. Rev. D* 100.3 (2019), p. 034510. DOI: 10.1103/PhysRevD.100.034510. arXiv: 1905.09708 [hep-lat].

[117] Pablo Navarrete and York Schröder. "The g^6 pressure of hot Yang-Mills theory: Canonical form of the integrand". In: (Aug. 2024). arXiv: 2408.15830 [hep-ph].

[118] Herbert Neuberger. "Exactly massless quarks on the lattice". In: *Phys. Lett. B* 417 (1998), pp. 141–144. DOI: 10.1016/S0370-2693(97)01368-3. arXiv: hep-lat/9707022.

[119] Herbert Neuberger. "More about exactly massless quarks on the lattice". In: *Phys. Lett. B* 427 (1998), pp. 353–355. DOI: 10.1016/S0370-2693(98)00355-4. arXiv: hep-lat/9801031.

[120] Holger Bech Nielsen and M. Ninomiya. "Absence of Neutrinos on a Lattice. 1. Proof by Homotopy Theory". In: *Nucl. Phys. B* 185 (1981). Ed. by J. Julve and M. Ramón-Medrano. [Erratum: Nucl.Phys.B 195, 541 (1982)], p. 20. DOI: 10.1016/0550-3213(82)90011-6.

[121] Holger Bech Nielsen and M. Ninomiya. "Absence of Neutrinos on a Lattice. 2. Intuitive Topological Proof". In: *Nucl. Phys. B* 193 (1981), pp. 173–194. DOI: 10.1016/0550-3213(81)90524-1.

[122] Holger Bech Nielsen and M. Ninomiya. "No Go Theorem for Regularizing Chiral Fermions". In: *Phys. Lett. B* 105 (1981), pp. 219–223. DOI: 10.1016/0370-2693(81)91026-1.

[123] I. P. Omelyan, I. M. Mryglod, and R. Folk. "Symplectic analytically integrable decomposition algorithms: classification, derivation, and application to molecular dynamics, quantum and celestial mechanics simulations". In: *Comput. Phys. Commun.* 151.3 (2003), pp. 272–314. DOI: 10.1016/s0010-4655(02)00754-3.

[124] H. Panagopoulos and Y. Proestos. "The Critical hopping parameter in O(a) improved lattice QCD". In: *Phys. Rev. D* 65 (2002), p. 014511. DOI: 10.1103/PhysRevD.65.014511. arXiv: hep-lat/0108021.

[125] Marco Panero, Kari Rummukainen, and Andreas Schäfer. "Lattice Study of the Jet Quenching Parameter". In: *Phys. Rev. Lett.* 112.16 (2014), p. 162001. DOI: 10.1103/PhysRevLett.112.162001. arXiv: 1307.5850 [hep-ph].

[126] Owe Philipsen. "Lattice QCD at non-zero temperature and baryon density". In: *Les Houches Summer School: Session 93: Modern perspectives in lattice QCD: Quantum field theory and high performance computing*. Sept. 2010, pp. 273–330. arXiv: 1009.4089 [hep-lat].

[127] Robert D. Pisarski and Frank Wilczek. "Remarks on the Chiral Phase Transition in Chromodynamics". In: *Phys. Rev. D* 29 (1984), pp. 338–341. DOI: 10.1103/PhysRevD.29.338.

[128] Isabel Campos Plasencia et al. "Nonperturbative running of the quark mass for Nf=3 QCD from the chirally rotated Schrödinger functional". In: *Phys. Rev. D* 105.5 (2022), p. 054506. DOI: 10.1103/PhysRevD.105.054506. arXiv: 2112.10606 [hep-lat].

[129] Alexander M. Polyakov. "Particle Spectrum in Quantum Field Theory". In: *JETP Lett.* 20 (1974). Ed. by J. C. Taylor, pp. 194–195.

[130] Alexander M. Polyakov. "Thermal Properties of Gauge Fields and Quark Liberation". In: *Phys. Lett. B* 72 (1978), pp. 477–480. DOI: 10.1016/0370-2693(78)90737-2.

[131] Philip Rabinowitz. "The exact degree of precision of generalized Gauss-Kronrod integration rules". In: *Mathematics of Computation* 35 (1980), pp. 1275–1283. URL: https://api.semanticscholar.org/CorpusID:42436978.

[132] Daniel Robaina and Harvey B. Meyer. "Renormalization of the momentum density on the lattice using shifted boundary conditions". In: *PoS* LATTICE2013 (2014), p. 323. DOI: 10.22323/1.187.0323. arXiv: 1310.6075 [hep-lat].

[133] Andre Roberge and Nathan Weiss. "Gauge Theories With Imaginary Chemical Potential and the Phases of QCD". In: *Nucl. Phys. B* 275 (1986), pp. 734–745. DOI: 10.1016/0550-3213(86)90582-1.

[134] Heinz J. Rothe. *Lattice Gauge Theories : An Introduction (Fourth Edition)*. Vol. 43. World Scientific Publishing Company, 2012. DOI: 10.1142/8229.

[135] Ken'ichi Saikawa and Satoshi Shirai. "Precise WIMP Dark Matter Abundance and Standard Model Thermodynamics". In: *JCAP* 08 (2020), p. 011. DOI: 10.1088/1475-7516/2020/08/011. arXiv: 2005.03544 [hep-ph].

[136] Ken'ichi Saikawa and Satoshi Shirai. "Primordial gravitational waves, precisely: The role of thermodynamics in the Standard Model". In: *JCAP* 05 (2018), p. 035. DOI: 10.1088/1475-7516/2018/05/035. arXiv: 1803.01038 [hep-ph].

[137] Stefan Schaefer, Rainer Sommer, and Francesco Virotta. "Critical slowing down and error analysis in lattice QCD simulations". In: *Nucl. Phys. B* 845 (2011), pp. 93–119. DOI: 10.1016/j.nuclphysb.2010.11.020. arXiv: 1009.5228 [hep-lat].

[138] York Schröder. "The pressure of hot QCD". In: *J. Phys. Conf. Ser.* 720.1 (2016). Ed. by Gonzalo Gutiérrez and Luis Roa, p. 012027. DOI: 10.1088/1742-6596/720/1/012027.

[139] J. C. Sexton and D. H. Weingarten. "Hamiltonian evolution for the hybrid Monte Carlo algorithm". In: *Nucl. Phys. B* 380 (1992), pp. 665–677. DOI: 10.1016/0550-3213(92)90263-B.

[140] B. Sheikholeslami and R. Wohlert. "Improved Continuum Limit Lattice Action for QCD with Wilson Fermions". In: *Nucl. Phys. B* 259 (1985), p. 572. DOI: 10.1016/0550-3213(85)90002-1.

[141] Edward V. Shuryak. "Theory of Hadronic Plasma". In: *Sov. Phys. JETP* 47 (1978), pp. 212–219.

[142] A. Skouroupathis and H. Panagopoulos. "Two-loop renormalization of vector, axial-vector and tensor fermion bilinears on the lattice". In: *Phys. Rev. D* 79 (2009), p. 094508. DOI: 10.1103/PhysRevD.79.094508. arXiv: 0811.4264 [hep-lat].

[143] Rainer Sommer. "O(a) improved lattice QCD". In: *Nucl. Phys. B Proc. Suppl.* 60 (1998). Ed. by Y. Iwasaki and A. Ukawa, pp. 279–294. DOI: 10.1016/S0920-5632(97)00490-8. arXiv: hep-lat/9705026.

[144] Rainer Sommer. "Scale setting in lattice QCD". In: *PoS* LATTICE2013 (2014), p. 015. DOI: 10.22323/1.187.0015. arXiv: 1401.3270 [hep-lat].

[145] Ernst Carl Gerlach Stueckelberg de Breidenbach and Andreas Petermann. "Normalization of constants in the quanta theory". In: *Helv. Phys. Acta* 26 (1953), pp. 499–520. DOI: 10.5169/seals-112426.

[146] Leonard Susskind. "Lattice Models of Quark Confinement at High Temperature". In: *Phys. Rev. D* 20 (1979), pp. 2610–2618. DOI: 10.1103/PhysRevD.20.2610.

[147] K. Symanzik. "Continuum Limit and Improved Action in Lattice Theories. 1. Principles and φ^4 Theory". In: *Nucl. Phys. B* 226 (1983), pp. 187–204. DOI: 10.1016/0550-3213(83)90468-6.

[148] K. Symanzik. "Small distance behavior in field theory and power counting". In: *Commun. Math. Phys.* 18 (1970), pp. 227–246. DOI: 10.1007/BF01649434.

[149] M. Testa. "Some observations on broken symmetries". In: *JHEP* 04 (1998), p. 002. DOI: 10.1088/1126-6708/1998/04/002. arXiv: hep-th/9803147.

[150] T. Toimela. "The Next Term in the Thermodynamic Potential of QCD". In: *Phys. Lett. B* 124 (1983), pp. 407–409. DOI: 10.1016/0370-2693(83)91484-3.

[151] Anastassios Vladikas. "Three Topics in Renormalization and Improvement". In: *Les Houches Summer School: Session 93: Modern perspectives in lattice QCD: Quantum field theory and high performance computing*. Mar. 2011, pp. 161–222. arXiv: 1103.1323 [hep-lat].

[152] Steven Weinberg. "New approach to the renormalization group". In: *Phys. Rev. D* 8 (1973), pp. 3497–3509. DOI: 10.1103/PhysRevD.8.3497.

[153] Steven Weinberg. *The Quantum theory of fields. Vol. 1: Foundations*. Cambridge University Press, June 2005. DOI: 10.1017/CBO9781139644167.

[154] P. Weisz. "Renormalization and lattice artifacts". In: *Les Houches Summer School: Session 93: Modern perspectives in lattice QCD: Quantum field theory and high performance computing*. Apr. 2010, pp. 93–160. arXiv: 1004.3462 [hep-lat].

[155] Kenneth G. Wilson. "Confinement of Quarks". In: *Phys. Rev. D* 10 (1974). Ed. by J. C. Taylor, pp. 2445–2459. DOI: 10.1103/PhysRevD.10.2445.

[156] Kenneth G. Wilson. "Quarks and Strings on a Lattice". In: *13th International School of Subnuclear Physics: New Phenomena in Subnuclear Physics*. Nov. 1975.

[157] R. Wohlert. "IMPROVED CONTINUUM LIMIT LATTICE ACTION FOR QUARKS". In: (July 1987).

[158] Ulli Wolff. "Monte Carlo errors with less errors". In: *Comput. Phys. Commun.* 156 (2004). [Erratum: Comput.Phys.Commun. 176, 383 (2007)], pp. 143–153. DOI: 10.1016/S0010-4655(03)00467-3. arXiv: hep-lat/0306017.

[159] L. G. Yaffe and B. Svetitsky. "First Order Phase Transition in the SU(3) Gauge Theory at Finite Temperature". In: *Phys. Rev. D* 26 (1982), p. 963. DOI: 10.1103/PhysRevD.26.963.

[160] N. Yamada et al. “Non-perturbative O(a)-improvement of Wilson quark action in three-flavor QCD with plaquette gauge action”. In: *Phys. Rev. D* 71 (2005), p. 054505. DOI: 10.1103/PhysRevD.71.054505. arXiv: hep-lat/0406028.

[161] Cheng-xing Zhai and Boris M. Kastening. “The Free energy of hot gauge theories with fermions through g**5”. In: *Phys. Rev. D* 52 (1995), pp. 7232–7246. DOI: 10.1103/PhysRevD.52.7232. arXiv: hep-ph/9507380.